THE UNIVERSITY OF HULL

INVESTIGATION OF A NOVEL SOLAR ASSISTED HEAT RECOVERY HEAT PUMP SYSTEM FOR BUILDING SPACE HEATING AND HOT WATER SUPPLY

being a Thesis submitted for the Degree of Doctor of Philosophy at the University of Hull

by

Yi Fan

MSc Taiyuan University of Technology, China

BEng Taiyuan University of Technology, China

November 2020

CONTENTS INDEX

ABBREVIATIONS

HVAC	Heating, ventilation and air conditioning
COP	Coefficient of performance
DHW	Domestic hot water
SAHP	Solar-assisted heat pump
ASHP	Air source heat pump
HSEU	Heat storage and exchange unit
SAHR-HP	Solar-assisted heat recovery heat pump
VIHR-ASHP	Vapour injection heat recovery air source heat pump
R&D	Research and development
IM	Iterative method
PDE	Partial differential equation
FEM	Finite element method
LCA	Life-cycle assessment
VI	Vapour injection
HRD	Heat recovery device
FER	Free energy ratio
SPF	Seasonal performance factor
SF	Solar Fraction
PVT	Photovoltaic/thermal
FPC	Flat plate collectors
USC	Unglazed solar collectors
ETC	Evacuated tube collectors
FPAC	Flat plate air collector
FPLC	Flat plate liquid collector
CPVT	Concentrating photovoltaic thermal
PFHE	Plate-fin heat exchanger
EER	Energy efficiency ratio
EEV	Electronic expansion valves
IHX	Internal heat exchanger
VIL	Vapour injection line
VILA	Vapour injection line EEV aperture
EL	Evaporation line
ELA	Evaporation line EEV aperture
HX	Heat exchanger
EV	Expansion valve
LCA	Life cycle assessment

ABSTRACT

With the rapid increment of energy consumption worldwide, the caused environmental contamination and global warming desperately necessitate the further development of renewable energy technologies. This study aims at presenting an in-depth investigation of a novel solar-assisted heat recovery heat pump (SAHR-HP) system for heating, cooling and domestic hot water (DHW) supply to resolve some barriers of the existing solar-assisted heat pump (SAHP) technologies, which include (1) performance reduction on the rear collectors of a solar collectors array; (2) poor performance at low ambient temperature; (3) long responding time due to the huge volume of the heat storage and exchange unit (HSEU); and (4) weak of strong complementarity between solar collector and heat pump. According to the barriers, the novel SAHR-HP system incorporates (1) a new designed mini-channel solar thermal collector with three inlets and outlets that can be connected with other solar collectors flexibly; (2) a solar collectors array with a novel multiple-throughout-flow connection method that can simultaneously increase the overall solar thermal efficiency and reduce the flowing resistance; (2) a novel vapour injection heat recovery air source heat pump (VIHR-ASHP) that can use both the exhausted air and the ambient air, thus leading a considerable performance increase of the heat pump in cold weather; (3) a novel fast-responding double-layered HSEU that can significantly shorten the response time.

The study combined theoretical analysis and experimental and simulative investigation, including the following elements; a critical literature review, optimal preliminary design, theoretical analysis, the development of simulation models, prototype construction, laboratory-controlled and field testing, validation and performance optimisation of the simulation models, energy performance, economic performance and environmental influence analysis.

The proposed SAHR-HP system has a COP from 3 to 8 according to the weather

conditions. The multiple-throughout-flowing connection can improve solar thermal efficiency of a solar collectors array by 10% when compared with that of the conventional one-to-one connection. The novel HSEU can decrease the responding time to 20mins compared with the 3 hours of the conventional HSEU with the same heat storage volume. Particularly, the VIHR-ASHP can save about 23% of electricity consumption as compared with a conventional ASHP at normal operation conditions of condensation temperature of 45°C and an ambient temperature of -10°C. A lower ambient temperature will increase its advantages over conventional air source heat pump and vapor injection heat pump. The integral test results indicated that the SAHR-HP system can perform in perfect union with the coordinative operation between different parts of the system under any environmental conditions. The energy performance and the economic and environmental analysis illustrated that this system could efficiently provide enough energy for space heating, cooling and DHW with high energy performance in cold climatic regions, such as Chongqing, Taiyuan and Urumqi. Compared with the coal-driven system, the novel system has a cost payback period of 13.8 years, 12.37 years, and 17.85 years in Chongqing, Taiyuan, and Urumqi and a life-cycle net cost saving of nearly 16145.84RMB, 20317.82RMB, and 9002RMB. Furthermore, the system reduces the emission of many other harmful substances, i.e., dust, SO_2 and NO_x, and is therefore a desirable approach for environment sustainability and clean air. Besides, the results can be extended to most cold areas worldwide, i.e., The UK and the European countries.

The research results are expected to configure feasible solutions for future SAHP technologies. The wide promotion of these core technologies worldwide could significantly reduce the consumption of fossil fuel and the associated carbon footprint in a built-up environment, thus providing a more ecological environment.

PUBLICATIONS

Book Chapter

Xudong Zhao, Yi Fan, Advanced Energy Efficiency Technologies for Solar Heating, Cooling and Power Generation - Chapter 15：Solar Heating, Cooling, and Power Generation Projects — Case Studies, ISBN 978-3-030-17283-1, *Springer-Verlag London 2019*; 487-539

Journal Publications

[1] Fan Y, Zhao X, Li J, Li G, Myers S, Cheng Y, et al. Economic and environmental analysis of a novel rural house heating and cooling system using a solar-assisted vapour injection heat pump. Appl Energy 2020;275:115323. https://doi.org/10.1016/j.apenergy.2020.115323.

[2] Fan Y, Zhao X, Li G, Cheng Y, Zhou J, Yu M, et al. Analytical and experimental study of an innovative multiple-throughout-flowing micro-channel-panels-array for a solar-powered rural house space heating system. Energy 2019;171:566–80. https://doi.org/10.1016/j.energy.2019.01.049.

[3] Fan Y, Zhao X, Li J, Cheng Y, Badiei A, Zhou J, et al. Operational performance of a novel fast-responsive heat storage/exchanging unit (HSEU) for solar heating systems. Renew Energy 2020;151:137–51. https://doi.org/10.1016/j.renene.2019.11.007.

Patents

1. Xudong Zhao, Jing Li, Yi Fan, Exhausted air vapour injection air source heat pump, UK patent, Application No 1916710.5, 20/11/2019.

2. Xudong Zhao, Jing Li, Yi Fan, Fast response heat storage and exchange unit, UK patent, Application No 1913520.1, 23/09/2019.

Presentations/posters/showcases

No.	Conference	Presentation
1	ICAE2019: The 11th International Conference on Applied Energy, Vasteras, Sweden	Solar-assisted heat recovery heat pump system
2	The First Chinese International Conference on Energy and Artificial Environment, 20-22.07.2019, Chengdu, China	Vapour injection heat recovery heat pump simulation
3	The 11th International Symposium on Heating, Ventilation and Air Conditioning (ISHVAC), 12-15.12.2019, Harbin, China	Vapour injection heat recovery heat pump experiment
4	2019 Researcher Links Workshop on Investigation of the Impact of Occupant Behaviour on Building Performance in the UK and China, 3-5.06.2019, Coventry, United Kingdom	The preliminary design of a novel vapour injection heat recovery heat pump
5	7th China Building and Environmental Conference, 18-19.10.2018, Taiyuan, China	Novel mini-channel solar thermal collector design
6	SET2018: 17th International Conference on Sustainable Technologies, 21-23.08.2018, Wuhan, China	Novel mini-channel solar thermal collector with multiple-throughout-flowing connection
7	EU-China Symposiums on Renewable Energy, Energy Efficiency, and Phase Change Energy Storage Technologies, 30.07.2018, Hull, UK	The design concept of solar-assisted heat pump system

8	UK-China Innovative Building Renewable Energy and Latent Heat Thermal Energy Storage Technologies, 9-11.10.2017, Chengdu, China	The novel fast-responding stratified heat storage and exchange unit
9	SET2017: 16th International Conference on Sustainable Technologies,17-20.07.2018, Bologna, Italy	The simulation of a novel fast-responding stratified heat storage and exchange unit

ACKNOWLEDGEMENTS

I would like to express my sincere and heartfelt gratitude to my supervisor, Professor Xudong Zhao, giving me ultimate and unlimited support and guidance, as well as his patience, motivation, immense knowledge and enthusiastic involvement throughout the whole process of my PhD research. His rigorous attitudes, which always inspire me to pursue the truth. From the initial to the final stage, his encouragement, advice and assistance will be with me in my rest of life.

I would also like to thank Dr Jing Li who gives me a lot of enlightening guidance and teach me how to do an in-depth research independently.

I especially appreciate the supportive works from Dr. Steve Myers and Dr. Ali Badiei for their assistance on the paper writing and proofreading my thesis.

I wish to thank the University of Hull, the Department for Business, Energy & Industrial Strategy (BEIS) - Low Carbon Heating Technology Innovation Fund 2018 Project.

Finally, I wish to thank and dedicate this thesis to my wife and parents for their unselfish, endless love, care and encouragement. I could never have accomplished so much without them.

LIST OF FIGURES

LIST OF TABLES

LIST OF TABLES

A	area (m^2)	Cp	heat capacity of the working fluid (kJ/kg·°C)
C_r	ratio of the minimal heat capacity to maximum heat capacity in heat exchanger	D	diameter (m)
F	fin efficiency	F'	efficiency factor of mini-channel solar thermal collector
F_R	thermal transfer factor of mini-channel solar thermal collector	g	acceleration of gravity (m/s^2)
g_m	inflation rate	h_m	local resistance (m)
h	enthalpy (kJ/kg)	h_c	convective heat transfer coefficient ($W/m^{2}\cdot°C$)
h_f	frictional resistance (m)	I	solar radiation (W/m^2)
K_m	heat transfer coefficient of the underfloor coil ($W/m^{2}\cdot°C$)	L	length (m)
m	mass flow rate (kg/s)	N_{com}	revolving speed of the compressor (r/min)
NTU	heat transfer units	Nu	Nusselt number
Pr	Prandtl Number	$Q_{\Delta t}$	heat transfer capacity (kWh)
q	heat transfer capacity (W/m^2)	Q	heat transfer power (W)
q'	heat transfer capacity per meter (W/m)	Re	Reynolds number
ΔT_m	logarithmic mean temperature difference (°C)	T	temperature (°C)
U	heat loss coefficient ($W/m^{2}\cdot°C$)	V	volume (m^3)
v	velocity of the fluid (m/s)	W	power consumption of a device (W)
x_{hp}	ratio of the ventilation heat loss to the heat supply	y_{hp}	mass flow ratio of ambient air to exhaust air
z	annual maintenance cost	α	absorptivity of the glass layer
λ	thermal conductivity coefficient of the working fluid (W/m·°C)	μ	viscosity of the working fluid (Pa·s)
η	efficiency	ρ	density (kg/m^3)
ε	heat transfer/exchange efficiency	ζ	resistance coefficient of the local resistance
τ	transmittance of the glass layer	δ	thickness of the wall (m)
Subscripts			
a	ambient	b	bottom

cl	cooling load	com	compressor
conv	conventional	con	condensation
e	east	exp	experimental
eva	evaporation	en	envelop of the building
exc	exchange coil pipe	ex	exhausted air
f	fluid	hl	heating load
hex	heat exchange	is	isentropic
in	inlet	inj	injection
il	insulation layer	ip	in the pipe
mo	motor	mtf	multiple-throughout-flowing connection method
mch	mini-channel	me	mechanical
nov	novel	n	north
op	out of the pipe	oto	one-to-one connection method
out	outlet	p	pipe
pa	number of the panel	run	number of the runner in a panel
ref	refrigerant	rep	report
suc	suction	sph	single phase
s	south	sp	solar panel
tph	two-phase	th	theoretical
tot	total	t	tank
ufc	under floor coil	v2	vapour injection compressor high pressure camber
ven	ventilation	v1	vapour injection compressor low pressure camber
wa	water	w	west
wf	working fluid		

CHAPTER 1: INTRODUCTION

1.1 Research Background

In recent years, the problems caused by global warming and environmental pollution have been attracting a great deal of attention [1]. According to research, the environmental pollution problems have various direct adverse health effects on human lives [2]. The morbidity and mortality of the environmental particulate exposure have been demonstrated by numerous studies have led to an increased risk of many diseases (e.g., organ disturbances, cancers and other chronic diseases) [3]. In addition, the other environmental problem, global warming, can also impose harmful consequences, i.e., extreme weather conditions (e.g., heat waves and tropical cyclones), flooding, drought and wildfires. Consequently, this has strongly affected natural biological systems. Despite the numerous harmful results caused by global warming, the current warming trend has been proceeding under an uncontrollable space since the mid-twentieth century [4]. Specifically, the average surface temperature of the earth has increased by approximately 2.05 degrees Fahrenheit (1.14 degrees Celsius) since the 1890s. This significant change has resulted from the increased greenhouse gas emissions into the atmosphere [5].

The increasing carbon dioxide and other emissions are mainly caused by power generation systems using fossil fuels. Along with the development of the human society, the total energy consumption is increasing gradually from 1800 to 2019, as shown in Fig. 1-1. In 2019, the fossil fuel consumption reached 147982TWh and accounted for 93% of the total energy consumption worldwide, which means that the main energy consumption is still from the fossil fuel. By contrast, the share of the renewable energy has increased over several recent decades, yet it only accounts for 7% of the total energy consumption worldwide, thus giving a huge potential for the development of the renewable energy to slow down the speed of global warming and

relieve the environmental pollution problems.

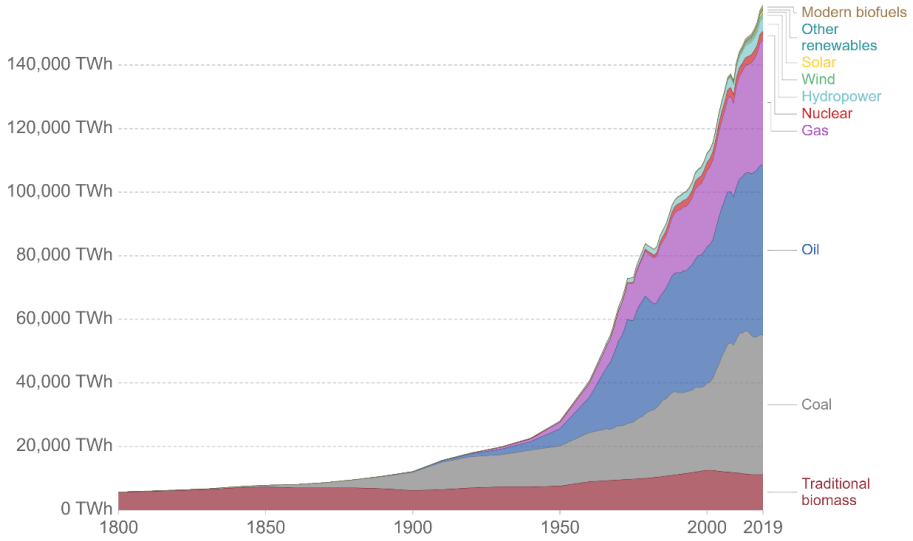

Fig. 1-1 Global direct primary energy consumption [6]

The share of primary energy from fossil fuels in different countries around the world in 2019 is shown in Fig. 1-2. Several countries such as, for example, Canada, New Zealand, Brazil and some other countries in Europe performed outstandingly in their use of renewable energy. However, most countries are still mainly relying on fossil fuels as their energy source.

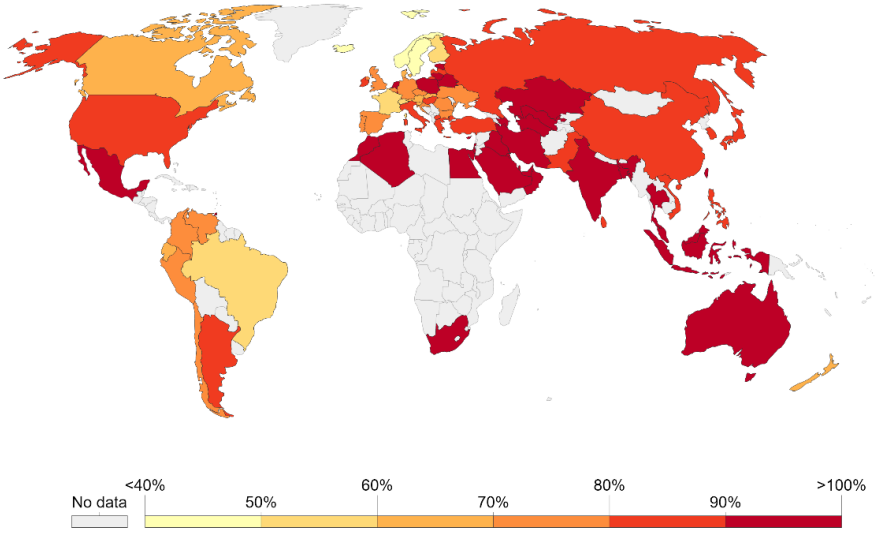

Fig. 1-2 The share of primary energy from fossil fuels different countries worldwide

With the increasing global warming concerns and the increasing contribution of building energy consumption, building energy efficiency has become the focus of worldwide attention [7]. The reason for this is because the buildings sector accounts for 39.8% of the total energy consumption and about 58% of the world's electricity when looking at the total consumed energy [8]. Among all building services, Heating, Ventilation and Air Conditioning (HVAC) systems are responsible for most building energy consumption [9]. A typical HVAC system takes up approximately 41% of the total building energy consumption and accounts for around 69.5% of the base building consumption. Thus, improving the energy performance of HVAC systems plays an essential role in improving the energy efficiency of buildings, reducing the energy consumption and providing habitable indoor environments for the occupants [10]. There are many factors which can determine the energy demand of HVAC directly, e.g., indoor pre-set temperature points, window type, window-wall ratio, fresh air load, building type, and climate and internal loads [11]. In addition, control strategy and optimisation method are the key factors that create an efficient HVAC system [12]. Many articles have emphasised the enhancement of the building energy efficiency through adjusting and optimising the control algorithms [13–15]. Insulation of a building, e.g., for the wall, roof, windows and ground, is also a key factor of an HVAC system's energy performance [16]. According to the heat transfer mechanisms, the insulation is classified into two types: thermal mass insulation and reflective insulation, which have been widely investigated and shown to improve the building efficiency [17,18].

Other than the aforementioned methods of improving the efficiency of an HVAC system, a heat pump, using the grid electrical energy and a commonly available low-grade energy source, can provide a stable and steady heat supply capacity to buildings and infrastructures, and has been widely used in HVAC systems to improve its efficiency. Heat pumps capture energy from renewable energy sources (air, ground and water) and is known as the most promising pieces of technology in increasing the energy efficiency in both residential and commercial buildings. According to a report

from the European Union, by 2020, the heat pump should help to increase the improvement of energy efficiency by 20% [19].

Despite the improved performance of the HAVC system by using heat pump technologies, the long period of operation and low grade (temperature) energy source which means the energy source has low energy transformation ratio (e.g., ambient air, water and ground) will reduce the energy efficiency of the heat pump significantly, leading to a lower coefficient of performance (COP) in the range 1.7 to 3.2. To improve the efficiency of the building further, solar energy technologies are widely investigated and are used to mitigate energy consumption from the HVAC in buildings within a short time period [20]. As an economical, non-polluting and readily-available energy source, the solar-powered system provided just 1.2%, 1.5% and 1.6% of the energy consumption in China, the UK and the EU respectively in 2018 [21–23]. From this perspective, the market potential for developing and implementing energy efficient and cost-effective solar heating systems is enormous. A single solar heating system has been widely applied to the domestic hot water (DHW) supply owing to its simple structure, low cost, stability and effective energy collection. However, its application in space heating is largely limited by the mismatch between the energy supply and demand, on daily and seasonal bases.

Accordingly, a combination of solar collectors and the pump is proposed, producing solar assisted heat pump (SAHP) systems, which can overcome the problems remaining in an independent solar heating system (i.e., a mismatch between heat supply and demand) or a single heat pump (i.e., low energy efficiency and high electrical bill), thus forming an energy efficient, stable, reliable and cost-effective heating system for the buildings and infrastructures. The high sensitivity for the variation of the environment and the flexibility configuration are also the advantages of solar SAHP systems. This kind of system, namely the SAHP, has attracted wide attention globally, and associated research, development and applications have been emerging rapidly over the past few decades. Hence, significant progress in SAHP

research and development has been made over recent years.

To date, there are around 90 companies running the SAHP related business globally [24]. In the UK, several companies, including SAHP [25], Eco Greenenergy Solutions [26], Energy How UK [27] and Arkaya Energy Limited [28] provide small scale direct-expansion SAHP technologies that, in conjunction with the roll-bond uncovered solar collectors, provide DHW and space heating for the residential houses. In Europe, there are numerous industry-dominated consortiums, e.g., SunHorizon [29] and HEAT4COOL [30], which are dedicated to promoting the development of the SAHP systems. SunHorizon is an ongoing EC-funded SAHP project which is aiming to demonstrate eight innovative SAHP systems in selected counties from the EU. Through the smart combination of the standard business development and innovation-driven technologies demonstration, the SAHP is expected to experience a dramatic growth over the next few decades.

Apart from the substantial market demand, the government policies also play an important role in promoting SAHP development. In the UK, the government declared that fossil fuel heating could be banned in all newly built homes after 2025. Furthermore, the EU requires the implementation of either heat pump or solar energy technologies for DHW production in 2027 [31]. China has committed to cutting its carbon emissions by 50% to 60% per unit GDP by 2030, which will be achieved by promoting the use of renewable energy and reducing the use of fossil fuel coal [32]. In the U.S., federal and state governments have established numerous policies to promote clean energy over the past four decades [33].To achieve the reduction plan in fossil fuel consumption, the air source heat pump (ASHP) is a key technology that can help these countries to fulfil the commitments for carbon emission.

However, in contrast to the achievement of SAHP, some challenges should be also noticed and improved. First of all, it is obvious that a single solar panel cannot provide sufficient heat with a suitable outlet temperature to fulfil the energy demand of a large

building. Accordingly, a solar collectors array in series connection comprising numerous panels is applied [34]. The conventional series connection is arranged in a one-to-one connection. Within such an array, panels are always connected one after another. This connection manner creates a continuous temperature rise along the flow path. On the rear panels of the array, the fluid temperature reaches a very high level, which is especially the case for the large-sized collectors array. As a result, the solar thermal efficiency of the rear panels will be significantly lower or even become a negative figure, owing to the inverse correlation between the panels' solar thermal efficiency and the temperature of the fluid across the panels. Therefore, the overall solar thermal efficiency of the array is smaller when the number of panels in the array is larger. Secondly, the heating demand is always low in the daytime and high at night. By contrast, the solar energy resource is high in the daytime and low at night, thus leading to the daily energy discrepancy between the solar energy supply and the energy demand. A compatible heat storage tank can mitigate this daily discrepancy. However, the existing heat storage and exchange units (HSEUs) are based on a single large-sized water tank which is embedded with heat exchanging coils for heat transfer from the solar panel-array to the bulk of tank water. In general, the heat from the solar panels and heat pump is first stored in the tank, and then released for space heating and DHW generation [35]. The huge volume of water leads to a significant delay in the reaction of the system to the variation in the indoor and outdoor environments, thus giving a great thermal discomfort to the occupants, especially when heating is required urgently, hence the heat pump must be brought into use which leads to a significant waste of electricity. Last but not least, with the reduction of outdoor temperatures in cold climate conditions, the SAHP system will encounter the reduction of the performance [36]. In addition, according to the daily variation tendency of the solar radiation and the ambient temperature which is high in the daytime and low at night, the performance of a SAHP system has a huge performance difference when between the daytime and night-time operations.

To solve the aforementioned challenges, this study proposed an innovative (SAHR-

HP) system which comprises three novel-designed components, i.e., a solar collectors array with a multiple-throughout-flow connection method, a novel double-source heat pump using the vapour injection and enthalpy increasing compressor, and a fast-responding heat storage/exchange unit. The system can greatly improve the solar thermal efficiency of the embedded solar collectors array, enhance the performance of the system under cold climate conditions and increase the reaction speed of the system to the variation of the indoor and outdoor environments. Eventually, the system has an excellent adaptation to any buildings and climate conditions. Moreover, the system also has a high energy efficiency and a low energy consumption, which can greatly alleviate the environmental pressure and air contamination.

1.2 Research Aim and Objectives

The investigations concerning the SAHP technologies have been conducted for decades and have produced many achievements. However, some critical challenges still remain and severely restrict the development of the SAHP technologies, such as low efficiency under cold ambient temperatures, an insufficient energy supply, daily and seasonal heat discrepancy, and an unbalanced heating supply. In addition, in order to improve the performance of the heat pump and reduce the energy waste in the ventilation system further, the aim of this investigation focuses on developing a novel solar-assisted heat recovery heat pump (SAHR-HP) system, which includes a detailed preliminary design, experimental platforms installation and a simulation model set-up. To achieve this research objective, six inter-relevant objectives are set up in this research as follows:

(1) To conduct an extensive literature review of SAHP and the relevant components technologies, recognise the practical challenges and propose solutions for the relevant challenges;

(2) To propose a preliminary SAHR-HP system design which incorporates the relevant research questions and approaches for solving the questions;

(3) To conduct the theoretical analysis and build up computer simulation models to simulate the performance of the SAHR-HP system and optimise the system structurally, including the steady models for system components and the dynamic simulation models for the integrated SAHR-HP system;

(4) To explain the construction method of the SAHR-HP system and its components, set up the experimental platforms for the system and evaluate the performance of the system by using the experimental data;

(5) To validate the simulation models of the SAHR-HP system, and conduct the simulation process to evaluate, optimise and enhance the performance of the system;

(6) To conduct an annually dynamic simulation of the SAHR-HP system, and evaluate the energy performance, economic and environmental influence of the integrated SAHR-HP system.

1.3 Description of the Research Concept

The initiative concept of the novel SAHR-HP system is to use multiple energy sources, i.e., electricity, solar energy, ambient air and wasted heat from the building ventilation system. Three energy sources are renewable energy that can increase the efficiency of the system greatly. The SAHR-HP system contains three major innovative parts to improve the energy usage from the renewable energy and reduce the electricity consumption. These include a novel mini-channel solar thermal collectors array with multiple-throughout-flow connection, a novel vapour injection heat recovery air source heat pump (VIHR-ASHP), and a newly-designed HSEU. The integral system can increase the solar thermal efficiency of the solar thermal collectors array significantly, the stratification of the novel HSEU, and fully use the wasted heat from the exhausted air. The system can provide space heating, hot water supply, ventilation and cooling. The visualisation scheme of the SAHR-HP system is shown in Fig. 1-3.

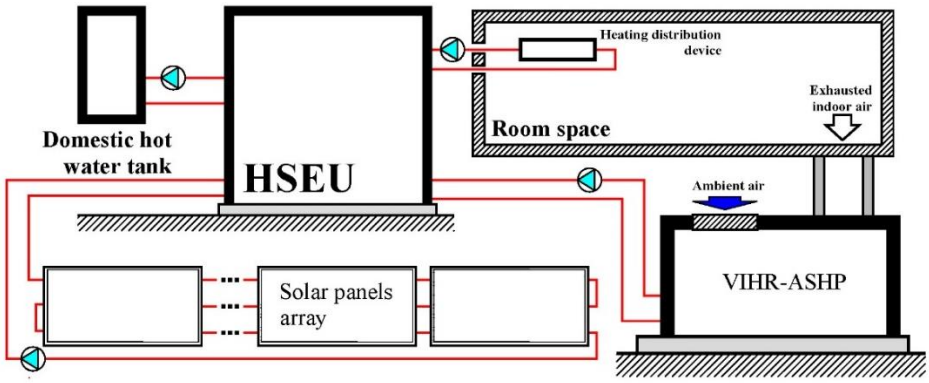

Fig. 1-3 The visualisation scheme of the solar system

The flexible operation scheme can also increase the adaptation and economy properties of the system. When there is enough solar radiation during the daytime, the solar collectors array is in operation to transfer the collected heat in the HSEU. The HSEU then provides energy for space heating and to the domestic water tank. While the collected solar energy surpasses the heating demand of the system, the novel HSEU can change the operating mode and store the spare heat automatically. The stored heat is used for space heating during the night when there is no solar radiation, and the room temperature is low. After the stored heat is used up, the system can operate the VIHR-ASHP to provide space heating to the served building. Consequently, the SAHR-HP system can flexibly store and transfer the generated heat of the solar energy conversion module and the VIHR-ASHP, thus eliminating the daily heat load discrepancy of the served building. The combination of these devices is expected to initiate a low energy consumption HVAC system driven by solar, air and exhausted energy.

1.4 Research Methodology

The proposed project aims to develop a new SAHR-HP system for heating, cooling and hot water supplying. This typically applied research followed the basic investigation procedure of system set-up, model validation and system optimisation.

The approaches to achieve the scientific aims and technological objects were as follows: (1) literature review and research questions identification (objective 1); (2) preliminary design of the SAHR-HP system (objective 2); (3) theoretical analysis and computer simulation models (objective 3); (4) components construction and experimental testing of the novel SAHR-HP system (objective 4); (5) computer model validation and simulation of the novel SAHR-HP system (objective 5); (6) energy performance evaluation, economic and environmental analysis (objective 6). Apparently, the approaches 1 and 2 included concept formation and preliminary design, while to investigate, analyse and optimise the SAHR-HP system further, the inter-linked approaches 3, 4, 5 and 6 were designed to do the relevant research, i.e., theoretical, experimental and socio-economic analysis progressively (as shown in Fig. 1-4). These approaches and the correlated objectives are presented briefly below.

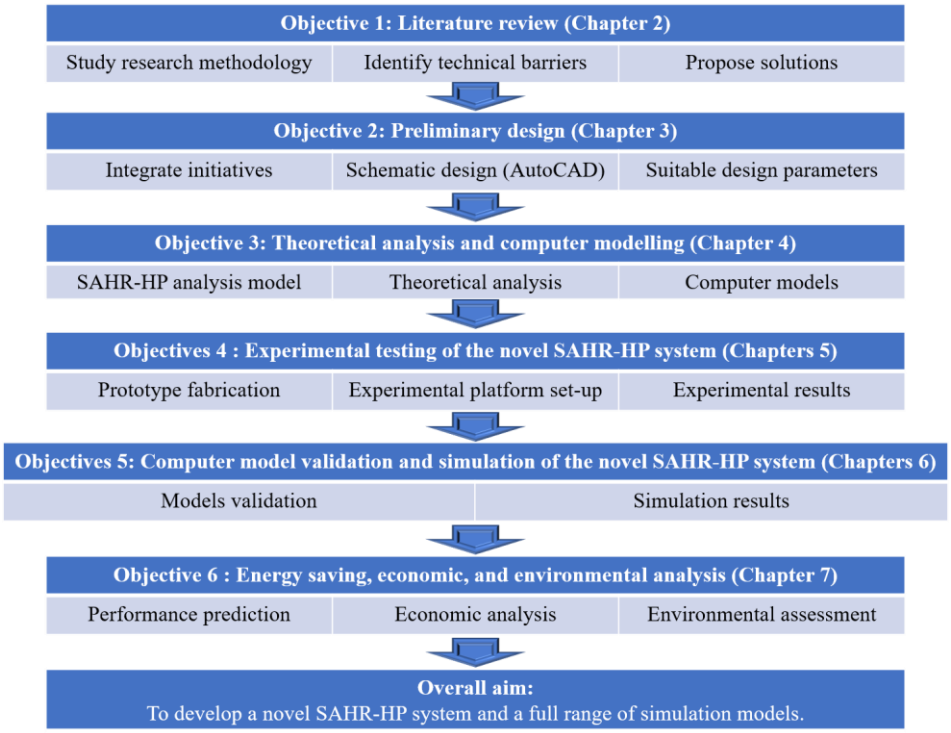

Fig. 1-4 Schematic of the research methodology

1.4.1 Approach to objective 1 – Literature review and research questions, identification of SAHP technology to identify potential challenges and relevant solutions

This approach would (1) characterise the conceptual SAHP structure, classification, operational mechanism and research methodology; (2) include the research and development (R&D) and the practical applications of existing SAHP reviews, both quantitatively and qualitatively; (3) characterise critical features of the SAHP components, investigation highlights and technical challenges regarding existing SAHP technologies; (4) propose possible solutions for breaking the theoretical and technical barriers. This approach would help to recognise the current research progress of SAHP technologies and build up basic knowledge for the rest of the objectives.

1.4.2 Approach to objective 2 – Preliminary design of the SAHR-HP system

This approach would (1) give the schematics of the SAHR-HP system and its components; (2) illustrate the control strategy and working principle of the proposed SAHR-HP system; (3) detail the type and geometric size of the components of the SAHR-HP system. This approach would illustrate the preliminary design of the system and set up the foundation for objectives 3, 4 and 5.

1.4.3 Approach to objective 3 – Theoretical analysis and computer simulation models

This approach would (1) conduct the fundamental theoretical analysis by using a mathematical approach to discover the heat transfer processes and the relevant energy balances existing in different components of the SAHR-HP system; (2) develop computer simulation models for components of the system on the basis of the iterative method (IM), partial differential equation (PDE) and finite element method (FEM) to characterise the components performance of the SAHR-HP system, which would evaluate the performance of the system and the relevant components against different

variables, and clarify the optimum design of the configuration and operational parameters; (3) develop a dynamic system simulation model by combining the computer models for the components and the corresponding heat transfer processes together to evaluate the system performance, which would predict the performance of the SAHR-HP system under real climate conditions, and then predict the annual system performance. This approach would produce an optimised SAHR-HP system design, experiment validation and the socio-economic analysis which will be undertaken in the following approaches.

1.4.4 Approach to objective 4 – Experimental testing of the novel SAHR-HP system

This approach would (1) illustrate the detailed fabrication methods for the components prototypes of the SAHR-HP system in practice; (2) construct the system and the relevant experimental platforms according to the design; (3) analyse the experimental results of the VIHR-ASHP under laboratory conditions; (4) characterise the performance of the SAHR-HP system under the real-time climate change conditions.

1.4.5 Approach to objective 5 – Computer model validation and simulation of the novel SAHR-HP system

This approach would (1) verify the computer models derived from objective 3; (2) simulate the performance of the components of the SAHR-HP system to optimise the numerical models and the relevant system components.

1.4.6 Approach to objective 6 – Energy performance, economic and environmental analysis

This approach would conduct the annual dynamic system simulation model to evaluate the operational and energy performance of the SAHR-HP system and discuss its economic performance by using the life-cycle assessment (LCA). The environmental

performance of the system under a typical climatic region would be analysed. This approach would evaluate the benefits and impact of the proposed system. The relevant parameters include the payback period, life-cycle cost saving and carbon emission reduction.

1.5 Novelty and Added Value of the Novel SAHR-HP System

A novel solar-assisted heat recovery air source heat pump system (SAHR-HP) is proposed to supply the heating, cooling and DHW by using solar energy, exhausted heat and ambient air energy. In terms of structure, the system contains three innovative parts: (1) a mini-channel solar thermal collectors array with a novel multiple-throughout-flow connection method; (2) a novel double-source heat pump using the vapour injection and enthalpy increasing compressor; (3) a novel fast responding heat storage and exchange unit that can significantly shorten the response time to heat demand of building (3 hours vs. 20 minutes). The dynamic integration of the components leads to the increased solar thermal efficiency and increased COP of the heat pump, thus giving the whole system an enhanced performance. The unique qualities and added value of the three innovative parts of the novel SAHR-HP system are as follows. In terms of materials, the mini-channel solar thermal collector applied a combination of new materials to combine the solar absorption plate and the mini-channel together. The materials include the thermal conductive adhesive and the structural adhesive. In terms of system simulation/optimisation, a novel dynamic system operation status forecasting method will be developed. This method will create a dynamic system computer model for the entire SAHR-HP system which can forecast the system operation status and change the heat transfer processes between the components of the SAHR-HP system, thus giving a great potential for increasing the efficiency of the system by optimising the control strategy.

1.5.1 Multiple-throughout-flow connection method

The innovative multiple-throughout-flow mini-channel collectors array is applicable

to a solar-powered heating system, as shown in Fig. 1-5.

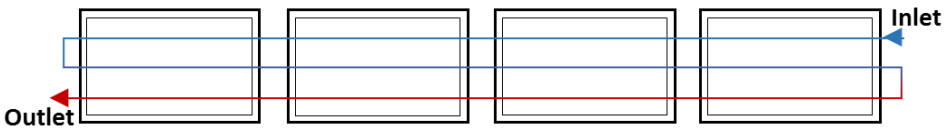

Fig. 1-5 Schematics of the multiple-throughout-flow solar collectors array

The novel multiple-throughout-flow connection method is the first time for the proposal of a new connection method to improve the overall performance of the solar thermal collectors array, and compared to the conventional one-to-one connection method, the novel connection method can (1) reduce the temperature difference between the head and rear panels, which can significantly increase the overall efficiency of the collectors array; (2) reduce the flow resistance of the fluid across the collectors array by reducing the turning number of fluid within the panels.

1.5.2 Novel double-source heat pump using the vapour injection and enthalpy increasing compressor

The novel vapour injection heat recovery air source heat pump (VIHR-ASHP) with two evaporators claims to be a more enhanced energy performance compared to the traditional pumps. This is the first time that a VI compressor has been used for waste heat recovery of exhaust air from the buildings. The heat pump has a unique indoor/outdoor air mixing process by using two evaporators, which makes it possible for the heat pump to collect heat from both the exhaust air and fresh air, thus removing the heating capacity restrictions associated with the limited volume flow rate of the exhaust air. The additional evaporator in the vapour injection line increases the heat transfer capacity and refrigerant mass flow rate, leading to a lower final compression ratio. In addition, utilising the exhaust air to defrost the heat pump significantly decreases the defrosting time and energy consumption. Consequently, the proposed novel VIHR-ASHP provides a new design of the heat recovery device (HRD) with

enhanced performance, flexibility and feasibility. This system can be applied widely to building ventilation systems in order to reduce energy consumption.

1.5.3 Fast responding heat storage/exchange unit to reflect the variation of the building's heat demand

A novel stratified heat storage/exchanging unit (HSEU) employing a double-tank configuration was developed, as shown in Fig. 1-6.

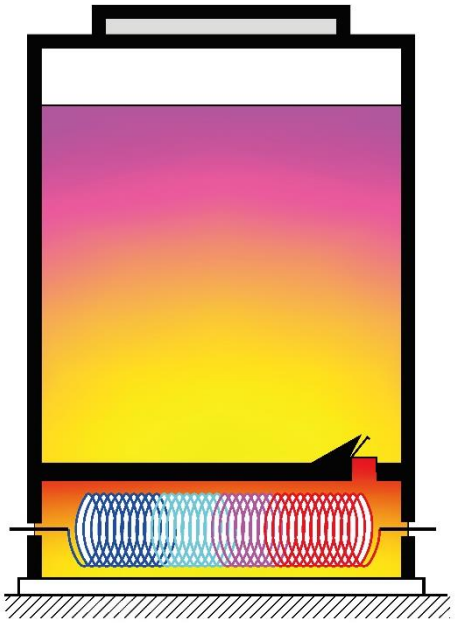

Fig. 1-6 Schematics of the HSEU

The new HSEU comprises a small tank (bottom part) for heat exchange combined with a large tank (upper part) for heat storage. It is the first time that a water storage tank consisting of the solar heat coils has been divided into two chambers; one of these is for heat transfer and the other is for heat storage. The thermal storage has a unique control strategy to fulfil the consumers' demands for space heating and DHW supply. The new interactive fast responding HSEU can provide heat to the served space in around twenty minutes, thus creating a heating system which can respond significantly faster than traditional systems. In addition, the solar thermal efficiency of the solar

panel-array in the new HSEU based system increased when compared to conventional HSEU based systems.

1.6 Thesis Structure

Chapter 1 – Introduction: this chapter briefly describes the research background, significance, objectives, research concept, methodology and novelty.

Chapter 2 – Literature review: this chapter involves an extensive review of the existing SAHP technologies, including basic concept, system classification, components development, evaluation standards, R&D processes and practical applications. In addition, the current challenges remaining in the existing SAHP technologies are analysed. Accordingly, the potential improvements and opportunities are studied.

Chapter 3 – Preliminary design: this chapter sets up the preliminary design of the SAHR-HP system and the key components. The working principle and the control strategy are also illustrated in detail. In addition, the geometric and operating conditions of the system are detailed for further investigation.

Chapter 4 – Theoretical analysis and computer modelling: this chapter conducts a series of theoretical analysis and develops a group of dedicated computer models for the SAHR-HP system and the key components by using the fundamental the energy balances equations, solar energy conversion, and heat transfer and fluid flow coupled processes. The developed dynamic system computer model can simulate the operation and energy performance of the SAHR-HP system under a specific climate region.

Chapter 5 – SAHR-HP system components experimental platform fabrication, and related experiments and results: this chapter describes the detailed process and method for the fabrication of the prototype of the SAHR-HP system and its components. A laboratory-based experimental platform is established to evaluate the performance of

the novel VIHR-ASHP, and three parallel SAHR-HP systems are established to explore the performance of the novel multiple-throughout-flow method and the novel double-layered fast-responding stratified HSEU. The experimental results are concluded to illustrate the advantages of the SAHR-HP system and its components.

Chapter 6 – SAHR-HP system numerical model validation and the simulation results: this chapter validates the numerical models proposed in Chapter 4 by using the experimental data. The results verify that the simulation models are at a reasonable level of accuracy. Consequently, the validated simulation models are ready to simulate the performance of the SAHE-HP system and its key components as well as optimising the system further.

Chapter 7 – Energy performance, economic, environmental analysis: this chapter evaluates the annual performance of the SAHR-HP system by using the dynamic simulation model. The payback periods and carbon emission reduction for the system under three cities in China which can represent most of the worldwide climate conditions are also analysed. This addresses the potential feasibility of such a system in comparison with a traditional coal-based heating system by assessing both economic and environmental benefits.

Chapter 8 – Conclusion and further works: this chapter concludes the main observations from this research. The future opportunities and investigations are stressed in this chapter. The recent and future demonstrations of this system are described. Challenges are discussed for further development of the technology. All of the above chapters are systematically connected to enable the achievement of the overall project aim. The new SAHR-HP system technology should enable a higher overall solar-energy conversion ratio, a higher energy saving potential and a higher thermal comfort. This will allow SAHP and VIHR-ASHP technologies to create a widely applicable system for building heat and DHW supplies. This innovation will have the potential to reduce fossil fuel consumption and CO_2 emission significantly.

CHAPTER 2: LITERATURE REVIEW

2.1 Chapter Introduction

This chapter will introduce a comprehensive review of results relating to the research and development (R&D) progress and the current applications of solar-assisted heat pump (SAHP) technologies. It will also help to: (i) recognise the current technical challenges in developing the SAHP system; (ii) establish the scientific methods for SAHP research; (iii) propose new research objectives according to the identified challenges; and (iv) give a clear logical research outline for following chapters. The primary objectives are briefly presented as follows:

(1) Concept of SAHP technologies and relevant fundamental theory.

(2) Evaluation standards in terms of the energy performance of SAHP.

(3) R&D works and practical applications of the SAHP systems and the components of the SAHP system.

(4) Types of the SAHP and research methodology.

(5) Major characteristics, investigation highlights, latest R&D status, and current technical challenges of various SAHP systems.

(6) Opportunities for further development of SAHP.

2.2 Basic Concept and Theory, Classification and Performance Evaluation Standards of Solar Assisted Heat Pump Systems

2.2.1 Fundamental concept and theory of SAHP system

Solar assisted heat pump systems (SAHP) have the potential to make a critical

improvement in reducing electricity consumption and increasing energy production. SAHP systems is a highly modularized system that contains three modules, i.e., solar energy conversion module, thermal storage module, and heat pump module. Whether a single module or a SAHP system is widely studied. The objectives of this research were to identify the current status and research on SAHP systems, identify the barriers that slow down their expansion, and give the future perspectives to exploit their usage at the maximum level. The literature review identified the most studied topics related to the SAHP systems which include the performance and the current technologies on separate modules and the whole SAHP system.

Providing space heating and domestic hot water (DHW) for buildings are the major functions of SAHP technologies. Fig. 2-1 shows that the functions for heating and DHW are detected in most situations [24]. On the contrary, few SAHP systems in the market are exclusively designed for domestic hot water supply. The most SAHP systems are from China and the Mediterranean countries (France, Italy, Spain), which is reckoned as a clear indicator showing the market-driven and climate-determined technology distribution. From the industrial aspect, these systems just with DHW functions can be classified into two categories. A SAHP system based on a thermosyphon solar heating device on the roof-top and supported by a heat pump is the most common structure in China. In contrast, an integrated indoor unit with a storage unit and an exhaust-air heat pump is typical in Europe. The condenser could be immersed in or coiled around the heat storage unit.

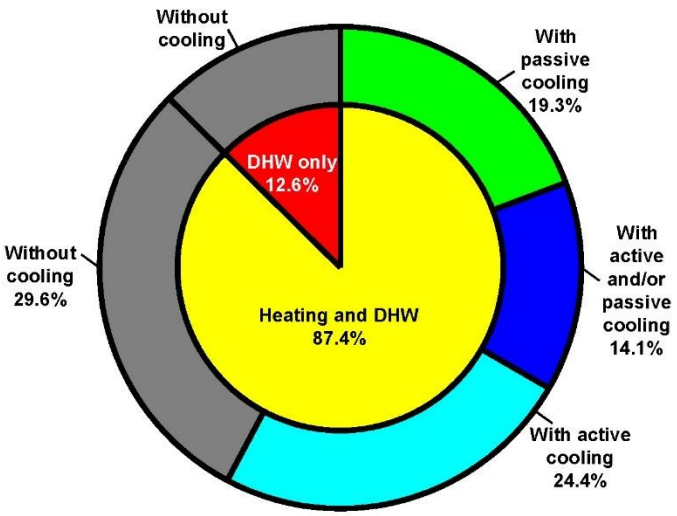

Fig. 2-1 The application of the SAHP systems

2.2.2 Classification of the SAHP systems

The main components of the SAHP systems are the solar energy conversion module, the heat pump module, and the heat storage and exchange module. The different combinations between modules with different technologies can form various SAHP systems [37]. To assist the SAHP systems design and comprehend the classification method, a simple visualisation scheme is provided and is widely used to depict a SAHP system [38]. It can clearly show the energy sources that utilised in the SAHP system, the functions of the SAHP system, and the interrelationships between the components. An example is shown in Fig. 2-2. Different kinds of lines represent different energy transfer types. The traditional energy sources are listed at the left of the form, and the renewable energy sources are listed at the top. By applying appropriate energy sources and relevant devices, the system can achieve different functions which are shown at the right of the form.

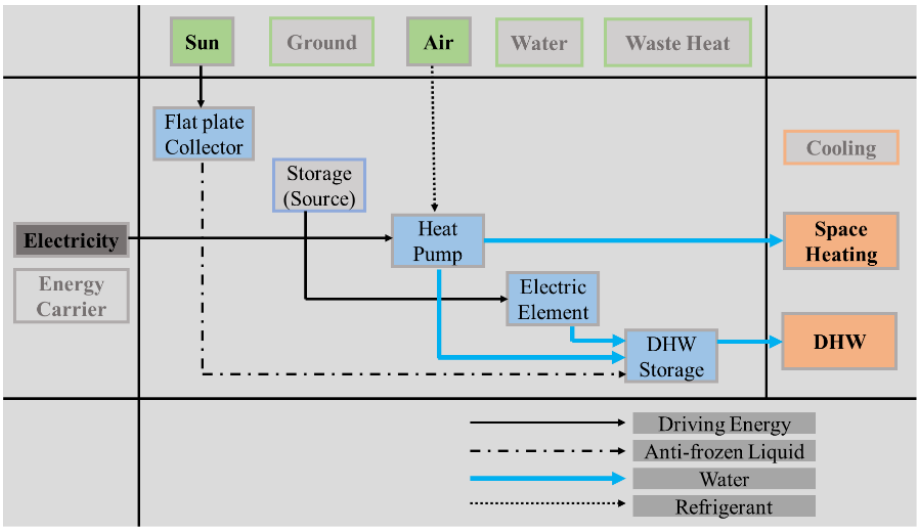

Fig. 2-2 Visualisation scheme of a SAHP system

The SAHP systems are classified by the integration way between the heat pump and the solar energy collection unit. Typically [39], the following distinction is made:

2.2.2.1 Parallel SAHP system

A parallel SAHP system is a configuration that solar collectors and heat pump supply energy to the served building via one or more energy storage units independently, which is shown in Fig. 2-3. The parallel SAHP system is a highly modularized system. Every module in the system is an independent functional module. Hence, based on the basic infrastructure of the parallel SAHP systems, structure transformations can be achieved flexibly. The solar energy collection unit can be either a major or an auxiliary energy source of the system, and the heat pump can provide heat either directly to the building or via a buffer tank.

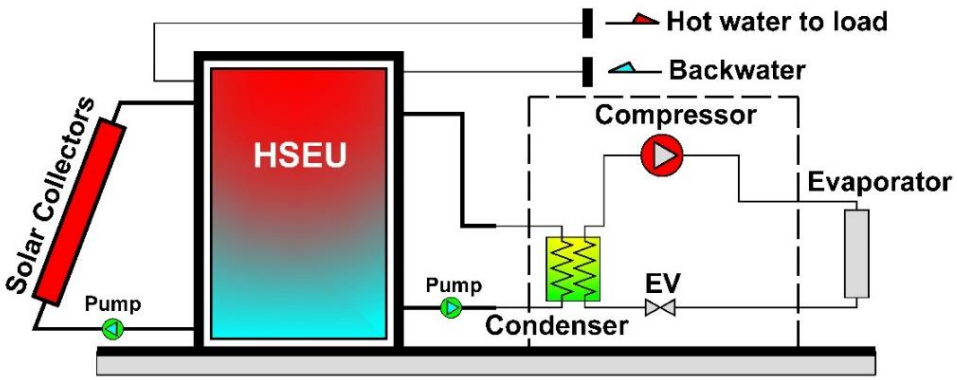

Fig. 2-3 Parallel SAHP system

2.2.2.2 Series SAHP system

In a series direct expansion SAHP system, the solar collector acts as an exclusive or additional energy source of the heat pump, and connects the heat pump directly. The series indirect expansion SAHP system is similar to the direct expansion SAHP system. The difference is that a heat exchanger is applied between the solar collector module and the heat pump module, thus separating the two modules into two loops. The schematic of a series indirect expansion SAHP system is shown in Fig. 2-5.

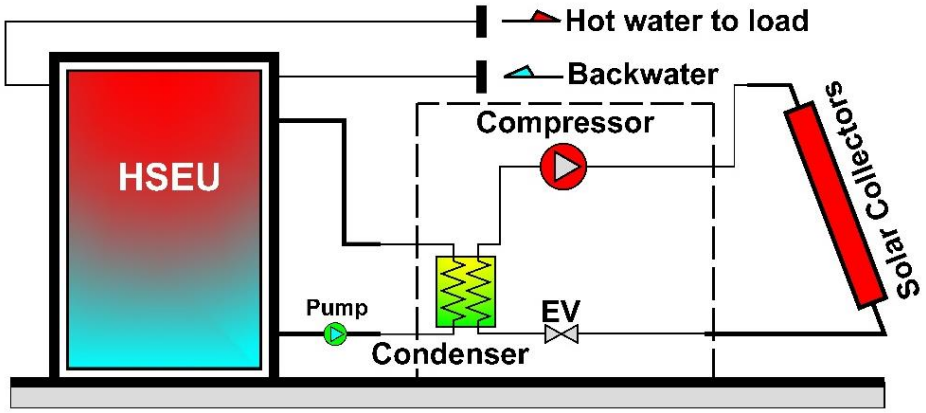

Fig. 2-4 Series direct expansion SAHP system

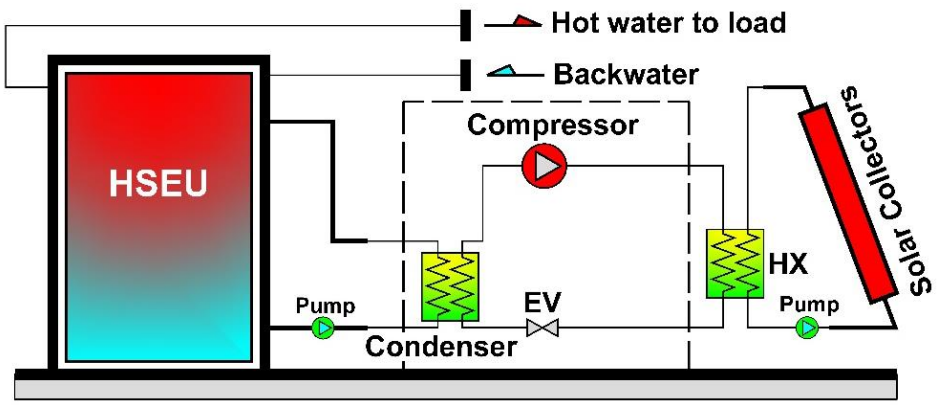

Fig. 2-5 Series indirect expansion SAHP system

Apparently, the series systems have a more compact configuration compared with the parallel system. However, there are also some drawbacks to this kind of system. Unstable solar radiation leads to the unstable performance of the heat pump. In addition, the solar collector module and the heat pump module have to be in operation simultaneously. To address this problem, a bypass of the solar collector module can be installed to supply the solar energy directly.

2.2.2.3 Dual-source SAHP system

The dual-source SAHP system is a configuration that combines the parallel SAHP system and the series SAHP system. This combined system can operate in three modes: (1) solar energy directly supplying mode; (2) heat pump energy directly supplying mode; and (3) SAHP energy supplying mode. The schematic of a dual-source SAHP system is shown in Fig. 2-6.

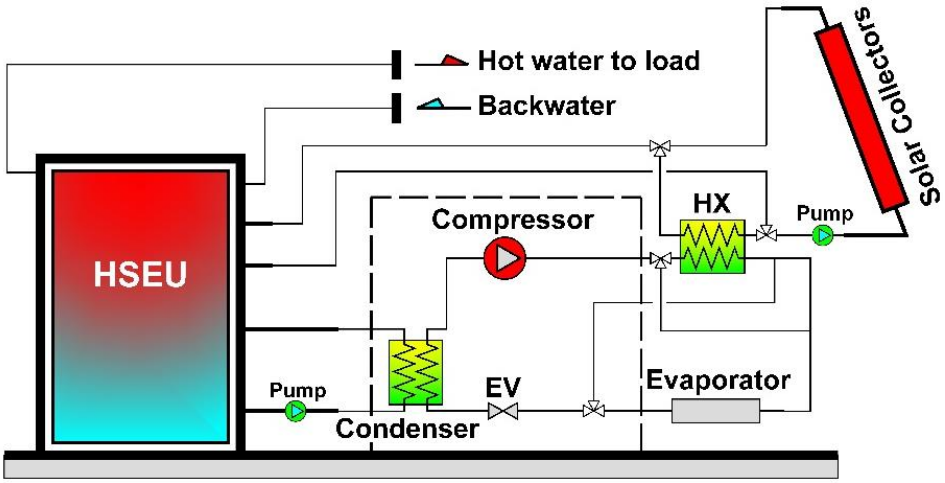

Fig. 2-6 Dual-source SAHP system

According to the relevant investigations, there is a disadvantage lies in the series SAHP systems: the performance of the heat pump can be decreased due to the deteriorative heat transfer between the solar collectors and the ambient air when solar radiation is not enough. Thus, dual-source SAHP systems become popular because they integral the advantageous characteristics of both parallel and series SAHP systems. Accordingly, the heat pump can flexibly switch between various energy sources, i.e., solar energy, ambient air, exhaust air, geothermal, or water [40].

2.2.2.4 Other SAHP systems

Another concept of the SAHP system is using solar energy to perform a regeneration process of a specific energy source for a heat pump, such as geothermal source, which is comprehensively illustrated and studied by Kjellson [41]. Although some conceptual and operational differences exist, the regenerative concept of the SAHP technology could be reckoned as another type of series system [24]. The regeneration status is always presented in summer when solar radiation is high and the heating demand is low. Currently, many practical SAHP systems on the market were featured with the regeneration mode to increase the energy efficiency of the system.

Although several basic SAHP system types have been mentioned, it was recognised

that one SAHP system can be integrated by different kinds of systems. To put it another way, the parallel and series systems do not repulse mutually. Accordingly, 7 system concepts have been proposed by counting all possible combinations, which is shown in Fig. 2-7. The parallel type system significantly dominates (60.7 %) because of its simple structure, installation process, and control strategy. In contrast, the "serial only" or "regenerative only" concepts are rare. In addition, the combination concepts between parallel, serial, and regeneration modes amount to more than 33 %.

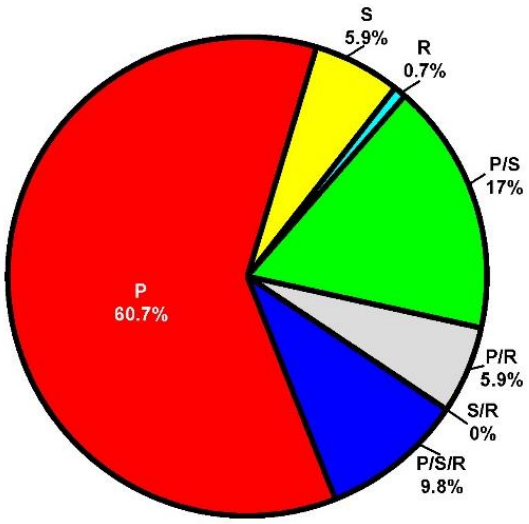

Fig. 2-7 Surveyed systems by concept [38]

Apart from air source heat pumps mainly employed in Mediterranean countries for DHW and space heating, the ground source heat pumps are the most common heat pump in Europe, while water and exhaust air heat pumps have a smaller market share [42]. Fig. 2-8 shows that the solar energy source can be combined with other energy sources. In terms of the most common energy sources used in SAHP systems, Fig. 2-8 represents that the air-source and ground-source heat pumps together account for half of the surveyed systems. Water source or exhaust air source is still rarely used in SAHP systems. Furthermore, the other sources of SAHP systems appear untraceable.

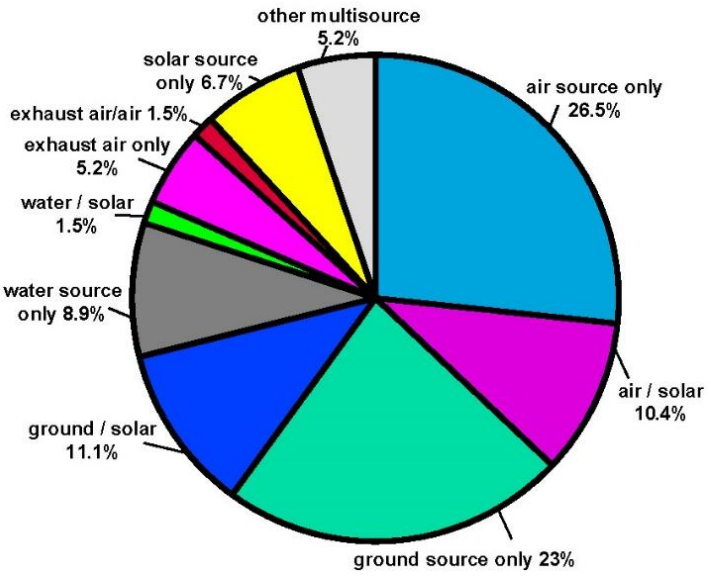

Fig. 2-8 Surveyed systems by source [38]

SAHP systems applying solar source as the only energy source accounts for 7 %. And the solar energy combined systems where the solar energy is employed as an additional energy source to other conventional sources (air, ground, or water) have a further 23 % share. Such multi-source SAHPs expect two special technical schemes, i.e., external and internal solutions. The external solution is relevant to adapting hydraulics between the heat pump and solar collectors, such as connecting by heat exchangers or by heat storage units. As a result, the solar collectors can be operated with conventional heat pumps.

2.2.3 Performance evaluation of the SAHP systems

(1) Overall COP of SAHP systems

Overall COP of SAHP systems is the ratio of generated energy to the electricity consumption of the system. It is derived from the first law of thermodynamics and presents the capacity of the energy converted from electricity.

$$COP_{SAHP} = \frac{Q_{SAHP.generated}}{Q_{SAHP.consumption}} \quad [2\text{- }1]$$

Where

COP_{SAHP} – The COP of the SAHP systems;

$Q_{SAHP.generated}$ – The generated heat of the SAHP systems;

$Q_{SAHP.consumption}$ – The electricity consumption of the SAHP systems.

(2) COP of the heat pump

COP of the heat pump in a SAHP system is the ratio of generated energy to the electricity consumption of the heat pump in a SAHP system.

$$\boldsymbol{COP_{HP} = \frac{Q_{HP.generated}}{Q_{HP.consumption}}} \quad \textbf{[2- 2]}$$

Where

COP_{HP} – The COP of the heat pump of the SAHP systems;

$Q_{HP.generated}$ – The generated heat of the heat pump of the SAHP systems;

$Q_{HP.consumption}$ – The electricity consumption of the heat pump of the SAHP systems.

(3) COP of the solar collectors

COP of the solar collectors in a SAHP system is the ratio of generated energy to the electricity consumption of the solar collectors in a SAHP system.

$$\boldsymbol{COP_{SC} = \frac{Q_{SC.generated}}{Q_{SC.consumption}}} \quad \textbf{[2- 3]}$$

Where

COP_{SC} – The COP of the solar collectors of the SAHP systems;

$Q_{SC.generated}$ – The generated heat of the solar collectors of the SAHP systems;

$Q_{SC.consumption}$ – The electricity consumption of the solar collectors of the SAHP systems.

(4) FER of the solar assisted heat pump system

FER is the abbreviation of the Free Energy Ratio which is the ratio of the consumed energy from renewable energy sources to the total energy consumption of a SAHP system.

$$\boldsymbol{FER = \frac{Q_{SAHP.consumed.renewable}}{Q_{SAHP.consumed.total}}} \quad \textbf{[2- 4]}$$

$\boldsymbol{Q_{SAHP.consumed.renewable}}$ –The consumed energy from renewable energy sources;

$\boldsymbol{Q_{SAHP.consumed.total}}$ – The total energy consumption of a SAHP system.

(5) SPF of the solar assisted heat pump system

SPF is the abbreviation of the Seasonal Performance Factor which is the ratio between the generated energy and electricity consumption of a SAHP system.

$$\boldsymbol{SPF = \frac{Q_{SAHP.generated.seasonal}}{Q_{SAHP.consumed.seasonal}}} \quad \textbf{[2- 5]}$$

$\boldsymbol{Q_{SAHP.generated.seasonal}}$ –The generated energy of a SAHP system;

$\boldsymbol{Q_{SAHP.consumed.seasonal}}$ – The electricity consumption of a SAHP system.

(6) Solar thermal efficiency of solar collectors

Solar thermal efficiency of solar collectors is a significant evaluation parameter that can assess the performance, which can be expressed as [43]:

$$T_m^* = \frac{T_m}{I} \quad [2\text{- }6]$$

$$T_m = t_m - t_a \quad [2\text{- }7]$$

$$t_m = t_{in} + \frac{\Delta T}{2} \quad [2\text{- }8]$$

$$\eta = \eta_0 - a_1 T_m^* - a_2 I (T_m^*)^2 \quad [2\text{- }9]$$

In summary, COP and energy efficiency are the most applicable parameters for evaluating the performance of a SAHP system, while solar fraction and primary energy-saving efficiency are infrequently applied to assess the conventional energy consumption saving capacity of SAHP systems. Practically, the energy demands are in accordance with the different end-users, which will directly influence the operation and performance of the SAHP systems. As a result, appropriate assessment standards for a SAHP system under a specific climate and building will require to take both factors into account.

2.3 R&D Progress and Practical Applications of SAHP Systems

2.3.1 Overview of R&D works in SAHP system

According to the mentioned styles of SAHP systems, a comparison literature review between different SAHP systems in one piece of literature is shown in Table 2-1.

Table 2-1 Comparison literature review between different SAHP systems with different structures in one piece of literature

Reference	SAHP Details	Results
Freeman et al. [39]	System types: dual-source, parallel, and series	FER: 0.38-0.8 (collector area of 0–60 m^2) in Madison 0.38-0.95 (collector area of 0–60 m^2)

	Collector type: flat plate Heat storage unit: liquid tank Functions: DHW and space-heating (120 m^2) Climate region: Wisconsin	COP of HP: parallel:2.0, dual source:2.53, series:2.84 in average Solar collector efficiency: Series:50%, dual source:50%, parallel:30% in January (collector area of 10 m^2) Series:45%, dual source:45%, parallel:35% in whole year (collector area of 10 m^2)
Kaygusuz et al. [44]	System types: dual-source, parallel, and series Heat pump: hermetic type, 1.5kW Collector type: flat plate Heat storage unit: PCM tank Functions: space-heating (75 m^2) Climate region: Turkey	FER: Series:0.6, parallel:0.75, dual-source:0.8 SPF: Series:3.3, parallel:3.37, dual-source:4.2 COP of HP: Series:4.0, parallel:3.0, dual-source:3.5 Solar collector efficiency: Series:0.56-0.64, parallel:0.48-0.54 (average monthly range)
Bertram et al. [45]	System types: dual-source, parallel, and series Collector type: flat plate Heat pump: 7.9 kW Other devices: borehole heat exchangers Heat storage unit: 300 L Functions: DHW and	SPF1: 3.85 (collector area of 15 m^2) SPF2: 4.95 (collector area of 5 m^2) SPF3:5.21 (collector area of 10 m^2) SF: 65% for DWH (collector area of 5 m^2) (SF: Solar Fraction)

	space-heating (140 m^2) Climate region: Strasbourg	
Haller et al. [46]	System types: dual-source, parallel, and series Collector type: covered-uncovered flat plate Heat pump: 16 kW Heat storage unit: 1000 L Functions: DHW and space-heating Climate region: Zurich	This study explores when to change utilising solar energy in a parallel configuration to indirect utilisation in a heat pump. The results show that indirect utilization is advantageous when COP rise by 1 while collector efficiency boost 150% in comparison to parallel configuration
Chandrashekar et al. [47]	System types: dual-source, parallel, and series Collector type: flat plate Functions: DHW and space-heating (124 m^2) Climate region: Vancouver, Winnipeg, Ottawa, Fredericton	In this study, the main method in assessing the performance of the systems was the Life Cycle unit cost of energy (LUC) in $/GJ. It is the ratio of the total cost over the total energy demand throughout the life cycle of the system.

The results of the investigations above show that a solar radiation limit exists on the collectors which can help to determine the SAHP system types. The SAHP system performs better in parallel type when solar radiation exceeds the limit. In contrast, it is better to choose the serials system type when the radiation below the limit. According to the studies, the characteristic performance curves of the heat pump and

solar collector can have a significant impact on the limit. Apparently, the limit can also be used as a criterion for dual-source systems to switch between the operation status [48]. In order to further enhance the performance of SAHP systems, hydraulics, and control strategies can lead to significant energy consumption reduction and improve energy efficiency [49]. In addition, the control strategy for the heat pump using a switching criterion is then of high interest [40]. There are several ways to improve the hydraulics designs and control strategies of SAHP systems: (1) pipeline arrangement [50]; (2) temperature setting [51]; (3) positions of the temperature sensors [52]; (4) operation of the system components [52]; (5) stratification of HSEU [53]; (6) compressor speed [54]; and (7) forecasting and predictive controls [55].

Regarding the latest literature, the series SAHP systems are under the spotlight. It has been suited to enhance the operational performance of heat pumps and solar collectors individually [40]. In regard to the simulation results of SAHP systems, the most fundamental parameter is the energy generation capacity of the equipment. Apparently, it can be concluded that enlarging the area of the embedded solar collectors can easily increase the SPF. However, the increased area of solar collectors can also lead to an increase in system cost. Accordingly, a reasonable area of solar collectors will be always in accordance with the economic criterion.

2.3.2 Overview of R&D works in solar energy conversion module

The solar energy conversion module of SAHP systems is the combination of different kinds of solar collectors. Solar collectors are devices with the function that converts solar radiation into electrical and thermal energy. Then, the generated energy is used directly or transported to a storage device, like batteries or heat storage and exchange unit (HSEU) for later use. Numerous relevant research articles investigating solar collectors were already being published in the past decades. According to the function, the current solar collectors are mainly divided into two categories, i.e., the solar thermal collectors and the photovoltaic/thermal (PVT) collectors, as shown in Fig. 2-

9. The solar thermal collectors are classified into the non-concentrating collectors and the concentrating collectors [56]. Non-concentrating collectors are usually applied for space heating and/or DHW in buildings, whereas concentrating collectors are generally for solar power plant applications [57]. The other type of solar collector which is a combination of a PV module and a solar thermal module is called PVT collector and is classified into three categories, i.e., the PVT flat plate collectors (PVTFPC), the unglazed PVT collectors, and the PVT concentrators [58].

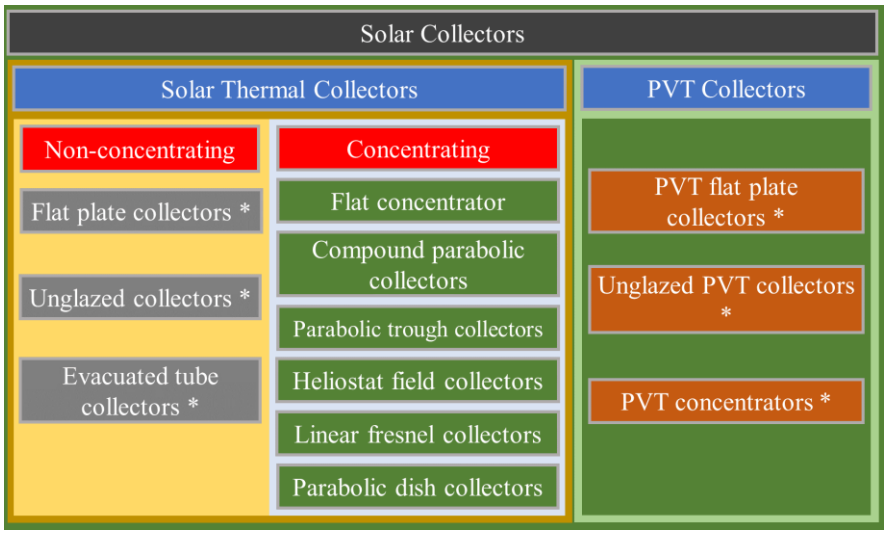

Fig. 2-9 Classification of solar collectors

Theoretically, all kinds of solar collectors are able to be applied in SAHP systems. However, apart from the complexity of the tracking system and higher cost, concentrating solar thermal collectors are normally used in the industry [43]. Accordingly, the non-concentrating solar collectors are prevailingly used in SAHP systems. Hence, in the following statement and analysis, the concentrating solar thermal collectors and most of the PVT concentrators on the market will not be considered. The widely investigated solar collectors that are being used in the SAHP systems are the flat plate collectors (FPC), the unglazed solar collectors (USC), the evacuated tube collectors (ETC), the PVTFPCs, the unglazed PVT collectors, and the low-concentrating PVT concentrators [59] (marked with * in Fig. 2-9).

The performance of the solar collectors, i.e., the output temperature of the solar collectors and the solar thermal efficiency variation can directly influence the operation of the SAHP systems. The output temperature, operating media, and the derived references of these solar collectors are shown in Table 2-2.

Table 2-2 Output temperature and operating media of solar collectors in SAHP systems

Reference	Solar Collectors	Output Temperature	Media
Majumdar et al. [60] Fudholi [61]	Flat plate collectors	30°C ~ 80°C	• water • refrigerant • air
Kalogirou [62]	Unglazed collectors	25°C ~ 50°C	• water • refrigerant
Yogi Goswami [63]	Evacuated tube collectors	60°C ~ 200°C	• water • refrigerant • air
Shyam [64]	PV/T collectors	25°C ~ 80°C	• water • refrigerant • air
Joshi [65]	Unglazed PV/T collectors	26.2°C ~ 40.02°C	• water • refrigerant • air
Walter [66]	PV/T concentrators	60°C ~ 220°C	• water • refrigerant

Over the past decades, FPC is widely used in SAHP systems and occupies most of the market share within a working temperature range of 30°C to 80°C because of its cheap cost and simple structure [61]. In contrast, with a working temperature over 200°C, the concentrating collectors are always applied to produce electricity, and there are

several practical applications, i.e., food processing, heating, cooling, and desalination. However, due to the relatively high cost compared with non-concentrating solar collectors and conventional energy sources, the application and development of concentrating solar collectors are limited [67]. Relatively, ETCs are affordable for producing the fluid with a working temperature above 100°C [68], which can be easily fitted in SAHP systems.

The efficiency characteristic curve of a solar thermal collector can present the efficiency of the collector under specific weather conditions. According to the previous investigation results, the solar thermal efficiency of different kinds of solar collectors against the T_m under 1,000W/m^2 solar radiation are shown in Fig. 2-10. According to the variation trends of different solar collectors, it can greatly help to choose proper solar collectors in the SAHP system design.

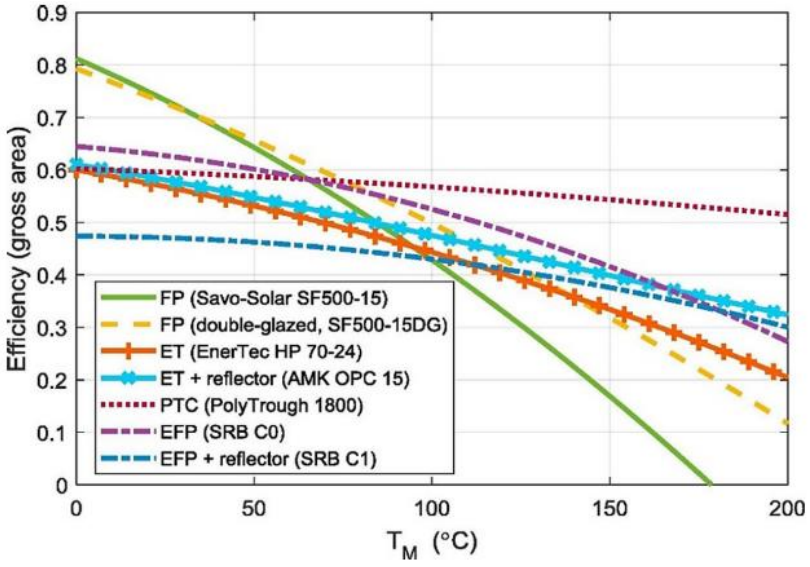

Fig. 2-10 Efficiency curves at I = 1000 W/m^2 for a variety of solar thermal collector [69]

These curves are given for a variety of mean temperature (T_m). Theoretically, the temperature increases of T_m leads to an acceleration in thermal losses. As shown in the figure, FPC has the highest optical efficiency, and a double-glazed panel cover can

minimise its heat loss. In particular, compared with FPC, ETCs have less heat loss [69,70].

The market orientation is also a significant factor leading the research direction. On the contrary, research progress also leads to market products. The market shares of solar thermal collectors in 2018 are shown in Fig. 2-11. The left pie chart represents the market share of the concentrating solar collectors and the non-concentrating solar collectors. The 85.7% market share illustrates the predominant role of the non-concentrating solar collectors in the market [71]. The four kinds of non-concentrating solar collectors market shares are shown in the right pie chart. The dominant one is the evacuated tube collectors with 70.7% market share, mainly in response to growing demand in China, and the second one is the flat plate collectors with 22.9% market share which are the first option in Europe [72]. The unglazed collectors just account for 6.4% market share worldwide, and are mainly used in the USA and Canada [73].

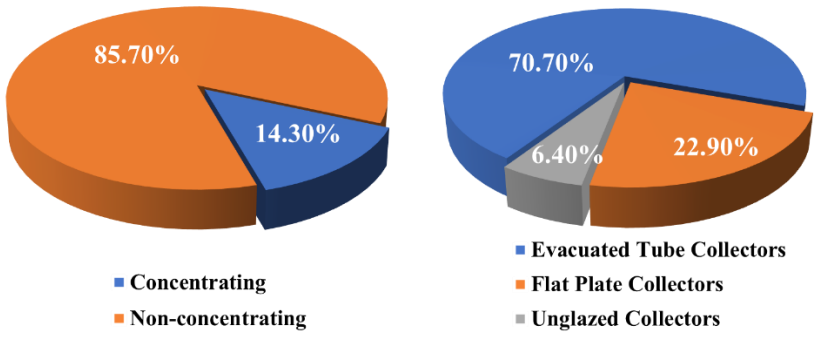

Fig. 2-11 Market shares of the solar thermal collectors in 2018

By the end of 2018, PVT collectors have a total of 1,075,247m² installation areas [74]. Fig. 2-12 shows the market distribution of the different kinds of PVT solar collectors [75]. Unlike the solar thermal collector, the market of the PVT collectors mainly comes from the unglazed PVT collectors with 48% market share, and the PVT evacuated tube collectors just accounts for merely 4% market share.

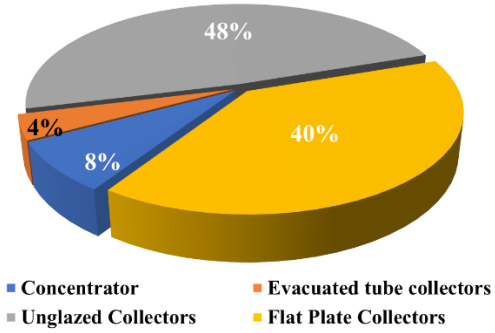

Fig. 2-12 Market shares of PVT collectors in 2018

The up-to-date research progress of the different kinds of solar thermal collectors in SAHP systems is as follows.

2.3.2.1 Flat plate solar thermal collectors

Flat plate solar thermal collectors include two types, one is the air collector, another is the liquid collector [61], as shown in Fig. 2-13. Fig. 2-13A and Fig. 2-13F present a conventional flat plate air collector (FPAC) and a flat plate liquid collector (FPLC) separately. Conventional FPACs have lower thermal efficiency compared with FPLCs. There is a lot of literature committed to enhancing the collector's efficiency. The main method is to expand the surface area through porous media (Fig. 2-13E) [76], matrix-type absorber [77], box-type absorber [78], compound honey-comb absorber [79], corrugated surfaces (Figs 2-13B and 2-13C) [80], finned absorber (Fig. 2-13D) [81,82] and absorber with slats [83], baffles [84], obstacles [85], and aluminium cans [86].

The conventional FPLC is also called tube-on-sheet FPLC, which uses copper tubes as the riser of the collector, and the tube is connected with the absorber plate with a line joint which is detrimental to the heat transfer. To improve the performance of the FPLC, two main methods are through increasing the contact area between the riser and the absorber plate and increasing the convective heat transfer coefficient of the flowing media in the riser, thus increasing the heat transfer capacity and the solar thermal efficiency. Some examples have been published, i.e., embedded copper tube (Fig. 2-

13G) [87], roll-bond absorber (Fig. 2-13H) [88], and mini-channel absorber (Fig. 2-13I) [34].

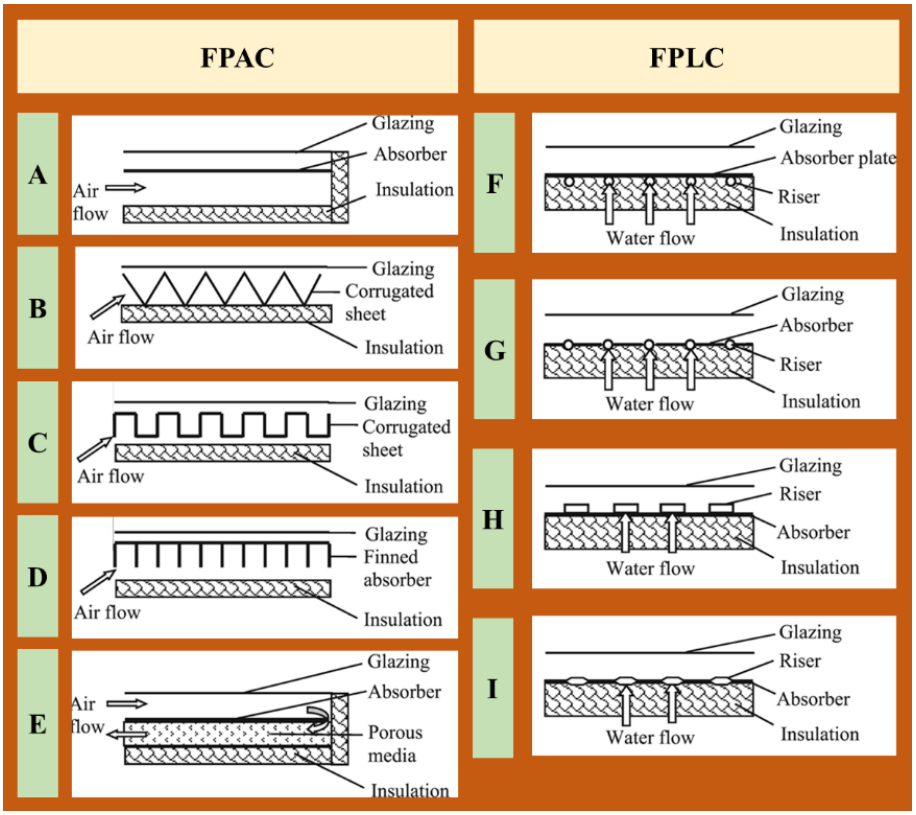

Fig. 2-13 Classification of FPCs: air-based solar collectors (A–E);

water-based solar collectors (F–H)

2.3.2.2 Unglazed solar thermal collectors

The uncovered (unglazed) solar (USC) collector is made of black plastic which is stabilised for resisting ultraviolet light, as shown in Fig. 2-14. The low-cost characteristic makes it a cost-effective application for DHW or heating of swimming pools, air heating, and space heating [62]. Due to the special unglazed structure, a large proportion of solar radiation can be absorbed. However, this kind of solar collector can only be used for low working temperature conditions (lower than 30°C) because of the no insulation structure which can lead to a significant heat loss. Consequently, the efficiency of USCs is less than that of FPCs, but much higher than that of the air

collector [89].

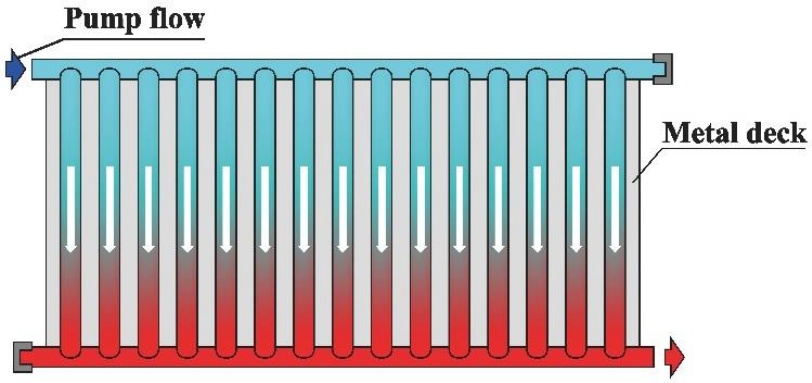

Fig. 2-14 Unglazed solar thermal collectors [90]

2.3.2.3 Evacuated tube solar thermal collectors

The evacuated tube solar thermal collectors (ETCs) are featured by a vacuum gap between the solar absorber plate and the glazed cover. Different from the USCs, the ETCs are often found applications under medium working temperature, from 60 °C to 80 °C. The schematics of three typical ETCs, i.e., water-in glass type, U-type and heat-pipe type, are represented in Fig. 2-15 (a), Fig. 2-15 (b) and Fig. 2-15 (c) separately. The water-in glass type ETC comprises single-end waterlogged tubes which are connected to a horizontal tank on the top. The natural convection heat transfer is the fundamental mechanism: the warmer water rises to the tank and is filled up by colder water. In contrast, the U-type ETC has two-ends tubes, and the inner fluid is always driven by the forced-convection heat transfer. The heat-pipe type ETC is a relatively new concept which mainly used for heat recovery applications.

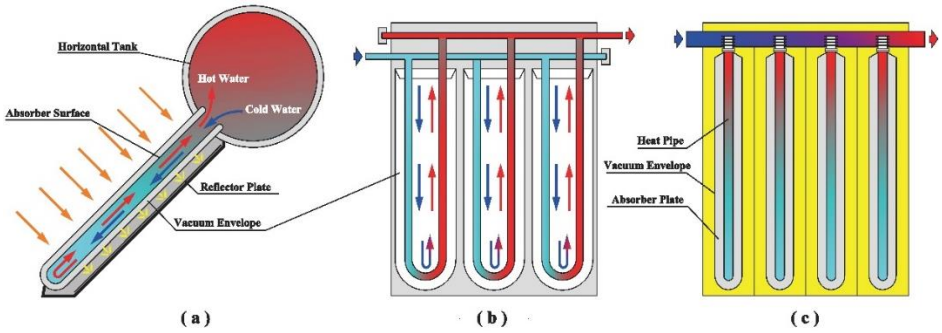

Fig. 2-15 (a) Water-in glass collector [91]; (b) U-type collector [92]; and (c) Heat-pipe collector [93].

2.3.2.4 PVT collectors

Photovoltaic–thermal (PVT) is a concept that combines PV technologies and solar thermal technologies. Thus, the PVT can convert solar radiation into heat and electricity simultaneously [94]. The air or water underneath the PV module can significantly decrease the temperature of the panel and therefore increase photoelectric efficiency [91]. In terms of the solar radiation collecting process, PVT collectors are mainly classified into three categories: the PVT flat plate collectors, the PVT unglazed solar collectors, and the concentrating PVT collectors. The common design of flat plate PVT is shown in Fig. 2-16(a).

The other type of PVT collector is the unglazed PVT solar collectors, the structure of which is similar to the glazed ones, but without the glass cover over the solar collector. The common designs of the unglazed PVT solar collectors are shown in Fig. 2-16(b), Fig. 2-16(c), and Fig. 2-16(d). Compared with the unglazed PVT, the glazed PVT can achieve higher solar thermal efficiency, since the glazing layer can significantly decrease the heat loss. However, it also can lead to a slight decrease in photoelectric efficiency [95]. Particularly, hot spots are regions of the PV module with elevated temperature when compared to the overall temperature of the module, and can cause efficiency decrease and even panel damage [96].

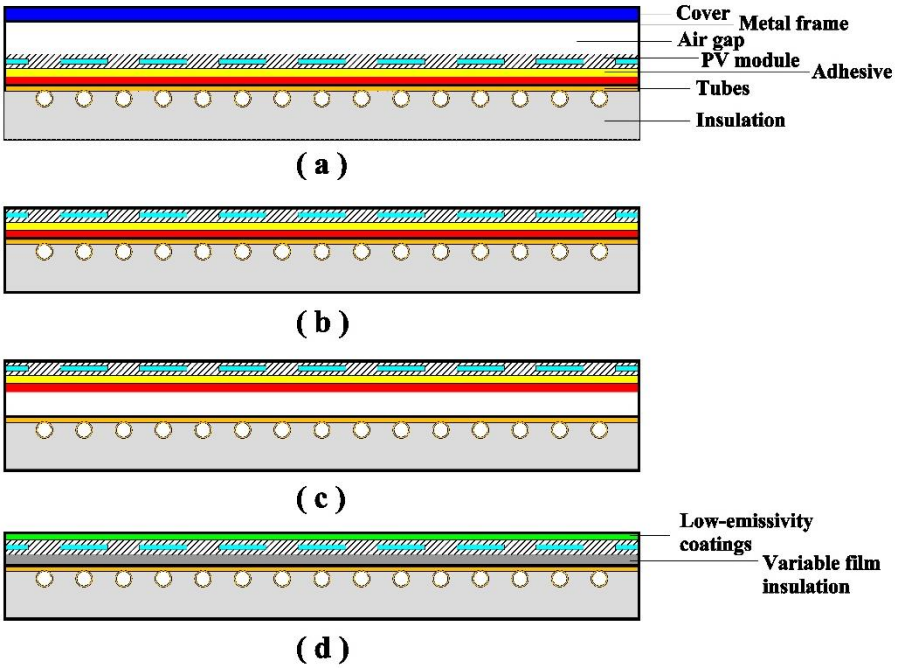

Fig. 2-16 PVT collectors

The solar collectors are the solar energy transfer module in SAHP systems, which can utilise the solar energy to increase the energy efficiency of the systems and reduce energy consumption from other energy sources, especially fossil energy sources and electricity. The selected type and size of solar collectors are determined by many factors, such as SAHPS functions, environmental conditions, and building structures. Currently, the evacuated thermal collectors and the flat plate collectors are the main solar energy transfer module applied in SAHP systems.

2.3.3 Overview of R&D works in heat pump module

The compression module in SAHP systems is a heat pump that can extract energy from a low-temperature energy source and boost the working temperature to a suitable degree for a specific application. The compression cycles and the refrigerants are two key factors that determine the performance of the heat pump. The up-to-date investigations of these compression cycles and the refrigerants are detailed as follows.

2.3.3.1 Compression cycles

For residential applications, the increase of ambient temperature can cause the performance enhancement of SAHP systems, which is in accordance with the decrease of the heating demand. As a result, the energy generation capacity will exceed the heat demand during the high ambient temperature period, thus leading to repetitive on-off operation. To avoid excessive on-off operation which can damage the device, the speed-control compressor has been proposed. Accordingly, the compressor can adapt to the variation of the heating load thus reducing the number of on-off operations and extending the compressor service life. There are a lot of investigations focusing on the capacity control of heat pumps [97]. A few of the studies are relevant to the comparison between the performance of the variable-speed compressor and the constant-speed compressor [98]. According to the literature, the variable-speed compressor is always cost-effective under a colder climate [99]. However, under other climate conditions, it is difficult to confirm which compressor is profitable because the swept volume of the variable-speed compressor is smaller, but an additional inverter is required to adjust the speed [98].

On the other hand, the performance of a heat pump can also be enhanced by improving the compression cycles. For the high condensing temperature or low evaporating temperature conditions, a single-stage compression cycle heat pump presents a poor performance and less efficient [100]. To solve the challenges, multistage or hybrid compression cycles were used to improve the performance of the heat pump, i.e., multi-stage compression cycles [101], cascade cycles [102], ejector assisted compression cycles [103], auto-cascade cycles [104], trans-critical cycles [105], and organic Rankine cycles [106].

2.3.3.2 Refrigerants

Table 2-3 shows the thermodynamic properties of the most common refrigerants used in SAHP systems. R22 and R134a are halogenated refrigerants and have been widely applied in SAHPS systems in terms of its excellent thermo-physical characteristics.

However, the extensive application of these refrigerants will cause severe global warming [100]. Hence, finding environment-friendly refrigerants with high performance is significant [107].

Table 2-3 Thermodynamic properties of existing refrigerants used in SAHP systems

Refrigerant	Molecular Weight	Critical properties		Boiling point
		Temperature (°C)	Pressure (MPa)	
R11	137.37	198.0	4.41	23.7
R12	120.9	112.0	4.14	-29.8
R22	86.47	96.2	4.99	-41.4
R113	187.37	214.06	3.39	48
R114	170.92	145.68	3.26	3.5
R115	154.47	79.95	3.12	-39.1
R123	152.93	82.0	3.66	27.8
R134A	102.03	101.1	4.06	-26.1
R410A	72.6	72.8	4.9	-48.5
R404A	97.6	72.16	3.74	-46.6
R407C	86.2	86.05	4.63	-43.8

Accordingly, many environment-friendly refrigerants have been proposed. For example, R744, R717, R290, R600, R600a, and R1270 are natural working refrigerants which can replace R22 in SAHP systems [108]. The performance of R290 and R1270 are similar to R22. However, the flammable property of these two natural refrigerants leads to more safety requirements in applications. In addition, CO_2 is also a natural refrigerant that can be used in SAHP systems, but the performance is lower than the system with R22 under the same working conditions.

Currently, hydro-fluoro-carbons (HFC) refrigerants are the most popular refrigerants in SACHP systems, such as R134a, R407C, and R410A. The miscibility between HFC refrigerants is the most distinct property.

By covering the shortage of the intermittent energy supply of the solar energy conversion module, the heat pump module provides energy to the SAHP system while the solar radiation and the stored energy are not enough. In addition to the timely energy supply function, the heat pump module can extract energy from many energy sources, such as air, water, ground, and wasted energy source, thus giving the SAHP systems flexibility and practicability. The versatile compression cycles and the refrigerant give researchers opportunities to improve the performance of the SAHP systems and adjust the systems under different conditions.

2.3.4 Overview of R&D works in heat storage and exchange module

The horizontal and vertical heat storage and exchange modules are both used in the solar systems. However, the horizontal one is mainly for solar water heaters without a heat pump. On the other hand, nearly all the SAHPSs use vertical thermal storage tanks standing on the ground with larger volume and heat storage capacity than the horizontal one. More importantly, the HSEU stratification of the vertical tank is better than the horizontal one [109].

Concerning the working pressure, HSEU can be divided into two main categories, i.e., pressurized HSEU and atmospheric HSEU [110]. The pressurized HSEU is mainly used in combination with a high-temperature district heating system. When the water temperature is up to 100°C, the pipeline pressure must be higher than the saturation pressure to avoid evaporation. The same constraint is imposed in the TES in order to avoid evaporation at the top of the system [111]. However, the working temperature of the SAHP systems is always lower than 100°C, and thus the atmospheric HSEU is more suitable to install in the SAHP systems.

2.3.5 Practical applications of SAHP systems

The investigations on SAHP systems are categorised into five major applications as follows: (a) drying; (b) space heating; (c) greenhouse heating; (d) water heating; and (e) desalination. Besides, few investigations place the focus on the desalination by SAHPs. The working fluid temperatures of these applications are shown in Table 2-4.

Table 2-4 Working fluid temperatures of applications

Application	**Working temperature scale**	**Reference**
Drying	30°C ~ 80°C	Daghigh [139]
Room space heating	40°C ~ 80°C	Mohanraj [140]
Agricultural greenhouse space heating	40°C ~ 60°C	Ozgener [141]
Water heating	40°C ~ 60°C	Mohanraj [140]
Desalination	60°C ~ 90°C	Kalogirou [142]

The details of the applications are as follows:

(a) Drying applications

Drying is the highest energy-consumed process for agricultural products. The first heat pump for drying purpose is proposed in 1973, and is identified as a cost-effective device which can produce dried agricultural products with high quality [143]. To further improve the performance of the heat pump dryer, solar energy was integrated into the system. The SAHP dryer can efficiently improve the energy efficiency of the system and overcome the drawback that the heat pump can only use the ambient source. The SAHP dryer presents the following properties: reduced energy consumption, sufficient energy reserves, safety operation, and products with high quality. There are many practical applications focusing on the integration of the heat pump with solar

energy to dry products, such as mint leaves SAHP drying system by using fluidised bed dryer [144] and red chilli SAHP dryer comprising a tray-type drying chamber [145]; mushroom SAHP dryer [146] and copra SAHP dryer [147].

(b) Room space heating

Heat pump technologies for space heating have developed rapidly during the last two decades [148]. Heat pumps are of great advantage over conventional space and water heating systems which directly or indirectly depend on fossil fuel combustion at low energy conversion efficiency. Moreover, solar energy, due to its cleanliness and accessibility, is potential in driving heat pumps for space heating. However, the system structure is usually relatively large and complex, which together with the investment cost limit the application. The fact is that the heat pumps suffer a lot from the declining heating capacity with the decreasing of ambient air temperature and the consequent insufficiency to the users' requirements and the resulting larger electricity consumption [149].

(c) Agricultural greenhouse space heating

The heating of the greenhouses is one of the most energy-consuming fields during cold climate conditions. Currently, due to the low operation cost and high COP, a geothermal energy-powered heat pump is widely used in greenhouses heating [150]. However, there are several disadvantages lying in the geothermal energy-powered heat pump, such as soil temperature reduction which will lead to a decreased COP. Other challenges are high initial cost and low reliability of using the geothermal energy-powered heat pump alone. The mentioned barriers can be solved by integrating solar energy into the system. There are many investigations about the combined solar-assisted geothermal heat pumps. And the applications of the solar-assisted geothermal heat pumps are founded in a wide range of topics, such as heating, cooling, and DHW [151].

(d) Water heating

In recent years, many investigations have been conducted on SAHP water heaters [140]. Currently, the direct expansion SAHP systems are commonly used to substitute the conventional water heaters by using electric or natural gas as the energy sources. Besides, some studies focus on the long-term energy performance and economic analysis of SAHP water heaters. The results show that the SAHP water heater is not only cost-effective because of the direct heat exchange process between the heat pump and solar collectors. It is noted that the refrigerant is applied as the working fluid in the heat pump as well as the solar collector, thus enabling the collectors to operate under the low ambient temperature [152].

(e) Desalination applications

The performance of the solar desalination systems is very susceptible to solar irradiation; consequently, the stable demand for freshwater will not be guaranteed [153]. In other words, other heat sources are still needed when the solar irradiation is weak or not available. In view of the working principle of the desalination process, both the heat pump evaporator and condenser can play a positive role in the process of desalination. In recent years, some studies on solar assisted heat pump desalination have been reported. In the SAHP desalination system, the latent heat released during condensation of vapour was regenerated for preheating the water entering the solar stills. In addition, the recent works on solar assisted heat pump desalination systems chose to focus on different combination types of solar energy and heat pump to enhance the system performance.

2.3.6 Summary of the current SAHP systems and its potential challenges

(1) Poor performance at low ambient temperature

When it comes to the operation under low evaporating temperature, the SAHP system

cannot perform as well as it does under moderate climates. Owing to the lower solar thermal efficiency of the solar collectors and lower COP of the heat pump [154]. When a heat pump system is operating under cold conditions, its heating efficiency can be significantly compromised [155] and this is associated with a number of problems such as reduced volumetric efficiency, elevated compressor discharge temperature, increased compression ratio, lower refrigerant mass flow, and decreased operating efficiency [156]. Also, the performance of the heat pump will be influence by the frost of the evaporator because the frost layer further blocks heat exchange, thereby significantly reducing the heating capacity [157] and COP [158]. It was concluded that the defrost penalty results in a reduction of heat pump efficiency of approximately 10-15% [159]. Demonstrations in the field resulted in a degradation in the coefficient of performance (COP) of as much as 40% and heating capacity reduction by as much as 43% [160]. Zhang et al. investigated a heat pump for the space heating of buildings in Harbin, the coldest provincial capital city in China, and experimental results showed that the coefficient of performance (COP) was only 1.04–1.89 under the conditions of −20.9 to −16.6°C outdoor temperature and 19.8 to 22.5°C indoor temperature [161]. Several investigations were conducted to improve this situation. Ma proposed an indirect-expansion SAHP with a two-stage CO_2 cycle, which concludes that the two-stage cycle more competitive than the other cycles in cold climates [162]. Liu added an auxiliary boiler into the SAHP system to increase the performance in cold winter [163]. Ji conducted an experimental study to improve the heat transfer under cold climate by using a finned-tube solar collector/evaporator. the results show that the finned-tube can increase the heat transferability, but the frosting can significantly decline the performance [164]. Similarly, Kong used micro-channel heat transfer technology in a direct-expansion solar-assisted heat pump water heater, which proved a higher COP under low ambient temperature [165]. Youssef added PCM for latent heat storage in indirect expansion solar assisted heat pump system, which greatly helped the saleability improvement and performance enhancement under cold weather [166]. Lu improved the performance of a SAHP system by employing a vapour

injection cycle [167]. However, the multi-stage compression cycle can increase the performance at the expense of the initial and operation cost. Although an auxiliary heating device can ensure thermal comfort, the energy consumption and the cost of the system is also increased. The low conductivity, high cost, and limited cycle times hampered its promotion. The coefficient of performance (COP) of an IHX-type vapor injection heat pump is just improved by 15% to 20% at an ambient temperature of −17.8°C [168]. Accordingly, although the investigations can improve the performance, there are still many challenges of the SAHP system under cold weather. As a result, the solution to improve the performance of the SAHP technology should be further discussed and investigated

(2) Weak of strong complementarity of solar collector and heat pump

Solar radiation is high in summer and low in winter. Hence, the main drawback of solar energy is its intermittence as they fluctuate based on a daily, weekly, and seasonally basis [128]. With respect to the daily solar energy discrepancy, the solar energy is sufficient in the daytime but weak during the night. Besides, the ambient temperature is also high in the daytime but low at the night. In addition, the application of a heat pump is the main way to reduce the carbon emission of buildings worldwide. Integrating the solar energy absorption module can enhance the performance of the SAHP systems. However, the heating demand is high in winter, but the performance of the heat pump is low because of the low ambient temperature. In the meantime, the collected heat of solar collectors is also low due to the low solar radiation. As a result, the solar thermal collector cannot improve the performance of the heat pump efficiently. Furthermore, the solar energy is not useful under the cooling mode in the summer, thus leading to the poor complementarity between the solar collector and the heat pump. Chen conducted a numerical study to simulate the long-term performance of a solar-assisted ground-coupled heat pump system. The result shows that, for a building in Beijing with an average heating load of 12.44 kW, the solar fraction for space heating in December is only 0.27 despite a large collector area of 45 m^2 [169].

From the daily aspect, the high solar efficiency and high heat pump performance both present during the daytime. On the contrary, the SAHP system always has a declined performance during the night.

(3) Lack of tools for system design, optimisation and performance evaluation

The SAHP system optimisation is an important research direction. There are many investigations about the component's optimisation, including solar energy conversion module optimisation (2.3.1), compression module optimisation (2.3.2). For making the components and the integral system optimisation, there are many useful tools and methods. Establishing a numerical model to simulate the heat transfer process is the main method to optimise the SAHP system. By using the method, the collector/evaporators [170] and the solar-assisted compression heat pump systems [171] are modelled and optimised. Besides, TRNSYS is the flexible simulation software package used for modelling, optimisation, and predicting the dynamic performance of SAHP with a good degree of accuracy [172]. CFD also provides the researchers with a useful tool to increase the performance of the SAHP, which are mainly used in components optimisation [173]. However, there is a shortage of the professional SAHP system optimisation software with high simulation speed.

(4) Lack of flexible structure of solar thermal collectors and low convective heat transfer coefficient and high flow resistance of the working fluid

The conventional flat-plate solar collectors just have one inlet and one outlet, thus giving the collectors an inflexible structure that can only be connected into a series or parallel layout [174]. Frequent flow directions change leads to the high flow resistance. Besides, the big interior spaces and the line-joint with the solar absorber plate cause a poor heat transfer process of conventional solar collectors [175]. Currently, the mini-channel structure has been introduced into the construction of flat-plate solar collectors. owing to the smaller interior spaces compared to the traditional flat-plate panels, a micro-channel collector presents a superior performance on many aspects, i.e., higher

heat transfer, lower convective heat loss, higher flow velocity and enhanced solar efficiencies [176].

2.4 Potential Opportunities in the Development of SAHP Technology

2.4.1 Developing optimised solar collectors array connection

Apparently, a single solar panel cannot provide enough energy for space heating. For increasing the proportion of the energy provided by solar collectors, a solar collectors array with several solar panels is proposed. A study about a solar system for space heating was conducted by Zhao et al. The PV/T solar collectors array was presented as a one-to-one connection method. The results show that the overall efficiency of the collectors array is 45.0% of which 13.8% came from photoelectric efficiency and 31.9% came from solar thermal efficiency [34]. Ling et al proposed a similar solar system by applying a solar collectors array with series and parallel connection. The overall solar thermal efficiency reached 31.6%, and the mean room temperature is 15℃[177]. Bava compared the performance of solar collectors arrays with different connection methods, which indicated that the layout of solar collectors array can significantly influence the overall solar efficiency [178]. Theoretically, the solar collectors array creates a continuous temperature rise along the flow path. Accordingly, the temperature of the working fluid will reach a very high level at the rear flow path, especially for a collectors array with numerous panels. As a result, owing to the inverse correlation between thermal efficiency and the fluid temperature, the increased fluid temperature will lead to the reduction of solar thermal efficiency. The efficiency of rear panels may even become a negative figure. Hence, the thermal efficiency of the solar collectors array becomes lower along with the increase in the number of panels. Consequently, it is important to design a novel layout of the solar collectors array to reduce the energy loss and enhance the efficiency of the solar collectors array.

2.4.2 Using wasted heat as energy source

The energy efficiency of a ventilation system is relevant to many factors such as building structure, ambient conditions, indoor conditions, building applications as well as occupants' behaviour [179]. Despite the investigations carried out on these factors for saving building energy consumption in recent years, adding heat recovery devices to a building ventilation system for recovering energy from the ventilated air is considered an important way to improve energy efficiency [180,181]. Heat recovery devices can easily decrease the building energy consumption by more than 20% [182], and recover about 60% to 95% of the heat in the exhaust air without limiting or affecting the function of the buildings [183]. Shurcliff [184] defines the heat energy recovery of any device in terms of extracting, recovering or salvaging of heat or mass from one air stream and transferring it to another air stream. In industry, the technology is called heat recovery ventilation (HRV) or enthalpy recovery ventilation (ERV) [185]. At present, many types of devices can perform the heat recovery function, and each device has its own characteristics [186]. Table 2-5 shows a comparison of the characteristics of some of the key devices identified.

Table 2-5 Comparison of characteristics of various ventilation heat recovery devices [187]

Devices	Recovery efficiency	Equipment cost	Space occupation	Cross-contamination	Flexible pipeline
Rotary wheel	High	High	Large	Yes	Bad
Plate exchanger	Medium	Medium	Large	Yes	Medium
Heat pipe	Relatively high	Medium	Large	No	Medium
Run-around	Low	Low	Medium	No	Good
Heat pump	High	High	Medium	No	Good

Among all these heat recovery devices, there are many classification criteria to classify different heat recovery technologies. For the heat transfer mechanism, these devices

divide into sensible heat recovery [188] and enthalpy (latent) heat recovery devices [189]. From the perspective of the system operation, the heat recovery systems include passive and active heat recovery systems [190]. The passive heat recovery systems are limited in supplying the heating and cooling capacity, and cannot fully use the heat from the exhausted air. The active heat recovery systems, i.e., heat pump heat recovery system, can provide more heating and cooling capacity than the passive one. However, the limited ventilation air also restricts the heating and cooling performance of the heat pump, which needs a redesign of the system to fulfil the heating and cooling load of the building.

2.4.3 HSEU structure

For a SAHP system, an appropriate HSEU can significantly improve its performance. For example, a study illustrates that the well-designed HSEU can indirectly reduce 40% heating load for a served house with 100 m^2 area [191]. Besides, an HSEU can store spare heating capacity and effectively switch the peak load for the served heating space. Thus the operational cost of the system can be reduced by around 7.8% [192]. The further study also testified that the combination of the HSEU and SAHP technologies can enable up to a 50% operational cost reduction [193].

Currently, the most widely used heat storage technology is the sensible heat storage because of its affordable characteristic and freely available materials, such as water, oil, rock, air, concrete, bricks or sand [194]. Particularly, a combined application of sensible heat storage unit and practical SAHP has been investigated by many researchers, which has a good performance in space heating because of its outstanding properties, i.e., simpler design, installation and control [24]. For a parallel SAHP system, the collected heat from solar collectors and the heat pump is transferred to an HSEU. Then, the stored heat is released to provide space heating or DHW [195]. The existing HSEUs are based on a single large-sized water tank that is embedded with heat exchanging coils for heat transfer from the solar collectors array to the bulk of

tank water. The tank, which usually holds a large volume of water in order to store at least one day's heat from the solar panel-array, acts as the heat storage as well as heat provider, thus ensuring the balance between the heat supply from the solar panel-array and heat demand of the served space. Due to the huge volume of water, the time needed for heating the tank water to the required temperature (i.e. temperature required for the secondary loop fluid to work) is long. This leads to a significant delay in heat delivery to the served space. For example, in the morning when the sun just rises, the heat collected from the solar collectors array cannot be used to provide space heating due to the low tank water temperature. Instead, the heat is used to raise the temperature of the tank water until it reaches 40-50^{o}C. This heating up time could long during which the space heating is unavailable. This would lead to great thermal discomfort to the occupants, especially when heating is required urgently, hence the heat pump must be brought into use which leads to a significant waste of electricity.

In addition to the above, there are also challenges with respect to the temperature control of a conventional HSEU. First, space heating and domestic hot water supply are basic applications of the SAHP. The temperature requirements for the two applications are different; A temperature of about 35^{o}C will be high enough for the underfloor heating system [196], while domestic hot water should be stored at 55 °C or higher to kill legionella bacteria [197]. The SAHP system needs to adjust the temperature when the operating mode changes, which can take place sporadically. With a large single HSEU, it is difficult for the system to react quickly to the user's demand. Second, the consumer's demand for heat varies from time to time and the heat load of the building is affected by ambient temperature. Without prompt temperature controls, the level of comfort will not live up to the residents' expectations.

2.4.4 Ground source SAHP system

Ground source heat pumps (GSHP) is another widely used promising heat pump technology with high performance and low operational costs. Due to the efficient

utilisation of the ground-source renewable energy, GSHPs can reach low carbon emissions [198]. To further improve the performance of the GSHP, the solar energy is combined with the GSHP technologies which is known as solar assisted ground source heat pump (SAGSHP). The schematics of the typical direct and indirect expansion SAGSHP system is shown in Fig. 2-17 (a) and (b) separately. According to the current investigations, the system integrating the direct expansion mode and indirect expansion mode is suitable for any climate condition. However, the indirect expansion SAGSHP configuration performs better under cold climates, which can be deeply investigated in the future to improve the feasibility and practicability of the technology.

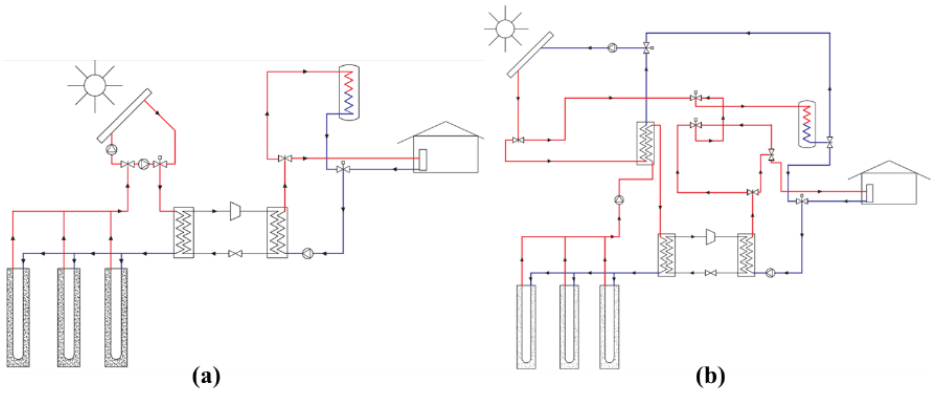

Fig. 2-17 The schematics of the typical SAGSHP systems [199] (a) Direct expansion SAGSHP system (DX-SAGSHP); (b) Indirect expansion SAGSHP system (IDX-SAGSHP).

Although the GSHPs have high energy efficiency, the performance will be continuously impaired by the imbalanced loads for long-time operation. In heating-dominated areas, the heat extraction (heating load) is not balanced with the heat injection (cooling load). This inequality directly leads to a decrease in the ground soil temperature, thus representing a lower performance year by year. To overcome this disadvantage, the SAGSHP can feed the collected solar energy into the soil to compensate the heat imbalance and maintain the stable performance of the system [200]. In addition, the solar energy can also be used to increase the inlet temperature of the evaporator, causing a decrease of compression ratio and increasing the

performance of the heat pump [201]. Consequently, the SAGSHP technology can solve the solar energy seasonal discrepancy.

There are also some technical and economical limitations in the SAGSHP technologies, the further in-depth investigations are required. According to the comprehensive review of all SAGSHP systems, the following research objects are presented for future studies [200]: 1. the investigation of the optimisation methods; 2. the feasibility for tertiary-use buildings; 3. the application of the environment-friendly refrigerants; 4. the environmental performance evaluation; 5. further investigation on improving the system energy performance; 6. further investigation on optimising the control strategies; and 7. further investigation on model build-up.

2.5 Chapter Summary

A comprehensive review of the investigations, the development, and the practical application of existing SAHP systems has been conducted and presented. The content of this chapter can assist to have a comprehensive understanding of the current status of SAHP technologies. Besides, by analysing the literature, the conclusions discover the potential challenges and barriers lying in the SAHP technologies, develop potential research topics/directions to improve the performance of SAHP technology.

The main components of SAHP systems are the solar energy conversion module, the heat pump module, and the heat storage and exchange module. The different combinations between modules with different technologies can form various SAHP systems. Generally, the SAHP systems are divided into two categories: the parallel system and the series system. Systems in series could be installed in a direct expansion or indirect expansion configuration. By integrating the parallel and the series systems together, a dual-source SAHP system is proposed. To assist the SAHPS design and comprehend the classification method, a simple visualisation scheme is provided and is widely used to depict a SAHP system.

The solar energy conversion module of SAHP systems is the combination of different kinds of solar collectors. the non-concentrating solar collectors are prevailingly used in SAHP systems. The widely investigated solar collectors that are being used in the SAHP systems are the flat plate collectors (FPC), the unglazed solar collectors (USC), the evacuated tube collectors (ETC), the PVTFPCs, the unglazed PVT collectors, and the low-concentrating PVT concentrators.

When it comes to the heat pump module, the single-stage compression systems become less efficient with loss of capacity. To overcome these limitations, multistage or hybrid compression cycles were proposed by many researchers, i.e., multi-stage compression cycles, cascade cycles, ejector assisted compression cycles, auto-cascade cycles, trans-critical cycles, and organic Rankine cycles. In addition, to protect the environment from being damaged by the harmful refrigerants and improve the performance of the refrigerants simultaneously, many environment-friendly refrigerants have been proposed.

The heart of SAHPSs is the HSEU. By improving the thermal gradient, so called storage stratification, system performances may be enhanced considerably. For example, the stratified HSEU can provide the lower inlet temperature of the solar collectors and the heat pump, thus increasing the solar thermal efficiency and the performance of the heat pump. Accordingly, the improvements were dependent on system design and operation as well as the solar fraction. During the last decades, the main research contents about the HSEU focus on the methods to increase the HSEU stratification. Apart from the most popular sensitive thermal storage material used in SAHP systems, water, the phase-change heat storage material can also be used as the heat storage medium in the water tank, which can improve the thermal efficiency and the thermal stratification of HSEU. More importantly, the phase change materials (PCMs) in the hot water tank can be used for shifting peak power demand.

The reported investigations on solar assisted heat pumps are categorized into five

major groups as follows: (1) drying; (2) room space heating; (3) agricultural greenhouse space heating; (4) water heating; and (5) desalination applications.

Furthermore, the established research in SAHP technology is substantial, and usually aims to (1) reveal the nature of the energy transfer and conversion occurring in SAHP modules and module-based systems; (2) identify common system types; (3) optimise the structural/geometric parameters of SAHP systems and suggest appropriate operational conditions; (4) build the link between theoretical analysis and practical application; and (5) analyse the economic and environmental benefits of SAHP systems and study their feasibility. All these efforts have contributed to developing SAHP systems that are as efficient as possible with the least cost and simplest structure.

Although numerous pieces of research have been carried out in the field of SAHP technology, the industry still faces various inherent technical challenges, such as poor performance at low ambient temperature, weak of strong complementarity of solar collector and heat pump, and lack of tools for system design, optimization and performance evaluation. To overcome these technical barriers, opportunities for further development of PV/T technology have been discussed, including: (1) increasing solar collector heat transfer capacity, (2) developing optimised solar collectors array connection methods, (3) using wasted heat as an energy source, (4) optimising HSEU structure, (5) employing ground source SAHP system, and (6)using artificial intelligent programming to optimise solar assisted heat pump system and its modules The review results helped to (1) identify the technical barriers existing in current SAHP technology, (2) establish a scientific methodology for the SAHP research, (3) propose new research opportunities, and (4) build the research direction for subsequent chapters.

CHAPTER 3: PRELIMINARY DESIGN OF THE SOLAR ASSISTED HEAT PUMP SPACE HEATING AND HOT WATER SUPPLY SYSTEM

3.1 Chapter Introduction

This chapter introduces a design process of a novel solar assisted heat recovery heat pump (SAHR-HP) system for space heating and hot water generation. The system comprises an innovative solar collectors array, a novel fast responsive heat storage/exchanger and a novel vapour injection heat recovery air source heat pump (VIHR-ASHP). The chapter includes the following parts:

(1) Preliminary design of the system and its associated components;

(2) Working principle of the system;

(3) Operational modes and schemes of the system;

(4) Major parameters relating to the system and associated components;

(5) Identification of the research questions and approaches for problem solving.

A preliminary design of the novel SAHR-HP system illustrates the general concept of the new ideas and builds the fundamental physical structure for the further investigations in the following chapters.

3.2 System Description and Working Principle

3.2.1 System description

The newly designed SAHR-HP system is intended to provide space heating, cooling and hot water for residential and office buildings. Solar energy and the waste heat from

the exhausted air of the ventilation system of the building are used to improve the energy efficiency and decrease the consumption of the electricity. The schematic of the proposed SAHR-HP system is shown in Fig. 3-1. The heating mode and the cooling mode of the system can be switched with each other by controlling the three-way valves laid in the pipeline of the system. The system comprises a few innovative parts: (1) a multiple-throughout-flowing mini-channel solar collectors array which, owing to the reciprocating flowing of the fluid across the array, can effectively reduce the temperature difference between the head and rear panels of the array and thus increase the overall solar thermal efficiency compared to existing flat-plate solar collectors which are arranged in series (i.e., one-to-one-connection); (2) a fast responsive heat storage/exchanger that allows the solar heat to be stored into the unit when the collected heat is greater than the heat demand of the building, and to be discharged into the loop water when the collected solar heat is less than the heat demand of the building; (3) a novel vapour injection heat recovery air source heat pump (VIHR-ASHP) linked with the operation of a heat recovery device (HRD). The HRD uses a counter-flow air-to-air plate-fin heat exchanger (PFHE), can provide fresh air all of the time and can recover part of the heat from the exhausted air of the building while the VIHR-ASHP stops. To achieve the device switch between the PFHE and VIHR-ASHP, a three-way air damper is installed in the exhausted air duct to lead the path of air; (4) a domestic hot water tank is also embedded into the system to use the collected heat from solar collectors for supplying hot water to the building; (5) alternative pipe routes (i.e., via or by-passing the heat exchanging/storage unit) that allow the fluid to be transported to the room under-floor heating coils directly when the loop fluid has a relatively lower temperature (e.g. 40℃~50℃) and to travel through the heat exchanging/storage unit when the loop fluid has a higher temperature (e.g. >50℃). An under-floor coil is implemented as the heat releasing part to supply heating and cooling to the building, which can improve the thermal comfort.

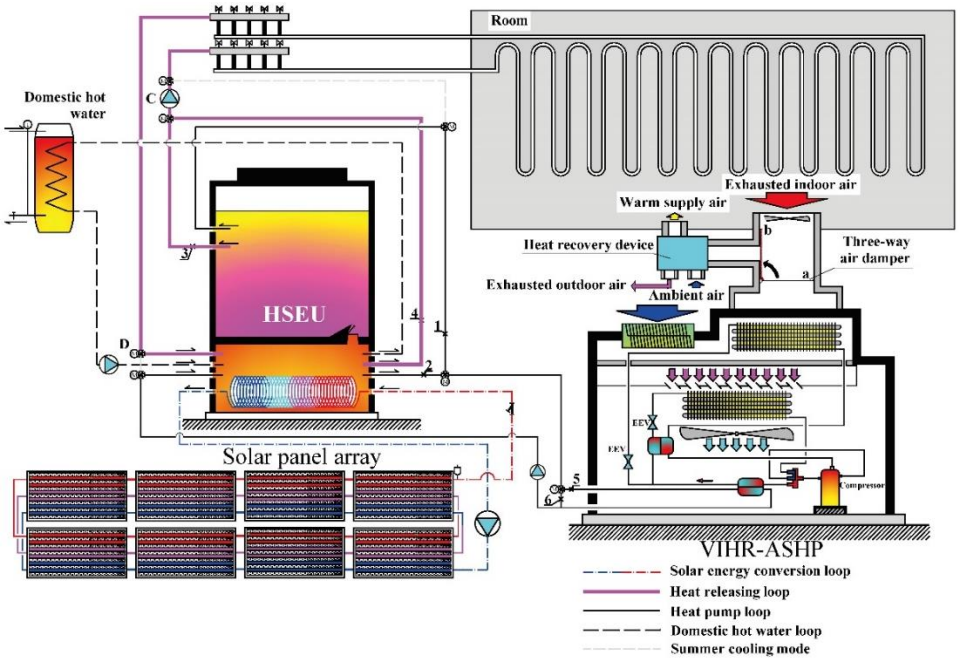

Fig. 3-1 Schematics of the SAHR-HP system under heating mode

In the under-heating mode, there are four liquid loops lying in the system, including the solar energy conversion loop, the heat pump loop, the domestic hot water loop and the heat releasing loop for space heating. The loops for the heating function are shown in Fig. 3-2.

The solar energy conversion loop is a self-closed loop filled with the anti-frozen liquid used for transferring the collected heat from the solar collectors array. In the heat releasing loop, a three-way magnetic valve is used to shift the inlet of the loop between the bottom part of the HSEU and the upper part of the HSEU (pipelines 4 and 3, respectively) according to the system operation status. In the heat pump loop, there are two three-way magnetic valves that are used to control the system operation. One of the valves is used to shift the inlet of the loop between the bottom part of the HSEU and the upper part of the HSEU (pipelines 2 and 1, respectively), and the other is used to control the by-pass (pipeline 6) of the heat pump. In addition, the domestic hot water loop is simply connected to the bottom part of the HSEU. Furthermore, a three-way air damper is installed in the air duct to switch the operation between the VIHR-ASHP and the PFHE to make full use of the exhausted indoor air. The air damper can be at

both Position a and Position b. When the damper is at Position a, the exhausted indoor air travels through the air duct, and then enters the PFHE. On the other hand, while the damper is at Position b, the exhausted indoor air enters the VIHR-ASHP directly to improve the performance of the heat pump.

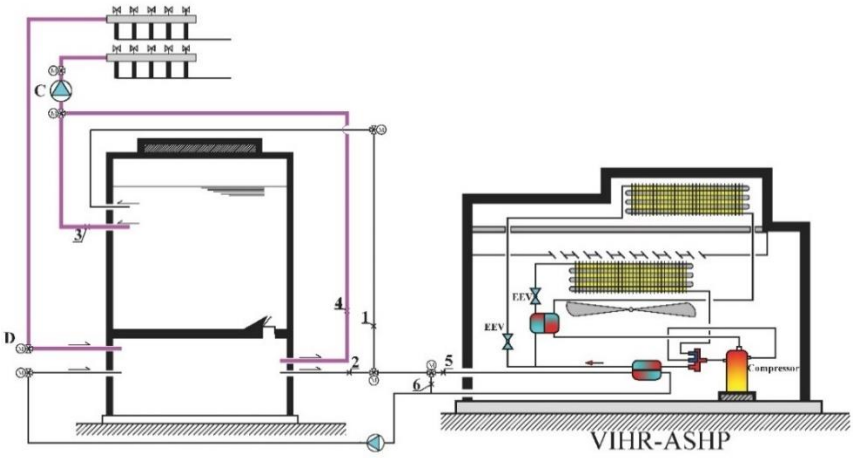

Fig. 3-2 Winter heating mode

Under the cooling mode, there are three liquid loops lying in the system, including the solar energy conversion loop, the heat pump loop, and the domestic hot water loop. There is no heat releasing loop because the heat pump supply cooling energy directly to the under-floor coil. The loop for the cooling operation is shown in Fig. 3-3.

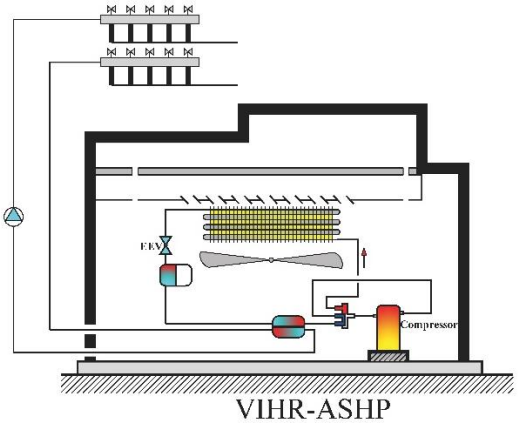

Fig. 3-3 The summer cooling mode of the system

The flow pattern of the solar energy conversion loop and the domestic hot water loop are the same as for the heating mode. The heat pump loop combines VIHR-ASHP and the under-floor coil together to supply cooling to the building directly. The operation of the PFHE is same as the heating mode.

3.2.2 Working principle

The core of the system is the HSEU which collects the heat generated by the solar collectors array and the VIHR-ASHP, and transfers the heat for space heating and domestic hot water. Three renewable energy sources are used in the SAHR-HPs, i.e., solar energy, air energy source and waste energy from the building. The solar energy can be converted into heat by using solar collectors. The air energy source and the waste energy from the building are used by the VIHR-ASHP.

According to the significant functions of the HSEU in the system, the control strategy is mainly relevant to the operation status of the HSEU. For winter heating, there are four operational modes with the new HSEU, i.e., the heat storing and release mode, the heating supply mode, the heat storage mode, and finally, the stagnant mode. Under the heat storing and release mode, the system stores the spare heat from the solar collectors array and provides space heating simultaneously. When the room temperature rises to a certain level, the space heating will pause, and the system will be switched into the heat storing mode, under which the solar thermal heat will be stored in the HSEU. The collected heat from the solar thermal collectors array or the heat pump will be provided for space heating directly from the lower part of the HSEU, during which time the system is switched into the heating supply mode. Furthermore, the system stops when the spare heat from the solar thermal collectors array is unavailable, during which time the room temperature remains at a certain level.

The four operation modes of the HSEU are illustrated in Section 3.4.3. Generally, control strategies of the system are classified into two types, i.e., Daytime Modes and Night-time Modes. During the daytime ($T_p \geq 45°C$), there are seven system operation

modes according to the different room temperatures (T_r), the HSEU bottom part temperature (T_{bt}), the HSEU upper part mean temperature (T_{upt}) and the domestic hot water tank mean temperature (T_{dht}) including the system stagnant mode, the solar energy heat storage mode, the solar energy bottom part heating supply mode, the solar energy heat storage and release mode, the solar energy and heat pump bottom part heating supply mode, the solar energy and heat pump heating up mode, and the domestic hot water heating mode. During the night-time (T_p<40°C), there are five system operation modes, including the system stagnant mode, the stored energy heating supply mode, the heat pump operation mode, the heat pump bottom part heating supply mode and the bottom part heating supply mode. The details of the system operation modes in daytime and night-time are listed in Table 3-1.

Table 3-1 The details of the system operation modes in daytime and night-time

Time mode	Operation mode	Conditions	Operation Details
Daytime Mode	System Stagnant Mode	$T_r \geq 23°C$ $T_{bt} < T_{upt}$	The whole system stops except the solar collectors array and the PFHE (AD**: a);
	Solar Energy Heat Storage Mode	$T_r \geq 23°C$ $T_{bt} - 5 \geq T_{upt}$	The collected solar energy is transferred from the bottom part of the HSEU to the upper part, and stored for later use (PL*:1 & 6; AD: a);
	Solar Energy Bottom Part Heating Supply Mode	$T_r < 18°C$ $T_{bt} > 42°C$	The collected solar energy is used for space heating directly from the bottom part of the HSEU (PL: 4; AD: a);
	Solar Energy Heat Storage and Release Mode	$T_r < 18°C$ $T_{bt} > 42°C$ $T_{bt} - 5 \geq T_{upt}$	The collected solar energy is transferred and stored to the upper part of the HSEU, and the system also provides space heating from the bottom part of the HSEU simultaneously (PL: 4, 1 & 6; AD: a);
	Solar Energy and Heat Pump Bottom	$T_r < 18°C$ $T_{bt} < 38°C$	The heat from the solar collectors and the VIHR-ASHP heats up the bottom part of the HSEU

	Part Heating Supply Mode		simultaneously, and space heating is supplied from the bottom part of the HSEU (PL: 4, 2 & 5; AD: b);
	Solar Energy and Heat Pump Heating Up Mode	$T_r < 18°C$ $T_{bt} < 35°C$	Due to the low HSEU bottom part temperature, the system cannot provide space heating for the residents, and the solar collectors and the VIHR-ASHP are used to heat up the bottom part of the HSEU simultaneously (PL: 2 & 5; AD: b);
	Domestic Hot Water Heating Mode	$T_{bt} > 50°C$ $T_{bt} > T_{dht}$	The domestic hot water heating control strategy is not linked with other system components, and is just controlled by the HSEU bottom part temperature under the daytime mode;
Night-time Mode	System Stagnant Mode	$T_r \geq 23°C$	The whole system stops except the PFHE (AD: a);
	Stored Energy Heating Supply Mode	$T_r < 18°C$ $T_{upt} > 35°C$	During the night-time mode, the stored heat in the upper part of the HSEU is preferentially used to provide space heating (PL: 3; AD: a);
	Heat Pump Operation Mode	$T_r < 18°C$ $T_{upt} < 32°C$ $T_{bt} < 35°C$	Due to the low HSEU bottom part temperature, the system cannot provide space heating for the residents, and the VIHR-ASHP is used to heat up the bottom part of the HSEU (PL: 2 & 5; AD: b);
	Heat Pump Bottom Part Heating Supply Mode	$T_r < 18°C$ $T_{bt} < 35°C \sim 45°C$	The VIHR-ASHP is used to heat up the bottom part of the HSEU. In the meantime, the system provides space heating from the bottom part of the HSEU (PL: 4, 2 & 5; AD: b);
	Bottom Part Heating Supply Mode	$T_r < 18°C$ $T_{bt} > 45°C$	The system provides space heating from the bottom part of the HSEU (PL: 4; AD: b);
*PL: Pipeline position under different three-way valve position; **AD: Three-way air damper valve position.			

For summer cooling, there is one operation status of the HSEU which is to store the

collected solar energy for the domestic hot water supply. The solar collectors array and the domestic hot water tank is controlled using the same strategy as the summer mode. The heat pump for space cooling is controlled by the room temperature (T_r). While T_r<23°C, the heat pump remains stopped, and the heat pump will be in operation for space cooling when T_r>23°C.

3.3 Parametrical Analysis of the New SAHP System

The technical specifications of the individual components of the system are presented in Table 3-2.

Table 3-2 The technical specifications of the components of the system

Name	Size	Technical index
Solar thermal collectors	1m x 2m	Maximum heat output: 1000W
Heat pump	1.5m x 0.5m x 1m	Nominal condition heating output: 12000W
Heat storage and exchange unit	Diameter: 1.19m, Height: 1.38m	Volume: 1.5m^3
PFHE	0.3m x 0.8m x 0.5m	Air flow rate: 250m^3/h
Under floor coil	Diameter: 16mm	Material: PE-X Length: 300m

3.4 Parametric Design of System Components

3.4.1 Solar panel and solar collectors array

The solar energy conversion module of the system is a novel mini-channel solar thermal collector, which is shown schematically in Fig. 3-4. The collector contains three lateral mini-channel tube bundles crossing the collector, thus forming three inlets and three outlets. This facilitates the connection of the solar collectors array with different connection methods. Every mini-channel tube bundle contains three mini-channel tubes which are connected together by manifolds at two ends of the tube. The mini-channel tube bundles are covered by an integral solar thermal absorbed plate

coated with the black chromium, which is shown in Fig. 3-5.

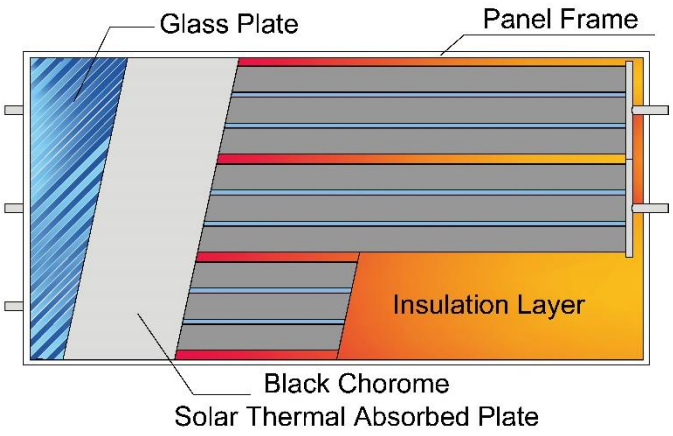

Fig. 3-4 The novel mini-channel solar thermal collector

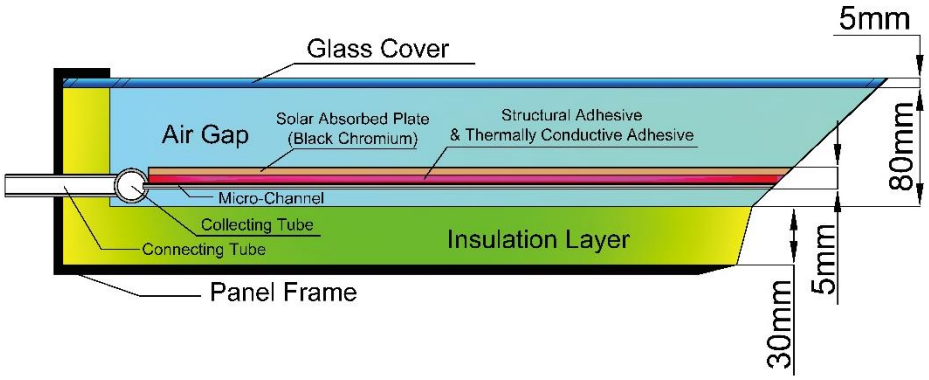

Fig. 3-5 The sectional view of the novel mini-channel solar thermal collector

Even with the novel mini-channel solar thermal collector, the solar collectors array also is connected with a novel connection method, to form a multiple-throughout-flow connection method, under which the solar thermal efficiency and the integral performance of the solar collectors array can be increased, explaining why this is necessary. Schematics of both the multiple-throughout-flowing mini-channel solar collectors array and the traditional one-to-one-connection mini-channel solar collectors array are shown in Figs. 3-6(a) and 3-6(b), respectively. Compared to the traditional one-to-one-connecting type, the new array, by applying the multiple-throughout-flow mode and associated

connection method, can achieve a significantly higher solar thermal efficiency, owing to the reduced temperature difference between the head and rear panels in the array, and increased flow rate of the fluid through the cross section of the panels. Furthermore, this layout can also significantly reduce the flow resistance of the fluid across the panels in the array, owing to the reduced fluid turning number and reduced quantity of local fittings through its pathway (i.e., elbows, T-junctions, bends et al.), thus leading to a significantly higher Energy Efficiency Ratio (EER) value. Based on the above system design platform, four panels of 1m x 2m each in an array are considered as the starting point of this research.

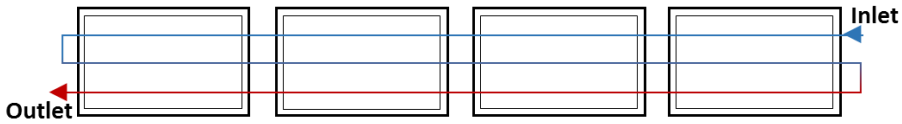

(a) Multiple-throughout-flowing type

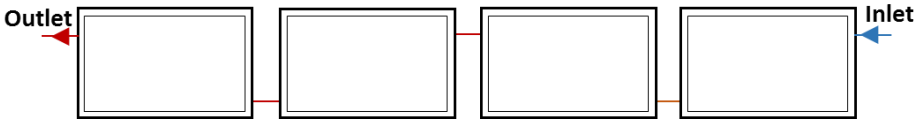

(b) Traditional one-to-one-connecting type

Fig. 3-6 Schematics of the new and traditional solar collectors arrays: (a) Multiple-throughout-flowing type; (b) Traditional one-to-one-connecting type

3.4.2 Heat pump

The composition and working principle under heating mode of the VIHR-ASHP are shown in Fig. 3-7. The system is mainly composed of six individual types of component, and eight items altogether: a vapour injected compressor, an internal heat

exchanger (IHX), a coil heat exchanger (condenser), two electronic expansion valves (EEVs), two evaporators and a refrigerant storage tank. In order to utilise the exhaust heat from the buildings fully, the novel VIHR-ASHP is innovatively fitted with an evaporator (Evaporator 1) after the EEV along the vapour injection line in order to extract a part of the heat directly from the exhaust air. The refrigerant in the vapour injection line will also acquire a part of the heat from the refrigerant in the evaporation line via the heat exchange process in IHX, thus leading to sub-cooling in the evaporation line and superheating in the vapour injection line. When it comes to the air path, after going through the Evaporator 1, the exhaust air still contains useable heat. However, the heat capacity existing in the exhaust air is not enough for the heat pump operating under the optimum working condition. Hence, fresh air is introduced as an energy source, which is mixed with the exhaust air coming through Evaporator 1. The mixed air will go through Evaporator 2 in the evaporation line for further heat extraction. This two-stage evaporation can greatly increase the exhausted energy utilisation, and can eventually increase the performance of the VIHR-ASHP.

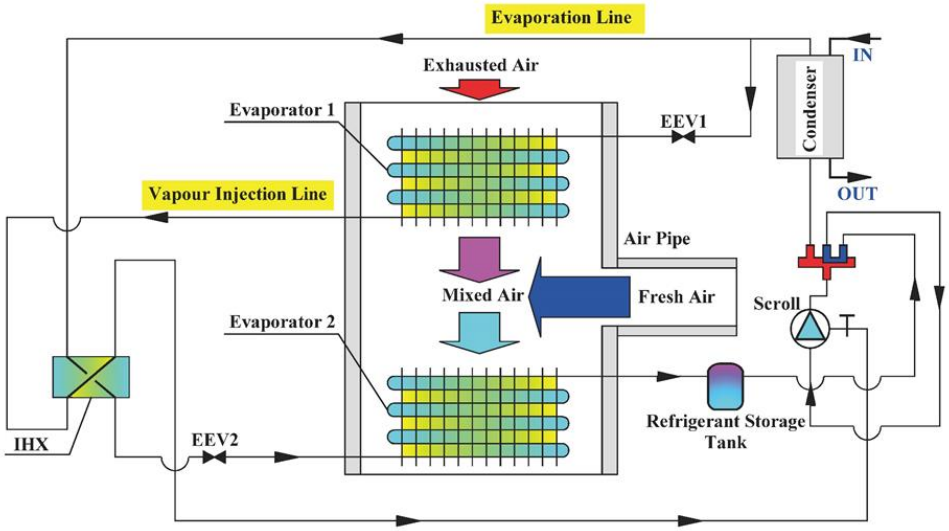

Fig. 3-7 Structure and work principle of the VIHR-ASHP system under heating mode

A schematic of the novel VIHR-ASHP is shown in Fig. 3-8. Unlike the conventional VIASHP (vapour injection air source heat pump), the novel VIHR-ASHP adds an

evaporator into the vapour injection line after EEV1 and before the IHX (the red component shown in Fig. 3-8).

In the compression process of the conventional VIASHP, the superheated refrigerant vapour from the compressor (State 1) enters the coil heat exchanger (condenser), where the vapour is condensed to State 2. The liquid refrigerant leaving the condenser (State 2) is separated into two pipelines (the vapour injection line and the evaporation line). After the refrigerant has expanded through EEV1 in the vapour injection line to State 3, it is directly transferred to the IHX, superheated to State 5 by the refrigerant with State 2 in the evaporation line, and sucked into the compressor through the injection port. Because the heat capacity of the State 2 refrigerant in the evaporation line is limited, the refrigerant mass flow rate in the vapour injection line is relatively small. In the evaporation line, after the IHX, the refrigerant reaches State 6. After that, it experiences an expansion process through EEV2 to State 7. Finally, superheated by the air in the evaporator to State 8, the refrigerant is sucked into the compressor through the suction port.

The compression process of the VIHR-ASHP is similar to that of the conventional VIASHP from State 1 to State 2. The refrigerant in the vapour injection line goes through EEV1 first to State 3 and then evaporates in Evaporator 1 to State 4 by extracting the heat from the exhaust air from the building's ventilation system. Afterwards, the refrigerant is transferred to the IHX to absorb a part of the heat from the evaporation line to State 5 and finally injects it into the vapour injection compressor. In addition to the vapour injection line after the condenser, a part of the refrigerant is transferred to the evaporation line which directs the refrigerant to release heat into the IHX. After coming out from the IHX (State 6), the refrigerant goes through EEV2 to State 7. The evaporating process then takes place in Evaporator 2 to State 8 by absorbing the heat from a mixed air which is the mixture of fresh air and the air coming from Evaporator 1. Finally, after going through the refrigerant storage tank, the superheated refrigerant vapour returns to the compressor via the suction inlet. In the

vapour injection compressor, the vapour refrigerant from the evaporation line is compressed initially, where it is mixed with the refrigerant vapour from the vapour injection line. In the end, the mixed refrigerant vapour is further compressed to the discharge pressure (State1).

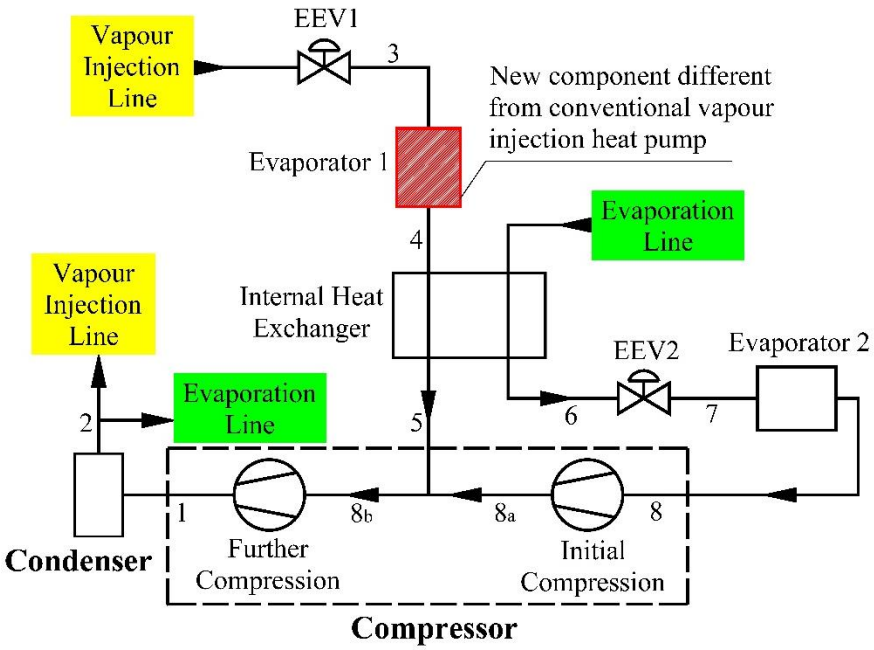

Fig. 3-8 Schematic of the conventional and novel vapour injected compression process.

A P-h diagram for the conventional vapour injection (VI) cycle and the novel heat recovery vapour injection (VIHR) cycle is shown in Fig. 3-9. As shown in the figure, the two compression cycles are similar and are typical for vapour injection cycles. The difference between the conventional VI cycle and the VIHR cycle is in the compression line, where the conventional VI cycle's evaporating pressure (depicted by the red dashed lines) is lower than the VIHR cycle's evaporating pressure (depicted by the black solid lines). Unlike the conventional VI cycle, there is an evaporator in the vapour injection line in the novel VIHR-ASHP, meaning that both the vapour injection line and the evaporation line contain an evaporation process. The newly added evaporator in the vapour injection line can increase the heat transfer capacity of the refrigerant significantly. As a result, this characteristic of the novel VIHR-ASHP

increases the refrigerant's mass flow rate in the vapour injection line, which directly leads to an increased refrigerant pressure in the evaporation line. Hence, the increased final compression ratio (a ratio between the condensing pressure and evaporating pressure in the evaporation line) increases the performance of the heat pump.

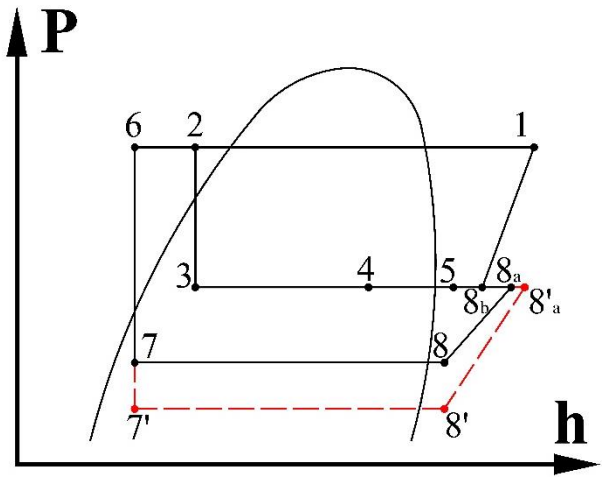

Fig. 3-9 P-h diagram for the conventional VIASHP and the novel VIHR-ASHP.

A T-S diagram for the conventional VI cycle and the novel VIHR cycle is shown in Fig. 3-10. As with the P-h diagram, two cycles experience similar compression and evaporation processes. The difference between the conventional VI cycle and the novel VIHR cycle is an extra evaporation process lying in the vapour injection line of the VIHR-ASHP, which can increase the heat transfer capacity and refrigerant mass flow rate of the vapour injection line. This, in turn, leads to an increased temperature in the evaporation line and the decline of the temperature difference between the condensing temperature and evaporating temperature in the evaporation line, giving an enhanced performance for the VIHR-ASHP.

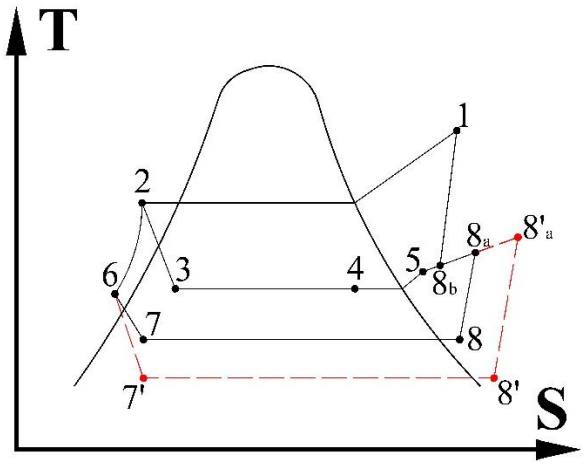

Fig. 3-10 T-S diagram for the conventional VIASHP and the novel VIHR-ASHP.

Under the cooling mode, the vapour injection line of VIHR-ASHP is closed, thus forming a normal heat pump cycle. A four-way reversing valve is used to switch the heat pump between heating and cooling mode. The cooling mode of VIHR-ASHP is shown in Fig. 3-11.

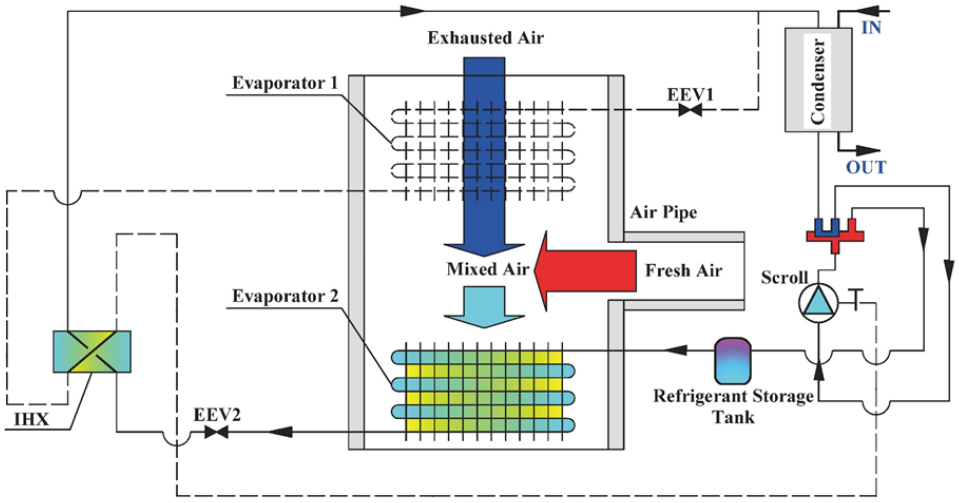

Fig. 3-11 Composition and working process of the VIHR-ASHP

device under cooling mode

3.4.3 Heat storage and exchange module

The schematic of the heat storage and exchange unite (HSEU) for the novel mini-channel solar thermal space heating and hot water system is shown in Fig. 3-12.

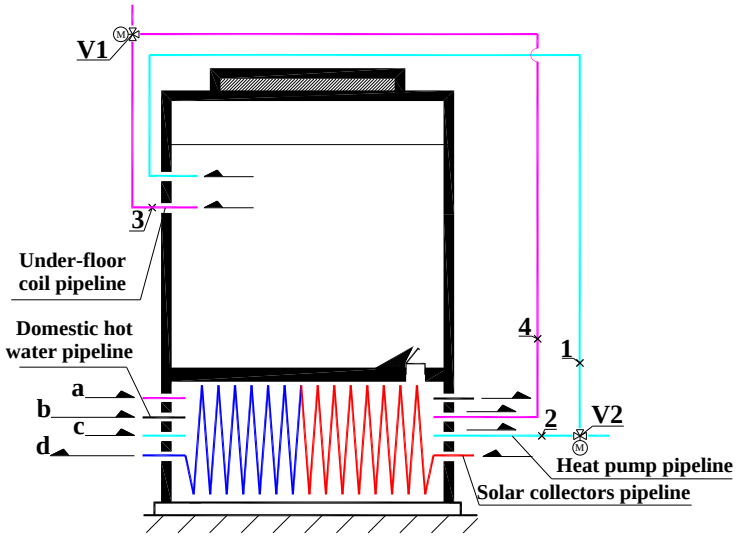

Fig. 3-12 The schematic of the HSEU

As shown in Fig. 3-12, the whole HSEU is divided by a thick insulated board into two main parts which are the heat storage part in the upper segment of the HSEU and the heat exchange part at the bottom of the HSEU. The plastic board can prevent the heat transfer process between the two main parts, and the small hole with a cap on the board can let the fluid pass from the heat exchange part to the heat storage part, which can help the novel HSEU to store the spare heat collected by the solar thermal collectors and the heat generated by the heat pump. The heat storage part contains a great amount of water which can store enough heat for space heating on nights or cloudy days when the collected heat from solar thermal collectors has a surplus, and the heat pumps can use the valley price of the electricity to generate heat.

More importantly, there are four pipelines placed onto the novel HSEU, i.e. the solar thermal collectors' pipeline, the heat pump pipeline, the domestic hot water pipeline and the underfloor coil pipeline. With the structure of the novel HSEU and the

pipelines, the HSEU can achieve seven operational modes: 1. the direct heat supply mode by using the collected heat from the mini-channel solar thermal collectors and the auxiliary heat supply from the heat pump; 2. the direct heat supply mode by using the heat generated by the heat pump; 3. the heat supply mode by using the stored heat; 4. the heat supply and storage mode by using the collected heat from the mini-channel solar thermal collectors; 5. the heat supply and storage mode by using the heat generated by the heat pump; 6. the heat storage mode by using the mini-channel solar thermal collectors; 7. the heat storage mode by using the heat pump.

In terms of the different parameters of the system, for example, ambient temperature, room temperature, inlet and outlet temperature of the underfloor coil, heat storage part temperature and solar thermal collectors temperature, these modes can be conveniently exchanged with each other under the control of an automatic control system. The system could inspect the parameters constantly. According to the pre-entered logic program, the system can control the actions of the pumps, magnetic valves and heat pumps to make sure the whole space system is under the right operation mode. The data will be transferred, saved and analysed by the computer of a control centre to improve and optimise the system.

3.4.4 The operation modes of the novel HSEU

As addressed in the former part, there are generally four operation statuses of the HSEU, i.e., the heat storage and release status, the bottom part heating supply status, the heat storage status and the stopped status. The details of these modes are given below.

(1) The bottom part heating supply status

Under the bottom part heating supply status, the heat transfer process takes place in the bottom part of the HSEU. The collected heat from the energy source is directly supplied to the underfloor coil and the domestic hot water tank. The low volume

capacity and the high heat transfer coefficient of the bottom part of the HSEU can ensure the rapid heating supply, thus maintaining the thermal comfort of the served house. The bottom part heating supply status can also be divided into two working conditions according to the energy source.

During the daytime, the energy source mainly comes from the solar collectors array. The operation graph of this working condition is shown in Fig. 3-13. When the solar energy is not enough for space heating, VIHR-ASHP can be an auxiliary heating device to support the space heating to maintain the thermal comfort of the house. In the meantime, when the temperature of the heat storage part reaches a certain level, it can also supply domestic hot water to the users.

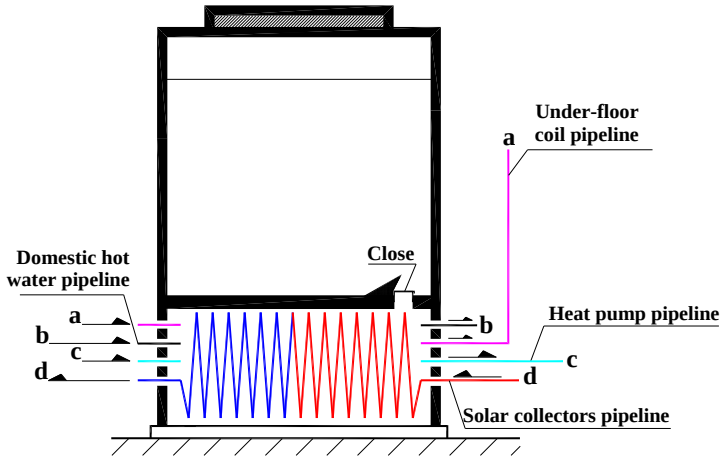

Fig. 3-13 The operation graph of the HSEU in the daytime

When it comes to night-time, the solar energy conversion loop will be stopped due to the low solar radiation. The pipeline under this working condition is shown in Fig. 3-14. When the room temperature reaches to the minimum limit, a VIHR-ASHP will be involved to provide heat for space heating. The maximum heat provided by the VIHR-ASHP is calculated and can fulfil the heat demand of the house in the most extreme local weather conditions, during which the provided and the demanded heats are equal, and the heat can be transferred directly to the under-floor coil pipeline without a heat exchanger.

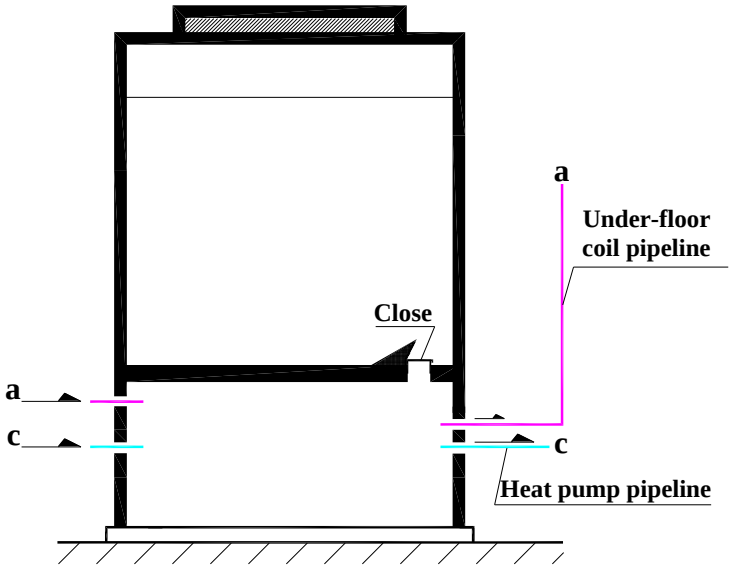

Fig.3-14 The operation graph of the HSEU at night-time

(2) The heat storage and release status

Under the heat storage and release status, there are two working conditions which include the heat storage or releasing process and relate to the upper part of the HSEU. By achieving the interaction between the bottom part and the upper part of the HSEU, the system can realise more practical functions to increase the performance and the efficiency of the whole SAHR-HP system.

During the daytime, under abundant solar radiation, the heat collected by the solar thermal collectors is more than the heat demand of the house, which means that there is spare heat needing to be stored, or the room temperature will otherwise surpass the limit, thus reducing the thermal comfort of the served house and wasting the spare energy. At the mean time of the operation of the under-floor coil loop of the bottom part of the HSEU, the operation of the heat pump loop through the upper part and bypass of the HSEU can help to store spare solar energy in the upper part of the HSEU. The pipeline under this working condition is shown in Fig. 3-15. Consequently, this working condition can store spare heat into the heat storage part of the HSEU and supply heat to the house simultaneously. When the room temperature reaches the upper

limit, the under-floor coil loop can stop and just store the solar energy into the upper part of the HSEU. In addition, when the temperature of the heat storage part reaches a certain level, it can also supply domestic hot water to the users.

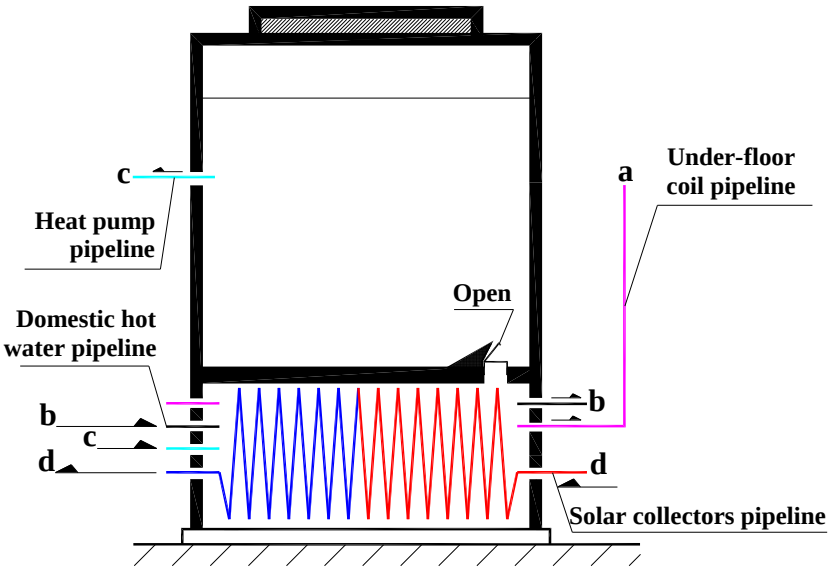

Fig. 3-15 Schematic of the HSEU under heat storage mode

During the night-time, as the solar radiation is not available to drive the solar thermal collectors, the room temperature decreases to the minimum, the space heating system should firstly use the stored heat to supply space heating. The operational process and the pipeline arrangement of this working condition is shown in Fig. 3-16. Transforming the under-floor coil loop to the upper part of the HSEU by manoeuvring the three-way magnetic valve under the control of the automatic control system, the system can circulate the fluid between the bottom part and the upper part of the HSEU, thus using the stored heat to supply heat to the house. In addition, the heat insulation board between the upper and bottom parts of the HSEU can reduce the mix between the water layers of the heat storage part, thus maintaining the stratification of the upper part of the HSEU and ensure the high heat transfer efficiency of the system.

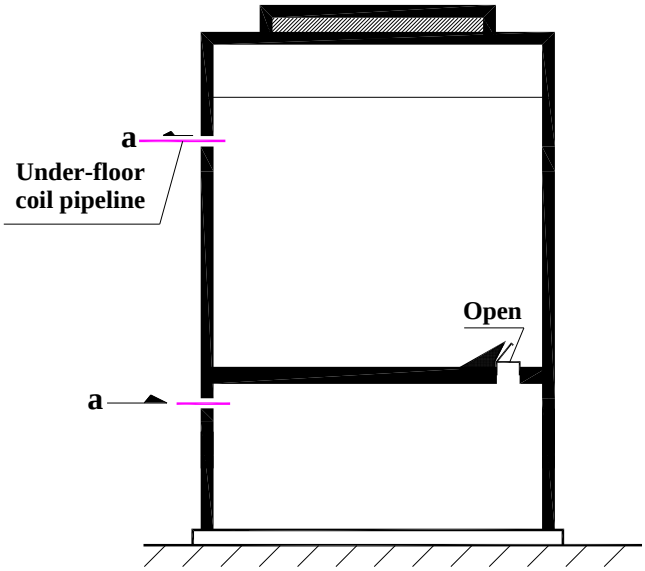

Fig. 3-16 The operation graph of the HSEU under heat release status

(3) The VIHR-ASHP heat storage status

If the system is installed in an office building or a school, the heat load of the building at night should be very low because there are no occupants in the building at night, and the room temperature for such a public building at night should only be maintained at 0^{o}C by applying the bottom part heating supply status or the heat releasing status, the choice of which depends on the electricity policy of power company. If the power company provides peak-valley electricity prices, the heat storage status should be involved to use VIHR-ASHP to store the generated heat into the upper part of the HSEU by using the lower price electricity, thus saving the operation cost of the system. The pipeline of this working condition is shown in Fig. 3-17.

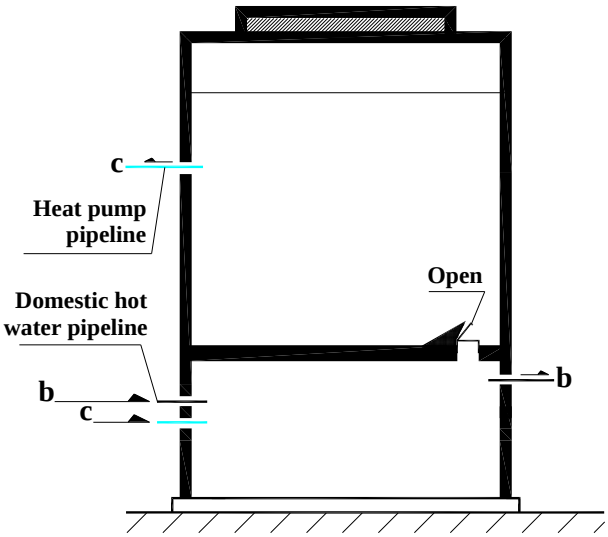

Fig. 3-17 The operation graph of the HSEU under VIHR-ASHP heat storage status

(4) The stagnant mode

When there is no heat transfer between different system components, the HSEU is in the stagnant mode. During the winter heating season, all of the components and the circulation loops will stop under this status because there is not enough solar radiation to drive the operation of the solar collectors array, and the room temperature reaches a certain level. During the summer cooling season, the heat pump loop is independent from the HSEU. Consequently, the VIHR-ASHP is placed to the stopped status of the HSEU for space cooling during the summer cooling time.

3.5 Research Questions and Approaches for Questions Solving

This chapter details the system structure and the functions of the proposed novel SAHR-HP system and its components. To investigate the performance of the system further, there are six research questions that need to be studied in detail: (1) the heat transfer mechanism lying in the SAHR-HP system and its components; (2) the numerical models of the SAHR-HP system and its components, which can be used to optimise and simulate the performance of the system; (3) the performance of the

practical SAHR-HP system and its components; (4) the validity and availability of the established numerical model; (5) the simulation and optimisation of the system; (6) the long-term operational, social-economic and environmental performance of the SAHR-HP system under different climate conditions.

The following chapters will investigate the proposed questions in detail, and the contents include: (1) the theoretical heat transfer process analysis and the establishment of the relevant numerical models (Chapter 4); (2) the construction and the experimental platforms establishment of the SAHR-HP system (Chapter 5); (3) the experiments of the SAHR-HP system and its components (Chapter 5); (4) the validation of the numerical models and the simulation process (Chapter 6); (5) the annually energetic, social-economic and environmental performance simulation under different climate conditions (Chapter 7).

3.6 Chapter Summary

This chapter has illustrated the general design of the SAHR-HP system, its associated system components and its working principles. The distinct features of the proposed SAHR-HP system can be seen below:

(1) The novel SAHR-HP system can be flexibly operated at different modes to adapt to the outdoor and indoor environment variations, thus giving the system a favourable adaptation under different climates and building conditions;

(2) The system can continuously recover heat from the exhausted air by using the PFHE or VIHR-ASHP;

(3) The novel multiple-throughout-flow method of the solar collectors array can achieve higher solar efficiency, lower flow resistance and higher energy efficiency, compared to the current solar collectors array;

(4) The novel VIHR-ASHP can use both ambient air and the exhausted air as the

energy source, which can greatly decrease the compression ratio and improve the performance of the heat pump;

(5) The novel HSEU can give a quick response to the variation of the indoor and outdoor environments and improve the efficiency of the solar collectors array and the whole system.

The system can be installed either on a building facade or as an independent heat and power generation unit. The parameters desired for further characterisation of the system performance were summarised, including the design (structure, geometry and material) and the operational and external parameters. The chapter also presented the parametrical design of the different system components with certain alternative varying ranges, including the mini-channel solar thermal collector, VIHR-ASHP and the novel HSEU. These parametrical data will be applied as the input figures for the modelling and optimisation in subsequent chapters.

CHAPTER 4: THEORETICAL ANALYSIS AND COMPUTER MODELLING OF THE NOVEL SOLAR HEAT PUMP SYSTEM

4.1 Chapter Introduction

Based on the established preliminary design in Chapter 3, this chapter presents the theoretical analysis and computer modelling process for the novel SAHR-HP system. The theoretical analysis is established based on the coupled energy balance equations within different parts of the system, including solar collectors array, VIHR-ASHP, HSEU, heat recovery ventilation device, domestic hot water tank, and under floor coil. Besides, the numerical models of the system and its components are established and simulated in MATLAB. The main contents of this chapter include:

(1) Theoretical analysis of the fluid flow and heat transfer processes taking place in the novel SAHR-HP system;

(2) Simulation methods, including the iterative method (IM), partial differential equation (PDE) and finite element method (FEM), applied to the developed computer models based on established mathematical theory and equations;

(3) Computer simulation models dedicated to the individual system components and the whole system, addressing steady state and dynamic operational performances;

(4) Integrated computer numerical model for simulation and optimisation of the SAHR-HP system.

The work in this chapter will establish the foundation for the works carried out and explained in the following chapters, i.e., prototype fabrication and experimental testing, results analysis, as well as economic and environmental performance analysis.

4.2 The Assumptions of the Mathematical Model

The system is simulated with the operation of its components, i.e., the mini-channel solar thermal collector array, the heat recovery device, the vapour injection heat recovery air source heat pump, and the HSEU. The simulation process of the system has been carried out by using the following assumptions.

(1) The mass flow rate of the working fluid in every mini-channel tube is constant and stable;

(2) The inlet temperature of a mini-channel solar collector is the outlet temperature of the previous collector;

(3) The mass flow rate of the refrigerant in the thermodynamic cycle analysis for the R410A special-designed VI compression cycle is constant and stable;

(4) There is no delayed operation when the system switches between the different operation modes;

4.3 Mathematical Theory and Computer Models for Different Parts of the System

4.3.1 Theoretical analysis and computer model establishment for the solar collectors array

4.3.1.1 Theoretical analysis of the mini-channel solar panel

The solar collectors array is a group of solar thermal collectors which can collect solar radiation and transfer the solar energy to the thermal energy, thus providing heating or DHW. Based on a conventional mini-channel flat-plate solar collector and a novel multiple-throughout-flow solar collectors array, dedicated theoretical analyses are

undertaken. The layouts of the two kinds of collectors are shown in Fig. 4-1(a) and (b), respectively.

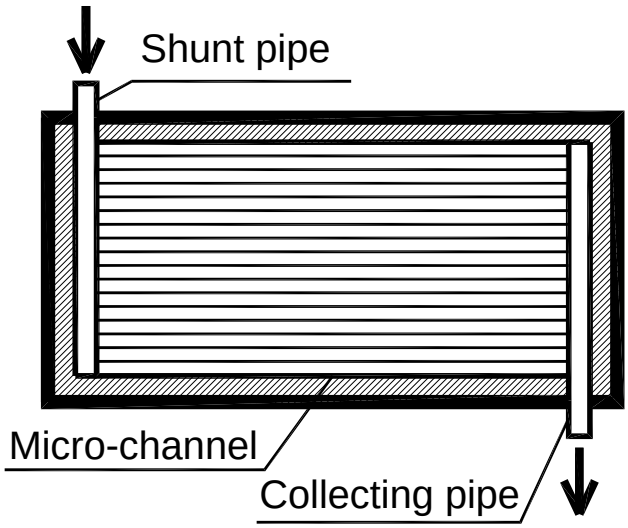

(a) Conventional one-to-one-connecting type

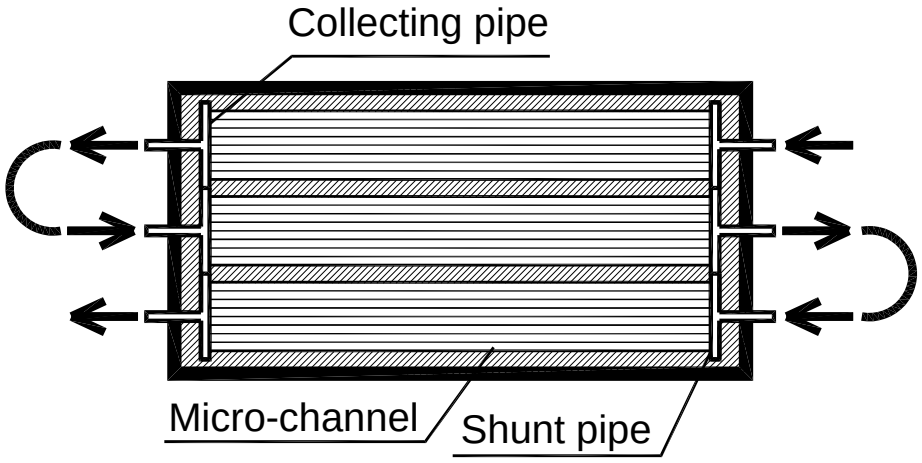

(b) Multiple-throughout-flowing type

Fig. 4-1 Two types of mini-channel flat-plate solar collectors

For the collector with one entry end and one exit end which is produced in China shown in Fig. 4-1 (a), the standard test made by China National Centre for Quality Supervision and Testing of Solar Heating System (Beijing) gave an experimental

thermal efficiency equation, i.e., equation [4-1]. Table 4-1 lists the measurement condition applied to this testing.

$$\eta_{sp.rep} = 0.73 - 3.5\frac{T_{sp.f.in} - T_a}{I} \quad \textbf{[4- 1]}$$

Table 4-1 Test conditions at the national laboratory [202]

Parameters	Test Conditions
Mass flow rate	0.02kg/m^2·s
Solar radiation	600W/m^2
Wind speed	4m/s
The accuracy of the inlet temperature	±0.1℃
Accuracy of the ambient temperature	±0.5℃

As the area of the mini-channel solar thermal collector is 2m^2, the volume flow rate was set to 0.04kg/s which means the testing volume flow rate is 0.15m/h, and flow velocity in the mini-channel is 0.04m/s. According to the parameters, the Reynolds number under the testing condition is taken as 145.6. Taking this as the start point, this section will establish the correlation between the solar thermal efficiency and velocity.

When this type of solar collector is applied to the arrays with one-to-one-connection mode shown in Fig. 4-1(a) and with multiple-throughout-flowing mode shown in Fig. 4-1(b). According to the mass flow rate under the practical conditions, the fluid flow velocity across the channel of the one-to-one connection and multiple-throughout-flowing mode are 0.12m/s and 0.36 m/s respectively, which are higher than the velocity for the standard lab condition (0.04 m/s). To obtain the updated efficiency equations, the following analysis is conducted.

The energy balance occurring in a solar thermal collector can be expressed as:

$$q_{aquire} = q_{use} + q_{loss} \quad [4\text{- }2]$$

In equation [4-2], q_{aquire} can be expressed as:

$$q_{aquire} = I(\tau_{sp}\alpha_{sp}) \quad [4\text{- }3]$$

For the mini-channel solar panel, the solar energy reaching per meter length of the mini-channel strip (shown in Fig. 4-2) can be expressed as:

$$q'_{aquire} = q_{aquire}(2L_{mch} + nD_{mch}) \quad [4\text{- }4]$$

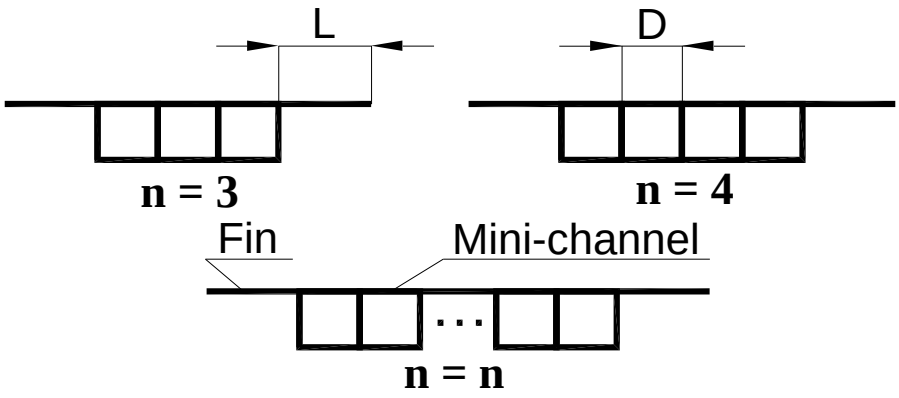

Fig. 4-2 Geometrical representation of a single mini-channel tube

Furthermore, the absorbed heat per meter length of a single mini-channel strip can also be expressed as:

$$q'_{use} = q'_{fin} + q'_{tube} \quad [4\text{- }5]$$

q'_{fin} and q'_{tube} can be further expressed as:

$$q'_{fin} = 2L_{mch}[q_{aquire} - U_{loss}(T_{sp.wall} - T_a)] \quad [4\text{- }6]$$

$$q'_{tube} = nD_{mch}\left[q_{aquire} - U_{loss}\left(T_{sp.wall} - T_a\right)\right] \quad [4\text{- }7]$$

In equation [4-6] and [4-7], U_{loss} can be expressed as:

$$U_{loss} = U_{loss.top} + U_{loss.bottom} + U_{loss.frame} \quad [4\text{- }8]$$

According to the configuration of the mini-channel solar thermal collector, the overall heat loss coefficient (U_{loss}) can be concluded as 4.5 W/m^2·℃. The total heat absorbed by the panel q'_{use} is the sum of q'_{fin} and q'_{tube}, thus

$$q'_{use} = (2L_{mch.fin} + nD_{mch})[q_{aquire} - U_{loss}(T_{sp.wall} - T_a)] \quad [4\text{- }9]$$

The absorbed heat per meter length of a single mini-channel strip can be expressed as:

$$q'_{use} = (2n + 2)D_{mch}h_{c\,sp.f}(T_{sp.wall} - T_f) \quad [4\text{- }10]$$

In equation [4-10], $h_{c\,sp.f}$ can be expressed as:

$$h_{c\,sp.f} = Nu_f \frac{\lambda_f}{D_{mch}} \quad [4\text{- }11]$$

$$Nu_f = 1.86{Re_f}^{1/3}\,{Pr_f}^{1/3}(D_{mch}/L_{mch.tube})^{1/3}(\mu_f/\mu_{sp.wall})^{0.14} \quad [4\text{- }12]$$

Combining equation [4-9] and [4-10] yields:

$$q'_{use} = F'_{sp}[q_{aquire} - U_{loss}(T_f - T_a)] \quad [4\text{- }13]$$

F' is defined as the efficiency factor of mini-channel solar thermal collector which can be expressed as:

$$F'_{sp} = \frac{1/U_{loss}}{\frac{1}{(2n+2)D_{mch}h_f} + \frac{1}{U_{loss}(2L_{mch.fin}F_{mch.fin}+4D_{mch})}} \quad [4\text{- }14]$$

The efficiency factor of a mini-channel solar thermal collector, F', used in equation [4-13] contains an unknown parameter, T_f. In this case, a known factor, $T_{f.in}$, should be used to calculate the absorbed heat q'_{use} instead of the unknown parameter T_f. This conversion process is described as below:

As shown in Fig. 4-3, an infinitesimal part of a mini-channel with a length of dy is

used for this analysis; the heat carried by the entering flow and exiting flow can be represented by $m_{sp.f}Cp_fT_{f,y}$ and $m_{sp.f}Cp_fT_{f,y+dy}$ respectively.

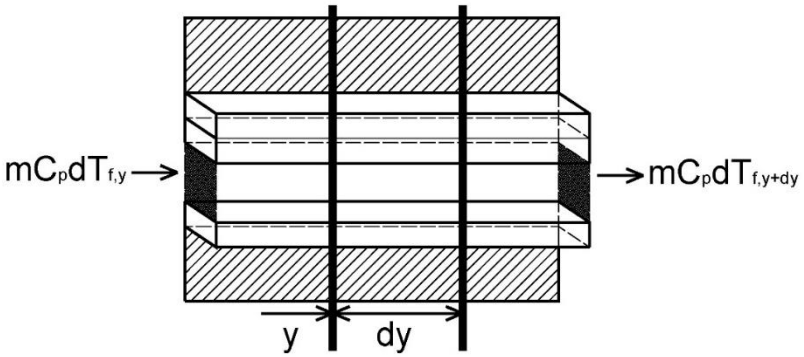

Fig. 4-3 Geometrical set-up of a mini-channel

The absorbed heat by this infinitesimal part of mini-channel with a length of dy can be expressed as:

$$m_{sp.f}Cp_f dT_f = q'_{use}dy \quad [4\text{- }15]$$

Combination of equation [4-13], [4-15], and [4-16] yields,

$$m_{sp.f}Cp_f dT_f = F'_{sp}[q_{aq} - U_L(T_f - T_a)]dy \quad [4\text{- }16]$$

Integrating the both sides of equation [4-16] yields,

$$\int m_{sp.f}Cp_f dT_f = \int F'_{sp}[q_{aq} - U_{loss}(T_f - T_a)]dy \quad [4\text{- }17]$$

Solving the integrating equation [4-17] yields:

$$\frac{T_f - T_a - q_{aquire}/U_{loss}}{T_{f.in} - T_a - q_{aquire}/U_{loss}} = \exp\left[-U_{loss}F'_{sp}y/m_{sp.f}Cp_f\right] \quad [4\text{- }18]$$

The length of mini-channel tube is l, which means the y in equation [4-18] equals l. As a result, the outlet temperature of working fluid ($T_{f.out}$) can be expressed as:

$$T_{f.out} = T_a + \frac{q_{aquire}}{U_{loss}} - \left[\frac{q_{aquire}}{U_{loss}} - \left(T_{f.in} - T_a\right)\right]\exp\left(-F'_{sp}U_{loss}L_{mch.tube}/m_{sp.f}Cp_f\right)$$

[4- 19]

The absorbed heat by mini-channel can be expressed as:

$$Q_{use} = m_{sp.f} Cp_f (T_{f.out} - T_{f.in}) \quad [4\text{- }20]$$

The absorbed heat by per unit area mini-channel can be written as:

$$q_{use} = \frac{m_{sp.f} Cp_f}{(2L_{mch.fin} + nD_{mch}) L_{mch.tube}} (T_{f.out} - T_{f.in}) \quad [4\text{- }21]$$

Inserting equation [4-19] into equation [4-21], the absorbed heat by per unit length of mini-channel can be expressed as:

$$q_{use} = F_R [q_{aquire} - U_{loss} (T_{f.in} - T_a)] \quad [4\text{- }22]$$

F_R is the heat transfer factor of the mini-channel solar thermal collector, which can be expressed as [203]:

$$F_R = \frac{m_{sp.f} Cp_f}{(2L_{mch.fin} + nD_{mch}) L_{mch.tube}} [1 - \exp(-F'_{sp} U_{loss} L_{mch.tube} / m_{sp.f} Cp_f)] \quad [4\text{- }23]$$

Based on above equations, the heat transfer factors of the mini-channel solar thermal collector (F_R) relating to the three types of panels-arrays are calculated as shown in Table 4-2.

Table 4-2 The heat transfer factors of the mini-channel solar thermal collector (F_R)

	Multiple-throughout -flowing	**One-to-one connecting**	**One-to-one connecting (testing)**
F_R	0.92	0.86	0.76

Solar thermal efficiency (η_{sp}) of the panel can be expressed as:

$$\eta_{sp} = \frac{q_{use}}{q_{aquire}} \quad [4\text{- }24]$$

Combining equation [4-22], [4-23], and [4-24] yields:

$$\eta_{sp} = \frac{F_R[q_{aquire} - U_{loss}(T_{f.in} - T_a)]}{q_{aquire}} = F_R(\tau_{sp}\alpha_{sp}) - F_R U_{loss}\frac{(T_{f.in} - T_a)}{I} \quad [4\text{- }25]$$

For the one-to-one connection with u value of 0.04 m/s, the solar thermal efficiency equation can be written as:

$$\eta_{sp.oto} = 0.74 - 3.3\left(\frac{T_{f.in} - T_a}{I}\right) \quad [4\text{- }26]$$

The theoretical equation (i.e., equation [4-25]) of solar thermal efficiency for one-to-one connecting methods under formal testing condition with u value of 0.04m/s has a good consistence with the equation [4-1]. This proves the availability and accuracy of the theoretical analysis.

For the one-to-one-connection type with u value of 0.12 m/s, F_R is 0.86 the thermal efficiency equation can be written as:

$$\eta_{sp.oto} = 0.81 - 3.6(\frac{T_{f.in} - T_a}{I}) \quad [4\text{- }27]$$

For the multiple-throughout-flowing type with u value of 0.36 m/s, F_R=0.92, thus, the thermal efficiency equation of the panel can be expressed as:

$$\eta_{sp.mtf} = 0.92 - 4.1(\frac{T_{f.in} - T_a}{I}) \quad [4\text{- }28]$$

4.3.1.2 The steady numerical model of the mini-channel solar collectors array with multiple-throughout-flow method

The numerical model of the mini-channel solar collectors array with multiple-throughout-flow method is based on the theoretical analysis. Due to three-runners

structure, the panel is divided into three parts along the height, and each runner is divided into n part which is shown in Fig. 4-4.

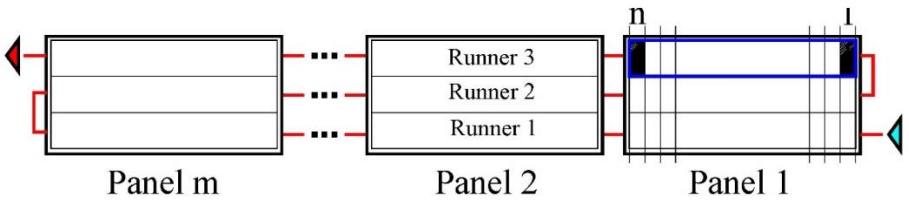

Fig. 4-4 Finite element set-up of the mini-channel solar collectors array

The solar energy which is collected by the finite element $A_{pa.run.n}$ can be expressed as:

$$Q_{pa.run.n} = A_{pa.run.n}\eta_{sp.pa.run.n} \quad [4\text{-}29]$$

In equation [4-29], the area of the finite element $A_{pa.run.n}$ and the solar thermal efficiency $\eta_{sp.pa.run.n}$ can be expressed as:

$$A_{pa.run.n} = A_{sp}/(3n) \quad [4\text{-}30]$$

$$\eta_{sp.pa.run.n} = 0.92 - 4.1\left(\frac{T_{f.in.pa.run.n} - T_a}{I}\right) \quad [4\text{-}31]$$

Accordingly, the outlet temperature of the finite element $T_{f.out.pa.run.n}$ can be expressed as:

$$T_{f.out.pa.run.n} = \frac{3600\, Q_{pa.run.n}}{V_{sp.f}\rho_{sp.f.pa.run.n}Cp_{sp.f.pa.run.n}} + T_{f.in.pa.run.n} \quad [4\text{-}32]$$

In equation [4-32], the density of the fluid $\rho_{sp.f.pa.run.n}$ and the volume specific heat $Cp_{sp.f.pa.run.n}$ is determined by the inlet temperature of the finite element $T_{f.in.pa.run.n}$. The outlet temperature of the n element $T_{f.out.pa.run.n}$ is the inlet temperature of the $n+1$ element $T_{f.in.pa.run.n+1}$. The algorithm for analysing the performance of the condenser by using above numerical models is indicated in Fig. 4-5, which gives a flow chart illustrating the computer programming process.

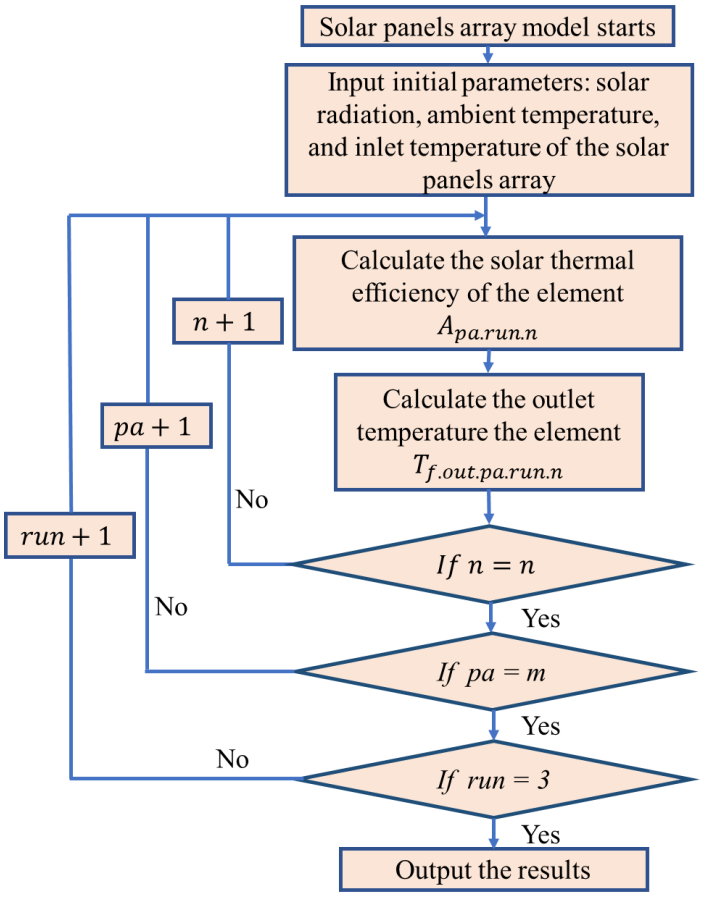

Fig. 4-5 The algorithm for analysing the performance of the solar collectors array

4.3.2 Theoretical analysis and steady state computer model for the heat pump

4.3.2.1 Theoretical analysis of the heat pump

- **The compressor**

The schematic of the vapor-injection compressor is showed as Fig. 4-6. Generally, the compressor consists of three chambers, i.e., a low-pressure chamber which compresses the refrigerant from the compression line, a high-pressure chamber which compresses the refrigerant from the mixing chamber, and a mixing chamber which mixes the compressed refrigerant from the low-pressure chamber and the vapour injection line. The compression processes are assumed as adiabatic compression, and the mixing

process taken apart in the mixing chamber is assumed as isobaric mixing. The governing equations for the relevant process are based on the mass and energy balances.

The refrigerant mass flow rate in the low-pressure chamber (m_{v1}) and the refrigerant mass flow rate in the high-pressure chamber (m_{tot}) can be expressed as [204]:

$$m_{ref.v1} = \rho_{ref.8} * \eta_{com.v1} * V_{v1} * \frac{N_{com}}{60} \quad [4\text{- }33]$$

$$m_{ref.tot} = \rho_{ref.5} * \eta_{com.v2} * V_{v2} * \frac{N_{com}}{60} \quad [4\text{- }34]$$

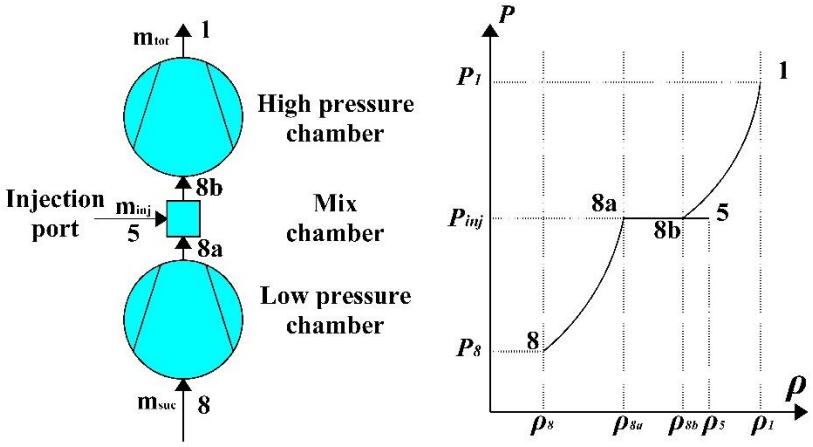

Fig. 4-6 Schematic of the vapour-injection compressor

V_{v1} is the displacement of the low-pressure chamber, and V_{v2} is the displacement of the high-pressure chamber, which were $8\times10^{-5}m^3$ and $5.6\times10^{-5}m^3$, respectively. The volumetric efficiency of the low-pressure chamber (η_{v1}) and the volumetric efficiency of the high-pressure chamber (η_{v2}) can be expressed as [205]:

$$\eta_{com.v1} = 1 + 0.0933 * \left(\frac{n_{v1}-1}{n_{v1}}\right) * \frac{P_{inj}}{P_{eva}} - 0.733 \quad [4\text{- }35]$$

$$\eta_{com.v2} = 1 + 0.0933 * \left(\frac{n_{v2}-1}{n_{v2}}\right) * \frac{P_{con}}{P_{inj}} - 0.733 \quad [4\text{- }36]$$

Energy and mass conservation criterion are used to analyse the heat transfer process

in the inner heat exchanger. The relationship between the total mass flow rate ($m_{ref.tot}$), the mass flow rate of the injection port ($m_{ref.inj}$) and the mass flow rate of refrigerant in the low-pressure chamber ($m_{ref.v1}$) is the showed in equation [4-37].

$$m_{ref.tot} = m_{ref.v1} + m_{ref.inj} \quad [4\text{-}37]$$

The enthalpy at the inlet of the high-pressure chamber is expressed as equation [4-38]. As shown in equation [4-39], h_1 represents the enthalpy at the outlet of the compressor under an isentropic process.

$$h_{8b} = \frac{m_{ref.v1}h_{8a} + m_{ref.inj}h_5}{m_{ref.tot}} \quad [4\text{-}38]$$

$$h_1 = h_{8b} + \frac{h_{1\_is} - h_{8b}}{\eta_{is\_v2}} \quad [4\text{-}39]$$

The enthalpy at the outlet of the low-pressure chamber is calculated by equation [4-40].

$$h_{8a} = h_8 + \frac{h_{8a\_is} - h_8}{\eta_{is\_v1}} \quad [4\text{-}40]$$

The mechanical efficiencies of the compressor ($\eta_{me.com}$), motor efficiencies of the compressor ($\eta_{mo.com}$) are calculated from the equations [4-41] to [4-44], respectively [206], and isentropic efficiencies (η_{is_v1} and η_{is_v2}) of the low- and high-pressure chamber are calculated from the equations [4-41] to [4-44], respectively. The compressor work is defined by equation [4-45].

$$\eta_{me.com} = -0.0003\left(\frac{P_{con} - P_{eva}}{P_{air}}\right)^2 + 0.0127\left(\frac{P_{con} - P_{eva}}{P_{air}}\right) + 0.6720 \quad [4\text{-}41]$$

$$\eta_{mo.com} = -0.0001\left(\frac{P_{con} - P_{eva}}{P_{air}}\right)^2 + 0.0038\left(\frac{P_{con} - P_{eva}}{P_{air}}\right) + 0.7995 \quad [4\text{-}42]$$

$$\eta_{is\_v1} = -0.0028\left(\frac{P_{inj} - P_{eva}}{P_{air}}\right) + 0.8498 \quad [4\text{-}43]$$

$$\eta_{is\_v2} = -0.0028\left(\frac{P_{con}-P_{inj}}{P_{air}}\right) + 0.8498 \quad [4\text{- }44]$$

$$W_{com} = W_{v1} + W_{v2} = \frac{m_{v1}(h_{8a}-h_8)+m_{tot}(h_1-h_{8b})}{\eta_{me.com}\eta_{mo.com}} \quad [4\text{- }45]$$

- **The condenser**

$\varepsilon - NTU$ based approach is used in the condenser. For refrigerant side heat transfer process, the calculation is divided into three regions, the liquid phase region, the two-phase region, and the gas phase region. The two-phase heat transfer region is derived from Dobson and Chatto [207], while the single-phase region uses the Dittus-Boelter model [208]. The heat transfer process in condenser is a counter-flow heat exchange process and is also divided into three regions, i.e., the liquid to liquid refrigerant heat transfer process (Region 1), the liquid to two-phase refrigerant heat transfer process (Region 2), and the liquid to gas refrigerant heat transfer process (Region 3). The heat transfer capacity (Q_{cond}) in different regions can be expressed as:

$$Q_{con.1} = \varepsilon_{\ con.1} C_{min.con.1}\left(T_{ref.con.liquid} - T_{wa.con.in}\right)$$

$$= m_{ref.tot}(h_{ref.con.liquid} - h_2) \quad [4\text{- }46]$$

$$Q_{con.2} = \varepsilon_{\ con.2} C_{min.con.2}\left(T_{ref.con.gas} - T_{wa.con.liquid}\right)$$

$$= m_{tot}(h_{ref.con.gas} - h_{ref.con.liquid}) \quad [4\text{- }47]$$

$$Q_{con.3} = \varepsilon_{\ con.3} C_{min.con.3}\left(T_{ref.con.in} - T_{wa.con.gas}\right)$$

$$= m_{tot}(h_{ref.con.1} - h_{ref.con.gas}) \quad [4\text{- }48]$$

$\varepsilon_{\ con.n}$ is the energy efficiency of different heat transfer processes; $T_{ref.con.in}$ is the inlet temperature of the refrigerant side in the condenser. $T_{ref.con.liquid}$ and $T_{ref.con.gas}$ are the temperatures of the refrigerant under saturation liquid state and saturation gas state at the condensing pressure (P_{con}). $T_{wa.con.in}$ is inlet temperature

of the water side in the condenser. $T_{wa.con.liquid}$ and $T_{wa.con.gas}$ are the water temperatures corresponding to the positions of the refrigerant under saturation liquid state and saturation gas state at the condensing pressure (P_{con}). In single phase heat exchange process, the $C_{min.con.n}$ should be chosen the minimum specific heat capacity between the two flowing working fluids. In two-phase heat exchange process, the $C_{min.n}$ is the specific heat capacity of the water. C is expressed as:

$$C = mCp \qquad [4\text{- }49]$$

m is the mass flow rate of the working fluid, Cp is the specific heat at constant pressure of the working fluid. Under different heat exchange regions, there are different energy efficiency (ε_n). In single phase heat exchange region (Region 1 and 3). The energy efficiency can be expressed as:

$$\varepsilon_{sph} = \frac{1-\exp\left[-NTU\left(1-\frac{C_{min}}{C_{max}}\right)\right]}{1-\frac{C_{min}}{C_{max}}\exp\left[-NTU\left(1-\frac{C_{min}}{C_{max}}\right)\right]} \qquad [4\text{- }50]$$

In two-phase heat exchange region (Region 2). The energy efficiency can be expressed as:

$$\varepsilon_{tph} = 1 - \exp\left(-NTU\right) \qquad [4\text{- }51]$$

NTU is the number of transfer units, which can be expressed as:

$$NTU = \frac{kA}{C_{min}} \qquad [4\text{- }52]$$

A is the heat exchange area of the corresponding region; k is the coefficient of heat transfer of the corresponding region, which can be expressed as:

$$k = \frac{1}{\frac{1}{h_{c\,wa}} + \frac{\delta}{\lambda} + \frac{1}{h_{c\,ref}}} \qquad [4\text{- }53]$$

h_{wa} and h_{ref} are the convective heat transfer coefficient of water and refrigerant

separately. δ is the wall thickness of the tube, and λ is the heat conductivity coefficient of the tube.

The algorithm for analysing the performance of the condenser by using above numerical models is presented in Fig. 4-7. This dedicated flow chart illustrates the simulation process of the condenser computer model. The iterative method was applied, especially in calculating the heat exchange area. The thermodynamic properties of the working fluids in the simulation process can be obtained from REFPROP (ref).

(i) Set the geometry parameters of the condenser. The technical parameters can be obtained from Tables 3-1 and 3-2.

(ii) Given certain system operating temperatures/pressures, i.e., the condensing temperatures/pressure, the condenser inlet temperature of the water tank side and the condenser volume flow rate of the water tank side.

(iii) Divide the heat transfer process into three parts: the liquid to liquid refrigerant heat transfer process, the liquid to two phase refrigerant heat transfer process and the liquid to gas refrigerant heat transfer process.

(iv) Assume the heat exchange area ($A1$) of the first heat exchange part, the liquid to liquid refrigerant heat transfer process.

(v) Calculate the three heat exchange processes separately by using equations [4-46] to [4-53] and obtain the heat exchange area of the liquid to two phase refrigerant heat transfer process ($A2$) and the liquid to gas refrigerant heat transfer process ($A3$).

(vi) Calculate the total heat exchange area A'_{tot} and compare with the practical total heat exchange area A_{tot} of the condenser.

(vii) If $\frac{|A'_{tot}-A_{tot}|}{A_{tot}} \leq 10\%$ (error allowance), then output the results.

(viii) If $\frac{|A'_{tot}-A_{tot}|}{A_{tot}} > 10\%$ (error allowance), then adjust the assumed heat exchange area $(A1)$ of the first heat exchange part and calculate the derived total heat exchange area A'_{tot} again, until the error allowance less than or equal to 10%.

(ix) If there is no suitable heat exchange area $(A1)$ of the first heat exchange part, it means that there is no refrigerant condensed to the liquid phase. As a result, the calculation of the heat exchange process should start from the liquid to two phase refrigerant heat transfer process and assume the relevant heat exchange area $A2$ and the total heat exchange area A'_{tot}.

(x) If $\frac{|A'_{tot}-A_{tot}|}{A_{tot}} \leq 10\%$ (error allowance), then output the results.

(xi) If $\frac{|A'_{tot}-A_{tot}|}{A_{tot}} > 10\%$ (error allowance), then adjust the assumed heat exchange area $(A2)$ of the second heat exchange part and calculate the derived total heat exchange area A'_{tot} until the error allowance less than or equal to 10%.

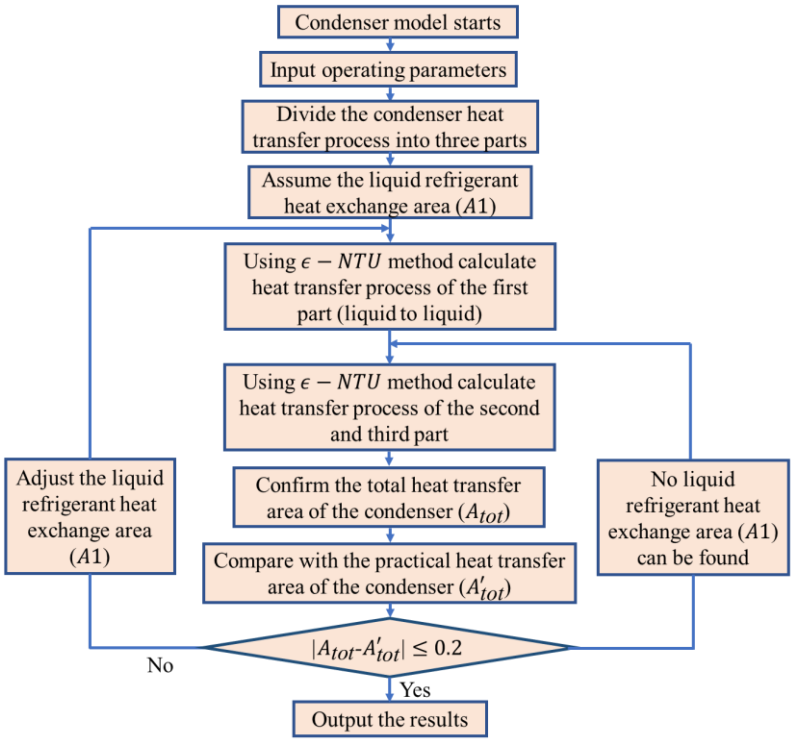

Fig. 4-7 The algorithm for analysing the performance of the condenser

- **The evaporators**

The evaporator of the heat pump in the vapour injection line contains 72 copper tubes with wavy fins, as shown in Fig. 4-8. The 72 copper tubes are organised into 6 heat exchange units. Every unit contains 12 copper tubes with independent inlet and outlet.

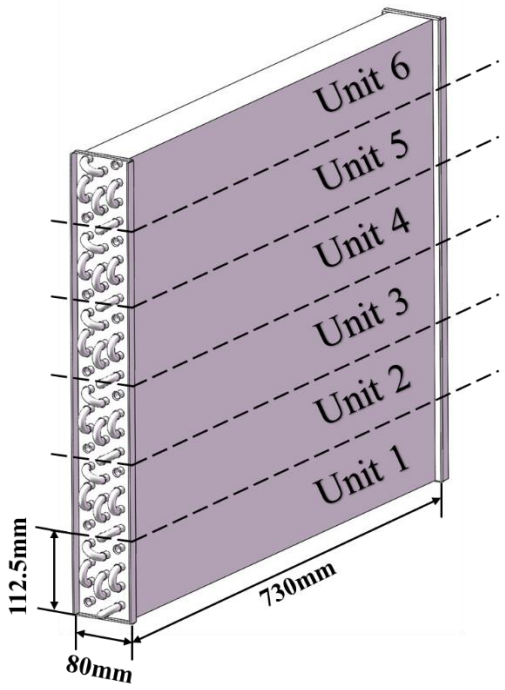

Fig. 4-8 The evaporator of the heat pump in the vapour injection line

The lateral view of a single heat transfer unit is shown in Fig.4-9. The calculation of the evaporator also uses the $\varepsilon - NTU$ based approach, and the heat exchange process includes single- and two-phase heat exchange process.

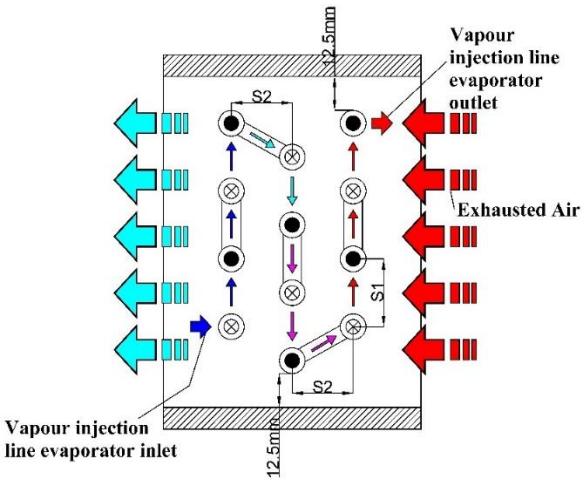

Fig. 4-9 The cross-section view of a single heat transfer unit

The heat exchange capacity between the liquid phase refrigerant and the exhausted air from building can be expressed as:

$$Q_{eva.inj.liquid} = \varepsilon_{\ eva.inj.liquid} C_{min.eva.inj.liquid}\left(T_{exa.inj.in} - T_{ref.inj.in}\right)$$

$$= m_{inj}(h_{ref.inj.liquid} - h_3\ ) \qquad [4\text{- }54]$$

The heat exchange capacity between the two-phase refrigerant and the exhausted air from building can be expressed as:

$$Q_{eva.inj.tph} = \varepsilon_{\ eva.inj.tph} C_{min.eva.inj.tph}\left(T_{exa.inj.in} - T_{ref.inj.liquid}\right)$$

$$= m_{inj}(h_4 - h_{ref.inj.liquid}\ ) \qquad [4\text{- }55]$$

The energy efficiencies ε of the heat exchange process in vapour injection line evaporator can be expressed as:

$$\varepsilon = \begin{cases} 1 - \exp(-NTU)\,, for\ two - phase\ region \\ 1 - \exp[\frac{exp(-NTU^{0.78}C_r)-1}{NTU^{-0.22}C_r}], for\ single - phase\ region \end{cases} \qquad [4\text{- }56]$$

C_r is the ratio of the minimum specific heat capacity C_{min} to the maximum specific heat capacity C_{max} of the two working fluids in the heat exchange process.

$$C_r = \frac{C_{min}}{C_{max}} \qquad [4\text{- }57]$$

4.3.2.2 The steady computer model of the VIHR-ASHP

The algorithm for analysing the performance of the heat pump by using above theoretical analysis is presented in Fig. 4-10, which shows the simulation process of the VIHR-ASHP computer model. The iterative method was applied, especially in calculating the vapor injection working point (Point 5 in Fig. 3-11). The thermodynamic properties of the working fluids in the simulation process can be obtained from REFPROP.

(i) Given the geometry of the VIHR-ASHP components. The technical parameters can be obtained from Tables 3-1 and 3-2.

(ii) Given certain system operating temperatures/pressures, i.e., the condensing temperatures/pressure, vapor injection temperatures/pressure, evaporation line temperatures/pressure, condenser inlet temperature of the water tank side, condenser volume flow rate of the water tank side, room temperature and ambient temperature.

(iii) Assume working point (5) in the vapour injection line before the compressor.

(iv) Calculate the working point at the outlet of the compressor using equations [4-33] to [4-45].

(v) Simulate the heat transfer process in the condenser by using the condenser numerical model.

(vi) Calculate the heat transfer processes in the evaporator in the vapour injection line and the IHX.

(vii) Calculate the working point in the vapour injection line after the IHX and before the compressor, which is called the obtained working point 5'.

(viii) If $\frac{|h5-h5'|}{h5} \leq 10\%$ (error allowance), then output the results.

(ix) If $\frac{|h5-h5'|}{h5} > 10\%$ (error allowance), then adjust the assumed $h5$ and calculate the derived working point 5' again, until the error allowance less than or equal to 10%.

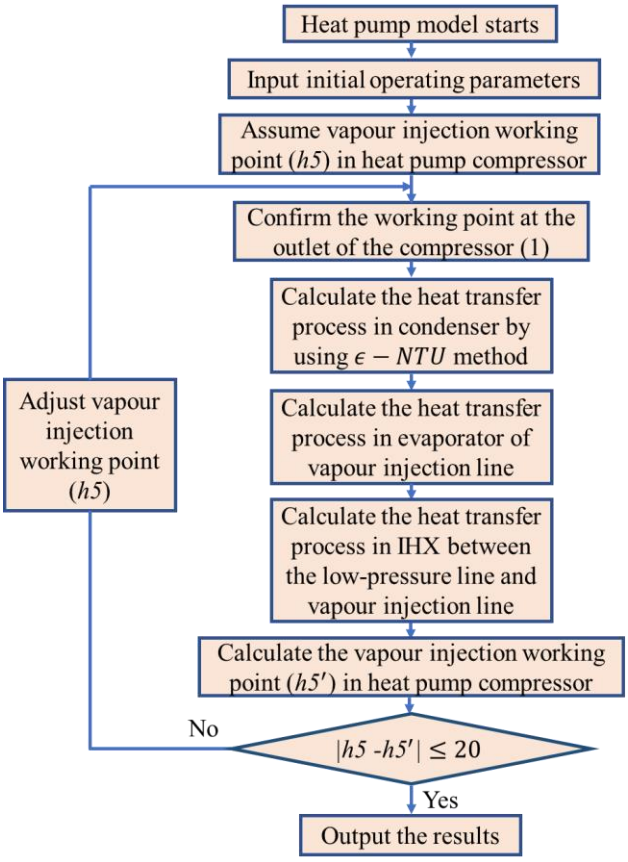

Fig. 4-10 The algorithm for analysing the performance of the heat pump

4.3.2.3 The performance justification parameters of the heat pump

The COP of a heat pump is the ratio of the output heat to the input power. In this simulation emphasis is placed on the thermodynamic cycle. The power consumption by fans and pumps are not considered. Therefore, the COP is defined by

$$COP = \frac{Q_{con}}{W_{com}} = \frac{h_{con,in} - h_{con,out}}{h_{com,out} - h_{com,in}} \quad [4\text{- }58]$$

$h_{cond,in}$ is the specific enthalpy at the inlet of the condenser; $h_{cond,out}$ is the specific enthalpy at the outlet of the condenser; $h_{comp,in}$ is specific enthalpy at the inlet of the compressor; and $h_{comp,out}$ is the specific enthalpy at the outlet of the compressor. The ventilation heat loss without recovery is

$$Q_{ven,l} = m_{ex} Cp_{ex} (T_{ex} - T_a) \quad [4\text{- }59]$$

m_{ex} is the exhaust air mass flow rate, and Cp_{ex} is the heat capacity. The mixing of ambient and exhaust air for heat pump is rarely studied in the literature, and hence special attention is given to the modelling of this process in this thesis. The air temperature after mixing (i.e., air temperature at the low-pressure evaporator inlet) is calculated by:

$$T_{mix,in} = \frac{m_{ex}T_{ex} + y_{hp} \cdot m_{ex}T_a}{m_{ex} + y_{hp} \cdot m_{ex}} = \frac{T_{ex} + y_{hp} \cdot T_a}{1 + y_{hp}} \quad [4\text{- }60]$$

$$y_{hp} = \frac{m_a}{m_{ex}} \quad [4\text{- }61]$$

m_a is the ambient air flow rate. The mixed air temperature leaving the evaporator is:

$$T_{mix,out} = T_{mix,in} - \frac{Q_{eva}}{m_{ex}(1 + y_{hp})Cp_{ex}}$$

$$= T_a - \frac{\frac{Q_{eva}}{m_{ex}Cp_{ex}} - (T_{ex} - T_a)}{1 + y_{hp}} \quad [4\text{- }62]$$

The temperature drop of air through the evaporator is an important parameter in the design of the heat exchanger. A smaller temperature drop can provide a higher COP but more fan power is needed owing to a larger flow rate. The optimum temperature drop is then a compromise.

$$C_P m_{ex}(1 + y_{hp})\Delta T = Q_{eva} \quad [4\text{- }63]$$

With $C = \frac{Q_{eva}}{m_{ex}C_P(T_{ex} - T_a)}$,

$$y_{hp} = \frac{(T_{ex} - T_a)C}{\Delta T} - 1 \quad [4\text{- }64]$$

$$T_{mix,out} = T_a - \frac{\frac{Q_{eva}}{m_{ex}C_P} - (T_{ex} - T_a)}{1 + \frac{m_a}{m_{ex}}} = T_a - \Delta T \frac{C - 1}{C} \quad [4\text{- }65]$$

It indicates that at a given C, the mixed air temperature leaving the evaporator is independent on the exhaust air temperature. The relative increment of $T_{mix,out}$ by that of air leaving the evaporator of a conventional ASHP is:

$$\Delta T_r = T_{mix,out} - (T_a - \Delta T) \quad = \frac{\Delta T}{C} \qquad [4\text{- }66]$$

The minimum temperature difference between the refrigerant and air in the evaporator shall take place at the air outlet, and is defined by:

$$\Delta T_{min} = T_{mix,out} - T_{eva} \qquad [4\text{- }67]$$

The ratio of the ventilation heat loss to the heat supply is defined as:

$$x_{hp} = \frac{Q_{ven}}{Q_{hp}} \qquad [4\text{- }68]$$

An insight to the thermodynamic irreversibility in the innovative VIHR-ASHP is provided. The exergy destruction in the components is expressed in Table 4-3. The subscripts '1-12' represent the thermodynamic states in Fig. 4-11. T_0 is the reference temperature, 0 ℃. m_{ex} and m_a are the mass flow rate of exhaust air and ambient air.

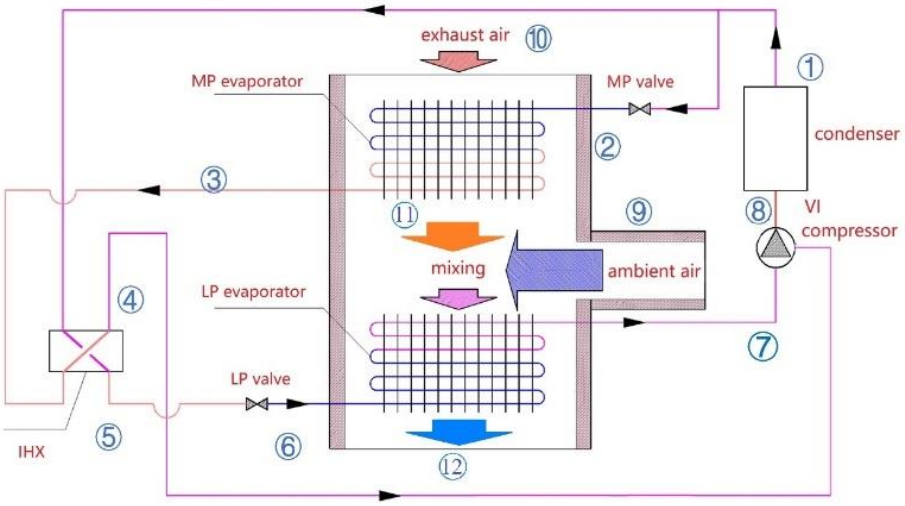

Fig. 4-11 Schematic diagram of the VIHR-ASHP

The flow rates of the two streams in the refrigerant cycle are $m_{ref.v1}$ and $m_{ref.inj}$, which are mentioned above ($m_{ref.tot} = m_{ref.v1} + m_{ref.inj}$).

Table 4-3 Exergy destruction equations for the main components of the VIHR-ASHP

Component	Equation	No.
Condenser	$[m_{ref.tot}(s_1 - s_8) + m_{wa}(s_{wa,out} - s_{wa,in})]T_0$	[4- 69]
EEV (vapour injection line)	$m_{ref.inj}(s_2 - s_1)T_0$	[4- 70]
EEV (evaporation line)	$m_{ref.v1}(s_6 - s_5)T_0$	[4- 71]
evaporator (vapour injection line)	$[m_{ref.inj}(s_3 - s_2) + m_{ex}(s_{11} - s_{10})]T_0$	[4- 72]
evaporator (evaporation line)	$[m_{ref.v1}(s_7 - s_6) + (m_{ex} + m_a)s_{12} - m_a s_9 - m_{ex}s_{11}]T_0$	[4- 73]
Internal heat exchanger	$[m_{ref.inj}(s_4 - s_3) + m_{ref.v1}(s_5 - s_1)]T_0$	[4- 74]
Compressor	$(m_{ref.tot}s_8 - m_{ref.v1}s_7 - m_{ref.inj}s_4)T_0$	[4- 75]

4.3.3 Theoretical analysis and computer model for the novel HSEU

4.3.3.1 Theoretical analysis of the bottom part of the novel HSEU

The cooper tube is used as the basic heat transfer elements of the heat exchanger. The advantages of the cooper tube lie in: (1) high thermal conductivity; (2) high reliability resulting a long working life, and (3) high plasticity and flexibility leading to the diverse heat exchanger. The structural layout of the heat exchanger in bottom part of

the novel HSEU is shown in Fig. 3-14.

The heat exchange area of the copper tube can be expressed as:

$$A_{exc} = L\pi \frac{D_o + D_i}{2} \quad [4\text{- }76]$$

The values for outer diameter (D_o) and inner diameter (D_i) of the cooper tube in equation [4-72] are 19mm and 17.5mm separately. As a result, the heat exchange area per meter length copper tube is 0.057m^2.

Convective heat transfer coefficient of the working fluid is a key factor in heat transfer process of the heat exchanger. The calculation of the convective heat transfer coefficient for the working fluid within the copper tube is given as:

$$h_{c\ b.op} = Nu_{b.op} \frac{\lambda_{b.op}}{D_o} \quad [4\text{- }77]$$

The Nu is the Nusselt number of the working fluid can be expressed as:

$$Nu_{b.op} = 0.27 Re_{b.op}^{0.63} Pr_{f.b.op}^{0.36} \left(\frac{Pr_{f.b.op}}{Pr_{w.b.op}}\right)^{0.25} \quad [4\text{- }78]$$

By using equation [4-76] to equation [4-78], convective heat transfer coefficient of the working fluid of the copper tube was calculated as 462W/(m^2·K).

Reynold number of the working fluid in the bottom part of the water tank can be expressed as:

$$Re_{b.op} = \frac{\rho_{b.op} v_{b.op} D_o}{\mu_{b.op}} \quad [4\text{- }79]$$

Where, velocity of the working fluid can be expressed as:

$$v_{f.ip} = V_f / 3600(Wa) \quad [4\text{- }80]$$

Structural layout of the heat exchanger in the small tank of the novel HSEU is shown in Fig. 4-12.

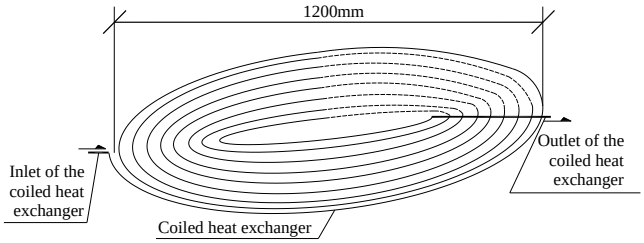

Fig. 4-12 The construction of the exchanger in bottom part of HSEU

Average velocity and the Reynold number of the working fluid inside the heat exchange tank are calculated as 0.01m/s and 200 respectively. The convective heat transfer coefficient of the working fluid within the heat exchange tank can be expressed as [209]:

$$Nu_{f.ip} = CRe_{f.ip}^{n} Pr_{f.ip}^{0.37} (\frac{Pr_{f.ip}}{Pr_{w.ip}})^{0.25} \quad [4\text{- }81]$$

Where the constant numbers C and n are listed in Table 4-4.

Table 4-4 List of parametrical data for equation [4-78]

Re	C	n
1~40	0.75	0.4
40~1x10^3	0.51	0.5
1x10^3~2x10^5	0.26	0.6

Hence, convective heat transfer coefficient of the working fluid within the heat exchanging water tank can be expressed as:

$$h_{c\,f.ip} = Nu_{f.ip} \frac{\lambda_f}{D_o} \quad [4\text{- }82]$$

Following the procedure described above, the convective heat transfer coefficient of

the working fluid within the heat exchanging water tank was calculated as 368W/(m^{2}·K).

The heat transfer coefficient can be expressed as:

$$k_{sp.ip\_op} = \frac{1}{\frac{1}{h_{c\,f.ip}} + \frac{\delta}{\lambda_p} + \frac{1}{h_{c\,f.op}}} \quad [4\text{- }83]$$

4.3.3.2 The dynamic numerical computer model of the upper part of HSEU

The upper part of the HSEU is a stratified heat storage tank, which is divided into ten layers, as shown in Fig. 4-13. The inlet and outlet of this part are all direct connections, which means a faster buoyancy effects compared with the indirect connections.

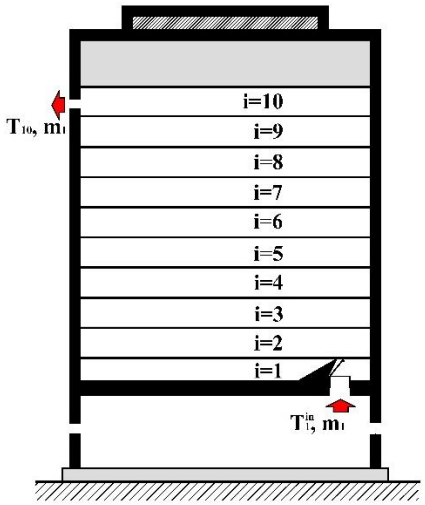

Fig. 4-13 The upper part of the HSEU is a stratified heat storage tank

A standard 1D model [210,211] is employed to simulate the heat transfer process and stratification of the heat storage part of HSEU. In order to set up the computer model, the heat storage part is divided into 10 layers. Then, each layer is applied with a partial differential equation (PDE) derived from the energy conservation equation. Generally, the temperature T_i of i layer is determined by the input mass flow rate m_i and the external input heat capacity $\dot{Q}_i$ from a heat sink or a heat source.

The PDE equation which characterises the heat transfer process of layer i is expressed as:

$$\frac{\partial T_i}{\partial t} = \alpha \frac{\partial^2 T_i}{\partial z^2} + \frac{P_i k_i}{\rho C p A_i}(T_\infty - T_i) + \frac{\dot{Q}_i}{\rho C p A_i \Delta z_i} + \frac{m_i (T_i^{in} - T_i)}{\rho A_i \Delta z_i} \quad [4\text{- }84]$$

where α, ρ and Cp indicate the fluid diffusivity, density, and specific heat respectively; A_i, P_i and Δz_i are the cross-sectional area, perimeter, and thickness of layer i; k_i is the thermal conductance of the isolation wall of layer i; and T_∞ is the ambient temperature. it is important to highlight that T_i can be T_{i-1} or T_{i+1} depending on whether the flow m_i comes from the bottom or top layer.

An inevitable drawback of this 1D model: as the simulation process is only based on heat transfer, it cannot model the mixing process between the layers because of buoyancy effects. To overcome this drawback, a post-processing non-smooth algorithm is applied into the traditional models after each modelling time step. The simulation process of the layers' temperature includes buoyancy effects checking process with this post-processing algorithm.

As long as the buoyancy effects are present, the relevant layers are proceeded with the mixing process. This mixing process will be continuously repeated until all buoyancy effects between layers are eliminated. In the dynamic simulation model, the PDE expressed in equation [4-84] is normally discretised and integrated on time using an expression of the following form:

$$T_{t+1,i} = F_i(T_t, Q_{t,i}, m_{t,i}, T_i^{in}, \Delta t) \quad [4\text{- }85]$$

where $T_{t.i}$ is the temperature of layer i at time step t; T_t is the vector of temperatures in the M layers at time step t; $Q_{t,i}$, $m_{t,i}$, and T_i^{in} are the control inputs of layer i at time step t, and Δt is the length of the time step. The F_i can be obtained with two steps by using an integration method:

1. Transforming the PDE into an ordinary differential equation (ODE) by approximating the second-order spatial derivatives by finite differences.

2. Using a numerical integration method to perform integration of the ODE.

By applying these two steps and a forward Euler method to perform the numerical integration, the equation [4-84] can be expressed as:

$$T_{t+1,i} = T_{t,i} + (\alpha \frac{T_{t,i+1} + T_{t,i-1} - 2T_{t,i}}{{\Delta z_i}^2} + \beta_i (T_\infty - T_{t,i}) + \frac{\lambda_i}{\Delta z_i} \dot{Q_{t,\iota}}$$

$$+ \frac{\emptyset}{\Delta z_i} \dot{m_{t,\iota}} ({T_{t,i}}^{in} - T_{t,i})) \Delta t \quad [4\text{- }86]$$

Where Δz_i is the thickness of layer i and β_i, λ_i, and $\emptyset$ can be expressed as:

$\beta_i = \frac{P_i k_i}{\rho C p A_i}$ [4- 87], $\lambda_i = \frac{1}{\rho C p A_i}$ [4- 88], $\emptyset = \frac{1}{\rho A_i}$ [4- 89]

As shown in [212], a single mixing iteration in the standard approach can be easily modelled using the max function by replacing line 13 by the following two expressions:

$$T[i] = T[i] + \theta_{i,i-1} \max(0, T[i-1] - T[i]) \quad [4\text{- }90]$$

$$T[i-1] = T[i-1] + (1 - \theta_{i,i-1}) \max(0, T[i-1] - T[i]) \quad [4\text{- }91]$$

where

$$\theta_{i,i-1} = \frac{A_{i-1} \Delta z_{i-1}}{A_i \Delta z_i + A_{i-1} \Delta z_{i-1}} \in [0,1] \quad [4\text{- }92]$$

$\theta_{i,i-1}$ is a ratio between the volume of $i-1$ layer to the total volumes of two layers, i.e., $i-1$ and i.

A single mixing iteration will be enough for the slow buoyancy effects. Importantly, a single mixing iteration can also keep pace with the dynamics of the buoyancy effects

if the time step Δt is small compared to the time span that can start to the detect buoyancy effects. In this case, the mixing algorithm can be directly integrated in the discrete dynamics by using equation [4-90] to equation [4-92]. More specifically, equation [4-84] can be expanded as follows:

$$T_{t+1,i} = F_i\left(T_t, \dot{Q}_{t,i}, \dot{m}_{t,i}, T_i^{in}, \Delta t\right) + \theta_{i,i-1} \max\left(0, T_{t,i-1} - T_{t,i}\right)$$

$$-\theta_{i,i+1} \max\left(0, T_{t,i} - T_{t,i+1}\right) \qquad [4\text{-}93]$$

The algorithm simulates the system using a simulation time step of length t and for a total of N time steps. The simulation routine of the upper tank stratification involves two steps: a first part where the PDE is solved and a second part where the buoyancy effects are included as an iterative algorithm. The flow diagram is shown in Fig. 4-14.

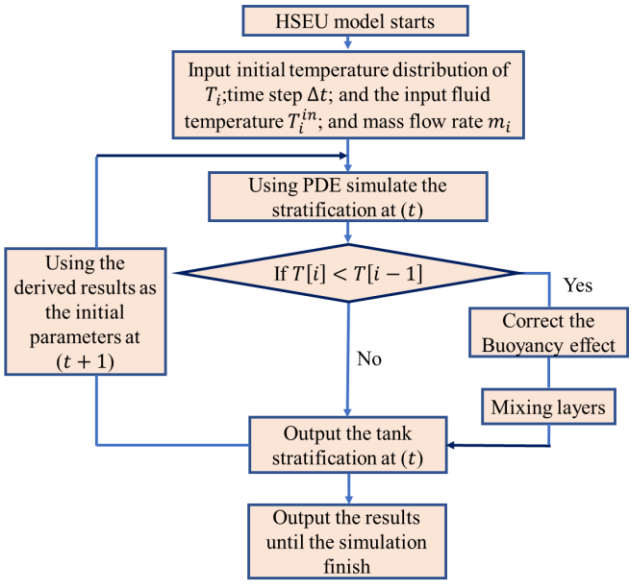

Fig. 4-14 The flow diagram of simulation routine of the upper tank stratification

(i) Given the geometry of the HSEU. The technical parameters can be obtained from Tables 3-1 and 3-2.

(ii) Input the initial temperature distribution of the upper part of the HSEU (T_i), time step Δt used in the calculation, input mass flow rate m_i and temperature T_i^{in} of the charging and discharging flow of every layer.

(iii) Using the derives PDF function simulate the new stratification at t.

(iv) If $T[i] < T[i-1]$, the simulation should correct the Buoyancy effect of the stratification temperature distribution by using equations [4-90] to [4-92] to mix layers.

(v) If $T[i] \geq T[i-1]$, the simulation can output the stratification results at t.

(vi) Then, continue the simulation loop to calculate the temperature distribution of the upper part of HSEU at $t+1$ by using the results concluded at t, until the simulation loop is finish, and finally output the integral result.

4.3.3.3 Heat transfer efficiency and the relevant evaluation parameters of HSEU

The exchanged heat in the new and conventional HSEUs can be expressed as:

$$Q_{hex} = A_{exc} k_{op-ip} \Delta T_m \quad [4\text{-}94]$$

The heat transfer capacity of HSEU Q_{hex} can also be expressed as:

$$Q_{hex} = Cp_{f.exc} m_{f.exc} (T_{f.exc.in} - T_{f.exc.out}) \quad [4\text{-}95]$$

To compare the performance of the novel HSEU and the conventional HSEU, the relevant evaluation parameters of both HSEUs are detailed in this part. The logarithmic mean temperature difference ΔT_m can be expressed as:

$$\Delta T_{m.nov} = \frac{\Delta T_{max} - \Delta T_{min}}{ln\frac{\Delta T_{max}}{\Delta T_{min}}} \quad [4\text{-}96]$$

$$\Delta T_{m.conv} = \frac{T_{ip.in} - T_{ip.out}}{ln\frac{T_{ip.in} - T_{conv.t}}{T_{ip.out} - T_{conv.t}}} \quad [4\text{- }97]$$

The theoretical heat exchange efficiency [213] of the new and conventional HSEUs can be expressed as:

$$\varepsilon_{nov.th} = \frac{A_{exc.nov} k_{nov} \Delta T_{m.nov}}{m_{f.exc} Cp_{f.exc} (T_{op.in} - T_{ip.in})} \quad [4\text{- }98]$$

$$\varepsilon_{conv.th} = \frac{A_{exc.conv} k_{conv} \Delta T_{m.conv}}{m_{f.exc} Cp_{f.exc} (T_{ip.in} - T_{conv.t})} \quad [4\text{- }99]$$

The experimental heat exchange efficiency of the new and conventional HSEUs can be expressed as:

$$\varepsilon_{nov.exp} = \frac{T_{ip.in} - T_{ip.out}}{T_{ip.in} - T_{op.in}} \quad [4\text{- }100]$$

$$\varepsilon_{conv.exp} = \frac{T_{op.in} - T_{op.out}}{T_{op.in} - T_{conv.t}} \quad [4\text{- }101]$$

4.3.4 The theoretical analysis of the plate-fin heat exchanger (HRD)

In the system, when the heat VIHR-ASHP stops, the counter-flow air-to-air plate-fin heat exchanger (PFHE) will be in operation for heat recovery and providing fresh air.

It is assumed that the both sides of the PFHE have the identical geometric structure and dimension. Under this structural approximation, the heat transfer and the flow resistance relations on both sides of the PFHE are same. Fig. 4-15 shows the general stricture of sides 1 and 2 of the PFHE.

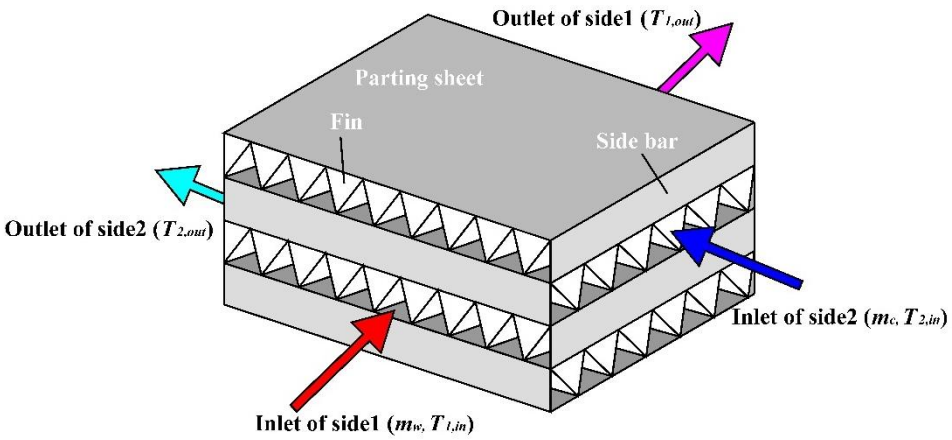

Fig. 4-15 Schematic of the heat exchange unit of PFHE

In order to set up the heat transfer model of the PFHE, the following assumptions are made: (1) The fouling and thema1 resistance of the material are neglected; (2) No leakage of airflow or heat loss to the environment occur; (3) The air pressure is considered approximately 1 bar; and (4) The specific heat capacity and Prandtl number of air and the fin efficiency are constant.

The following mathematical derivation of heat transfer adopts the effectiveness-NTU method [21]. Here, the actual heat transfer Q_{PFHE} can be expressed as:

$$Q_{PFHE} = \varepsilon C_{min}(T_{1.in} - T_{2.in}) = C_1(T_{1.in} - T_{1.out}) = C_2(T_{2.out} - T_{2.in}) \quad [4\text{- }102]$$

The heat transfer process in heat recovery device (HRD) is the cross-flow heat exchanger with both streams unmixed. Accordingly, the dimensionless heat transfer effectiveness ε can be expressed as:

$$\varepsilon = 1 - \exp\{\frac{NTU^{0.22}}{C_r}[\exp(-C_r NTU^{0.78}) - 1]\} \quad [4\text{- }103]$$

Where the dimensionless number of heat transfer units (NTU) and C_r can are defined as:

$$NTU = \frac{kA}{C_{min}} \quad [4\text{- }104]$$

$$C_r = \frac{C_{min}}{C_{max}} \quad [4\text{- }105]$$

In equation [4-105], C_{min} and C_{max} are expressed as:

$$C_{min} = \min(C_1, C_2) \quad [4\text{- }106]$$

$$C_{max} = \max(C_1, C_2) \quad [4\text{- }107]$$

where T is inlet temperature or outlet temperature of two sides of the heat exchanger, and $\dot{C}$ is the capacity flow and is the product of mass flow rate ṁ and specific heat capacity of air Cp:

$$C_1 = m_1 Cp_1 \quad [4\text{- }108]$$

$$C_2 = m_2 Cp_2 \quad [4\text{- }109]$$

4.4 Heat Transfer Processes Lying in the SAHR-HP System

The characterisation of the heat transfer processes lying in the SAHR-HP system can greatly help to build up the dynamic computer model for the integral SAHR-HP system. The heat transfer processes are mainly based on the HSEU, because most components of the system are connected to the HSEU, and conduct the heat transfer with the HSEU. Another place where the heat transfer processes are taken place is the served house. The heating and cooling load is on account of the heat transfer process between the indoor and outdoor environments, and the heat transfer processes occur between the indoor environment and the energy supplying devices. Generally, there are 6 heat transfer processes lying in the system: (1) the heat transfer between the underfloor coil and the HSEU; (2) the heat transfer between the VIHR-ASHP and the HSEU; (3) the heat transfer between the solar collectors array and the HSEU; (4) the heat transfer between the domestic hot water tank and the HSEU; (5) the heat transfer between the VIHR-ASHP and the under-floor coil; and (6) the heat transfer between the indoor thermal condition and the ambient environment. The specific details are as follows.

4.4.1 The heat transfer between the underfloor coil and the HSEU

The heat exchange capacity of the underfloor coil is expressed as:

$$Q_{ufc\ to\ HSEU} = Cp_{ufc.f} m_{ufc.f} (T_{out.ufc} - T_{in.ufc}) \quad [4\text{-}110]$$

The structure of the floor of the residential house is shown in Fig. 4-16. and the thermal conductivity and the thickness of every layer is shown in Table 4-5.

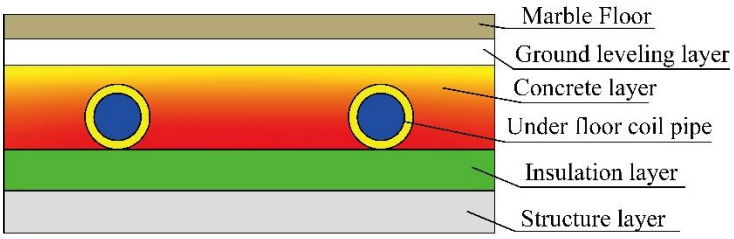

Fig. 4-16 The structure of the underfloor coil

Table 4-5 The thermophysical properties of the layers of the underfloor coil

Layer	**Material**	**Conductivity (W/m·°C)**	**Thickness (mm)**
Marble floor	Marble	2.94	8
Ground levelling layer	Ground compounds	1.2	3
Concrete layer	Concrete	0.8	5
Under floor coil pipe	PERT	0.45	2

According to the structure of the floor of the residential house, the heat transfer coefficient of the underfloor coil is 34 W/m^2·°C (K_{ufc}). To simulate the heat exchange process between the under-floor heating coil and the room air, infinitesimal method is adopted into the model. The space heating area of the residential house is divided into 100 non-dimensional points. At time t, the heat transfer of the under-floor coil at the

j point can be expressed as:

$$(T_{t,j+1} - T_{t,j})\, V_m\, \rho\, C_p = K_{ufc}(T_{t,j} - T_{room}) \quad [4\text{- }111]$$

Accordingly, the total heat exchange capacity during the time step Δt can be expressed as:

$$Q_{\Delta t.ufc\ to\ HSEU} = \Delta t \sum_{j=1}^{100} K_{ufc}\,(T_{t,j} - T_{room}) \quad [4\text{- }112]$$

4.4.2 The heat transfer between the VIHR-ASHP and the HSEU

The heat transfer between the VIHR-ASHP and the HSEU is between the heat pump loop water and the refrigerant in condenser. The heat transfer capacity during the time step Δt can be expressed as:

$$Q_{\Delta t.VIHR-ASHP\ to\ HSEU} = \Delta t(Q_{con.1} + Q_{con.2} + Q_{con.3}) \quad [4\text{- }113]$$

4.4.3 The heat transfer between the solar collectors array and the HSEU

The solar collectors array exchange heat with the HSEU by using the coiled copper heat exchanger situated in the bottom part of HSEU. The simulation of the heat exchange process adopts the non-dimensional infinitesimal method. The total heat exchange area of the copper tube exchanger is divided into n parts. The heat exchange capacity of the i part can be expressed as:

$$Q_i = \Delta A_{sp.exc} k_{sp.op-ip}(T_i - T_{bt}) \quad [4\text{- }114]$$

The T_{i+1} can be expressed as:

$$T_{i+1} = T_i - \frac{Q_i}{Cp_f\, \rho_f} \quad [4\text{- }115]$$

The total heat exchange capacity between the solar collectors array and the bottom part of HSEU can be expressed as:

$$Q_{sp\ to\ HSEU} = \sum_{i=1}^{n} Q_i \quad [4\text{- }116]$$

In addition, the solar collectors array inlet temperature is the outlet temperature of the coiled copper tube heat exchanger (T_n), And the HSEU bottom part temperature of the next time step $(t+1)$ can be expressed as:

$$T_{bt,t+1} = \frac{Q}{C_{b.t}} + T_{b.t,t} \quad [4\text{- }117]$$

Where C_{bt} can be expressed as:

$$C_{bt} = V_{bt}\rho_f Cp_f \quad [4\text{- }118]$$

The heat transfer capacity between the solar collectors array and the HSEU during the time step Δt can be expressed as:

$$Q_{sp\ to\ HSEU} = \Delta t \sum_{i=1}^{n} Q_i \quad [4\text{- }119]$$

4.4.4 The heat transfer between the domestic hot water tank and the HSEU

The heat transfer process simulation between the domestic hot water tank and the HSEU is similar to the heat transfer process between the solar collectors array and the HSEU. The difference is the heat exchanger between the domestic hot water tank and the HSEU is placed inside the domestic hot water tank. The heat transfer capacity between the domestic hot water tank and the HSEU during the time step Δt can be expressed as:

$$Q_{DHW\ to\ HSEU} = \Delta t \sum_{i=1}^{n} \Delta A_{sp.exc} k_{DHW.op-ip}(T_{bt} - T_i) \quad [4\text{- }120]$$

4.4.5 The heat transfer between the VIHR-ASHP and the under-floor coil

During the summer, the system can provide cooling to the residential house. However, this heat transfer process does not need the operation of the HSEU. The VIHR-ASHP will provide cooling capacity to the under-floor coil directly. The heat transfer capacity

between VIHR-ASHP and under-floor coil during the time step Δt can be expressed as:

$$Q_{\Delta t.VIHR-ASHP\ to\ ufc} = \Delta t \sum_{j=1}^{100} K_{ufc}\ (T_{t,j} - T_{room}) \quad [4\text{- }121]$$

4.4.6 The heat transfer between the indoor thermal condition and the ambient environment

The heat transfer process between the indoor thermal condition and the ambient environment directly decides the operation statue of the SAHR-HP system. The basic envelop loads of the residential house can be expressed as:

$$Q_{wall} = k_{wall} A_{wall} (T_{room} - T_a) \quad [4\text{- }122]$$

$$Q_{roof} = k_{roof} A_{roof} (T_{room} - T_a) \quad [4\text{- }123]$$

$$Q_{total} = Q_{wall} + Q_{roof} \quad [4\text{- }124]$$

The room temperature should be limited in the range from 18°C to 23°C. Accordingly, when the ambient temperature is lower than 18°C, the room has heating load through the envelop of the residential house, and when the ambient temperature is higher than 23°C, the room has cooling load through the envelop of the residential house.

In equation [4-122], the heating load of house envelops $Q_{hl.a}$ can be expressed as:

$$Q_{hl.a} = [(1 + \alpha_{hl.e}) A_{en.e} + (1 + \alpha_{hl.w}) A_{en.w}$$

$$+(1 + \alpha_{hl.s}) A_{en.s} + (1 + \alpha_{hl.n}) A_{en.n}] \tau_{hl} h_{room\_a} (T_r - T_a) \quad [4\text{- }125]$$

In order to take solar radiation as an impact factor, the orientation correction coefficients are integrated into the heat load calculation. In equation [4-125], $\alpha_{hl.e}$, $\alpha_{hl.w}$, $\alpha_{hl.s}$ and $\alpha_{hl.n}$ are the coefficients of the house envelops orientation

correction facing east, west, south and north separately, and the values of which are -5%, -5%, -15% and 5% respectively [214]. $A_{en.e}$, $A_{en.w}$, $A_{en.s}$ and $A_{en.n}$ stand for the envelopes area facing corresponding direction, m^2.

Except the heat transfer driven by temperature difference of the envelop, the heat collection from solar radiation is also a main factor influencing the cooling load. The cooling load from the solar radiation can be expressed as:

The cooling load generated by solar radiation $Q_{cl.solar}$ can be expressed as:

$$Q_{cl.solar} = 570 C_{clc} C_z A_{en} \quad [4\text{-}126]$$

In equation [4-126], C_{clc} is the solar radiation cooling load factor. The value of C_{clc} is determined by the orientation and the time and can be obtained from a local building design standard, GB 50736-2012. The comprehensive shielding coefficient of the outer window C_z can be expressed as:

$$C_z = C_w C_n C_s \quad [4\text{-}127]$$

In equation [4-127], C_w is the outer shielding device correction factor, C_n is the inner shielding device correction factor, C_s is the window glass correction factor. For the normal residential building with double-layer glass, C_w 0.95 is C_n is 0.9, and C_s is 1.

The ventilation load should be considered both under heating and cooling mode of the system. According to the operation strategies of the SAHR-HP system, the PFHE and the VIHR-ASHP operate dependently, and there are different heating or cooling ventilation loads for the operation of different devices. Consequently, the calculation is divided into two parts: 1. the ventilation load under the operation of the PFHE; 2. the ventilation load under the operation of the VIHR-ASHP.

The ventilation load under the operation of the PFHE (HRD) can be expressed as:

$$Q_{hl.ven} = Cp_{air}\rho_{air}V_{air}(T_{HRD.out} - T_a) \quad [4\text{- }128]$$

The ventilation load under the operation of the VIHR-ASHP can be expressed as:

$$Q_{hl.ven} = Cp_{air}\rho_{air}V_{air}(T_{room} - T_a) \quad [4\text{- }129]$$

The heat transfer capacity between the indoor thermal condition and the ambient environment during the time step Δt can be expressed as:

$$Q_{\Delta t.indoor\ to\ outdoor} = \Delta t\ (Q_{hl.a} + Q_{hl.ven} + Q_{cl.solar}) \quad [4\text{- }130]$$

4.4.7 The heat loss from pipe lines of the SAHR-HP System

The heat loss of per meter long pipe lines of the SAHR-HP system can be expressed as:

$$q'_{loss.pipe\ lines} = \frac{T_{wf} - T_a}{R_p + R_{il}} \quad [4\text{- }131]$$

The thermal resistance of the pipe R_p and the insulation layer R_{il} can be expressed as:

$$R_p = \frac{1}{2\pi\lambda_{pipe}} ln \frac{d_{in.pipe}}{d_{out.pipe}} \quad [4\text{- }132]$$

$$R_{il} = \frac{1}{2\pi\lambda_{il}} ln \frac{d_{in.il}}{d_{out.il}} \quad [4\text{- }133]$$

The heat loss of pipe lines of the SAHR-HP system during the time step Δt can be expressed as:

$$Q_{\Delta t.loss.pipe\ lines} = \Delta t L_{pipe\ lines} q'_{loss.pipe\ lines} \quad [4\text{- }134]$$

4.5 The Dynamic Computer Model for the Integral SAHR-HP System

According to the theoretical analysis and the heat transfer processes between the

components of the SAHR-HP system. An integral dynamic computer model for the integral SAHR-HP system can be set up and used to simulate the performance of the system. A novel dynamic system operation status forecasting method will be developed. This method will create a dynamic system computer model which can forecast the system operation status and change the heat transfer processes between the components of the SAHR-HP system, thus giving a great potential in increasing the efficiency of the system by optimising the control strategy.

The flow diagram of the algorithm of the dynamic model is shown in Fig. 4-17.

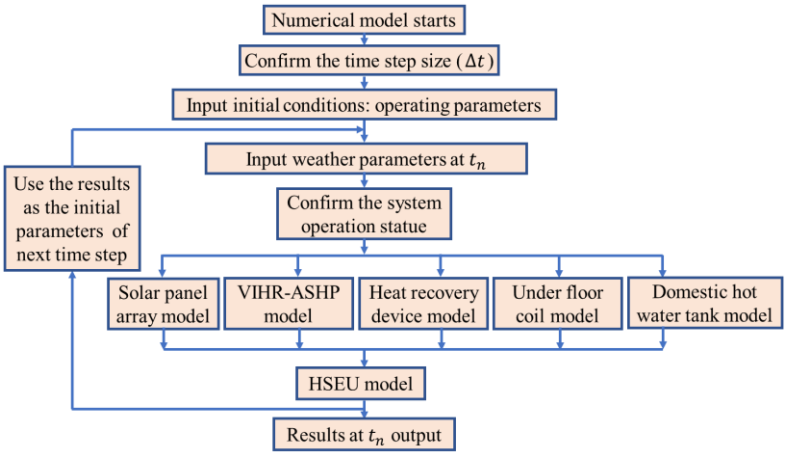

Fig. 4-17 The dynamic model for the integral SAHR-HP system

An initial temperature distribution (t = 0) from the module cover to the water in the tank is desired before starting the iteration. The corresponding initial operating parameters were assumed from the experimental records. The weather parameters, i.e., solar radiation, air temperature, and wind speed, are obtained from the local weather data files. The algorithm is interpreted as follows:

(i) Confirm the simulation time step Δt;

(ii) Input the initial operating parameters of the system, for example, the room temperature, the initial temperature distribution of the HSET, the initial

temperature of the bottom part of the HSEU, the domestic water tank, and the solar collectors array.

(iii) Input the weather parameters at t. The weather parameters include the solar radiation, the ambient temperature, and the wind speed.

(iv) Confirm the system operation statue by using the weather parameters and the initial operating parameters of the system.

(v) Conduct the system simulation by simulate the operation of the system components according to the system operation statue. The numerical simulation of the system components includes solar collectors array numerical model, VIHR-ASHP numerical model, PFHE numerical model, domestic hot water tank numerical model, under floor coil numerical model.

(vi) Conduct the simulation of the numerical model of HSEU to integral the heat transfer from other components.

(vii) Continue the simulation loop by using the derived outcomes as the initial input parameters of next time step $(t + 1)$ until the simulation loop is finished.

4.6 Chapter Summary

This chapter investigated the theory and computer models relating to the SAHR-HP system and its components. On this base, four main components of the system i.e., the multiple-throughout-flow solar collectors array with mini-channel structure, the VIHR-ASHP, the HSEU and, the counter-flow air-to-air PFHE, are analysed theoretically, and the steady computer models of the components are built up.

The numerical steady computer model for the mini-channel solar thermal collectors array is based on the theoretical analysis by using the fluid dynamics, thermodynamic

equilibrium theory, and the one-dimensional infinitesimal method. The VIHR-ASHP steady computer model is developed by establishing the energy conservation equations between the compressor, the condenser, the evaporators, and the EEVs. The theoretical analysis of the condenser and the evaporators use the ε-NTU based approach to analyse the heat transfer process. Similar to the condenser and the evaporators of the VIHR-ASHP, the heat transfer of the PFHE adopts the effectiveness-NTU method. The mathematical analysis of the novel HSEU is divided into two parts, the theoretical analysis of the bottom part of HSEU and the numerical model of the upper part of HSEU. Due to the small volume, the heat transfer of the bottom part of HSEU is based on the energy conservation theory. On the contrary, the upper part use standard 1D model for a heat storage vessel divides the tank in 10 segments/layers. Then, it models each layer with a partial differential equation (PDE) based on the heat transfer equation. Furthermore, a non-smooth post-processing algorithm is used to model the mixing of layers due to buoyancy effects.

For the heat transfer processes of the SAHR-HP system, HSEU and the served house are the two main parts, because most components of the system are connected to the HSEU and the served house. Accordingly, 6 heat transfer processes between the system components are also included to characterise the energy , i.e., the heat transfer between the underfloor coil and the HSEU, the heat transfer between the VIHR-ASHP and the HSEU, the heat transfer between the solar collectors array and the HSEU, the heat transfer between the domestic hot water tank and the HSEU, the heat transfer between the VIHR-ASHP and the under-floor coil, and the heat transfer between the indoor thermal condition and the ambient environment.

Through the established steady-state models, and the heat transfer processes study, the dynamic computer model of the integral SAHR-HP system is proposed to conduct the system simulation.

According to the established steady state models of the components of the SAHR-HP

system, parametric studies of the components, i.e., solar collectors array and VIHR-ASHP could, therefore, be conducted, including the impacts of ambient temperature, indoor temperature, air flow volume of the exhausted air, heat pump evaporation temperature, condensing temperature, and the apertures of the electrical expansion valves. More detailed discussion will be expanded in the Chapter 6.

Through the established dynamic model of the SAHR-HP system, the simulation could, therefore, be conducted in real climate conditions. A detailed discussion for whole system simulation will be provided in Chapter 7.

CHAPTER 5: SAHR-HP SYSTEM EXPERIMENTAL PROTOTYPE CONSTRUCTION AND TESTING

5.1 Chapter Introduction

This chapter introduces the processes of the experimental prototype construction and testing, as well as the testing results. These are detailed as:

(1) Description of both the system construction and the experiment rig construction;

(2) Description of the testing processes;

(3) Discussion of the test results and conclusion;

5.2 Fabrication of SAHR-HP System Components and Their Integration Process

5.2.1 VIHR-ASHP

The rendered view of the proposed VIHR-ASHP production from the front and the back is shown in Fig. 5-1. At the front, there are two draught fans to extract mixed air from the mixing chamber to transfer the heat to the refrigerant in Evaporator 2. Under the devices and controller cover, there is the heat pump controller which controls the operation of the VIHR-ASHP components. In addition, EEVs, IHX, condenser, compressor, and refrigerant storage tank are all installed in this chamber. On the side of the VIHR-ASHP, there are two pressure gauges which show the pressure of the compressor outlet (high pressure) and the compressor inlet on the evaporation line (low pressure), which can be used to calculate the final compression ratio of the heat pump. Similarly, the back view of the VIHR-ASHP is shown in Fig. 5-1 (b). Evaporator 1 is connected with the vapour injection line of the VIHR-ASHP and is

attached to a section of the air pipe which is connected to the building ventilation pipe. The ventilation pipe is attached to the mixing chamber with the fresh air inlet. A meshed screen is installed in the mixing chamber, which helps the fresh air and the exhaust air to mix evenly.

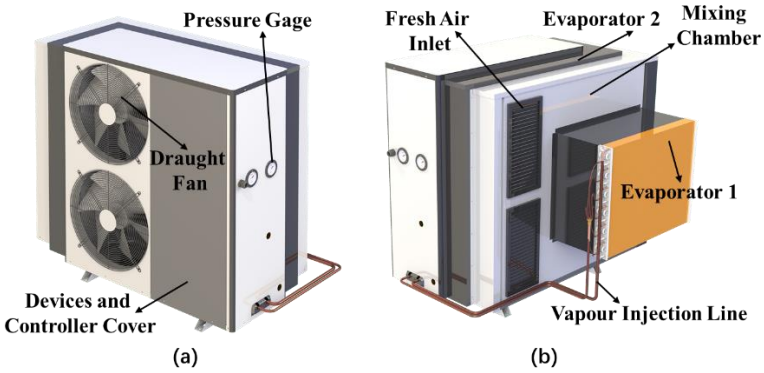

Fig. 5-1 (a) Front view of the VIHR-ASHP. (b) Back view of the VIHR-ASHP

Comparative analyses of the conventional and the novel VI cycle

The components of the VIHR-ASHP are listed in Table 5-1.

Table 5-1 The main components and details of the novel VIHR-ASHP

Component	Number	Detail
Compressor	1	Vapour injection compressor (ZW059HSP) Refrigerant: R410A; Power 3HP; Power supply: 220V(AC).
Internal heat exchanger	1	Brazed Plate Heat Exchanger (HL20-30D) Heat transfer capacity: 73kW to 97kW; Dimensions: 10cm*30cm; Plate number: 30; Effective heat exchange area: 0.9m^2
Condenser	1	Shell-and-tube heat exchanger (155CS070) Media: refrigerant and water.

Expansion valve	2	Electronic expansion valve (DPF(Q)2.4C-11RK) Media temperature: -30ºC to 70ºC; Working temperature: -30ºC to 60ºC.
Evaporator 1	1	Air heating evaporator Location: vapour injection line; Dimensions: 73 cm*66cm; Tube row number: 3; 72 passes.
Evaporator 2	1	L-type air heating evaporator Location: evaporation line; Dimensions: 70cm*33cm*1200cm; Tube row number: 2; 48 passes.
Refrigerant storage tank	1	Liquid-vapour separator (KFR120WLG-OLA) Volume: 2.8L.
Draught fan	2	Axial flow fan (YWF4D-350) Rated air flow volume: 3500m^3/h

5.2.2 Mini-channel solar thermal collectors and collectors array

The solar thermal collectors are novel mini-channel solar thermal collectors, and this is shown schematically in Fig.5-2. Each collector contains three lateral mini-channel tube bundles crossing the collector, thus forming three inlets and three outlets, which facilitate the connection of the solar collectors array with different connection methods. Each mini-channel tube cluster contains three mini-channel tubes which are linked together by using the manifolds at its two ends. The mini-channel tube clusters are covered by an integral solar thermal absorber plate coated with black chromium (shown in Fig. 5-3).

The collector is 2m in length and 1m in height. The width of the solar collector frame is 0.02m. As a result, the effective solar thermal absorber area is 1.98m^2. The structure of the novel mini-channel solar thermal collector is shown in Fig. 5-2.

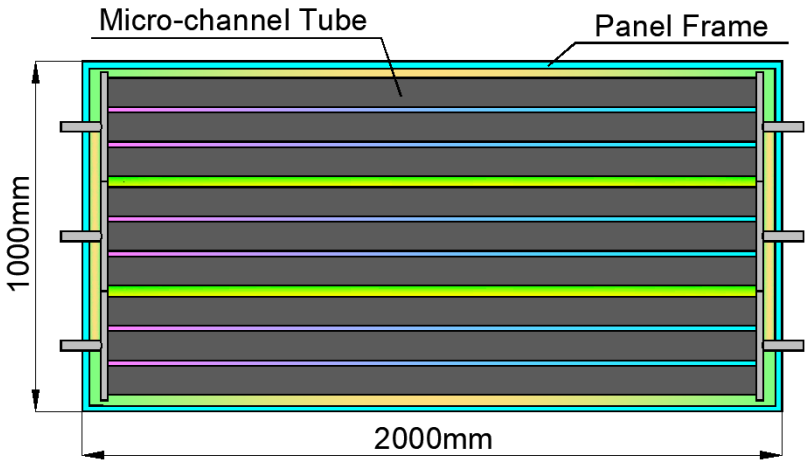

Fig. 5-2 The novel mini-channel solar thermal collector

The mini-channel tube layout is shown in Fig. 5-3. The tube is bonded to a solar absorber plate using two kinds of adhesives, i.e., the structural adhesive and the thermal conductive adhesive. The thermal conductivities of the thermal conductive adhesive and the structural adhesive are 2.6W/m·°C and 0.45W/m·°C, respectively. Of these two, the heat transfer ability of the thermal conductive adhesive is better than the structural adhesive. However, the viscidity of the structural adhesive is better than that of the thermal conductive adhesive, thus giving the solar collector a stable structure. According to the characteristics of the two kinds of adhesives, the thermal conductive adhesive is mainly used for transferring the heat between the solar thermal absorber plate and the mini-channel tube, and is spread from the centre to the edge of the tube. In addition, the structural adhesive is used at the two edges of the tube to enhance the stability and the reliability of the collector. The thickness and the thermal conductivity of the layers of the integral solar thermal absorber module is shown in Table 5-2.

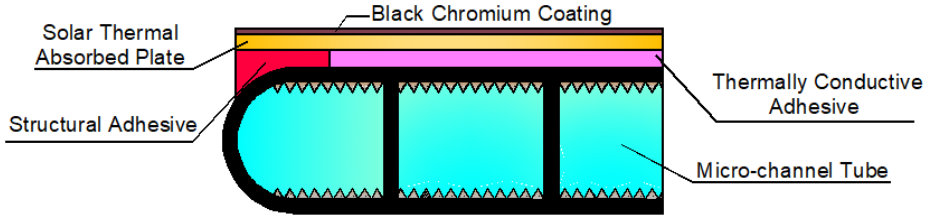

Fig. 5-3 Mini-channel tube layered structure

Table 5-2 The characteristics of the layers of the integral solar thermal absorber module

Layer	Thermal conductivity (W/m·K)	Thickness (mm)
Black chromium coating	93.9	0.01
Thermally adhesive	2.6	2
Mini-channel tube wall	205	0.8

The mini-channel tube is shown in Fig. 5-4. A mini-channel tube contains 25 mini-channels with an 81.3mm width. Other than the two channels of the two edges of the tube, the channels are all 2.5mm wide and 2.5mm high. With the same height, the two channels of the two edges of the tube have a width of 1.5mm. The thickness of the channel is 0.8mm. In addition, the 0.2mm high channel wall jagged embossment effectively enhances the convection heat transfer process and the solar thermal efficiency.

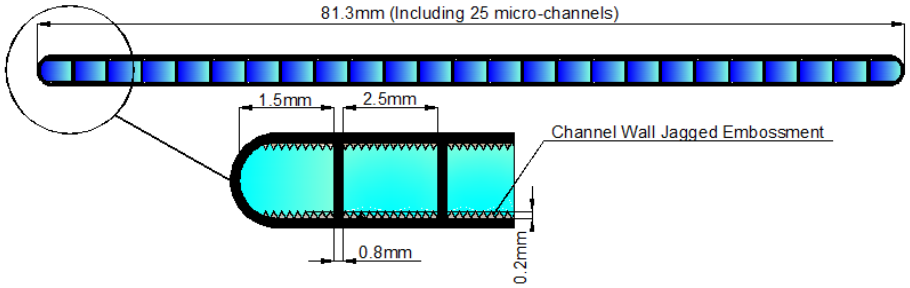

Fig. 5-4 The mini-channel tube and its enlarged figure

The fabrication of the mini-channel solar thermal collector contains three parts: (1) The construction of the frame of the collector; (2) The construction of the solar thermal energy absorption module; (3) Assemble four parts, i.e., the frame, the solar thermal energy absorption module, the glass cover and the insulation layer, into an integral mini-channel solar thermal collector. The assembly figure of the mini-channel solar thermal collector is shown in Fig. 5-5.

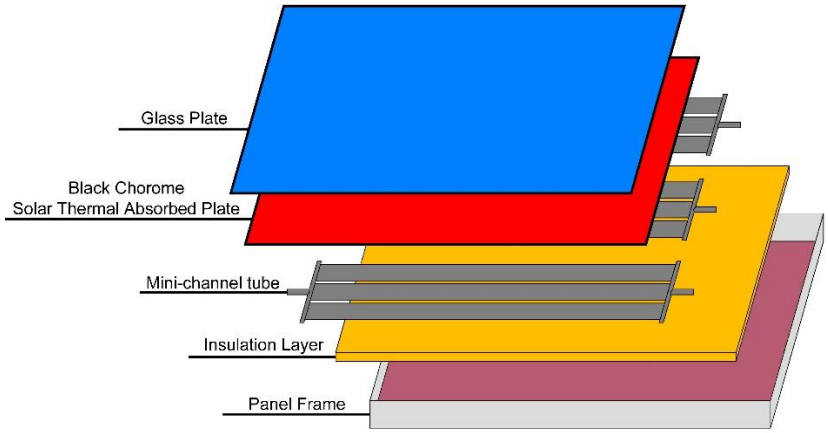

Fig. 5-5 Schematic of the assembly process of the mini-channel solar thermal collector

5.2.3 HSEU

The dimensions of the different parts of the HSEU and the functions of the different connectors of the HSEU are shown in Fig. 5-6. The inner wall of the HSEU is made of stainless steel, and the outer wall is made of colour steel board. The space between the walls is filled with foam insulation material between the layers. The heat insulation board between the lower and upper parts is made using the same method. The trepanning on the board is used to transfer heat between the two parts of the HSEU.

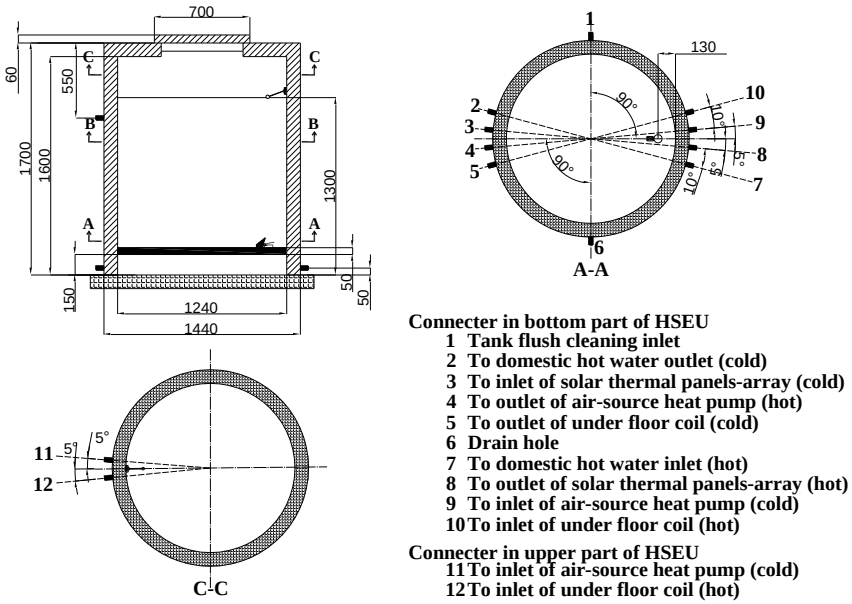

Fig. 5-6 The dimensions of the different parts of the HSEU and the functions of the different connectors of the HSEU

A coil copper heat exchanger is installed between the outlet and the inlet of the solar thermal collectors array, linked separately to connectors 8 and 3. The coil copper heat exchanger can transfer the collected heat from the solar collectors array to the buffer tank, and then separate the working fluid in the solar loop from the water in the HSEU. The structure of the heat exchanger in the lower part of the HSEU is shown in Fig. 5-7.

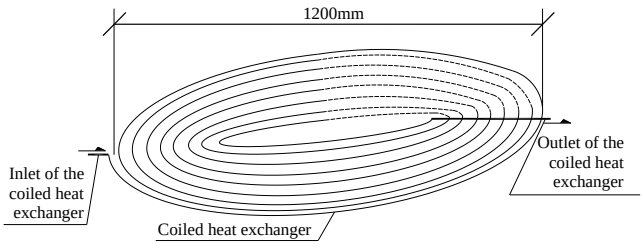

Fig. 5-7 The construction of the exchanger in the lower part of HSEU

The materials of the different parts of the HSEU are listed in Table 5-3.

Table 5-3 Materials of the HSEU elements

Part	Material	Thermal conductivity (W/m·°C)	Thickness (cm)
Outer protection layer	Colour steel plate	40	0.1
Inner layer	Stainless steel	31	0.15
Insulation layer	Spray foam	0.02	5
Heat exchanger coil	Copper	385	0.15

5.2.4 SAHR-HP system assembly and connection

The HSEU is the heart of the SAHR-HPs and it is responsible for conveying and distributing different parts of working fluids (i.e. fluids within the solar collectors array, the domestic hot water tank, the under-floor coil, and the VIHR-ASHP) and enabling effective heat transfer between them. The system connection is shown Fig. 5-8.

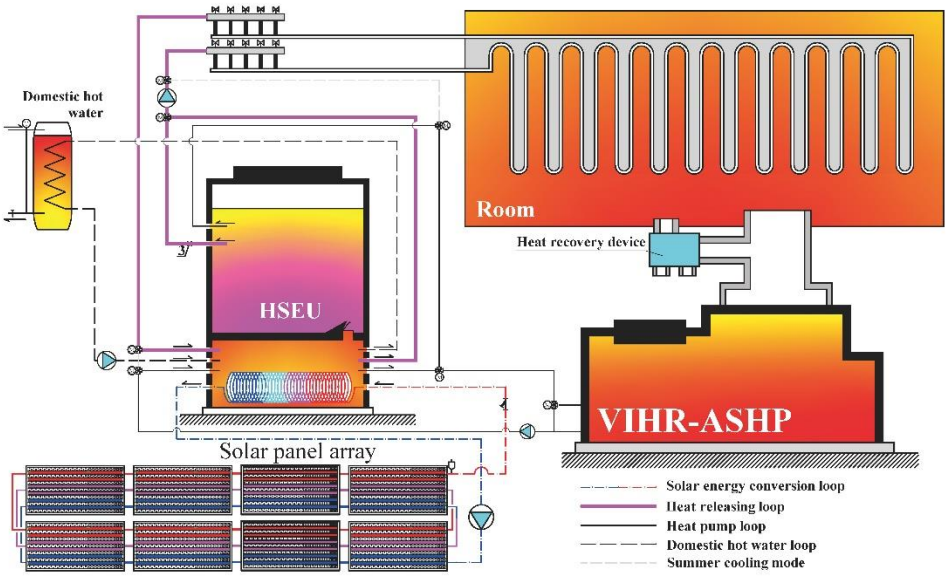

Fig. 5-8 The system connection schematic

The connection between the components uses the copper pipe and is insulated with the rubber insulation cotton which is coated with a waterproof layer on the outside of the insulation layer, as shown separately in Fig. 5-9 (a) and Fig. 5-9 (b).

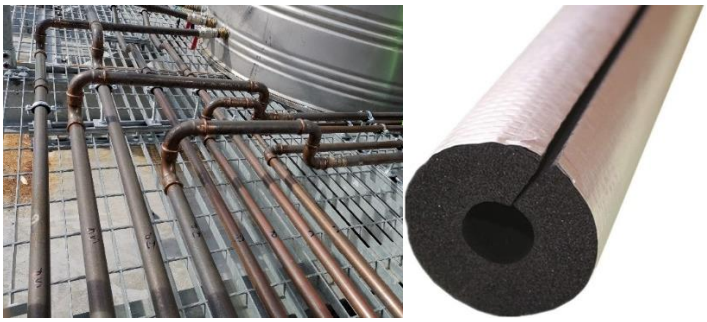

Fig. 5-9 (a) Copper pipe in system connection; (b) Rubber insulation cotton and waterproof layer

The solar thermal collectors array is directly connected to the lower part of the HSEU. In the solar thermal collectors array, the constant pressure equipment, the pressure relief devices and the air discharge equipment are installed. The connection between different panels uses the stainless-steel flexible pipe. In addition, the insulation method is the same as for the copper pipework. Because the solar loop is a closed loop, a number of independent working fluid charging devices are installed. The working fluid charging device will detect the inlet pressure of the solar loop circulating pump. When the pressure is lower than 2mH2O, the working fluid charging pump will be operated to charge the solar loop. Furthermore, a one-way valve is fitted to the fluid charging pipe to avoid the working fluid flowing back to the working fluid charging device. The domestic hot water tank also needs to install the constant pressure equipment, the pressure relief devices and the air discharge equipment on the domestic water side to ensure the security of the device which is shown in Fig. 5-10.

Fig. 5-10 The connection strategy of domestic hot water tank

The other components of the system have no constant pressure equipment, because the other loops are open loops connected with HSEU, and the heights of the loops are lower than the HSEU. Air discharge equipment is installed within the under-floor heating loop to ensure that the pipework is unobstructed.

5.3 Experimental System Development

5.3.1 VIHR-ASHP experimental system

The experimental system of the VIHR-ASHP was established in a specialised heat pump laboratory, which is shown in Fig. 5-11.

Fig. 5-11 Experimental platform of the VIHR-ASHP

The heat pump laboratory is designed to be able to simulate the winter operational conditions with a simulated ambient temperature from around -15°C to 10°C. As noted above, the novel VIHR-ASHP is designed to be integrated with a ventilation system that can provide a high-temperature exhaust air as the heat source (around 26°C room temperature), which couldn't be provided by the laboratory. The experiment was undertaken between October and December 2019 in Dongguan City, Guangdong Province, China (23.02°N, 113.75°E). During this period, the regional ambient temperature was relatively stable during the daytime, ranging from 24°C to 31°C, which is in accordance with the building exhaust air temperature requirements. Hence, instead of using the laboratory to provide exhaust air, the laboratory outdoor air was regarded as the exhaust air for this experiment. To achieve this aim, the exhaust air inlet of the air source heat pump was connected to the window of the laboratory by using an exhaust air duct, as shown in Fig. 5-12.

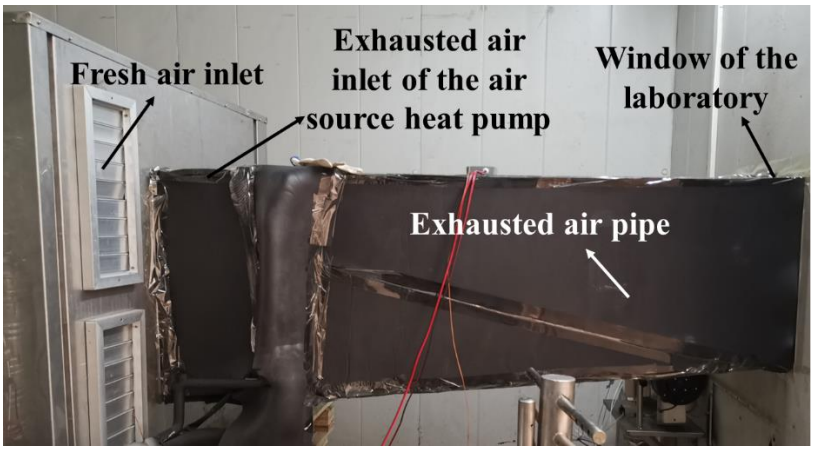

Fig. 5-12 Arrangement of the VIHR-ASHP air inlets

The laboratory can maintain indoor temperature and humidity at a certain level using the laboratory controlling devices as shown in Fig. 5-13 (a), and this can conveniently support the steady-state experimental conditions. To control the airflow rate of the exhaust air at the inlet of the air source heat pump, an air volume damper was installed on the inlet of the air duct as in Fig. 5-13 (b). The air duct was insulated thoroughly in order to prevent any interference between the laboratory's inside and outside

environments.

(a) (b)

Fig. 5-13 (a) Laboratory environment control system; (b) Air volume damper.

The schematic of the VIHR-ASHP experimental set-up and corresponding experimental instruments are shown in Fig. 5-14. There are two circuits between the experimental devices, i.e., the VIHR-ASHP circuit and the water tank circuit. These two circuits are connected with each other in the condenser of the heat pump to complete the heat transfer cycle. For the VIHR-ASHP circuit, there are seven main components: (1) a vapour injection compressor; (2) a condenser; (3) the first EEV in the vapour injection line; (4) an evaporator in the vapour injection line; (5) an inner heat exchanger; (6) the second EEV in the evaporation line; (7) an evaporator in the evaporation line. A temperature sensor and a pressure gauge are installed between every two components along the circuit. In addition, an electrical detector is connected to the compressor which can detect and collect the power capacity of the compressor in real-time, and the collected data was transferred to a data logger, and then saved into a computer.

The water tank circulation line connects the condenser of the heat pump with a water tank with a capacity of four tons, which can release the generated heat from the VIHR-ASHP to the water tank for heat storage purposes. Two temperature sensors and a mass flow rate meter are installed in the circulation line for the sake of calculating the collected heat from the heat pump. Four temperature sensors are fixed to the water tank to monitor the temperature variation of the tank water. To maintain the water tank

temperature at a certain level, the city water is charged into the water tank continuously as the city water has a comparatively constant temperature. A water tank drain outlet is used to maintain the volume of the water tank and to avoid the overflow. The specifications of the experimental devices are shown in Table 5-4.

In addition to the data collected from the two circuits, the environmental parameters of the experiment were also collected and recorded. In order to monitor these parameters, two temperature sensors are placed in the heat pump laboratory to measure the room temperature and the exhaust air pipe temperature to record the ambient temperature from outside the laboratory. A flow velocity sensor is also installed in the exhaust air pipe to calculate the air volume flow rate (where the sectional area of the air duct is 0.34m^2). Furthermore, an electrical detector is connected to the fan for monitoring the power capacity.

Table 5-4 List of experimental testing and monitoring devices

Devices	Specifications	Range	Accuracy	Quantity	Location
Water mass flowmeter	DS-CMF-I-DN25 (DOYI China) 0-6.4t/h	0-6.4t/h	0.2%	1	Water tank loop;
Anemometer	JY-GD650 (Zhongyi, China)	0-10m/s	0.2%	1	Exhaust air duct;
Platinum resistance thermometer	PT1000 (Zhongjia, China) -200-350	-200-350 ºC	0.2%	6	Water tank, water tank loop;
Pressure sensor	551.32 (HUBA, Swiss)	0-25bar	0.3%	8	Heat pump cycle loop;
Thermocouple	TT-T-36-SLE (OMEGA, USA)	-200-260ºC	0.2%	10	Heat pump cycle loop; laboratory, exhaust air duct;
Electric	PM9802	2-	0.4%	2	Air blower,

parameter meter	(Napui, China)	600V; 5mA-40A			compressor;
Heat pump laboratory control devices	Control box (Phnix, China)	/	/	1	Data collecting room;
Data logger and computing unit	34970A (Agilent, USA)	/	/	1	Data collecting room.

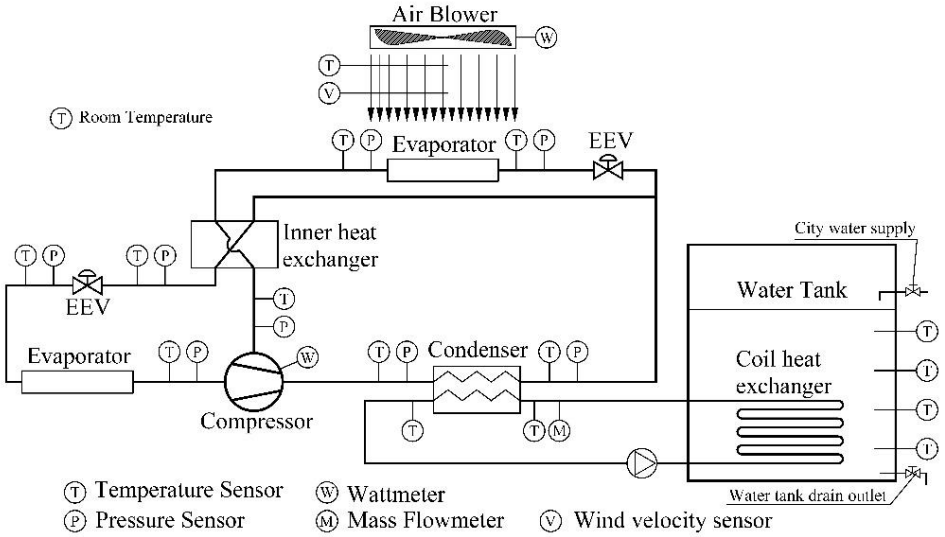

Fig. 5-14 Schematic of the VIHR-ASHP experimental system and experimental instruments

All of the outputs from the sensors and instruments were transmitted into a Data Logger and then stored onto the computer; these are shown in Fig. 5-15.

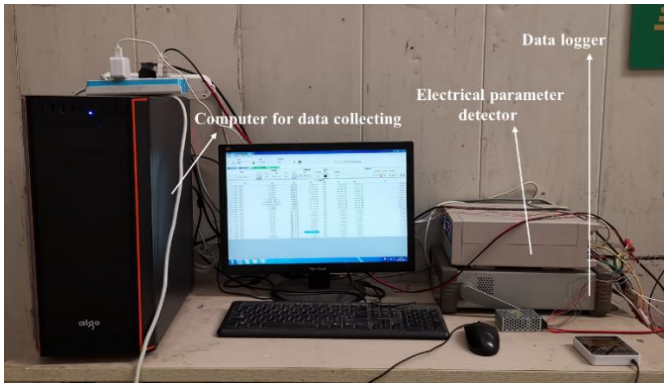

Fig. 5-15 Data collecting devices for the heat pump experiment

The performance of the VIHR-ASHP was tested and evaluated based on several operating parameters by varying the temperature of the laboratory (fresh air), the volume flow rate of the air from the outside of the laboratory (exhaust air), the refrigerant charging capacity and the opening degree of the two EEVs.

5.3.2 Solar thermal collectors array and HSEU experimental system

Three experimental systems were established under real climatic conditions. One system is equipped with the novel mini-channel solar thermal collectors array connected by the multiple-throughout-following way and the novel stratified HSEU. One system is equipped with the novel mini-channel solar thermal collectors array connected by the one-to-one method and the novel stratified HSEU, and the other is equipped with the novel mini-channel solar thermal collectors array connected by the multiple-throughout-following method and the conventional HSEU. The schematics of the three experimental systems are shown separately in Fig. 5-16(a), Fig. 5-16(b) and Fig. 5-16 (c). Every system consists of sixteen solar panels (which form an integrated solar panel-array), an HSEU and a heat pump. This system enables: (1) collection and conversion of the solar radiation from the solar panel-array into useful heat; (2) transfer of the solar heat to either the HSEU tank water or the heating loop fluid and (3) transfer and transportation of the solar/tank heat into the served space via the HSEU and the heating elements fitted into the served space.

In order to compare the performance between the solar collectors array connected by the novel multiple-throughout-flowing method with the solar collectors array connected by the conventional one-to-one method, the data from the two systems shown in Fig. 5-16(a) and Fig. 5-16(b) are compared and analysed. This is also done to compare the performance between the novel double-layer HSEU and the conventional HSEU.

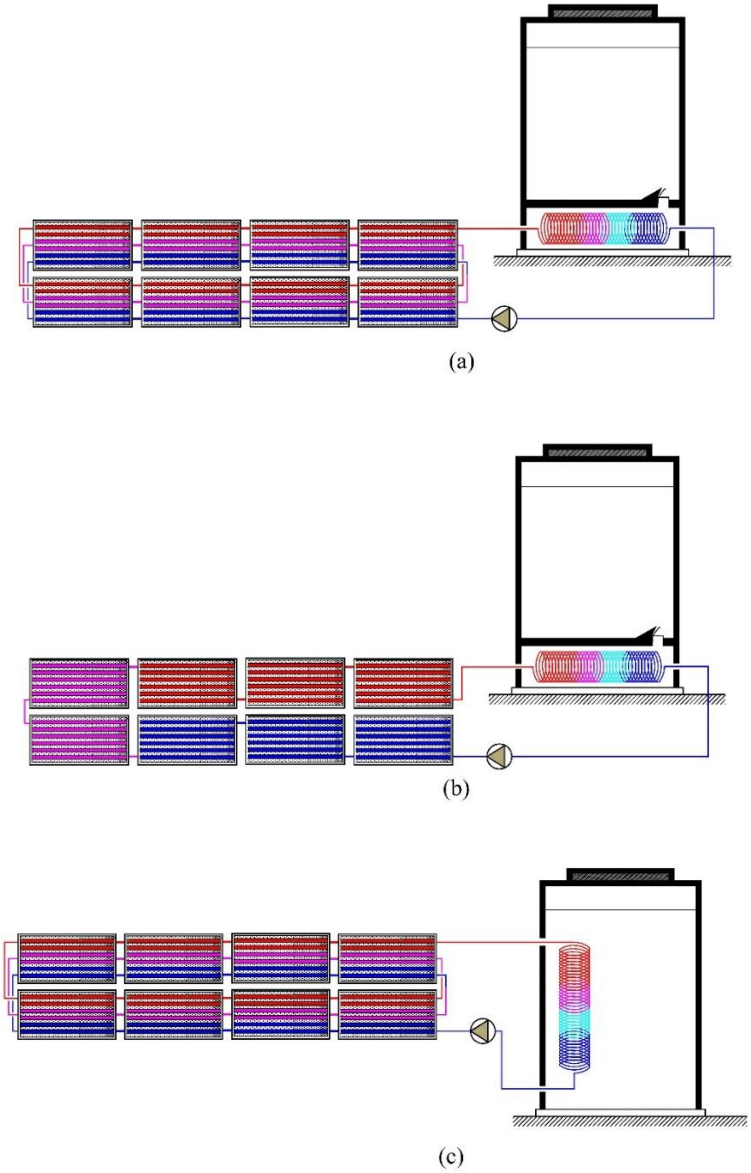

Fig. 5-16 The schematics of the three experimental systems: (a) multiple-throughout-following connection methods with novel stratified HSEU; (b) one-to-one connection methods with novel stratified HSEU; (c) multiple-throughout-

following connection methods with conventional HSEU.

The conventional HSEU has a 1500L water tank incorporating a coil-type-heat-exchanger connected to the solar collector's loop and another coil-type-heat-exchanger connected to the heating loop. The in-lab configuration display of the conventional HSEU is shown in Fig. 5-17.

Fig. 5-17 Photographic display of the conventional HSEU, created in the laboratory environment

The novel HSEU is shown in Fig. 5-18.

Fig. 5-18 Photographic display of the novel stratified HSEU

Three identical test rooms were used to operate and test the systems. The test rooms have a length of 14m, a width of 7m, a height of 4m and a floor area of 100 m^2. The front façade of the house faces south. Table 5-5 lists the heat transfer coefficients of building envelopes, which are measured using a BES-GP intelligent multi-channel temperature/heat flow detector. The thermal properties of the building components are the same as the actual parameters of common rural houses, thus enabling a real reflection of the heat load for a rural house.

Table 5-5 The heat transfer coefficients of the building envelope

Part	**Structure**	**K [W/(m^2·°C)]**
Wall	370mm brick wall Plastering + 50mm extruded polystyrene board	0.47
External doors	Pinewood door	2.9
Window	3mm common glass aluminium alloy window frame (two layers)	1.54
Roof	Cement mortar +Insulation layer + Waterproof layer + Tile.	0.37

The three experimental systems were equipped with various measurement instruments and sensors. The temperature, flow rate and pressure of the fluids in the solar and heating loops were measured using platinum resistance thermometer probes, flow meters and pressure gauges respectively. All the outputs of the sensors and instruments were transmitted into a Data Logger and then stored on the computer. The specifications, quantity and installation position of the sensors/meters used for the measurement process are outlined in Table 5-6. The tests were carried out under real-time operational conditions in Dongguan City, Guangdong Province, China (23.02°N, 113.75°E), which has a typical dry climatic condition and enjoys the sun shining on most days of the year.

Table 5-6 List of experimental testing and monitoring devices

Devices	Specifications	Quantity	Location
Pyranometer	TQB-2C (Sunlight, China)	1	Top of the collector
Water flowmeter	LWGY-MK-DN25(MACON China)	2	One branch of solar thermal collectors; Solar thermal collectors main entrance;
Anemometer	HS-FS01(Huakong single, China)	1	Top of the collector
Platinum resistance thermometer	PT1000(Zhongjia China)	40	Solar thermal collectors; testing room; water tank; ambient, etc.
Data logger and computing unit	34970A (Agilent, USA)	1	Testing room
Pressure gauge	YN60 0-0.6Mpa (Jiangyin, China)	6	Inlet and outlet of water pump; Inlet and outlet of solar thermal collectors; Inlet and outlet of the water tank;

In order to consider the water tank's temperature stratification problem, five platinum resistance thermometers (TM_1 to TM_5) were installed at various depths, which is shown in Fig. 5-19. The average temperature of the water tank can be calculated by using the data collected from the thermometers.

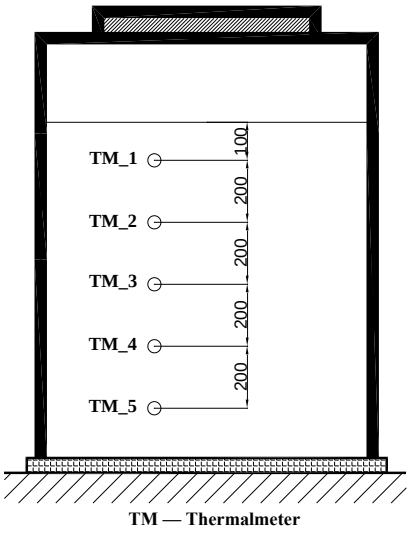

Fig. 5-19 The distribution of the thermometers in the water tank

5.4 Results and Discussion

5.4.1 VIHR-ASHP experiment results

5.4.1.1 Refrigerant charging quantity

The experiment was conducted under steady experimental conditions, and started by confirming the optimal refrigerant charging quantity. The testing environment for this experiment was the standard conditions, i.e., temperature 0°C and pressure 101kPa in the laboratory. The exhaust air from the laboratory outside had a temperature of 24°C. The apertures of the two EEVs in the vapour injection line and the evaporation line were 32% and 24%, respectively. The refrigerant charging quantity increased from 1 to 3.04 kg. The experimental results of the relevant parameters in the water tank circuit, including the condenser inlet temperature, the condenser outlet temperature, and the volume flow rate are shown in Table 5-7. Along with the increase of the refrigerant charging quantity, the volume flow rate and the condenser inlet temperature remained stable.

Table 5-7 Water tank circuit parameters and the increasing refrigerant charging quantity

Refrigerant charging quantity (kg)	1	1.2	1.4	1.64	1.76	1.88	2.01
Condenser inlet temperature (ºC)	31.6	27.2	26.0	25.6	25.5	25.5	25.1
Condenser outlet temperature (ºC)	34.7	30.0	28.9	28.7	28.8	28.9	28.6
Volume flow rate (m^3/h)	1.27	1.36	1.36	1.36	1.37	1.36	1.34
Refrigerant charging quantity (kg)	2.14	2.27	2.4	2.53	2.68	2.917	3.037

Condenser inlet temperature (ºC)	25.2	25.3	25.4	25.4	25.5	25.4	25.4
Condenser outlet temperature (ºC)	28.8	28.9	29.2	29.2	29.4	29.4	29.3
Volume flow rate (m^3/h)	1.34	1.34	1.34	1.34	1.34	1.34	1.34

As shown in Fig. 5-20, with an increase of the refrigerant charging quantity, meaning that the power capacity of the heat pump decreased slightly from 2800W to 2500W. However, the generated heat from the VIHR-ASHP increased gradually from 4500W to 6100W and remained constant after the refrigerant charging quantity reached 2.7kg. The decrease of the power capacity and the increase of the generated heat resulted in an overall improvement of the VIHR-ASHP performance.

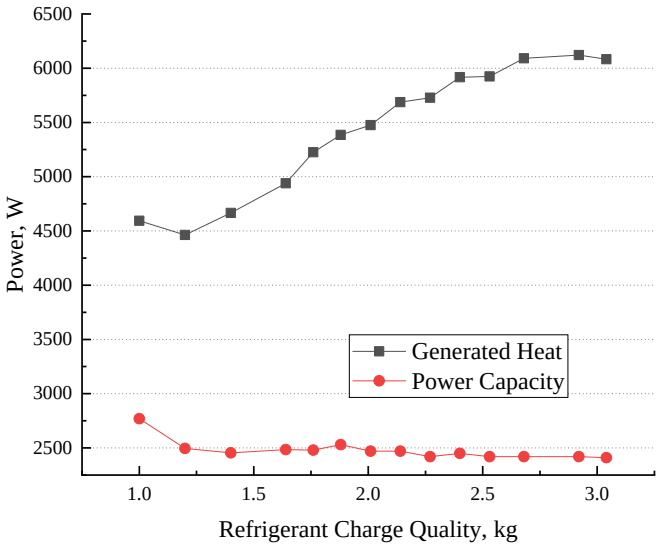

Fig. 5-20 Variation of the power capacity and the collected heat with the refrigerant charge quantity

Based on the variations of the power capacity and generated heat, the COP of the heat pump is calculated and these are shown in Fig. 5-21. The COP increased gradually with the increasing refrigerant charging quantity and peaked at 2.5 when the charging

quantity reached 2.7kg. When the charging quantity passed 2.7kg, the COP of the heat pump remained around 2.5. Hence, the optimal refrigerant charging quantity of the heat pump is identified as 2.7kg.

Fig. 5-21 Variation of the COP with the refrigerant charge quantity

The experimental results for the relevant parameters in the heat pump compression circuit, including the condensing pressure, the condensing temperature, the evaporating pressure, the evaporating temperature, and the vapour injection pressure, are shown in Table 5-8. As the refrigerant charging quantity was increased, the condensing, evaporating, and vapour injection pressures initially experienced a decrease followed by an increase. In addition, the condensing temperature decreased gradually whilst the evaporating temperature increased.

Table 5-8 Variation of heat pump circulation parameters with increasing refrigerant charging quantity

Refrigerant charging quantity (kg)	1	1.2	1.4	1.64	1.76	1.88	2.01
Condensing	2.169	1.868	1.83	1.822	1.838	1.845	1.849

pressure (Mpa)							
Condensing temperature (ºC)	79.17	76.29	71.45	65.62	61.17	56.93	50.64
Evaporating pressure (Mpa)	0.563	0.551	0.579	0.604	0.626	0.633	0.641
Evaporating temperature (ºC)	-11.5	-11.49	-11.02	-9.79	-8.73	-8.37	-7.82
Vapour injection pressure (Mpa)	1.82	1.649	1.656	1.666	1.696	1.692	1.691
Refrigerant charging quantity (kg)	2.14	2.27	2.4	2.53	2.68	2.917	3.037
Condensing pressure (Mpa)	1.86	1.864	1.882	1.89	1.899	1.902	1.902
Condensing temperature (ºC)	51.22	50.78	48.83	45.01	41.6	41.25	37.75
Evaporating pressure (Mpa)	0.659	0.67	0.687	0.702	0.709	0.723	0.73
Evaporating temperature (ºC)	-7	-6.56	-5.85	-5.19	-4.97	-4.28	-4.07
Vapour injection pressure (Mpa)	1.709	1.714	1.742	1.745	1.733	1.755	1.742

In order to further investigate the relationship between the refrigerant charging quantity and other operating parameters of the heat pump, the variation of the total refrigerant mass flow rate with respect to the refrigerant charging quantity is shown in

Fig.5-22. The variation trend of the refrigerant total mass flow rate is similar to that of the COP with respect to the refrigerant charging quantity. When the charging quantity reached 2.7kg, the total mass flow rate of the refrigerant became constant at around 0.38kg/s. This indicates that the maximum total mass flow rate of the heat pump under EEVs' aperture is 32% in the vapour injection line and 24% in the evaporation line separately. The increasing refrigerant mass flow rate directly results in the increased heat transfer capacity of the heat pump, which can explain the reason why the COP of the heat pump kept rising with the increase of refrigerant charging quantity.

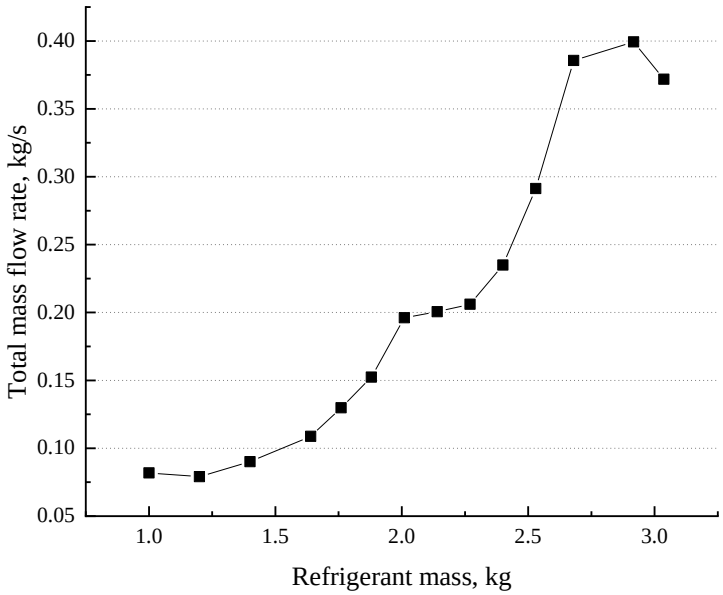

Fig. 5-22 Variation of the total mass flow rate of R410a with respect to the charge quantity

The intermedium compression ratio decreased slightly from 1.2 to 1.1 and then remained constant, which illustrates a certain stability ratio. Fig. 5-23 shows the variation of the intermedium and final compression ratios as well as the evaporation temperature in the evaporation line along with the refrigerant charging quantity. The final compression ratio decreased from 4 to 2.6 while the refrigerant charging quantity increased from 1kg to 3kg. The decline of the final compression ratio was accompanied by an increase in the evaporation temperature of the heat pump which

increased from -11ºC to -4ºC. Accordingly, the increase of the refrigerant mass flow rate, the decrease of the final compression ratio, and the increase of the evaporation temperature contributed to improving the heat pump performance considerably.

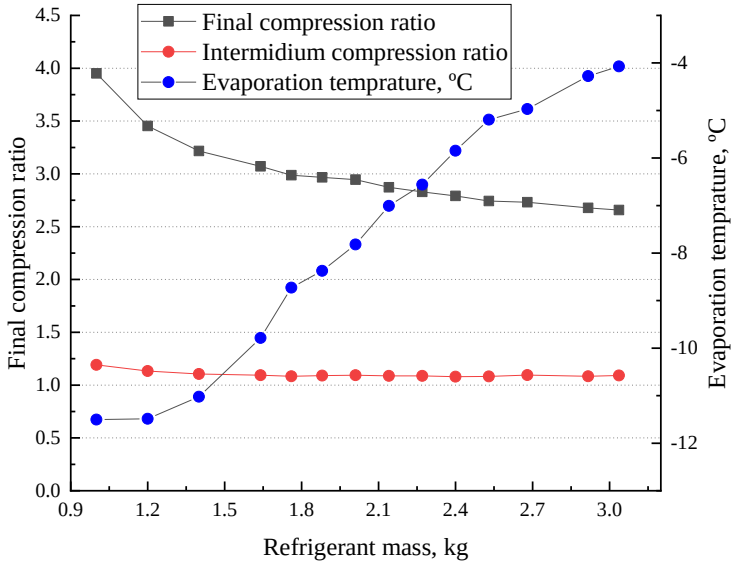

Fig. 5-23 Variation of the compression ratios with respect to the charge quantity

5.4.1.2 EEVs apertures

After finding the optimal refrigerant charging quantity, the apertures of the two EEVs in the vapour injection line and the evaporation line was adjusted to test the performance of the VIHR-ASHP under the standard test conditions. For simplicity, the aperture of the EEV in the vapour injection line will be called the vapour injection line aperture (VILA), and the aperture of the EEV in the evaporation line will be called the evaporation line aperture (ELA). The experimental results for the relevant parameters in the water tank circuit, including the condenser inlet temperature, the condenser outlet temperature, and the volume flow rate, are shown in Table 5-9 Along with the variation of the EEV's apertures, the volume flow rate and the condenser inlet temperature remained stable.

Table 5-9 Water tank circuit parameters along with the variation of the EEV's

apertures

ELA	VILA	Condenser inlet temperature (ºC)	Condenser outlet temperature (ºC)	Volume flow rate (m^3/h)
15%	5%	25.47	29.67	1.36
	10%	25.48	30.48	1.36
	15%	25.77	30.39	1.34
	20%	25.56	29.73	1.39
20%	5%	25.57	30.49	1.36
	10%	25.62	30.73	1.36
	15%	25.64	30.04	1.36
	20%	25.68	29.86	1.37
25%	5%	25.2	29.89	1.39
	10%	25.16	30.06	1.39
	15%	25.15	29.68	1.4
	20%	25.27	29.36	1.39
30%	5%	25.31	29.71	1.39
	10%	25.33	29.75	1.39
	15%	25.34	29.52	1.39
	20%	25.35	29.42	1.39

The variation of the generated heat and the power capacity along with the different apertures of the two EEVs is shown in Fig. 5-24 and Fig. 5-25, respectively. The separate lines in these figures' present variations for different ELAs. Under every ELA, the variation of the collected heat and the power capacity was also changed along with the different VILA, thus forming the operation points with different apertures of both EEVs.

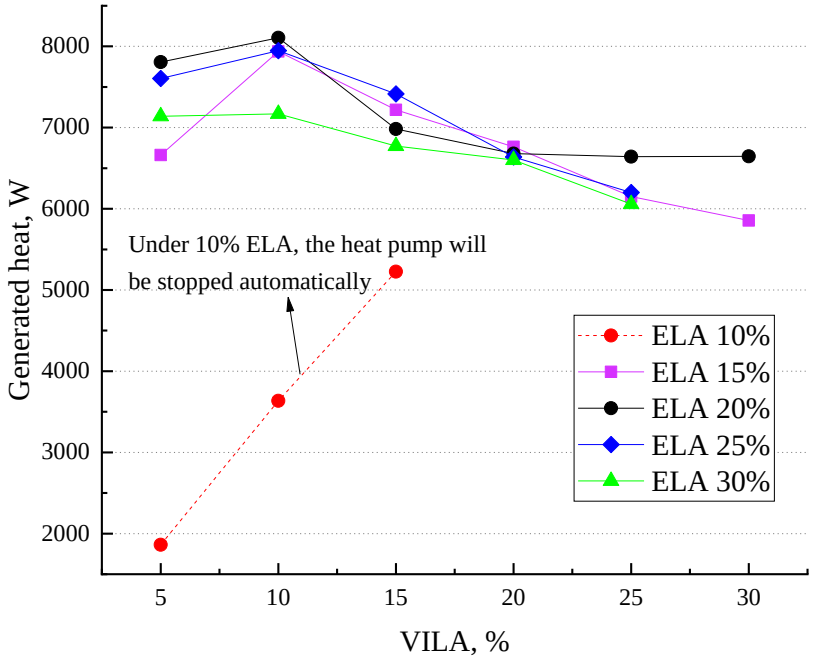

Fig. 5-24 Variation of the generated heat with different EEVs' apertures

As shown in Fig. 5-24, when ELA reached 10%, the refrigerant mass flow rate was seriously limited by the small aperture, and the compressor could not receive enough refrigerant, thus causing the compressor not to operate properly. Consequently, the self-protection program of the heat pump was activated and the heat pump was shut down automatically. Under other ELAs from 15% to 25%, the generated heat was increased when VILA varied from 5% to 10% and peaked at 10%. Then, the generated heat decreased when VILA increased from 10% to 30%. The generated heat first raised and then descended mainly because the refrigerant mass flow rate in the vapour injection line increased with the increase of VILA. From 5% to 10% VILA, the increased mass flow rate in the vapour injection line can benefit the heat transfer, thus enhancing the generated heat. However, the continuous growth of the refrigerant mass flow rate in the vapour injection line eventually surpasses the line's heat transfer capacity, thereby using refrigerant without overheat and hence reduced the generated heat. In addition, under 10% VILA, when ELA increasing from 15% to 30%, the generated heat decreased drastically. The analysis revealed that under 10% VILA and 15% ELA conditions, the heat pump generated maximum heat. The reason for the

optimum EEVs' apertures lies in the refrigerant mass flow rate in the vapour injection line. Along with the increasing EEV aperture in the vapour injection line, the relevant refrigerant mass flow rate also increases, thus leading the increase of the heat transfer capacity of the vapour injection line. However, the refrigerant mass flow rate in the evaporation line decreased, and the limited energy capacity that can be extracted from the exhausted air restricts the heat transfer capacity of the vapour injection line. Consequently, the total generated heat decreased eventually.

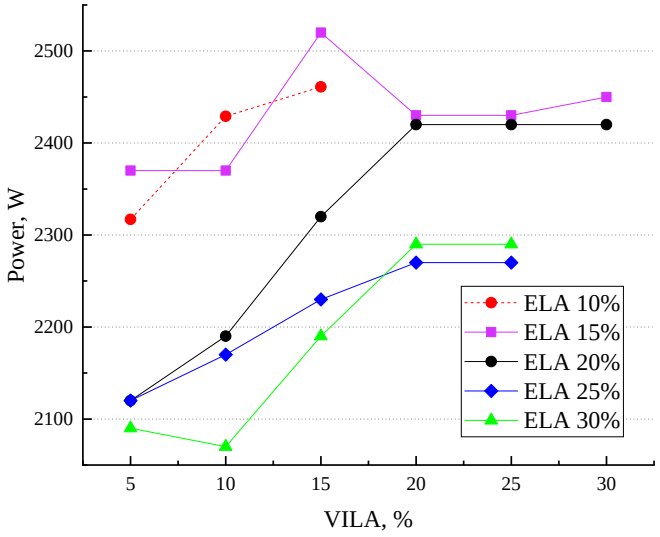

Fig. 5-25 Variation of the power capacity with different EEVs' apertures

As shown in Fig. 5-25, similar to the variation of the generated heat, when ELA reaches 10%, the heat pump automatically activated the self-protection program and shuts down. When ELA increased from 15% to 25%, the power capacities increased with the increase of VILA. After VILA peaked at 15% or 20%, the power capacities dropped or remained constant. Furthermore, when ELA was 30%, the power capacity decreased firstly and then increased after 10% VILA, then remained constant after the VILA reached 20%. According to the analysis, the 10% VILA and 30% ELA lead to the lowest energy consumption of the VIHR-ASHP.

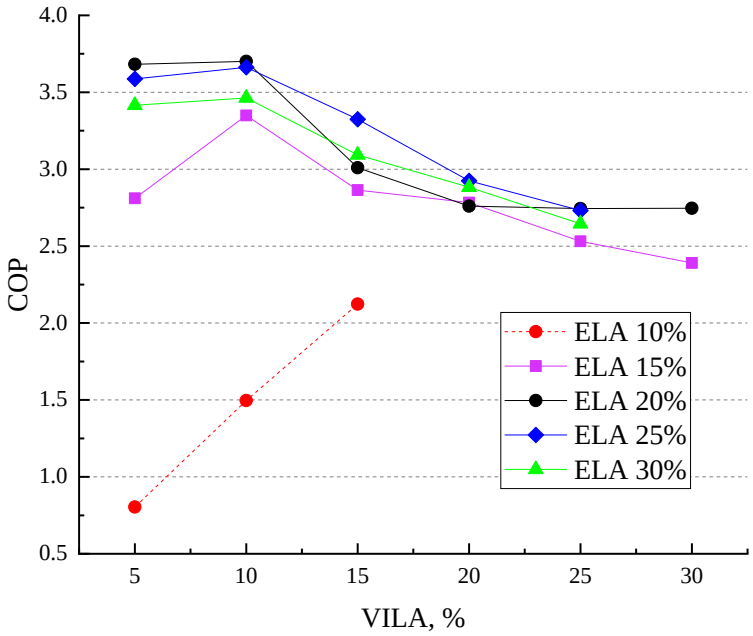

Fig. 5-26 Variation of the COP with different EEVs' apertures

Based on the generated heat and the power capacity of the VIHR-ASHP, the COP was calculated and is shown in Fig. 5-26. Under 10% ELA, the heat pump automatically activated the self-protection program and shut down the device. When ELA increased from 15% to 30%, the COP of the VIHR-ASHP increased slightly with the increase of VILA from 5% to 10%. Then, the COP dropped with an increase of VILA. Consequently, the heat pump with 10% VILA and 20% ELA reached the highest COP. The analysis showed that the main factor influencing the COP of the heat pump was the generated heat.

Table 5-10 Heat pump circuit parameters along with the variation of the EEV's apertures

ELA	VILA	Condensing pressure (Mpa)	Condensing temperature (ºC)	Evaporating pressure (Mpa)	Evaporating temperature (ºC)	Vapour injection pressure (Mpa)
15%	5%	3.058	76.73	0.583	-10.69	1.10

	10%	2.166	43.29	0.676	-6.16	1.15
	15%	2.036	41.90	0.465	-16.03	1.30
	20%	1.942	31.93	0.474	-16.61	1.44
20%	5%	2.053	45.94	0.801	-3.18	1.26
	10%	2.006	56.29	0.759	-2.91	1.30
	15%	1.923	69.17	0.692	-5.66	1.53
	20%	1.918	62.98	0.693	-5.66	1.64
25%	5%	1.959	44.37	0.799	-1.20	1.27
	10%	1.968	45.56	0.809	-0.85	1.34
	15%	1.940	44.50	0.770	-2.27	1.40
	20%	1.894	45.78	0.693	-5.34	1.49
30%	5%	1.944	43.44	0.803	-1.04	1.26
	10%	1.946	43.26	0.806	-0.94	1.26
	15%	1.921	43.38	0.782	-1.85	1.42
	20%	1.956	53.03	0.736	-3.61	1.55

The experimental results for the relevant parameters in the heat pump circuit, including the condensing pressure, the condensing temperature, the evaporating pressure, the evaporating temperature, and the vapour injection pressure, are shown in Table 5-10. With the increase of the ELA, the condensing pressure and the evaporating pressure under the same VILA showed an increase trend.

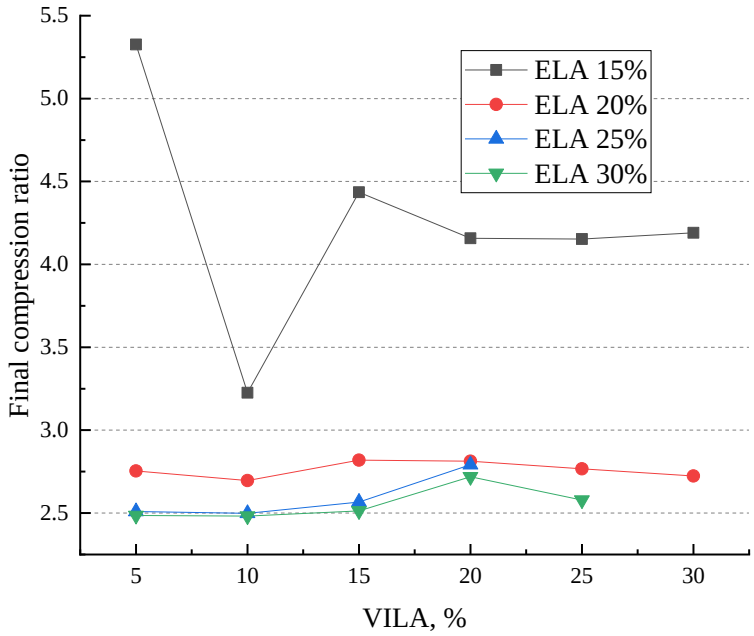

Fig. 5-27 Variation of the final compression ratio with respect to EEVs apertures

Furthermore, the final compression and the intermedium compression ratios can also reflect the performance of the heat pump. Fig. 5-27 shows the variation of the final compression ratio with respect to the EEVs' apertures. Under any ELA, the final compression ratio bottomed at the lowest value under 10% VILA, which can explain why the heat pump can operate better under 10% VILA compared to other apertures. When it comes to ELA, the final compression ratio reached the highest under 15% ELA. The excessive final compression ratio led to an unfavourable effect on the performance of the heat pump and thus lower COP. Under 20% ELA, the lowest final compression ratio was also achieved at 10% VILA. The fluctuation range of the final compression ratio was low and the value of it remained around 2.7. Under the spare ELAs of 25% and 30%, the final compression ratios were similar around 2.5.

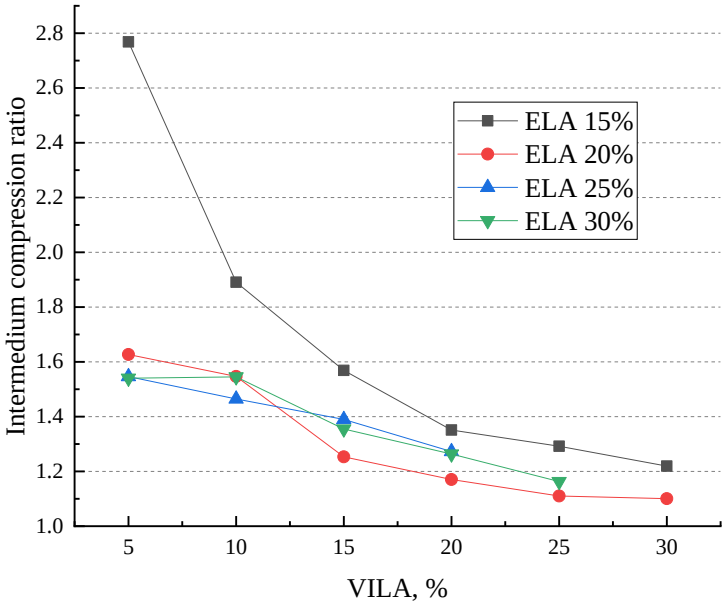

Fig. 5-28 Variation of the intermedium compression ratio with respect to EEVs apertures

Fig. 5-28 shows the variation of intermedium compression ratio with respect to the variation of the EEVs apertures. As with the final intermedium compression ratio, the intermedium compression ratio reached the highest value when the aperture of the ELA was 15%, which was detrimental to the heat pump performance. Along with the increase of VILA, the intermedium compression ratios under different ELAs showed similar variation trends and decreased gradually.

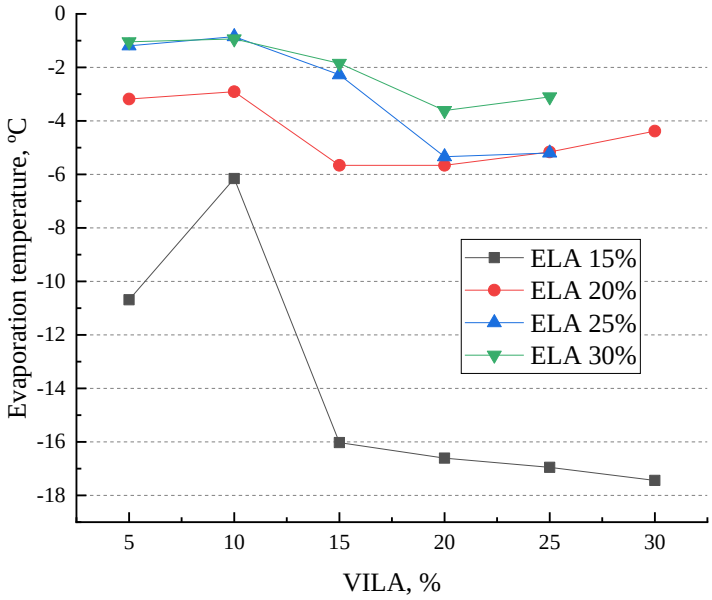

Fig. 5-29 Variation of the evaporation temperature with respect to EEVs apertures

Fig. 5-29 shows the evaporation temperature varied along with the variation of the EEVs' apertures. It is seen that the highest evaporation temperatures appeared when VILA reached 10%. In addition, with the increase of ELA, the evaporation temperature increased, which means the higher ELAs can help reduce the final compression ratio and indirectly increase the performance of the heat pump.

5.4.1.3 Volume flow rate of the exhaust air

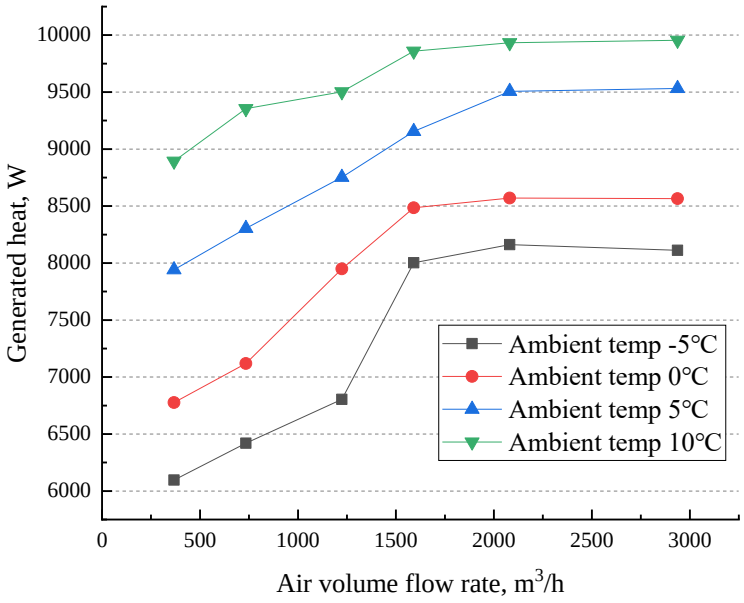

Fig. 5-30 Variation of the generated heat with different exhaust air volume flow rates

The performance of the heat pump is also affected by the air volume flow rate of the exhaust air. This can greatly affect the available heat of the exhaust air and the evaporation temperature of the evaporator in the evaporation line. In order to simulate a real winter ambient environment, the laboratory temperature was set to 4 individual temperature points from -5°C to 10°C with 5°C intervals. The experimental results for the relevant parameters in the water tank circuit are shown in Table 5-11, including the condenser inlet temperature, the condenser outlet temperature, and the volume flow rate. When the exhaust airflow rate was varied, the volume flow rate of the water tank circuit and the condenser inlet temperature remained stable. Under different ambient temperatures, the condenser outlet temperature increased along with the increase of the exhaust air volume flow rate.

Table 5-11 Water tank circuit parameters along with the different exhaust air volume flow rate

Ambient temperature (ºC)	Exhaust air volume flow rate (m^3/h)	Condenser inlet temperature (ºC)	Condenser outlet temperature (ºC)	Volume flow rate (m^3/h)
-5	367.2	24.21	27.86	1.43
	734.4	24.20	28.05	1.43
	1224	24.21	28.29	1.43
	1591.2	24.22	29.02	1.43
0	367.2	24.22	28.28	1.43
	734.4	24.21	28.48	1.43
	1224	24.25	29.01	1.43
	1591.2	24.26	29.34	1.43
5	367.2	24.39	29.15	1.43
	734.4	24.40	29.38	1.43
	1224	24.42	29.67	1.43
	1591.2	24.43	29.92	1.43
10	367.2	24.58	29.94	1.42
	734.4	24.57	30.22	1.42
	1224	24.58	30.32	1.42
	1591.2	24.58	30.53	1.42

Under the pre-set laboratory temperatures, the generated heat varied with the increase of the exhaust air volume flow rate, as shown in Fig. 5-30. The variations of the generated heat under different laboratory temperatures showed the same trend. The generated heat increased with the increase of the exhaust airflow rate. When the exhaust airflow rate reached 1584m^3/h, the increasing trend of the generated heat

reduced and the generated heat remained constant.

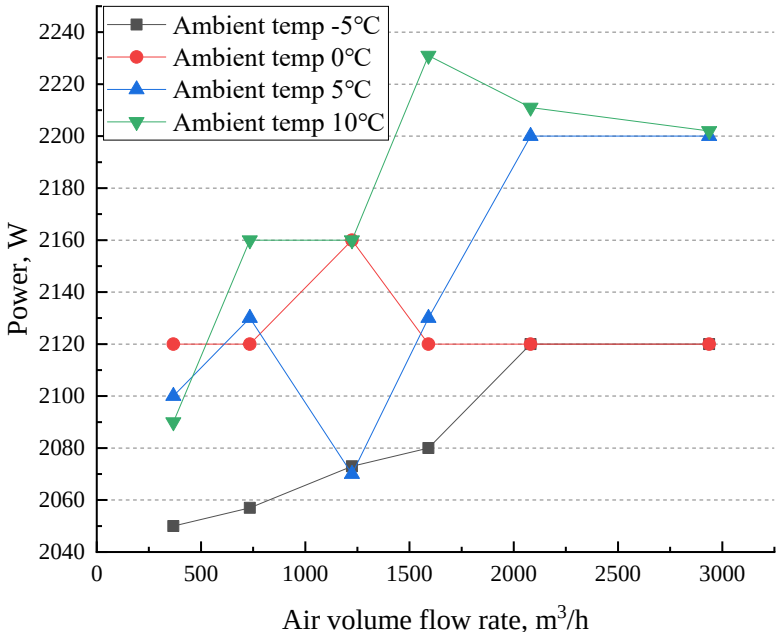

Fig. 5-31 Variation of the power capacity with different exhaust air volume flow rates

Fig. 5-31 shows the variation of the power capacity with the increasing exhaust airflow rate. Unlike the generated heat, the variation of the power capacity of the heat pump has no uniform pattern which is mainly due to the mechanical characteristics of the compressor. However, under different ambient temperatures, the absolute differences of the power capacity are very small, from 10W to 130W. Hence, under different exhaust airflow rates, the generated power is the determining factor for the performance of the heat pump.

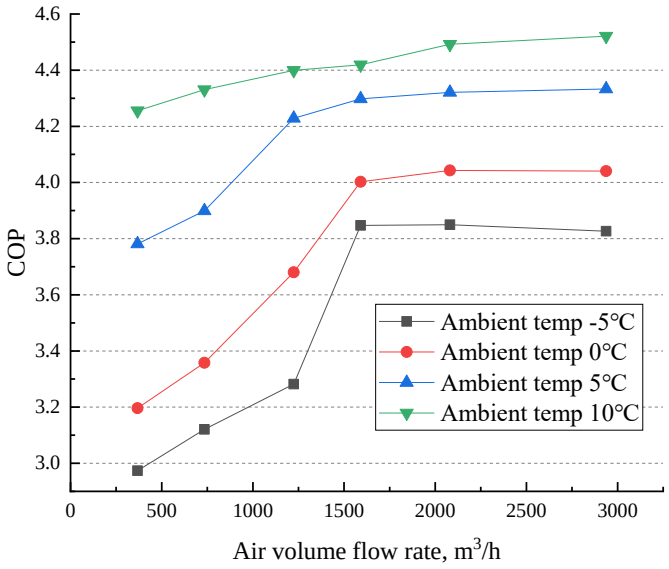

Fig. 5-32 Variation of the COP with different exhaust air volume flow rates

As shown in Fig. 5-32, the variation of COP of the heat pump was similar to that of the generated heat. Under different ambient temperatures, the COP increased with the rise of the airflow rate. Once the exhaust airflow rate reached 1584m^3/h, the increasing trend of the COP slowed down and remained constant. This means that the heat pump can make full use of the heat from the exhaust air when the exhaust airflow rate reaches 1584m^3/h, and the additional spare heat was wasted when the exhaust airflow rate surpassed this level.

Table 5-12 Heat pump circulation parameters along with the variation of the EEV's apertures

Ambient temperature (ºC)	Exhaust air volume flow rate (m^3/h)	Condensing pressure (Mpa)	Condensing temperature (ºC)	Evaporating pressure (Mpa)	Evaporating temperature (ºC)	Vapour injection pressure (Mpa)
-5	367.2	1.838	46.24	0.598	-9.95	0.952
	734.4	1.851	45.41	0.637	-8.09	1.003

	1224	1.869	43.79	0.677	-6.33	1.060
	1591.2	1.919	43.42	0.797	-1.40	1.245
0	367.2	1.868	44.55	0.680	-5.98	1.071
	734.4	1.881	43.70	0.711	-4.67	1.120
	1224	1.917	43.80	0.796	-1.18	1.249
	1591.2	1.968	44.13	0.820	-0.31	1.287
5	367.2	1.920	44.42	0.784	-1.40	1.237
	734.4	1.944	44.16	0.801	-0.68	1.282
	1224	1.978	46.30	0.838	0.66	1.323
	1591.2	2.070	48.60	0.867	1.69	1.368
10	367.2	1.974	47.40	0.867	1.63	1.373
	734.4	2.035	48.14	0.882	2.23	1.429
	1224	2.062	48.26	0.907	3.11	1.437
	1591.2	2.151	50.86	0.937	4.23	1.478

The experimental results for the relevant parameters in the heat pump circuit are shown in Table 5-12. With the increase of the exhaust air volume flow rate, the condensing, evaporating, and vapour injection pressures all increased under different ambient temperatures. However, the condensing and the evaporating temperatures of the heat pump experienced the reverse trends. While the condensing temperature decreased, the evaporating temperature increased gradually.

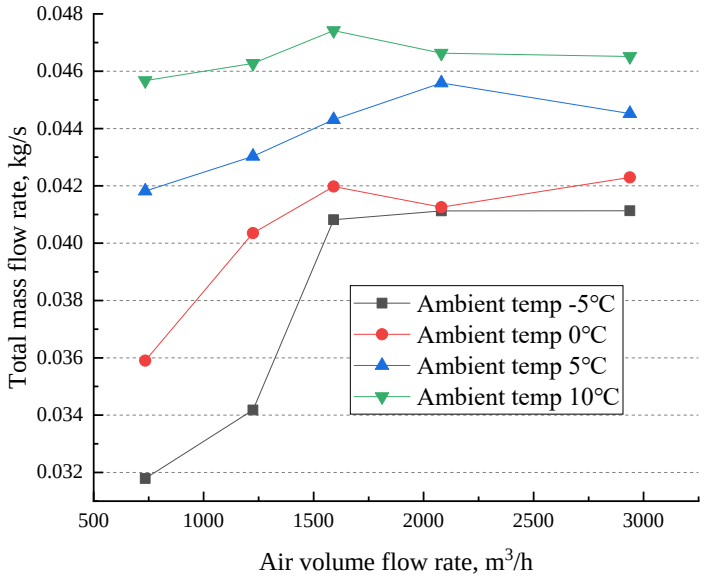

Fig. 5-33 Variation of the total refrigerant mass flow rate with exhaust air volume flow rates

As shown in Fig. 5-33, the variation trend of the total refrigerant mass flow rate was similar to that of the COP and increased with the growth of the exhaust airflow rate up to 1584m^3/h. Once the volume flow rate passed 1584m^3/h, the total refrigerant mass flow rate remained constant. The ambient temperature is another factor influencing the total refrigerant mass flow rate. The lower the ambient temperature, the lower the total refrigerant mass flow rate is. This rule is more obvious when the exhaust airflow rate is low. The difference between the total refrigerant mass flow rates under different ambient temperatures became smaller when the exhaust air volume flow rate increased.

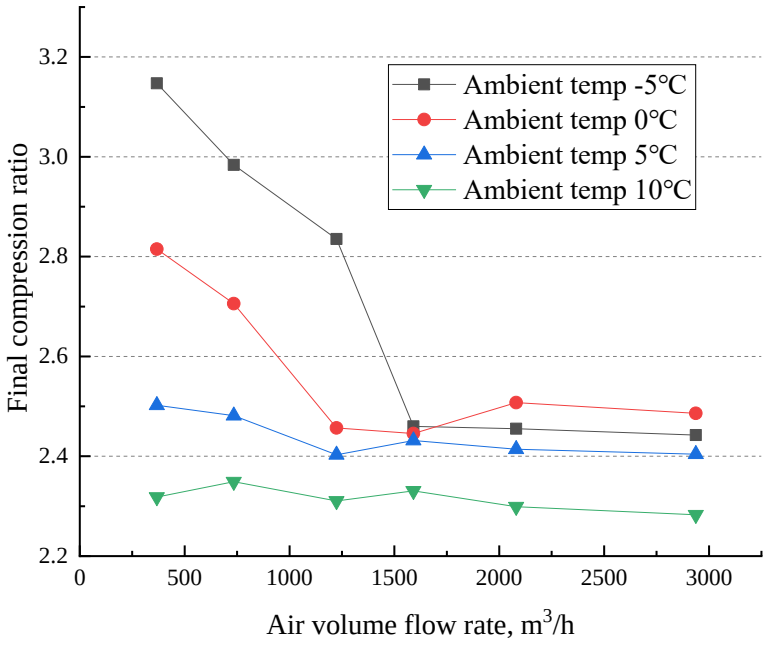

Fig. 5-34 Variation of the final compression ratio with different exhaust air volume flow rates

Fig. 5-34 shows the final compression ratio variation along with the increase of the exhaust air volume flow rate. For ambient temperatures from -5°C to 5°C, it decreased when the exhaust airflow rate increased from 367m^3/h to 1584m^3/h, and the degree of variation for the final compression ratio was more obvious under lower temperatures. After the exhaust air volume flow rate passed 1584m^3/h, the final compression ratio remained constant.

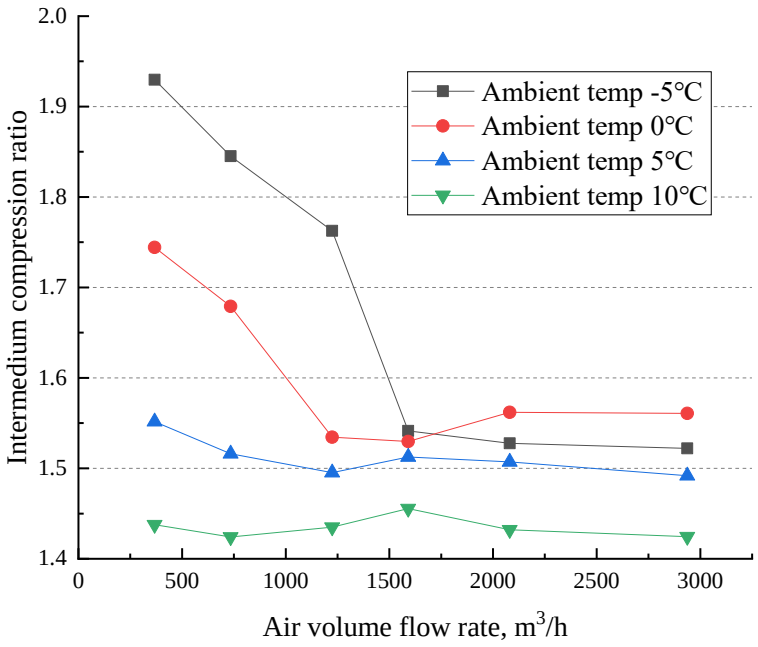

Fig. 5-35 Variation of the intermedium compression ratio with exhaust air volume flow rates

Fig. 5-35 shows that the intermedium compression ratio is similar to the final compression ratio. At ambient temperatures from -5°C to 5°C, it decreased when the exhaust air volume flow rate increased from 367m^3/h to 1584m^3/h and the degree of variation for the final compression ratio was more obvious under lower temperatures. After the exhaust air volume flow rate passed 1584m^3/h, the intermedium compression ratio remained constant.

5.4.1.4 Defrosting process

The quick and efficient defrosting process is another prominent advantage of the proposed VIHR-ASHP. Frost on the evaporator surface can be removed quickly by using exhaust air from the building, during which the heat pump can be turned off and thus reduce the energy consumption of the compressor. Two defrosting processes were spotted on the 16th and 17th of November 2019 under the steady experimental conditions, and are presented in this study. The power capacity variation of the heat pump during the defrosting processes is shown in Fig. 5-36 and Fig. 5-37, respectively.

On the 16th of November, the power capacity dropped to 0W during the defrosting process as the exhaust air extracted from the building was used to defrost the ice. The exhaust air is extracted by a ventilation system with high temperature and then sent to the heat pump evaporators directly to defrost the ice. After 4mins of the defrosting process, the heat pump commenced operation and took 7mins staring time to return working performance gets back to normal. During the heat pump starting time, the power capacity increased to 1800W initially, then it fluctuated from 1800W to 2300W before eventually settling around 2400W. Similar to the defrosting process on the 16th of November, the defrosting process on the 17th of November also experienced defrosting time and heat pump starting time, 4mins and 3mins respectively. The short defrosting time illustrates the efficient and effective performance of the novel VIHR-ASHP in the defrosting process.

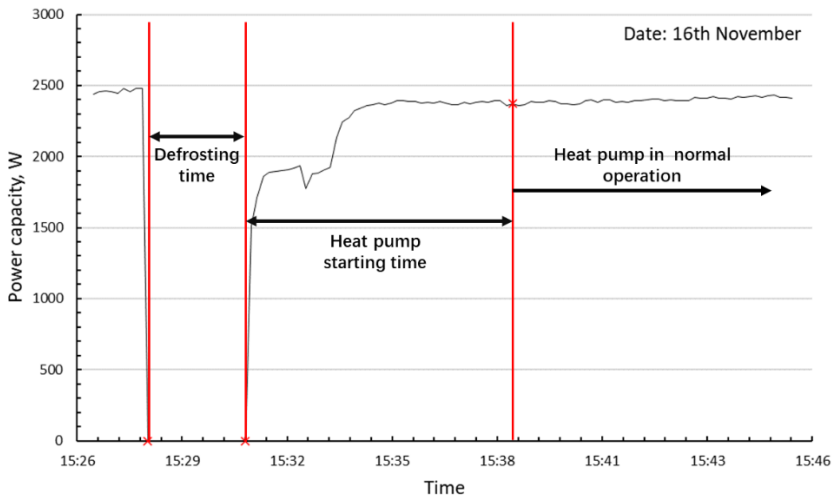

Fig. 5-36 Heat pump power capacity for the defrosting process on the 16th November

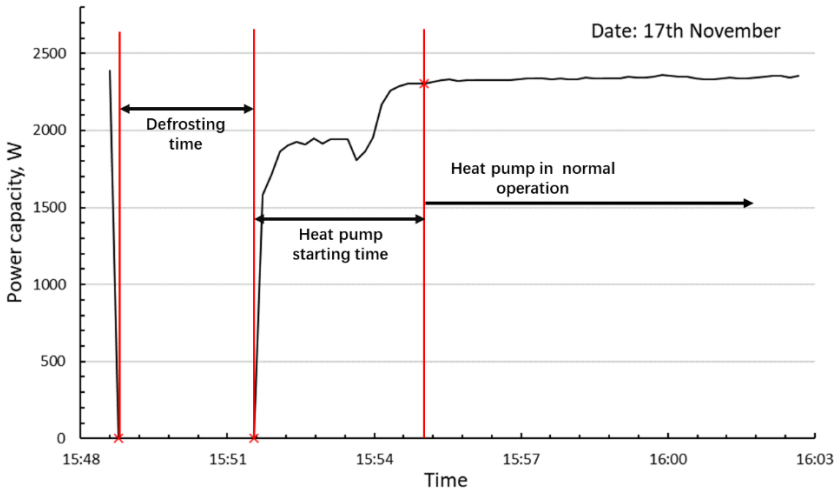

Fig. 5-37 Heat pump power capacity of the defrosting process on the 17th November

The variation of the evaporator temperature and COP during the defrosting processes was also monitored and is presented in Fig. 5-38 and Fig. 5-39. During the defrosting time, the evaporator temperature increased rapidly due to the high temperature of the exhaust air. In order to defrost the ice completely, the minimum defrosting time is 4mins. The compressor will operate when the temperature difference between the evaporator surface and the exhaust air is below 20ºC. On the 16th of November, after the defrosting time, the heat pump restarted and commenced the heat pump starting time. Initially, the evaporator temperature remained at around 4ºC because the compressor had a gradual start, thus leading to a gradual increase of COP. Along with the increasing COP, the evaporator temperature fell to -12ºC due to the low refrigerant mass flow rate. After 15:35, the operational state of the compressor returned to normal gradually. As the COP and the refrigerant mass flow rate increased, the evaporator temperature also increased gradually until it reached -5.5ºC. On the 17th of November, the defrosting process is similar to the defrosting process on the 16th of November, the evaporator temperature increased rapidly during the defrosting time and remained around 5ºC at the beginning of the heat pump starting time. The evaporator temperature then fell with the continuous increase of the COP before becoming

constant as the heat pump returned to normal operation.

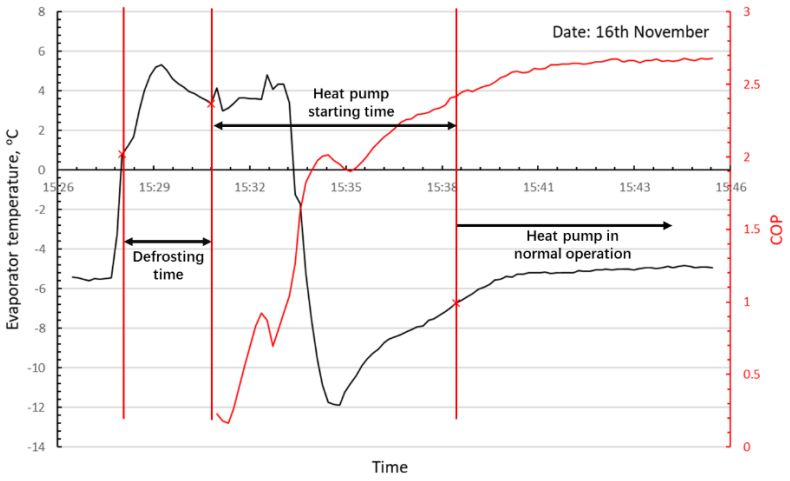

Fig. 5-38 Heat pump evaporator temperature and the COP of the defrosting process on the 16th November

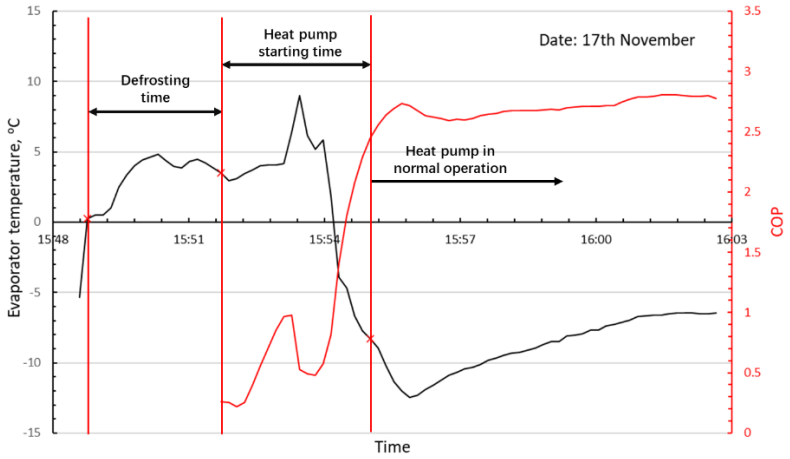

Fig. 5-39 Heat pump evaporator temperature and the COP of the defrosting process on the 17th November

5.4.1.5 Uncertainty analysis of the results

The relative uncertainties of the generated heat (Q_{hp}), the coefficient of performance (COP), the total refrigerant mass flow rate (m_{ref}), the final compression ratio (R_{fcr}), and the intermedium compression ratio (R_{icr}) are determined by using the Pythagorean

summation of discrete uncertainties with a confidence interval of 95% [215]. According to Chapter 4, the uncertainties of the evaluated values are shown in Table 5-13. According to the derived uncertainty values, the results of the evaluated values are satisfactory for this study.

Table 5-13 The uncertainties of the evaluated values

Parameter	Uncertainty
Q_{hp}	0.35%
COP	0.53%
m_{ref}	0.61%
R_{fcr}	0.42%
R_{icr}	0.42%

5.4.2 Mini-channel solar thermal module experiment results

The experimental data of the mini-channel solar thermal module comparison experiment were collected from the systems: (1) the mini-channel solar thermal collector with the novel multiple-throughout-flowing connection method which is shown in Fig. 3-9 (a), and (2) the mini-channel solar thermal collector with the conventional one-to-one connection method which is shown in Fig. 3-9 (b).

Fig. 5-40 and Fig. 5-41 show the variation of the ambient temperature and the solar radiation on the 22nd, 23rd, and 24th respectively. According to the figures, the ambient temperature and solar radiation increased gradually from around 9:30 to 13:30, and decreased from around 13:30 to 16:30 during the three days. However, due to unstable atmospheric flow and intermittent cloud cover, the ambient temperature and the solar radiation experienced unexpected fluctuations, and thus the performances of the HSEUs were influenced by the weather conditions.

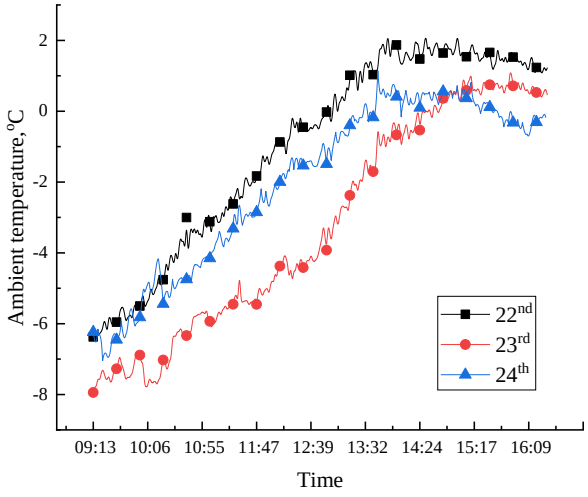

Fig. 5-40 Variation of the ambient temperature on the 22nd, 23rd, and 24th

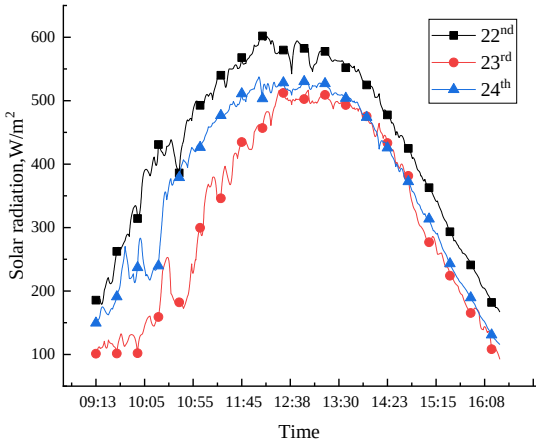

Fig. 5-41 Variation of solar radiation on the 22nd, 23rd, and 24th

The inlet temperature of the two solar collectors arrays during the experimental period on the 22nd, 23rd, and 24th are shown in Fig. 5-42, Fig. 5-43, and Fig. 5-44 separately. As shown in the figures, the inlet temperature of the mini-channel solar thermal collectors array with the novel multiple-throughout-flow connection method is higher than that of the mini-channel solar thermal collectors array with the conventional multiple-throughout-flowing connection method. The variation tendency of two solar collectors arrays is similar. The main reason leads the lower inlet temperature of the conventional solar collectors array is that the lower solar thermal efficiency leads to the lower outlet temperature, and thus, with the same heat exchange condition (the

bottom part of the novel HSEU), the inlet temperature of the conventional solar collectors array became lower. In addition, the immediate temperature drops around 11:00 and the immediate temperature increases around 15:30 is based on the start and the stop of the heat storage process taking place in the novel HSEU. The temperature drops of the conventional solar collectors array were always lag behind the novel one, and the temperature increases of the conventional solar collectors array were ahead of the novel one because the temperature of the conventional solar collectors array is lower which means that it needs more time to heat the lower part of the novel HSEU to the presupposed temperature.

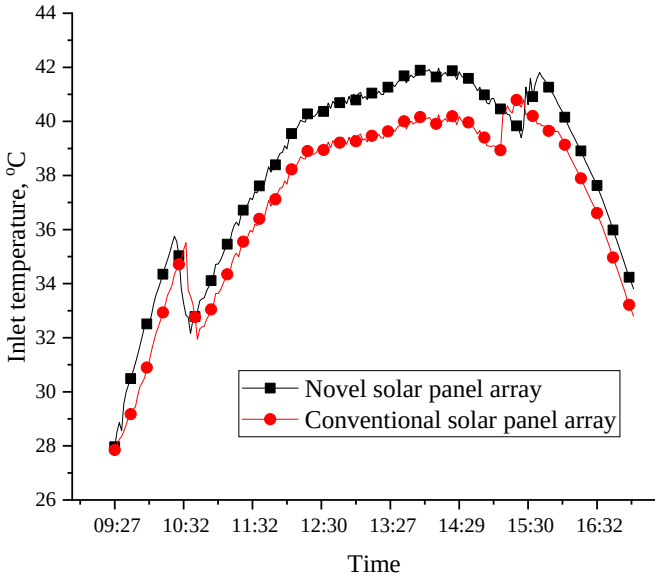

Fig. 5-42 22nd inlet temperature of the solar collectors array

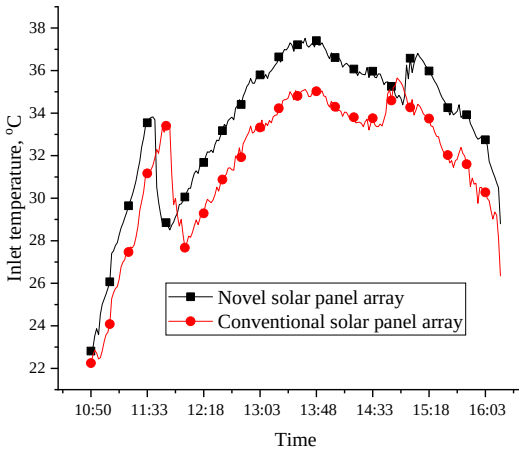

Fig. 5-43 23rd inlet temperature of the solar collectors array

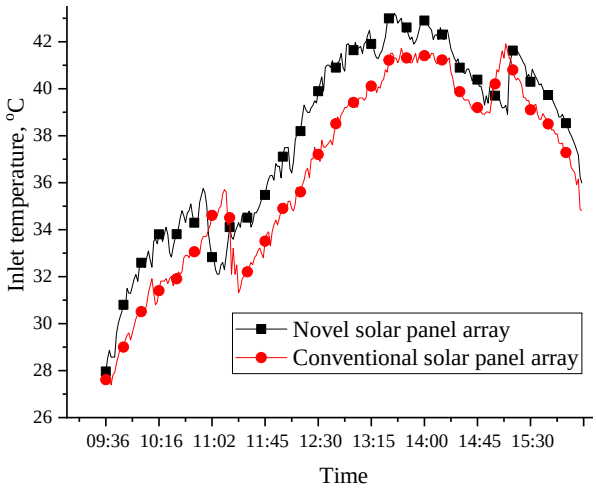

Fig. 5-44 24th inlet temperature of the solar collectors array

The outlet temperature of the two solar collectors arrays during the experimental period on the 22nd, 23rd, and 24th are shown in Fig. 5-45, Fig. 5-46, and Fig. 5-47 separately. The variation tendency was similar to the inlet temperature of the solar collectors arrays. The outlet temperature of the conventional solar collectors array was lower than the novel solar collectors array because the lower solar energy collection capacity of the conventional solar collectors array.

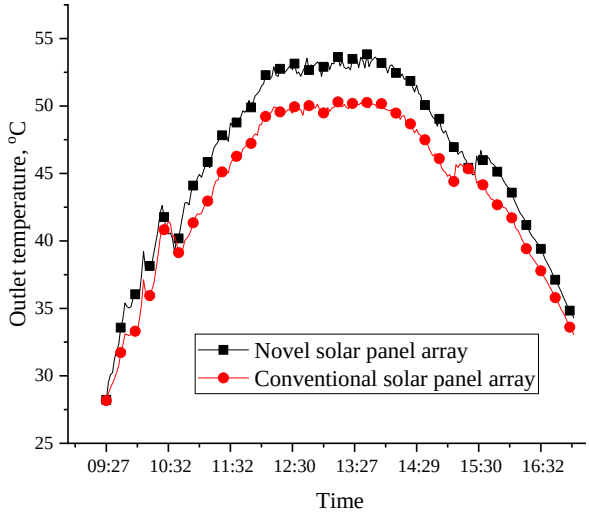

Fig. 5-45 22nd outlet temperature of the solar collectors array

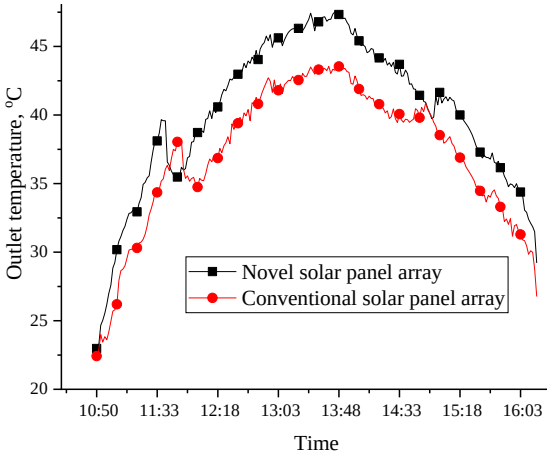

Fig. 5-46 23rd outlet temperature of the solar collectors array

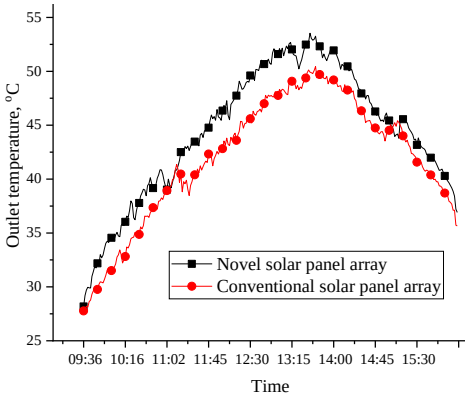

Fig. 5-47 24th outlet temperature of the solar collectors array

The solar thermal efficiency of the two solar collectors arrays during the experimental period on the 22nd, 23rd, and 24th are shown in Fig. 5-48, Fig. 5-49, and Fig. 5-50 separately. The higher solar thermal efficiency also shows the good performance of the novel solar collectors array with multiple-throughout-flowing connection method.

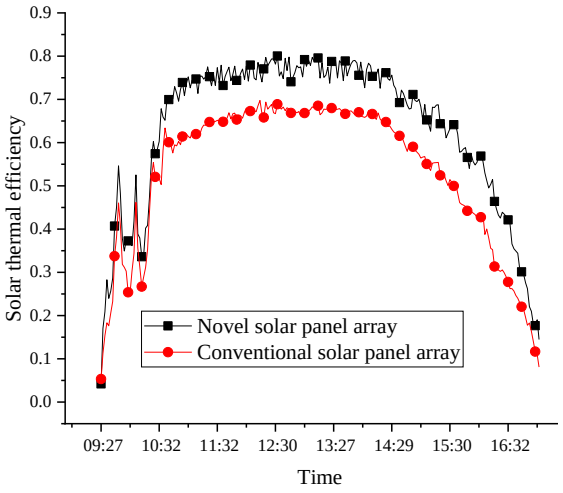

Fig. 5-48 22nd solar thermal efficiency of the solar collectors array

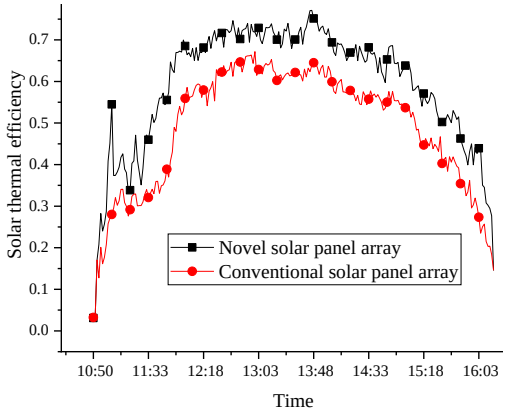

Fig. 5-49 23rd solar thermal efficiency of the solar collectors array

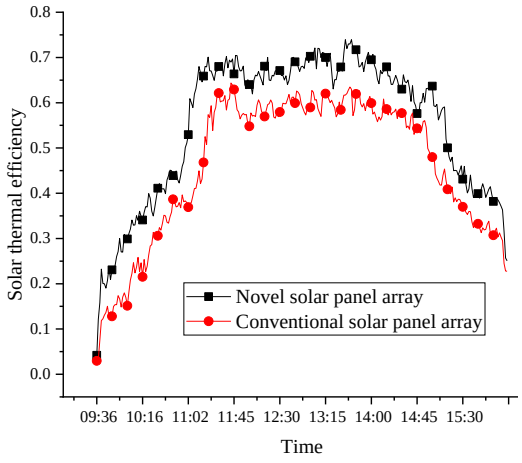

Fig. 5-50 24th solar thermal efficiency of the solar collectors array

5.4.3 HSEU experiment results

To assess the performance of the HSEUs, a comparison between the two systems with new and conventional HSEUs which are shown in Fig. 5-16(a) and Fig. 5-16(c) was undertaken. To enhance the reliability of the assessment, three representative days in December 2017 namely, 22nd, 23rd, and 24th were chosen to perform this analysis.

5.4.3.1 Impact of the HSEUs on the served space temperature

The configuration of the HSEUs directly influences the variation of the temperature in the served space. Fig. 5-51 shows the testing room temperature data recorded from 9:00 to 12:00 on 24th December 2017. Compared to the room with the conventional HSEU, which has a warm-up time of 240 minutes and a temperature rise from 16°C to 19°C, the room with the new HSEU has a shorter warm-up time of 120 minutes for the air temperature to rise to the same level. The faster rise of room temperature can effectively reduce the thermal discomfort to the occupants and thus increase the commercial attractiveness of the solar heating systems.

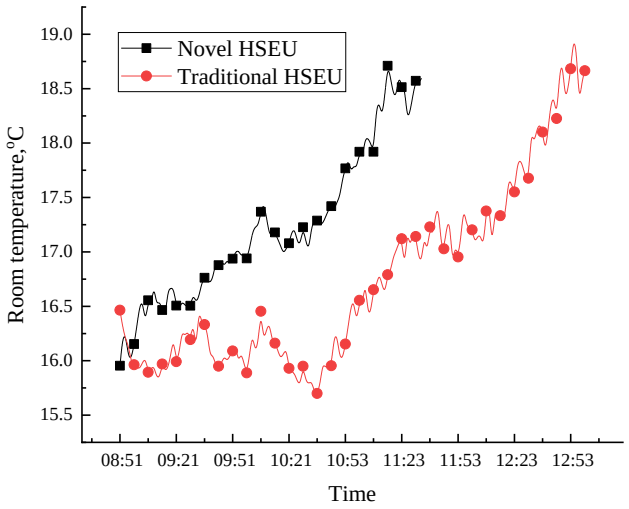

Fig. 5-51 The variation of room temperature for the two HSEUs

5.4.3.2 Comparison of the thermal efficiencies of the solar panel-arrays of the new and conventional systems

The new HSEUs produced a significant difference in the temperature of the fluid at the inlet of the solar panel-array compared to the old HSEU, and consequently led to a considerable difference in solar thermal efficiency. Fig. 5-52, Fig. 5-53, and Fig. 5-54 show the experimental temperature data from the inlet of the solar panel-array with the conventional and new HSEU on 22nd, 23rd, and 24th of December separately. For the system with conventional HSEU, the temperature increased gradually from 29°C to 50°C between 9:30 to 14:30 and then fell to 36°C by 17:00. For the system with the new HSEU, the intermittent operation of the submerged pump enabled the heat charge and discharge processes between the large and small tanks to take place using the dedicated control mechanism. This led to a more frequent variation of the inlet temperature of the solar collectors array, which rose from 28°C to 36°C between 9:30 and 10:30, and fell to 33°C by 10:40. The temperature fall was caused by the starting of the submerged pump. Similarly, the temperature rises from 15:30 to 15:40 was caused by switching off the submerged pump. The inlet temperature of the panel-array can directly influence the outlet temperature and the solar thermal efficiency.

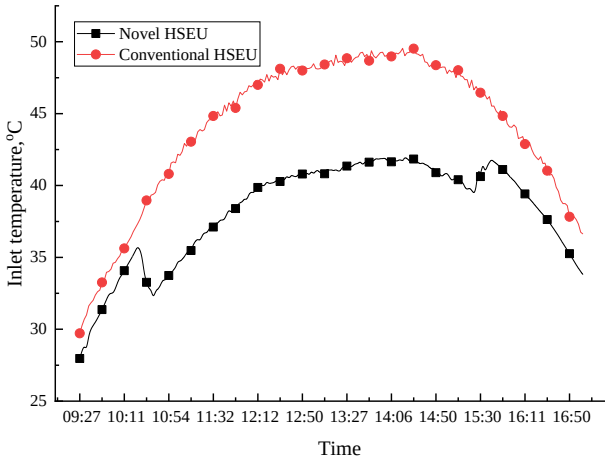

Fig. 5-52 22nd inlet temperature of the solar thermal array

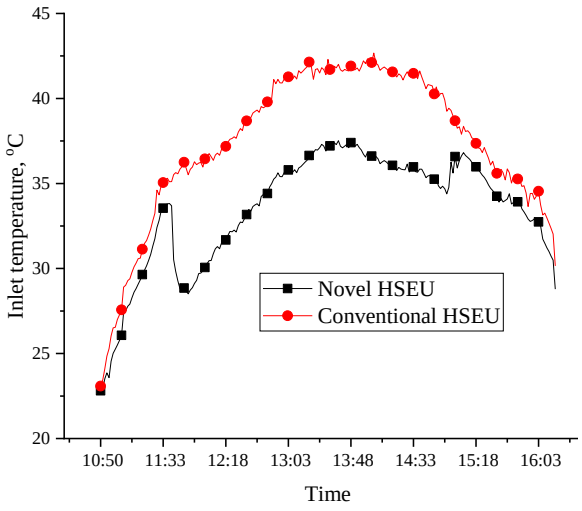

Fig. 5-53 23rd inlet temperature of the solar thermal array

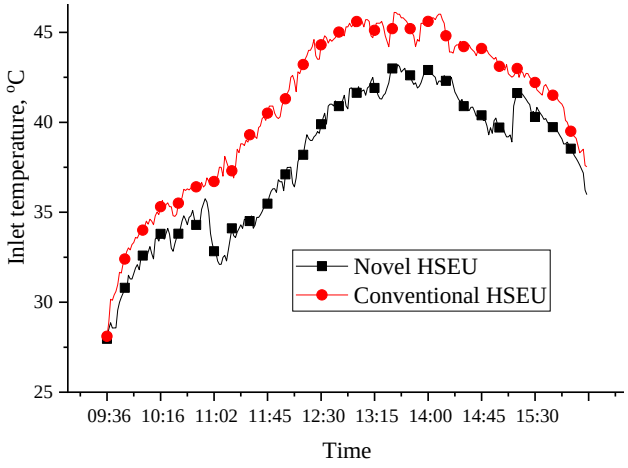

Fig. 5-54 24th inlet temperature of the solar thermal array

Fig. 5-55, Fig. 5-56, and Fig. 5-57 shows the experimental temperature data from the outlet of the solar panel-array on the 22nd, 23rd, and 24th of December separately. For the system with the conventional HSEU, the outlet temperature rose from 30°C to 58°C between 9:30 and 14:30 and fell from 58°C to 38°C between 14:30 and 17:00. For the system with the novel HSEU, the outlet temperature rose from 30°C to 43°C between 9:30 and 10:30, and fell to 40°C from 10:30 to 10:40. The temperature fall in the morning was caused by switching on the submerged pump. Similarly, the temperature rises from 15:30 to 15:40 was caused by switching off the submerged pump. When the submerged pump was on, heat charge and discharge took place involving the mass

exchange between the large and small tanks. A comparison of the two systems indicates that the system with the new HSEU can achieve a more stable outlet temperature from the solar collectors array. Consequently, the temperature of the heating loop can be maintained at a more stable level.

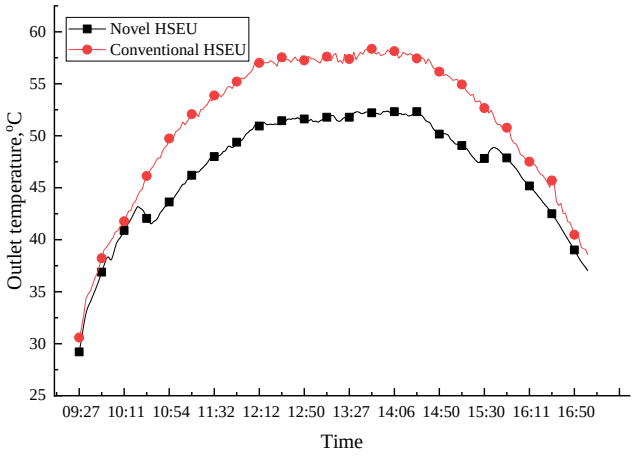

Fig. 5-55 22nd outlet temperature of the solar thermal array

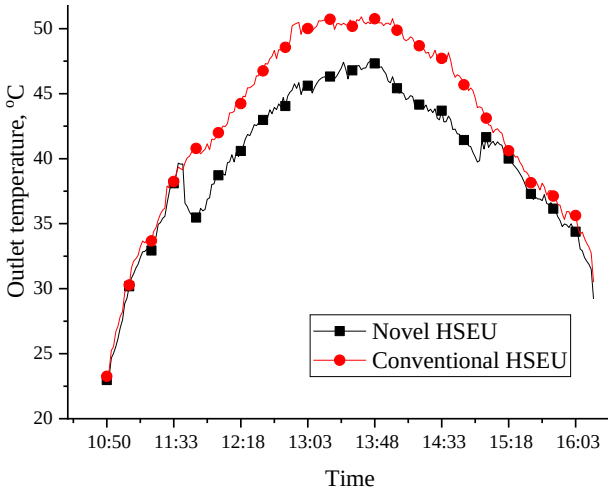

Fig. 5-56 23rd outlet temperature of the solar thermal array

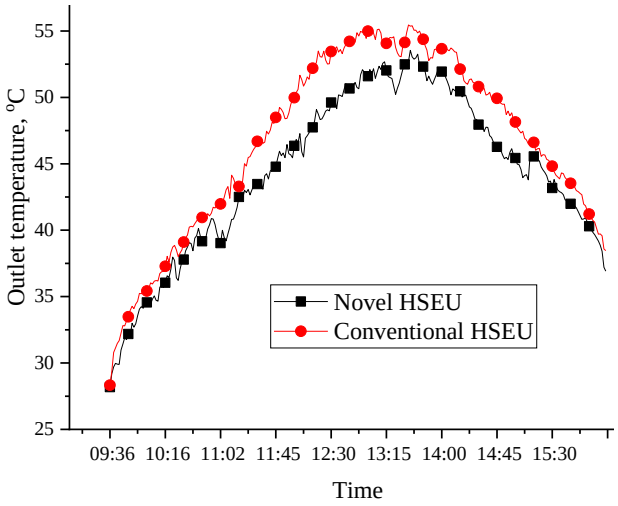

Fig. 5-57 24th outlet temperature of the solar thermal array

Based on instant heat supply and solar radiation measurements, the hourly variation of the solar thermal efficiency of the panel-arrays was calculated and analysed. The results for the novel and traditional HSEU's are shown in Fig. 5-58, Fig. 5-59, and Fig. 5-60 which are on 22nd, 23rd, and 24th of December separately. The system with the new HSEU achieved a higher solar thermal efficiency throughout the daytime operation, relative to the system with the conventional HSEU. The reasons for this are: (1) Enhanced heat transfer coefficient of the new HSEU which resulted in a reduced return temperature for the solar loop fluid, enhancing the solar thermal efficiency of the panel-array; (2) Faster response to space heating and effective heat exchange between the small and large tanks, which resulted in reduced thermal resistance and an increased thermal conversion factor for the HSEU, increasing the solar thermal efficiency of the collectors array. It is shown that during the morning hours between 9:00 and 10:30, both systems had a similar solar efficiency, due to relatively low solar radiation and solar loop fluid temperature, which in turn led to similar heat output to the tank water or heating loop fluid. The solar efficiencies of the two HSEUs remained almost constant from 12:30 to 13:30 and the solar efficiency of the novel HSEU was 14.7% higher than that of the conventional HSEU. During this same period, the average temperatures of the novel HSEU small tank and the conventional tank both equalled 43°C, which means they had the same space heating ability. However, due to

the high convective heat transfer coefficient the novel HSEU was able to reduce the inlet temperature of solar thermal collector-array, thus giving a higher solar thermal efficiency.

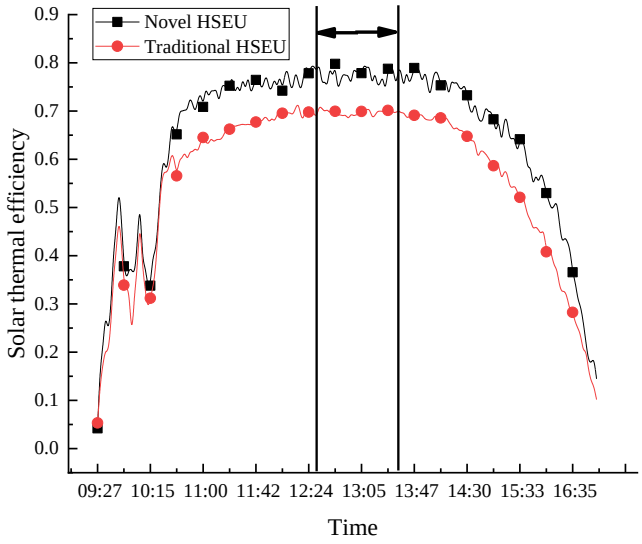

Fig. 5-58 22nd solar thermal efficiency of the solar thermal collector array with different HSEUs

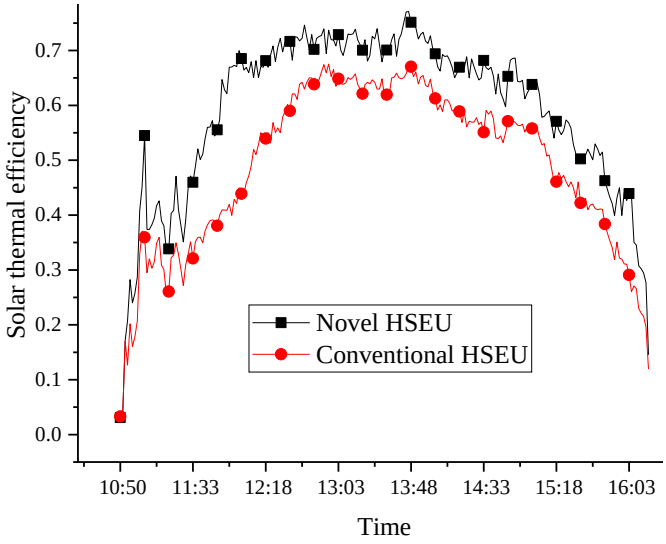

Fig. 5-59 23rd solar thermal efficiency of the solar thermal collector array with different HSEUs

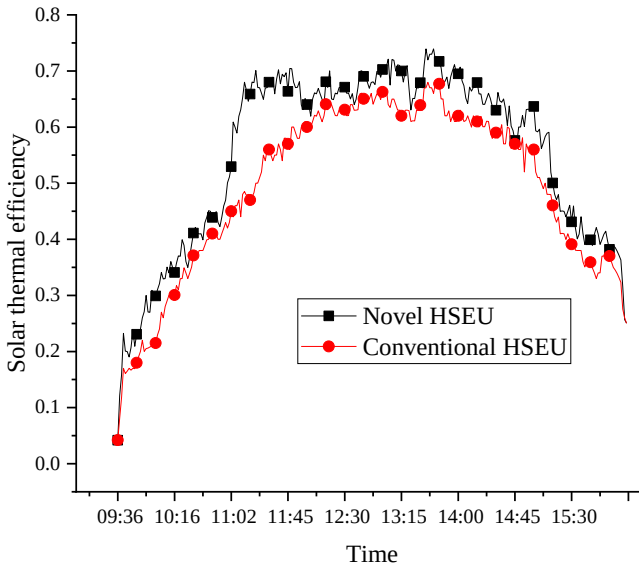

Fig. 5-60 24th solar thermal efficiency of the solar thermal collector array with different HSEUs

5.4.3.3 The heat charge and discharge processes of the new HSEU

During daytime operation, when the heat supply from the solar panel-array is usually larger than the heat demand of the served space, the heat storage process takes place leading to the transfer of heat from the small tank to the large tank. In this case, the sub-merged pump was on from 10:30 to 15:30 which enabled the mass and heat transfer between the small and large tanks, resulting in the rise of temperature for the large tank from 35°C to 48°C. The heat charge process for a typical day is shown in Fig. 5-61. To summarise, a total of 25kWh heat was charged into the large tank (1.5ton capacity) during day-time operation, this amount of heat was then discharged into the small tank during the evening and night, thus enabling an extended heating service time for the served space.

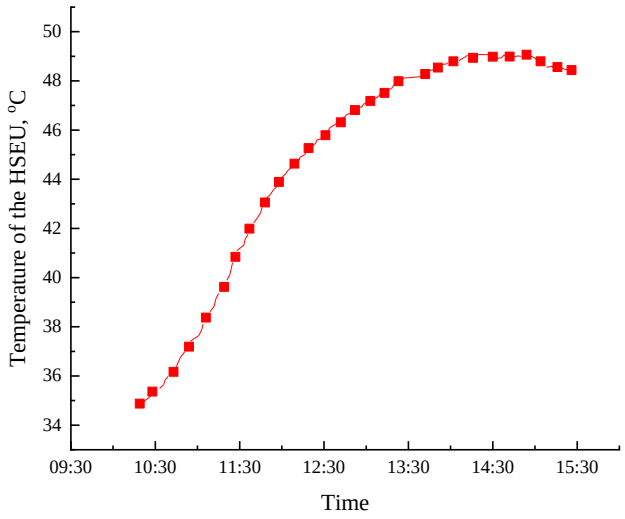

Fig. 5-61 The temperature variation of the heat storage tank

Fig. 5-62 shows the heat discharge process taking place between 16:30 and 03:00 the next day. The large tank experienced a minor temperature fall (from 48°C to 47°C) during the period between 16:30 and 24:00, indicating that a small heat discharge process took place between the large tank and the small tank. During the period between 0:00 and 3:00, the large tank temperature fell from 47°C to 35°C indicating that a significant heat discharge took place. This resulted in a total of 20kWh heat being transferred to the heating loop fluid via the small tank, which enabled an extended heating service time to the served space.

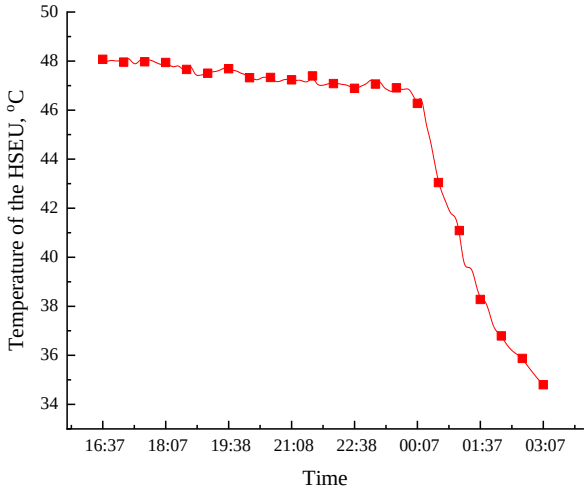

Fig. 5-62 Variation of the temperature of the heat storage tank during the night

5.5 Integral System Experiment

To assess the performance of the integral system, an experimental study of the SAHR-HP system was undertaken on the 27th of December under real-time conditions in Dongguan City, Guangdong Province, China (23.02°N, 113.75°E). The ambient temperature and solar radiation are shown in Fig. 5-63.

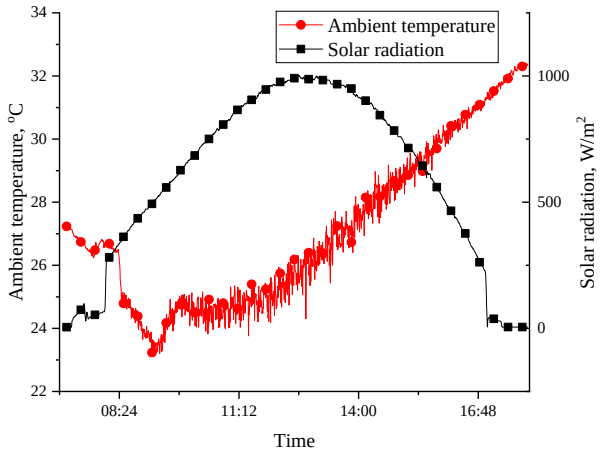

Fig. 5-63 Variation of ambient temperature and solar radiation on the 27th of December

The solar heat collection efficiency of the solar collectors array on the 27th of December is shown in Fig. 5-64. The solar array has an efficiency of about 80%, which is higher than that of a conventional flat plate solar collector operating at the same temperature. The reason for this is that mini-channels can offer a larger contact area with the absorber, leading to lower thermal resistance, and the multiple-throughout-flow connection method gives the solar collectors array a great advantage in integral performance.

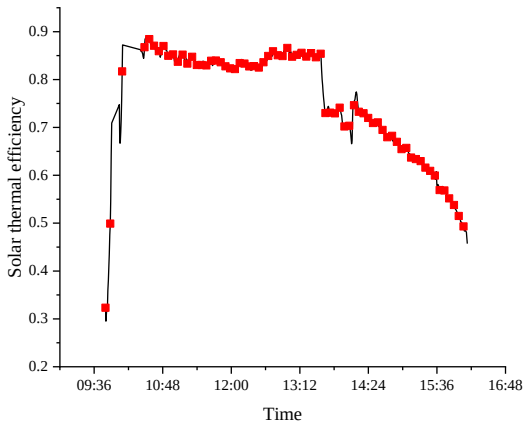

Fig. 5-64 The solar thermal efficiency on the 27th of December

The temperature of water of the upper tank of the novel HSEU is shown in Fig.5-65. This tank was divided into three parts, and the temperature of these different parts increased gradually. Obviously, the temperature decreased as the height of the HSEU decreased.

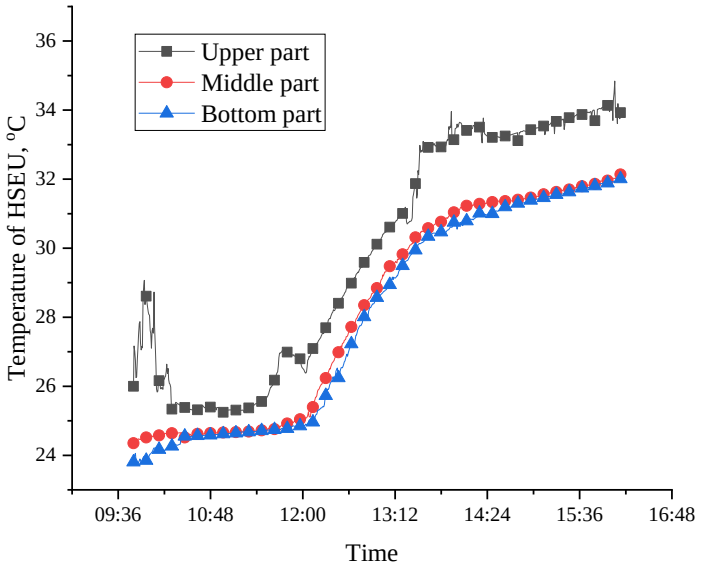

Fig. 5-65 The temperature of different parts of the novel HSEU

Fig. 5-66 shows the temperature variation of the domestic hot water tank. According to the test, the system can heat the water up for domestic use to 60°C within two hours.

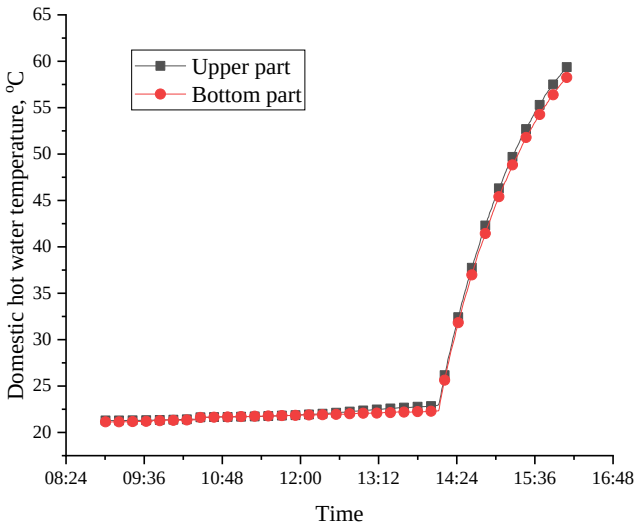

Fig. 5-66 The temperature of different parts of the domestic hot water tank

As shown in Fig. 5-67, there are two heat pump heating processes during the day when solar radiation was not enough. The COP of the heat pump ranges from 3 to 4.5 depending on the operating temperature of the storage tank. The data provided in this quarter is for the outdoor performance at a relatively high ambient temperature, which can represent the summer hot water supply process. The mixed indoor/outdoor air source heat pump is more advantageous under low ambient temperature conditions than when compared to a conventional air source heat pump.

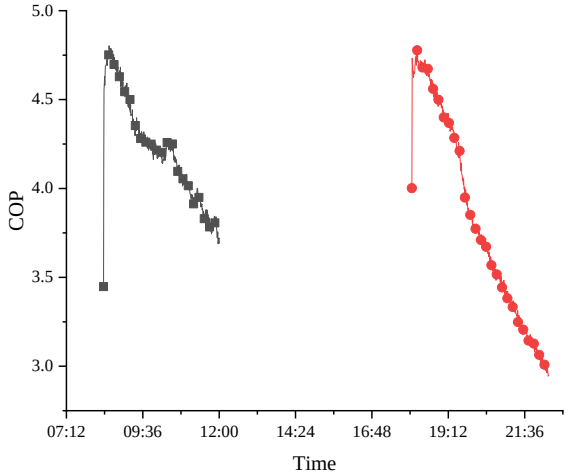

Fig. 5-67 The COP variation of the heat pump on the 27th of December

5.6 Chapter Summary

This chapter introduces the specific process for the fabrication, installation and the testing of the solar assisted heat pump. Furthermore, this chapter also presents and analyses the testing results of the SAHR-HP system and its key parts, i.e., the VIHR-ASHP, the solar collectors array with a multiple-throughout-flow method and the HSEU.

The proposed VIHR-ASHP with two evaporators was tested under steady laboratory conditions. It is the first time that a vapour injection compressor has been applied into a heat recovery heat pump system (HRHPS) in order to improve the performance of the heat pump. The novel VIHR-ASHP can flexibly use either exhaust air or fresh air as the energy sources, thus removing the restrictions introduced by the heating capacity and the limited volume of exhaust air. In addition, the evaporator in the vapour injection line can significantly increase the heat transfer capacity and refrigerant mass flow rate on the intermedium pressure side. This results in a lower final compression ratio, leading to an increased performance for the heat pump. Another advantage of the novel VIHR-ASHP lies in the effective defrosting process, which uses exhaust air to defrost the heat pump and can significantly decrease the defrosting time and energy consumption. A summary of the key findings and conclusions of the study is given below:

1. First, the experiment tested the influence of the refrigerant charging quantity on the performance of the heat pump. The results showed that the COP reached 2.5 when the refrigerant charging quantity reached 2.7kg, as the increased refrigerant mass flow rate directly results in an increased heat transfer capacity for the heat pump. While the refrigerant charging quantity increased further, the COP remained constant, which means that the optimal refrigerant charging quantity is 2.7kg.

2. The experiment also tested the performance of the VIHR-ASHP under different

Electrical Expansion Valve (EEV) apertures. The heat pump cannot operate under a 10% Evaporation Line Aperture (ELA), under which the shortage of the refrigerant in the compressor will trigger the self-protection programme and the heat pump will shut down automatically. When the ELA increased from 15% to 30%, the generated heat and COP of the heat pump increased with a vapour injection line aperture (VILA) ranging from 5% to 10% and then decreased when the VILA ranged from 10% to 30%. When ELA and VILA were under 20% and 10% respectively, the generated heat and the COP of the heat pump peaked at 8.3kW and 3.65kW respectively, and the final compression ratio reached its lowest level. When the heat pump was used under the optimal working conditions, the evaporation temperature on the evaporation line also reached its highest value.

3. Different exhaust air volume flow rates were tested for the VIHR-ASHP. It was found that the heat capacity and the COP increased with an increase in air velocity, and remained constant when the air volume flow rate passed 1584m^3/h. At 1584m^3/h, the refrigerant mass flow rate increased, and the two compression ratios decreased with the increase of the exhaust airflow rate.

4. For the defrosting process, the novel VIHR-ASHP does not use the compressor to perform the reverse-compression cycle, unlike the conventional air-source heat pumps. The exhaust air can perform the defrosting process directly. The result of the experiment was that the defrosting process of the VIHR-ASHP was just four minutes without any power consumption, which is quick and very energy efficient.

The novel multiple-throughout-flowing connection method of the solar collectors array and the novel HSEU are tested under an on-site real-time comparison experiment by comparing the experimental results of three systems. The three systems include: (1) a system with the novel mini-channel solar thermal collectors array connected by the multiple-throughout-following method and the novel stratified HSEU; (2) a system with the novel mini-channel solar thermal collectors array connected by the one-to-

one method and the novel stratified HSEU; (3) a system with the novel mini-channel solar thermal collectors array connected by the multiple-throughout-following method and the conventional HSEU. The results show that:

1. The multiple-throughout-following connection method of the solar thermal collectors array is higher than the conventional one-to-one connection.

2. The interactive double-tank structure enables the novel HSEU based solar energy space heating system to respond to the heat demand of the served space in a faster and more energy efficient way. While a conventional HSEU is much slower at providing heating after sunrise, the system with the new HSEU can provide heating to the served space within approximately twenty minutes of sunrise.

3. The novel HSEU led to an increase in solar thermal efficiency of the panel-array, due to a reduced temperature at the inlet of the solar panel-array. This leads to enhanced heat transfer between the solar loop and the heating loop fluids, and between the small and large water tanks.

4. The capability of the novel HSEU to store the spare heat and maintain the room temperature was also investigated. During the daytime, the temperature of the HSEU increased from 35°C to 48°C, thus storing 25kWh heat within the heat storage water tank. At night-time, when the room temperature reached the lower limit, the HSEU released the stored heat to maintain the room temperature, which indicates that the HSEU can extend the heating service time to the served space.

According to the test results from the integral system test, the solar array has an efficiency of approximately 80%, which is higher than that of a conventional flat plate solar collector operating at the same temperature, and the COP of the heat pump ranges from 3 to 4.5, depending on the operating temperature of the storage tank.

CHAPTER 6: SIMULATION RESULTS DISCUSSION AND MODEL VALIDATION

6.1 Chapter Introduction

In this chapter, the simulation results are presented, thus suggesting the optimised system configuration and operational condition. Further, a comparison between the simulation and experimental results was undertaken, leading to validation/refinement of the established computer models that could be used for the system performance characterisation, simulation, and optimisation. In addition, as a result of the above, the prototype system was proven to have repeatable and reliable performance in real climatic conditions. Such a dedicated dynamic simulation model is thus regarded as being reliable in predicting the annual system performance for the socio-economic analysis in Chapter 7.

6.2 Model Validation

6.2.1 VIHR-ASHP model validation

The performance of the demonstrative VIHR-ASHP system can be simulated by using the model developed in Chpater.4. To validate the mathematical model of the VIHR-ASHP, the simulation results are compared with the experimental data. Some assumptions are made: (1) minimum temperature difference of 5°C for heat transfer in the evaporation line (EL) and vapour injection line (VIL) evaporators, condenser and internal heat exchanger, (2) air temperature drop of 5°C for the EL evaporator of the VIHR-ASHP, (3) exhaust air flow rate of 1.0 kg/s, (4) refrigerant of R410a. The fan power is not included and the pressure drop of refrigerant in the heat exchangers is neglected. The computer model and the experiment of the VIHR-ASHP are under steady operational conditions. The experiment and simulation conditions are shown in

Table. 6-1.

Table 6-1 Parameter for experiment and simulation of the VIHR-ASHP

EEV aperture of the vapour injection line	10%
EEV aperture of the evaporation line	20%
Exhaust air temperature (°C)	28
Condenser inlet temperature (°C)	20

According to the given test and simulation conditions, the results can be compared with each other. The variation of the COP and heat production of the VIHR-ASHP along with the ambient temperature is shown in Fig. 6-1 and Fig. 6-2 separately.

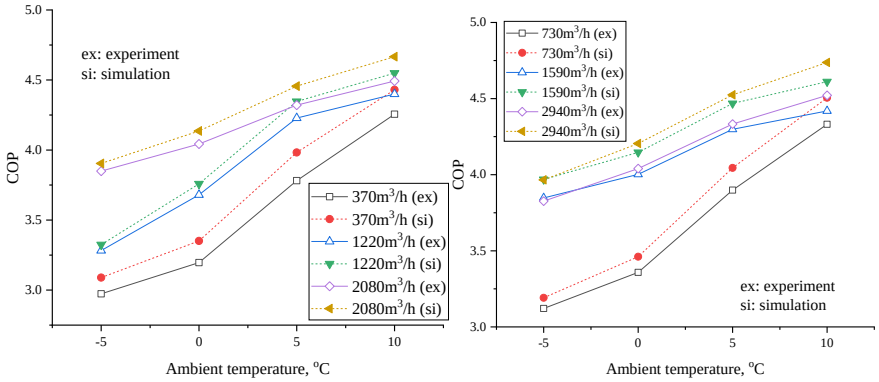

Fig. 6-1 Variation of the COP with respect to the ambient temperature

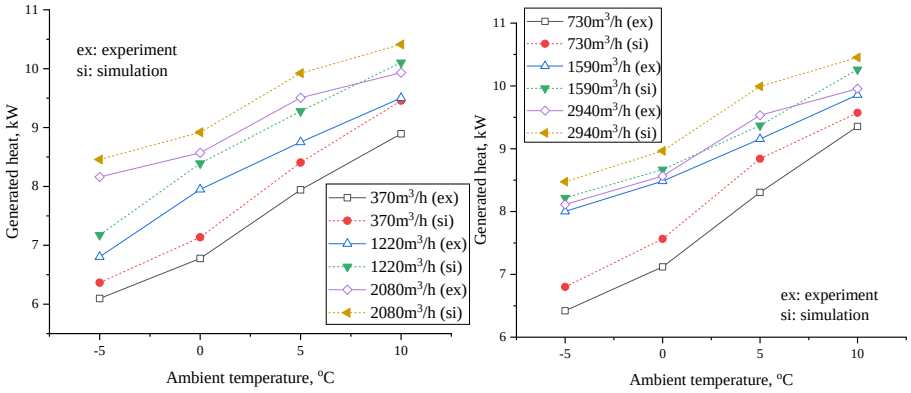

Fig. 6-2 Variation of the heat production with respect to the ambient temperature

Comparing the experimental data of the demonstrative VIHR-ASHP under different ambient temperatures, the simulation results are in close agreement with the experimental results, with the deviation between results of less than 6.2%. The deviation is mainly caused by the performance decrease of the heat pump under the practical operation. As a result, the proposed numerical module in Chpater.4 can accurately predict the performance of VIHR-ASHP.

6.2.2 Mini-channel solar thermal collectors array model validation

6.2.2.1 Solar efficiency against $(T_{in} - T_a)/I$

Based on the experimental data of the two parallel systems, a variation of the solar efficiencies of the panels-arrays against $(T_{in} - T_a)/I$ were established and these are depicted in Figs. 6-3 and Figs. 6-4 respectively. Meanwhile, the above-established model will be run on the basis of the variation of $(T_{in} - T_a)/I$, which will be made by keeping the T_{in} and T_a unchanged (i.e., 25°C and 5°C) and varying solar radiation from 100W/m^2 to 600W/m^2. The range of the solar radiation is derived from the practical experiment. Pulling together both the modelling and experimental data in the same Figures (Figs. 6-3 for the multiple-throughout-flowing mode and Figs. 6-4 for the one-to-one-connection mode) indicates that both experimental results and

modelling data have good agreement with each other, with a derivation ratio in the range 0.1% to 10%.

Comparison between Figs. 6-3 and Figs. 6-4 indicates that under the same value of $(T_{in} - T_a)/I$, the overall solar thermal efficiency of the multiple-throughout-flowing panels-array is higher than that of the one-to-one-connection panels-array, with the increase rate in the range of 0.5% to 10%. This further approves the advantage of the multiple-throughout-flowing type panels-array.

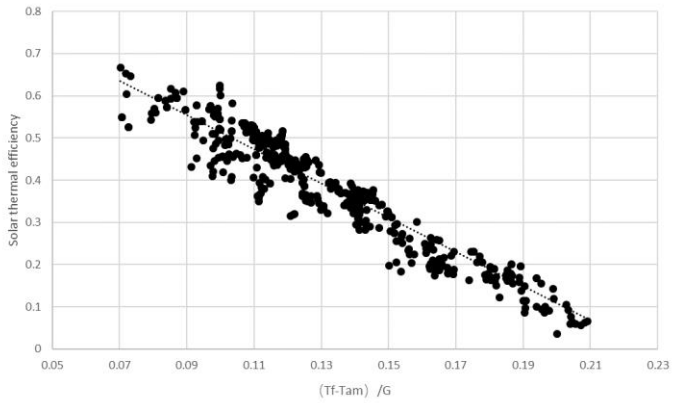

Fig. 6-3 Solar efficiency against $(T_{in} - T_a)/I$ for the multiple-throughout-connecting type

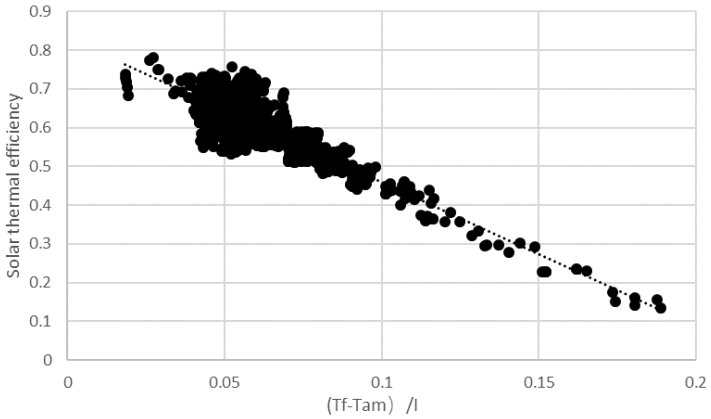

Fig. 6-4 Solar efficiency against $(T_{in} - T_a)/I$ for the one-to-one-connection flowing type

6.2.2.2 EER against $(T_{in} - T_a)/I$

Based on the experimental data of the two parallel systems, the variation of the Energy Efficiency Ratios of the panels-arrays against $(T_{in} - T_a)/I$ can also be established and these are depicted in Figs. 6-5 and Figs. 6-6 respectively. Meanwhile, the above-established model will run on the basis of the variation of $(T_{in} - T_a)/I$, which will be made by keeping the T_{in} and T_a unchanged (i.e., 25°C and 5°C) and varying solar radiation from 100 W/m^2 to 600 W/m^2. Pulling together both the modelling and experimental data in the same figures (Figs. 6-5 referring to the multiple-throughout-flowing mode and Figs. 6-6 to the one-to-one-connection mode) indicates that both experimental results and modelling data have good agreement with each other, with derivation ratio in the range 0.1% to 10%.

Comparison between Figs. 6-5 and Figs. 6-6 indicate that under the same value of (T_{in} – T_a)/I, the overall Energy Efficiency Ratio of the multiple-throughout-flowing panels-array is significantly higher than that of the one-to-one-connection panels-array, with the increase rate in the range 62% to 68%. This indicates that the multiple-throughout-flowing type is superior to the traditional one-to-one-connection type.

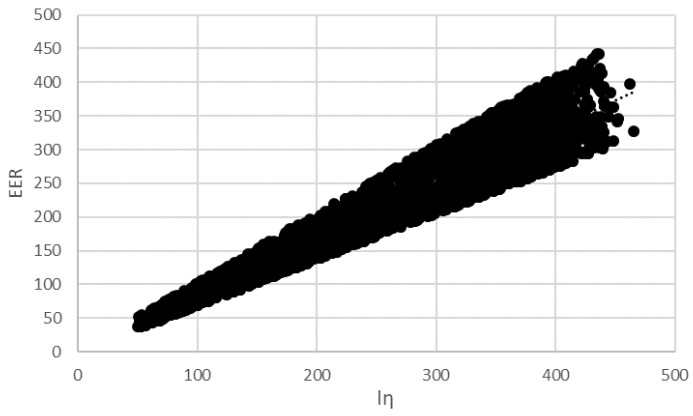

Fig. 6-5 EER against $I\eta$ for multiple-throughout-connecting type

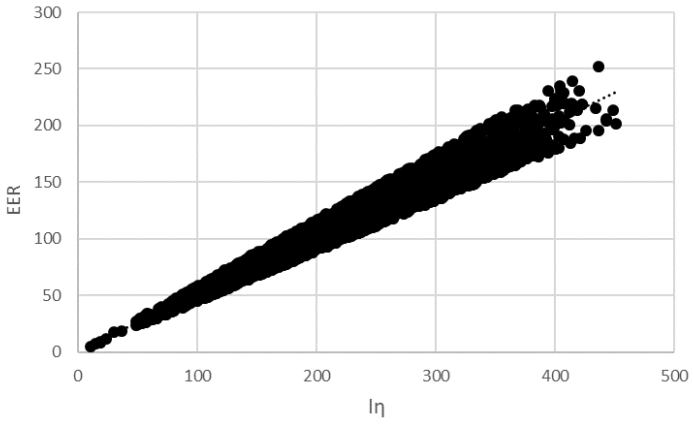

Fig. 6-6 EER against $I\eta$ for one-to-one connecting type

6.2.2.3 Temperature variation across the panels-arrays

To facilitate the comparison between the modelling and experimental results, the measurement data for a selected single winter day (i.e., 24th December 2017) were extracted. These data, including those for the fluid's inlet temperature, ambient temperature, air velocity, fluid flow rate, were further divided into three groups according to the relevant time zones, i.e., 9:00 to 12:00, 12:00 to 15:00, and 15:00 to 18:00. For each time zone, the data for each single parameter were averaged, thus giving the average value of this parameter which forms the foundation of the consequent parallel simulation.

The average data of the temperature of the working fluid of each panel as three different time zones are depicted in Figs. 6-7 and Figs. 6-8 respectively which refer to the multiple-throughout-flowing and one-to-one-connection modes. Meanwhile, the above-established model was run based on the average data for an inlet temperature and flow rate of the fluid, as well as ambient temperature. This gave the average data of the fluid temperature at the outlet of each panel. Pulling together the modelling and experimental data together in the same Figures (Figs. 6-7 referring to the multiple-throughout-flowing mode and Figs. 6-8 to the one-to-one-connection mode) gives a good comparable image for both the experimental results and modelling data; this

indicates that a good agreement was achieved between the both, with derivation ratio in the range 0.3% to 8.1%.

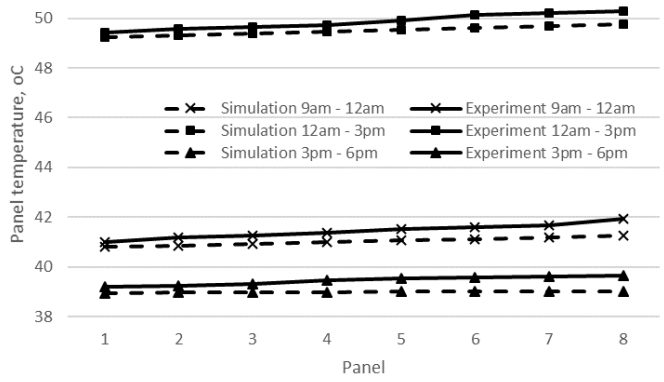

Fig. 6-7 The average temperature of the working fluid of each panel at three different time zones for the multiple-throughout-flowing type

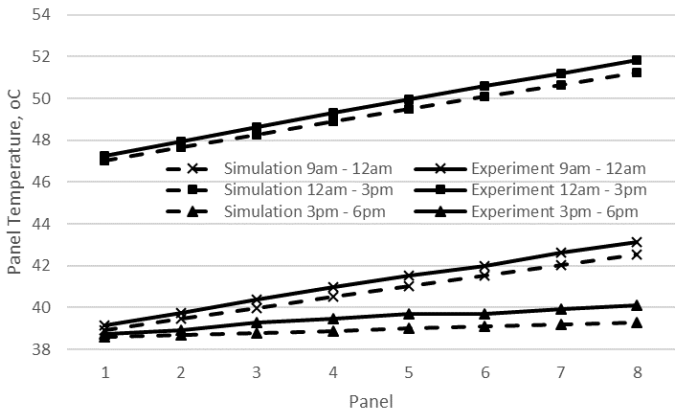

Fig. 6-8 The average temperature of the working fluid of each panel at three different time zones for the one-to-one connecting type

Comparison between Figs. 6-7 and Figs. 6-8 indicates that under the same operational condition (i.e., same flow rate and inlet temperature and ambient temperature), the temperature of the working fluid at the outlet of the rear panel is lower for the multiple-throughout-flowing panels-array compared to the one-to-one-connection type, with a

difference in the range 0.6% to 3%. The temperature difference between the head and rear panels in the multiple-throughout-flowing model is lower than that in the one-to-one-connection mode. This indicates the multiple-throughout-flowing type can effectively reduce the temperature of the rear panel in an array compared to the one-to-one-connection array. It can also effectively lower the temperature difference between the head and read panels in an array, thus improving the overall thermal efficiency of the array.

6.2.2.4 The solar thermal efficiency of the different panels for two types of arrays

Similarly, the experimental solar thermal efficiency of the individual panels under three different time zones was depicted in Figs. 6-9 and Figs. 6-10 respectively, which are for the multiple-throughout-flowing and one-to-one-connection modes respectively. Meanwhile, the above-established model was run based on the average data for the inlet temperature and flow rate of the fluid, as well as ambient temperature. This gave the solar thermal efficiency data of the panels in two different arrays. Pulling together both the modelling and experimental data in the same figures gives a good comparable image of both the experimental results and modelling data, indicating that a good agreement was achieved between the both, with a derivation ratio in the range 1% to 9%.

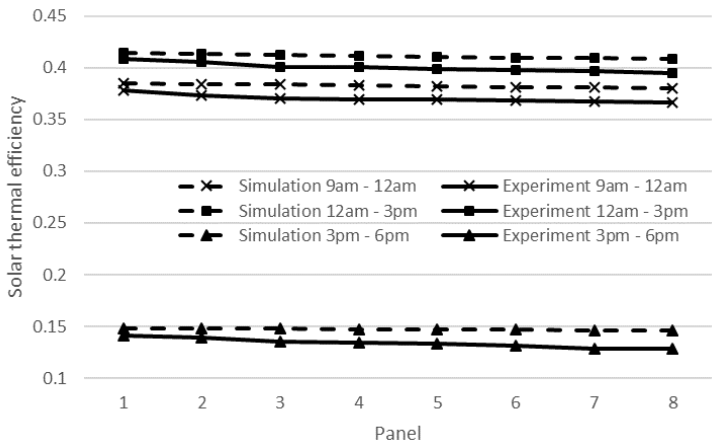

Fig. 6-9 The solar thermal efficiency of the individual panels under three different time zones for the multiple-throughout-flowing type

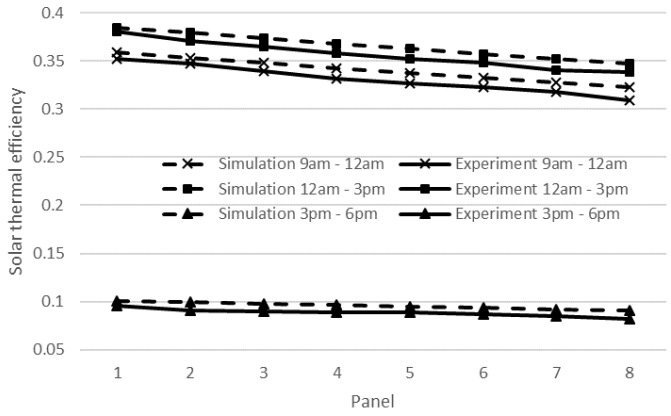

Fig. 6-10 The solar thermal efficiency of the individual panels under three different time zones for the one-to-one connecting type

Comparison between Figs. 6-9 and Figs. 6-10 indicates that for the multiple-throughout-flowing mode, the solar thermal efficiency of the head panel is somehow lower than that of the one-to-one-connection mode. However, the solar thermal efficiency of the rear panel is higher than that of the one-to-one-connection mode. As a result, the overall solar thermal efficiency of the multiple-throughout-flowing array is higher than that of the one-to-one-connection array, with the increasing ratio of around 5%. This indicates that the multiple-throughout-flowing mode is an effective measure of increasing solar thermal efficiency of the panels-array, compared to the

one-to-one-connection mode. Between 3pm to 6pm, the low solar radiation directly results the low solar thermal efficiency of the solar thermal collector array which leads to a small temperature difference between collectors. Hence, the collector array represents a steady solar thermal efficiency.

Based on the above validated computerized model and experimental conditions, further simulation and optimization were carried out to determine the best geometrical set-up and operational conditions. This involves the determination of the best panel number, piping turning number, as well as the appropriate velocity of the fluid flow.

6.2.3 HSEU model validation

The simulations were run using the exact same conditions as the experiments in order to enable a comparison of key performance parameters of the system. Such comparison allows the calibration of computer models and provides solid grounds for drawing conclusions from the system performance. The simulation and experimental results were also compared to each other in order to investigate the operational performance of the new HSEU against the conventional one. The following sections provide details of the calibration and comparison work carried out.

6.2.3.1 Start-up time of the systems with the new and conventional HSEUs

Fig. 6-11 to Fig. 6-13 present theoretical and experimental average temperature variations of the water tanks for each system. As seen in the figures, experimental and simulation results are in close agreement, with just small deviations ranging from 0.1% to 5%. Since the simulation did not take into account the heat loss and thermal inertia of the HSEU, this means that the experimental temperature of the HSEUs is slightly lower than that of the simulation data. Additionally, Fig. 6-11, Fig. 6-12 and Fig. 6-13 present a rapid water temperature escalation in the new HSEU, giving a 35 minutes time span for the temperature rise while the conventional HSEU has a time span of 175 minutes for a similar temperature rise. This shows that the new HSEU has a much

faster temperature response compared to the traditional HSEU, which significantly reduces the period that heating is unavailable. Such a fast response will mitigate the possible thermal discomfort of occupants and increase the marketability of heat pump system.

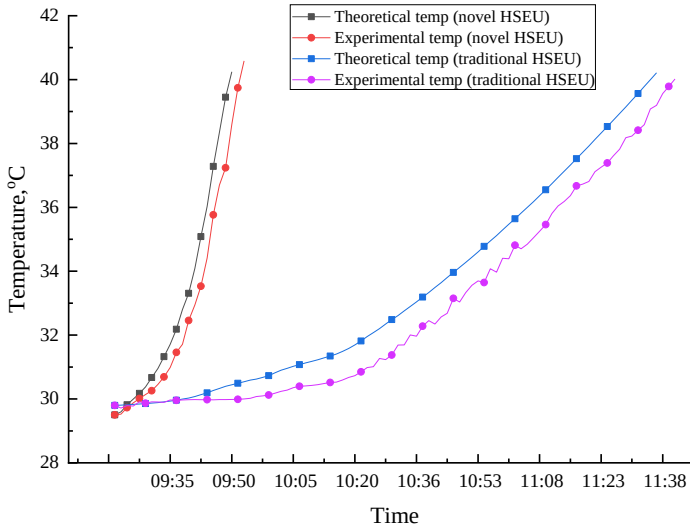

Fig. 6-11 Variation of the water temperature in the HSEUs 22nd Dec

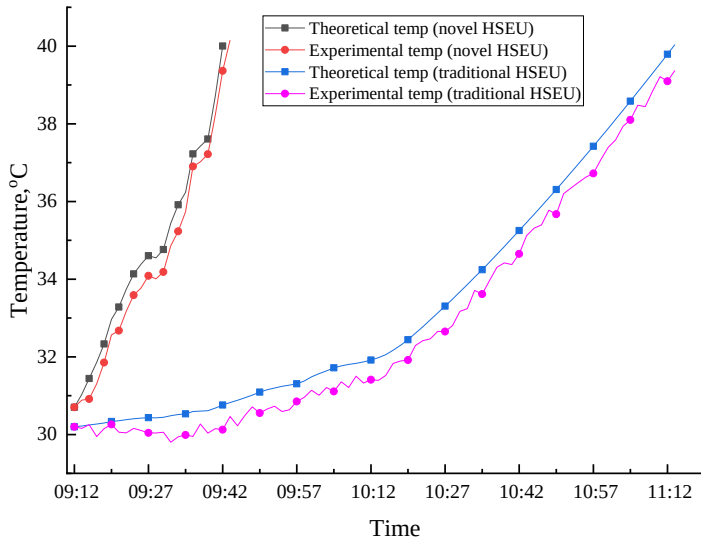

Fig. 6-12 The variation of temperature of the HSEUs 23rd Dec

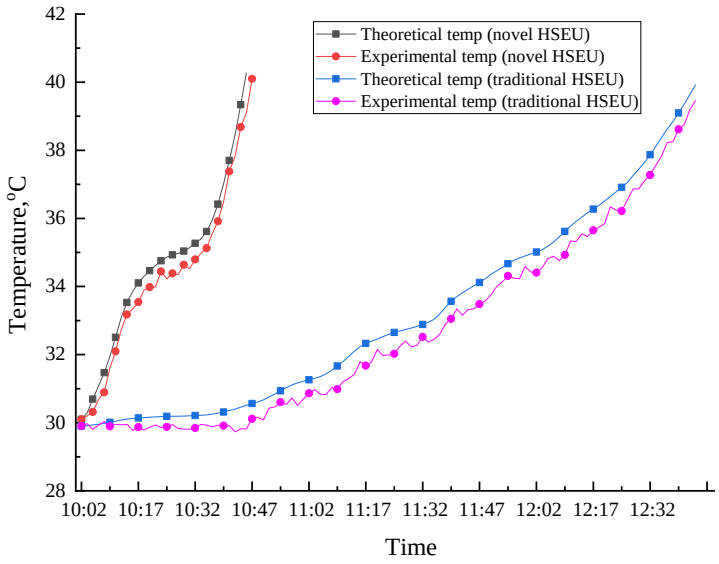

Fig. 6-13 The variation of temperature of the HSEUs 24th Dec

6.2.3.2 Comparison of the heat exchange efficiency of the HSEUs

Fig. 6-14 shows the variation of the heat exchange efficiency against $\Delta T_m/\Delta T_{max}$ for the new HSEU. Comparing the modelling and experimental heat transfer efficiencies, it was found that both the experimental and modelling data agreed closely, giving deviations of 0.1% to 10%.

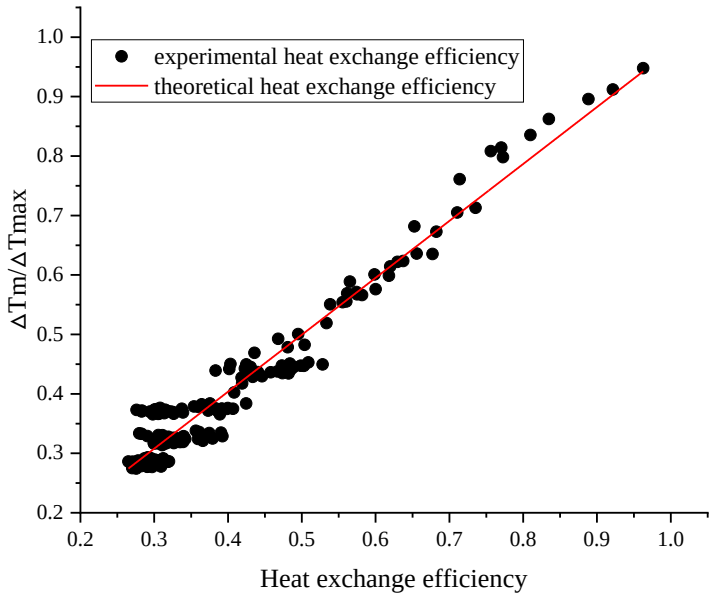

Fig. 6-14 The heat transfer efficiency of the novel HSEU

Fig. 6-15 shows the variation of the heat exchange efficiency against $\Delta T_m/\Delta T_{max}$ for the conventional HSEU. Comparing the modelling and experimental heat transfer efficiencies, the deviations were found to range from 0.1% to 10%, indicating a good agreement between the experimental and modelling data.

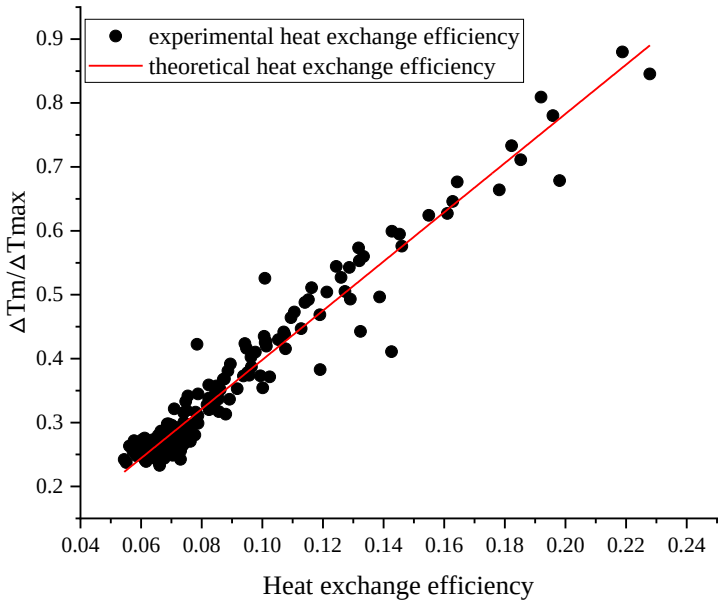

Fig. 6-15 The heat transfer efficiency of the conventional HSEU

The data comparison shown in Figs. 6-14 and Figs. 6-15 shows that the new HSEU has a much higher heat transfer efficiency than the conventional HSEU, by up to 70%. This increased efficiency was achieved by two factors: (1) confined tank space and (2) formation of the counter-flow between the solar loop fluid and the heating loop fluid, which led to the increased convective heat transfer between the tank water and the coil wall.

6.3 Deviation Analysis

The deviation between the experimental and simulative data from the investigation of the SAHR-HP system is mainly caused by the performance decrease of the heat pump under the practical operation. When the heat pump is under operation, the voltage fluctuation and the practical refrigerant compression process will significantly

decrease the performance of the VI compressor. In addition, along with the operation of the heat pump, the frost on the evaporator will also reduce the heat transfer capacity of the heat pump considerably. Hence, the practical operation of the heat pump will lower than the simulation results.

The deviation of the mini-channel solar thermal collector array investigation is mainly come from the assumption of the numerical model. The assumption stressed that the mass flow rate of the working fluid in the mini-channel tube is constant and stable. However, in the actual situation, every mini-channel tube may have different flow resistance according to the practical production process which increases the irreversible loss, thus leading the lower solar thermal efficiency under the practical experiment than the simulation results.

For the investigation of the novel HSEU, the deviation between the experimental and simulative results mainly comes from the mix effect in the upper heat storage part of the HSEU and the heat transfer between the bottom part and upper part under the bottom part heating supply status of the HSEU. These two factors will both cause the irreversible loss, thus leading the lower temperature increment of the HSEU.

6.4 Simulation Results

6.4.1 VIHR-ASHP results

In this simulation, the influences of the ambient temperature, condensation temperature, vapour injection temperature and mass flow ratio of ambient air to exhaust air on the performance of the novel VIHR-ASHP are analysed. A comparison with a conventional vapour injection heat pump (VIHP) and air source heat pump (ASHP) are implemented. For the assumed exhaust air flow rate of 1.0 kg/s, the value might be larger than that of a common residential house. Notably, the proposed system is also applicable in public buildings, such as hospitals, libraries, offices and schools where the heating demand is large. A flow rate of 1.0 kg/s can be reasonable.

6.4.1.1 Influences of ambient temperature

A comparison among the COPs for the innovative VIHR-ASHP, convectional VIHP and ASHP is presented in Fig. 6-16 at variable ambient temperature. The condensation temperature for all the heat pumps is 45°C. For the VIHR-ASHP, the air flow rate of ambient air and the vapor inject temperature (T_2) are 6 kg/s and 5°C. The COP of the VIHR-ASHP ranges from about 3.72 to 4.16 when the ambient temperature increases from -10 to 0°C, and it is 3.34 to 3.88 for the VIHP and 3.02 to 3.61 for the ASHP. It is obvious that the innovative heat pump has a higher COP and the advantage is more remarkable at a lower ambient temperature. For example, the relative COP increment over that of the VIHP and ASHP is 11.3% and 23.3% respectively at -10°C. Two reasons can be given for the higher cop: first, the VIHR-ASHP has a larger vapor injection ratio than the conventional VIHP. The mass flow ratio of the injected to the un-injected refrigerant at -5°C is 79.23% for the VIHR-VIHP, which is about twice that of the VIHP (39.89%). The VIHR-ASHP can be deemed as a combination of a VIHP using ambient air as the heat source and an ASHP using exhaust air as the heat source. It has a higher equivalent temperature in the vaporisation process than the VIHP due to the heat input from the exhaust air. Second, the exhaust air leaving the evaporator in the vapour injection line still has a higher temperature than the ambient air. The mixture elevates the evaporation temperature in the evaporator in the evaporator line. A detailed parameter distribution of the VIHR-ASHP at an ambient temperature of -5°C is provided in Table 6-2. given the temperature of the mixture leaving the evaporator in the evaporation line of -7.8°C, the waste heat recovery from the exhaust air is about 111%. The waste heat recovery ratio is higher than that of a conventional exhaust air heat pump.

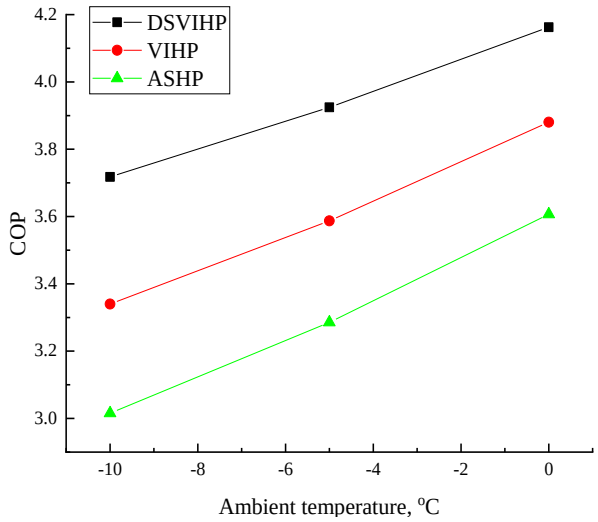

Fig. 6-16 COP variations with the ambient temperature for the VIHR-ASHP, conventional VIHP and ASHP

Table 6-2 parameter distribution of the VIHR-ASHP at an ambient temperature of -5℃

State point	Fluid	Flow rate, kg/s	Temperature, ℃	Pressure, MPa	Enthalpy, kJ/kg	Quality, %
1	R410A	0.308	45.0	2.733	275.85	0
2	R410A	0.136	5.03	0.936	275.85	31.68
3	R410A	0.136	5.07	0.936	348.83	65.59
4	R410A	0.136	5.10	0.936	422.84	100
5	R410A	0.172	11.23	2.733	217.21	Subcooled
6	R410A	0.172	-12.83	0.520	217.21	15.39
7	R410A	0.172	-12.75	0.520	417.02	100
8	R410A	0.308	74.69	2.733	468.75	Superheated
9	Outdoor air	6.0	-5	0.1	394.26	Superheated

10	Exhaust air	1.0	20	0.1	419.41	Superheated
11	Exhaust air	1.0	10.1	0.1	409.45	Superheated
12	Mixed air	7.0	-7.8	0.1	391.45	Superheated

The power input of the compressor and temperature drop of ambient air through the evaporator in the EL varying with the ambient temperature for the VIHR-ASHP are depicted in Fig.6-17. Given the mass flow rates of the exhaust and ambient air, the evaporation pressure in the evaporator of EL rises with the increment in the ambient temperature, leading to lower power input. Although the temperature drops of 5°C of the mixture through the EL is independent on the ambient temperature, the temperature drop of the ambient air from the entrance to the exit is actually less than 5°C (2~3°C as shown in the figure). This can be explained by an increased temperature of the ambient air after a mixing process with the exhaust air.

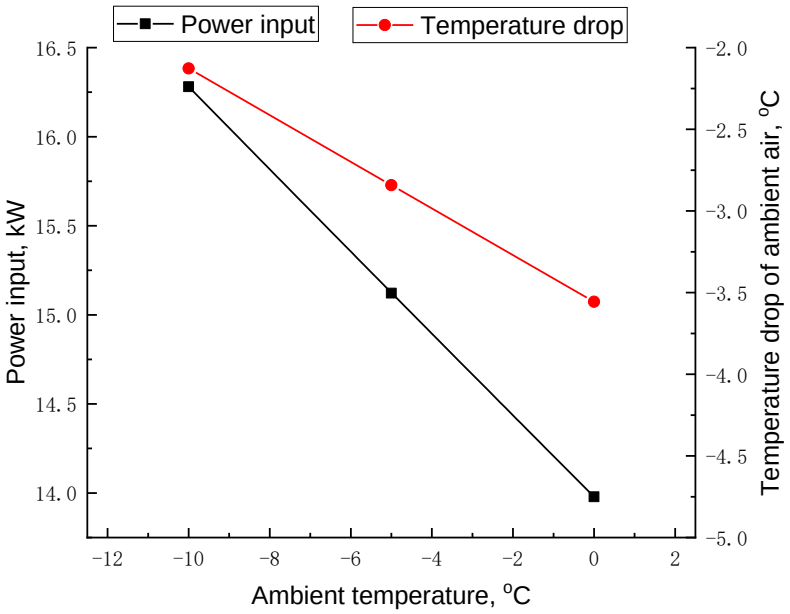

Fig. 6-17 variations of the power input and temperature drop with the ambient temperature for the VIHR-ASHP

6.4.1.2 Influences of condensation temperature

Variations of the COPs for the three types of heat pumps with the condensation temperature are displayed in Fig. 6-18. the ambient temperature is -5°C. The COP decreases with the increment in the condensation temperature. However, the decrements are different, which are 1.45, 1.19, 1.18 for the VIHR-ASHP, VIHP and ASHP respectively when the condensation temperature increases from 40 to 60°C. The relative decrements are 33.3%, 30.2% and 32.5%. At a higher condensation temperature, the novel heat pump still has a higher efficiency but the superiority becomes less appreciable. The results indicate that the VIHR-ASHP is more preferable in applications of relatively low condensation temperature and ambient temperature. For example, in northern China where the ambient temperature in winter can be lower than -10°C, the VIHR-ASHP will be desirable for an underfloor heating unit of inlet temperature of about 40°C.

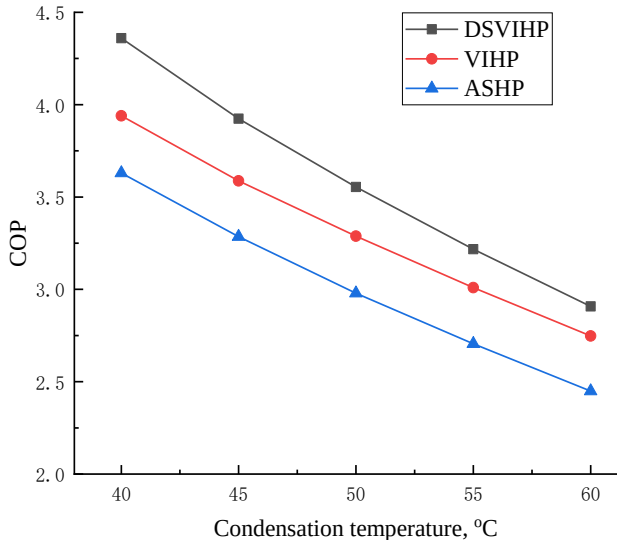

Fig. 6-18 Variations of the COPs of the VIHR-ASHP, conventional VIHP and ASHP with the condensation temperature

The VIHR-ASHP has a higher COP than a conventional VIHP due to the utilisation of exhaust air. In contrast to the ambient temperature, the condensation temperature does not have an impact on the waste heat utilisation. As the condensation temperature rises, temperatures of the exhaust air leaving the evaporator in the VIL and the mixture leaving the evaporator in the EL are not changed. The increasing condensation temperature will only lead to increments in the compressor power consumption and mass flow rate of injected refrigerant, as shown in Fig. 6-19, which is similar to the situation in a conventional VIHP. As a result, the COPs of the VIHR-ASHP and VIHP get closer at a higher condensation temperature.

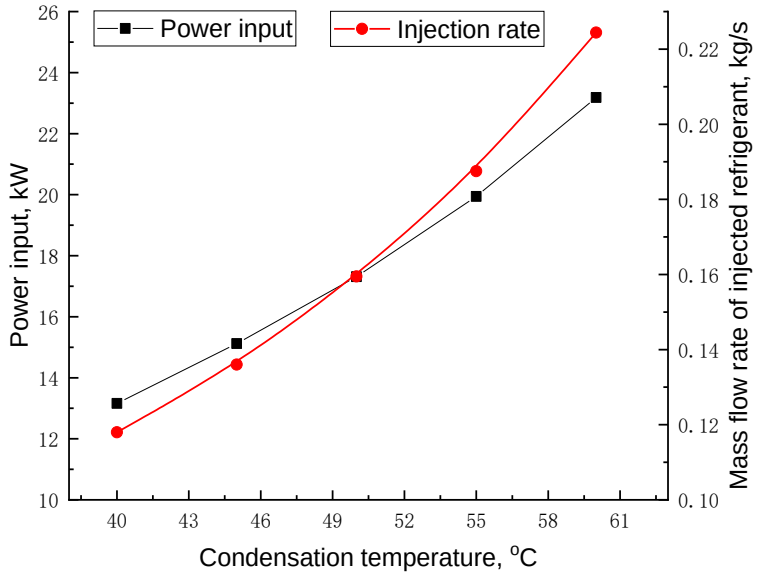

Fig. 6-19 Variations of the power input and mass flow rate of injected R410A with the condensation temperature for the VIHR-ASHP

6.4.1.3 Influences of vapor injection temperature

Aside from the ambient temperature and condensation temperature, the vapour injection temperature (T_2) affects the performance of the VIHR-ASHP. As shown in Fig. 6-20, the ambient temperature is -10°C and the condensation temperature is 45°C and 55°C, respectively. The injection temperature varies from 0 to 14°C. A maximum

COP appears at (T_2) of about 5°C when the condensation temperature is 45°C. A higher injection temperature can increase the mixture temperature of the exhaust and ambient air and reduce the difference between evaporation and condensation temperature, which has a positive impact on the COP. However, the waste heat recovery from the exhaust air in the evaporator in the VIL and vapor injection ratio are decreased. For instance, $M_{R410A,3}/M_{R410A,6}$ can drop from 114.37% to 34.13% with the increment in T_2. Due to the compromise between the evaporation temperature and injection ratio, there is an optimum injection temperature. The optimum temperature goes up as the condensation temperature increases. It is about 10°C at a condensation temperature of 55°C.

Unlike the COP, the heating capacity decreases monotonically as the injection temperature increases. It ranges from 63.6 to 48.6kW and 73.7 to 52.2kW for the condensation temperature of 45°C and 55°C respectively. Given mass flow rates of exhaust and ambient air of 1.0 and 6.0kg/s, a higher T_2 is accompanied with a lower heat input through the evaporator in the VIL. The temperature of the air mixture is elevated, resulting in a higher evaporation temperature in the evaporator in VIL. The mass flow rate of the injected R410A and input power of the compressor are decreased as shown in Fig. 6-21. the results indicate that a higher injection temperature is more suitable at a larger proportion of the ventilation heat loss to the total building energy losses. It is also deduced that if the exhaust air from buildings is mixed directly with the ambient air to heat the evaporator in the EL for which the injection temperature is close to 20°C, the heat supply of the heat pump will be small with a low COP.

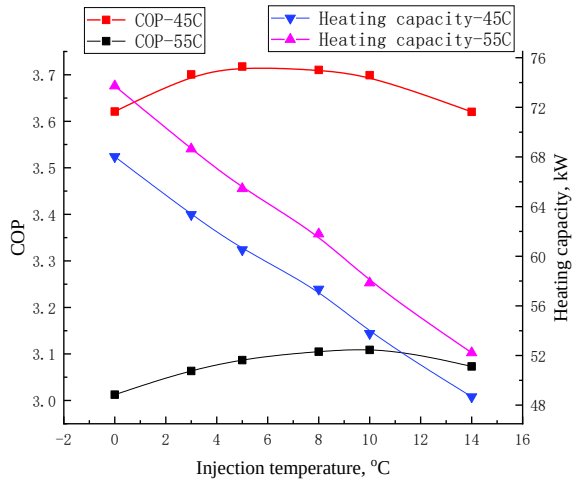

Fig. 6-20 Variations of COP and heating supply with the injection temperature for the VIHR-ASHP

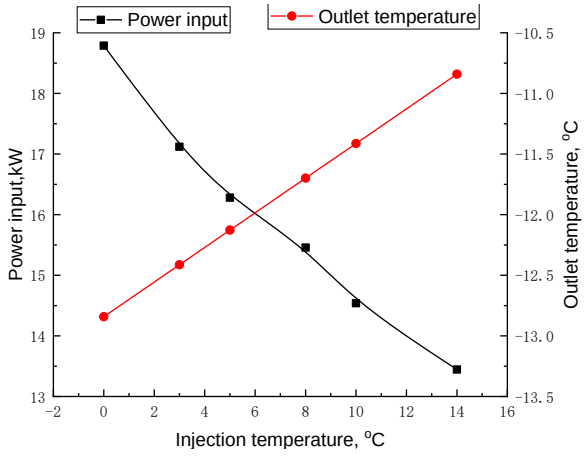

Fig. 6-21 Variations of the power input and outlet temperature of the mixture leaving the evaporator in the EL with the injection temperature for the VIHR-ASHP

6.4.1.4 Influences of mass flow ratio of ambient air to exhaust air

Variations of the COP and heat supply of the VIHR-ASHP with the mass flow ratio of the ambient air and exhaust air (y) are shown in Fig. 6-22. The ambient temperature, condensation temperature and vapour injection temperature are -10, 45 and 5°C. Given the mass flow of the exhaust air (1.0 kg/s) and the temperature drop (5°C) of the mixture through the evaporator in the EL, a higher y leads to more heat input to the

evaporator in the evaporation line. The mass flow rate of R410A in the evaporator in the EL and the heating capacity are thereby increased. Because the exhaust air leaving the evaporator in the VIL is almost constant (10°C), an increment in y also results in a decrement in the mixture temperature. The outlet temperature of the mixture declines from about -11 to -13°C when y increases from 5 to 10, as shown in Fig. 6-23.

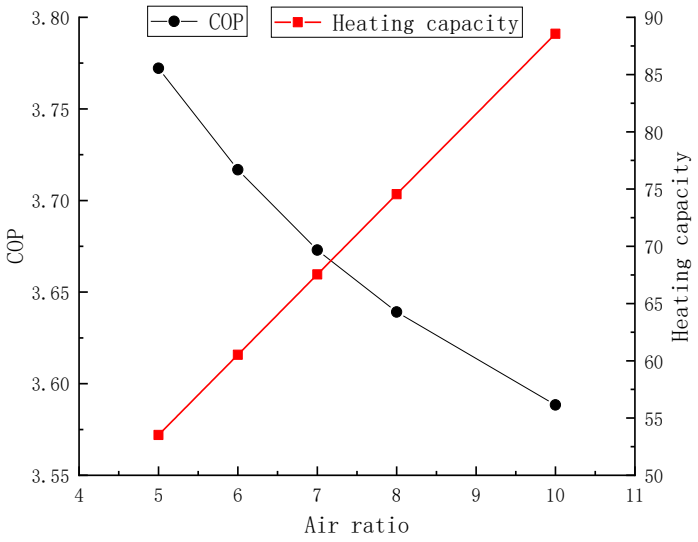

Fig. 6-22 Variations of the COP and heat supply with the air flow ratio for the VIHR-ASHP

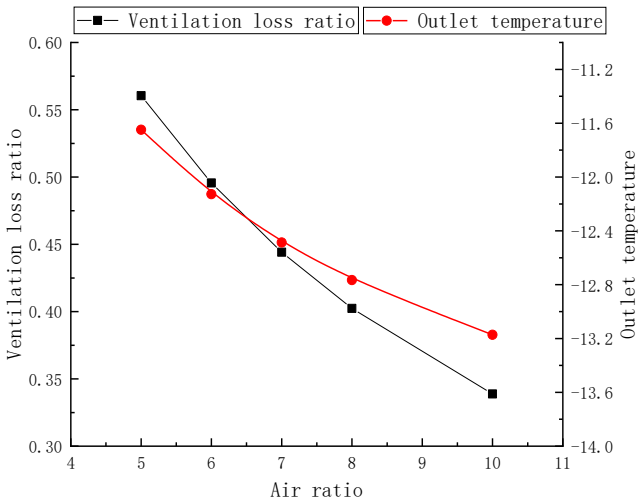

Fig. 6-23 Variations of the ventilation heat loss ratio and outlet temperature of the mixture with the air flow ratio for the VIHR-ASHP

With a larger R410A flow rate in the evaporator in the EL, the COP falls since the average evaporation temperature of the VIHR-ASHP decreases. The ratio of the ventilation heat loss to the heat supply (x) also drops from about 56% to 33%.

6.4.1.5 Thermodynamic irreversibility in the components

The thermodynamic irreversibility in the components is revealed in Fig. 6-24. The ambient temperature, condensation temperature, vapor injection temperature and the air flow ratio are -10°C, 45°C, 5°C and 6, respectively. The largest exergy destruction takes place in the compressor, which amounts for about one-third of the total system losses. It is followed by the destruction in the condenser owing to a large heat transfer irreversibility between the superheated refrigerant and cooling water.

The total exergy loss in the throttle valves (EL and VIL valves) is less than that in the compressor and the ratio of the former to the latter is about 58%. As a comparison, for a conventional ASHP operating at a condensation temperature of 45°C and an ambient temperature of -10°C, the ratio of the exergy destruction in the throttle valve to that in the compressor is about 142%, indicating the thermodynamic irreversibility during throttling is much more remarkable. The novel VIHR-ASHP is able to reduce the exergy destruction in the valves by two means: (1) The refrigerant leaving the condenser is split into two streams. The irreversibility of the first stream in the VIL throttle valve is weakened due to a higher pressure at the outlet of the valve. (2) The second stream is supercooled prior to the expansion. The irreversibility in the LP throttle valve is reduced by the lower quality and specific volume of the refrigerant. The quality of R410A at the EL valve outlet is only 17%, while is about 43% for that in a conventional ASHP. The throttling is an adiabatic process, and the exergy destruction can be determined by $\int_{p1}^{p2} vdp$. A lower pressure drop and specific volume will diminish the losses. The exergy losses in the components vary with the air flow ratio. As shown in Fig. 6-25, when y is increased to 10, there are slight increments in the compressor and condenser losses and decrements in the valve losses.

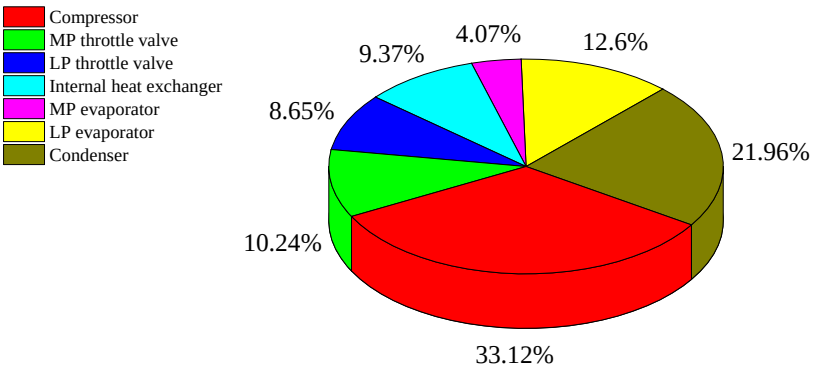

Fig. 6-24 Exergy destruction in the VIHR-ASHP at $y = 6$

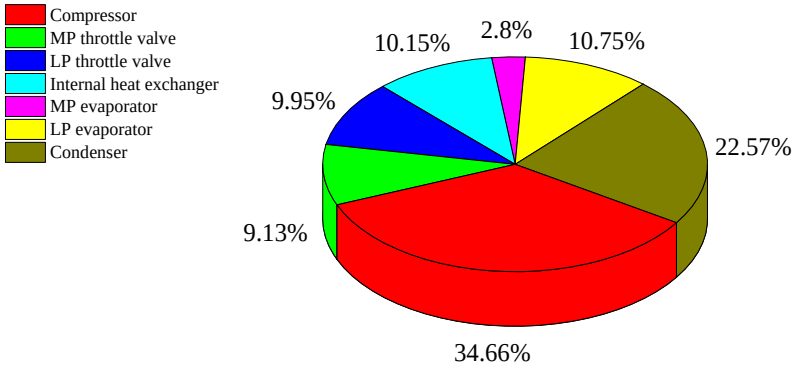

Fig. 6-25 Exergy destruction in the VIHR-ASHP at $y = 10$

6.4.2 Mini-channel solar thermal collectors array results

6.4.2.1 The overall solar thermal efficiency of the panels-arrays under the operational modes of 'multiple-throughout-flowing' and the 'one-to-one-connection'

For the one-to-one connection mode, the thermal efficiency of a single panel is given as equation [4-27]. Assuming the inlet temperature of the working fluid (water with glycol) of 25^{o}C, solar radiation of 600W/m^{2}, ambient temperature of 5^{o}C, and fluid flow rate of 0.5m^{3}/h which gives the channel velocity of 0.12m/s, and the temperature variation of the fluid throughout the 8 panels in the array can be obtained by using equation [4-27]; this is shown in Fig. 6-26.

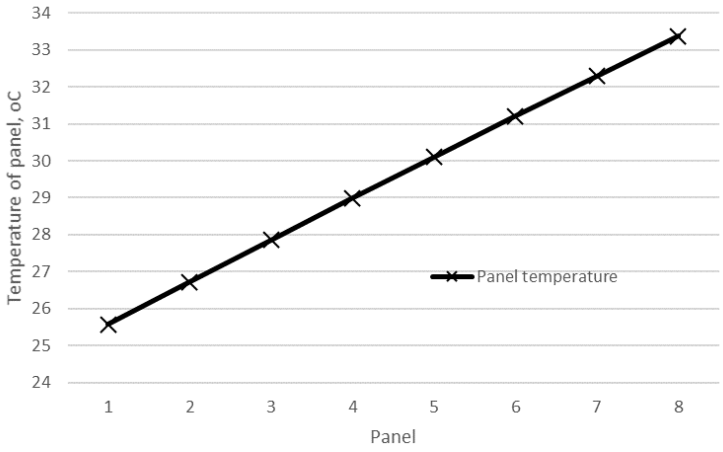

Fig. 6-26 Temperature variation of the fluid throughout the panels for the one-to-one connection mode

As a result, the overall efficiency of the whole panels-array is calculated by the following equation:

$$\eta = C_p \dot{m}(T_{8-o} - T_{1-i})/(8IA) \qquad [6\text{- }1]$$

The thermal efficiency of different panels in the array is shown in Fig. 6-27; thus, the overall solar thermal efficiency of the panels-array is 67%.

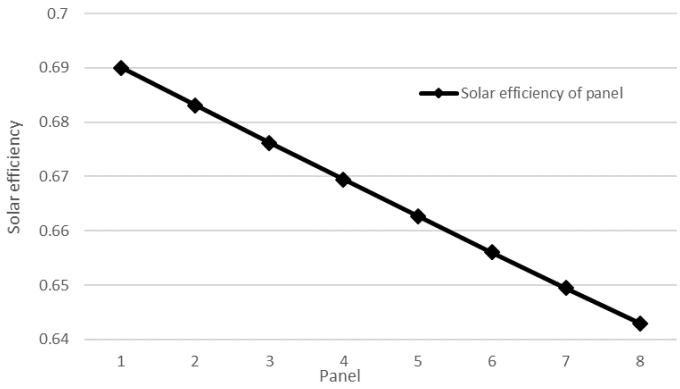

Fig. 6-27 Solar thermal efficiency variation throughout the panels for the one-to-one connection mode

For the 'multiple-throughout-flowing' connection mode, the solar thermal efficiency of a single panel is given as equation [4-28]. Assuming the same inlet temperature (i.e. 25°C) of the working fluid (i.e., water with glycol), solar radiation of 600W/m^2, the ambient temperature of 5°C, and the same volume flow rate of 0.5m^3/h which gives the channel velocity of 0.36m/s, the temperature variation of the fluid at the different points of the panels can be obtained by using equation [4-28]; these are shown in Fig. 4-6.

$$\eta = C_p m(t_{24} - t_0)/(8IA) \qquad [6\text{- }2]$$

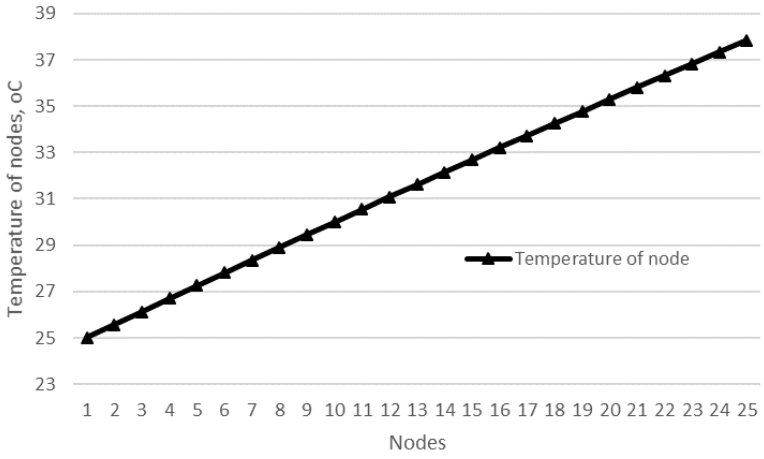

Fig. 6-28 Temperature along with the nodes of panels for 'multiple-throughout-flowing' connection mode

The overall thermal efficiency of the panels-array is given by

$$\eta = Cpm(t_{24} - t_0)/(8IA) \qquad [6\text{- }3]$$

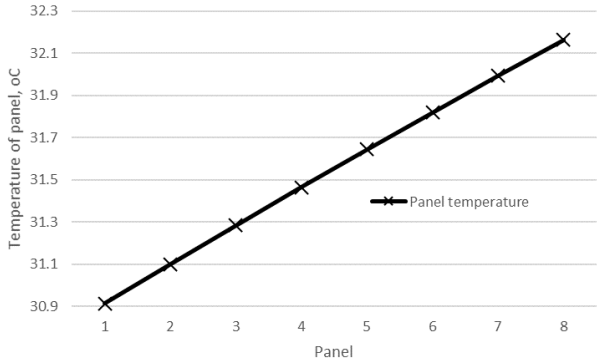

Fig. 6-29 Temperature variation of the fluid throughout the panels in the multiple-throughout-flowing connection mode

The temperature variation of the fluid throughout the panels in the array is shown in Fig. 6-29. Furthermore, Fig. 6-30 indicates the average thermal efficiency of the different panels in an array, thus, the overall thermal efficiency of the panels-array is 74%.

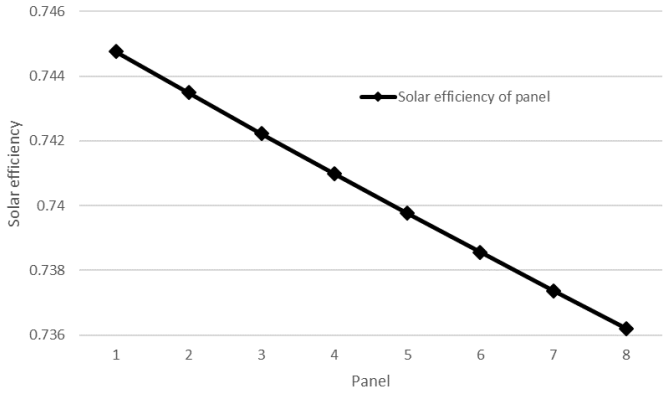

Fig. 6-30 Solar efficiency variation throughout the panels in the 'multiple-throughout-flowing' connection mode

6.4.2.2 Comparison between the 'one-to-one-connection' and 'multiple-throughout- flowing' modes

Figs. 6-31 and Figs. 6-32 show the comparison between multiple-throughout-flowing and one-to-one-connecting modes, which give the panels' average

temperature and associated solar thermal efficiency respectively. For an array with 8 panels, the multiple-throughout-flowing mode can achieve 10.4% higher solar thermal efficiency compared to the one-to-one-connection mode (74% against 67%). The temperature of the panels at the rear of the array will be reduced from 33.4°C to 32.2°C, leading to the increase of its thermal efficiency by 14.5% (i.e., from 64.3% to 73.6%). Furthermore, the temperature difference between the head and rear panels of the array will be reduced by 84%, leading to the increased overall solar thermal efficiency by 10.4% (i.e., from 67% to 74%).

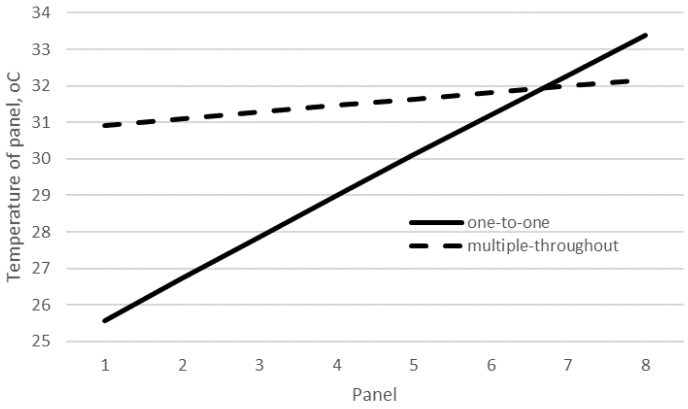

Fig. 6-31 Temperature variation of the fluid through the panels

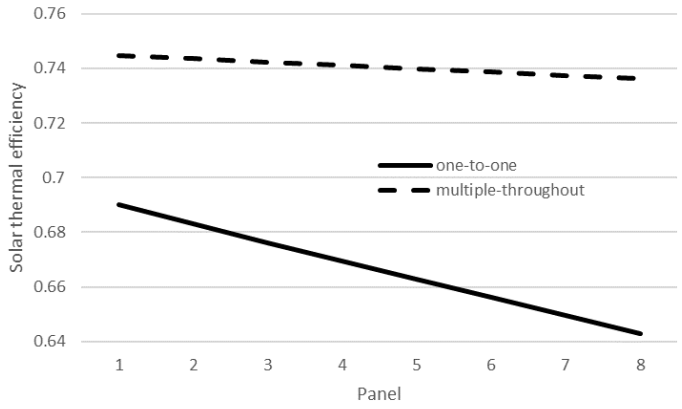

Fig. 6-32 Solar thermal efficiency variation through the panels

The comparison of the fittings and local resistance factor between two configurations can show another advantage of the multiple-throughout-flowing configuration. The flow resistance of the fluid across the panels-array can be calculated in the following way:

The resistance through the pipeline can be divided into two parts: the local resistance and the along-the-way frictional resistance. The equations of the along-the-way frictional resistance can be given as:

$$h_f = \lambda_r \frac{l}{D} \frac{v^2}{2g} \quad [6\text{- }4]$$

$$h_m = \zeta \frac{v^2}{2g} \quad [6\text{- }5]$$

According to the above formulas, the pipe resistance at every node along the pipeline can be theoretically calculated, and the results are shown in Fig. 6-33. The pipe resistance of both connection configurations shows an approximate linear increasing trend along the pipeline. However, owing to the larger number of elbows in the one-to-one configuration compared to the multiple-throughout-flowing, the pipe resistance of the one-to-one configuration grew much faster than that of the multiple-throughout-flowing. As a result, with the same number of solar thermal collectors, i.e., 8 panels, and under the same flow volume rate, i.e., 0.5m^3/h, the total pipe resistance of the one-to-one connection configuration is around 6 m higher than that of the multiple-throughout-flowing mode. Furthermore, the results based on the theoretical calculation is very close to the data collected from the on-site testing, indicating that the theoretical calculation can be used to determine the pipe resistance.

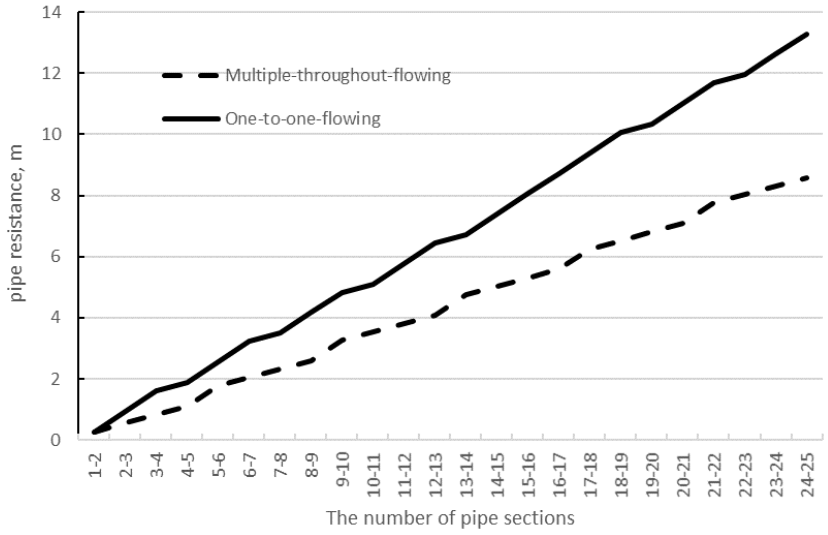

Fig. 6-33 Pipe resistance along the flowing path

The flow resistance of the fluid across the multiple-throughout-flowing array is significantly lower than that in the one-to-one flowing array (8m vs. 13m). Meanwhile, the heat output from the multiple-throughout-flowing array is 10.4% higher than that from the one-to-one-flowing array. This leads to a significantly higher Energy Efficiency Ratio (EER) (i.e., a ratio of the collected heat to the consumed energy by the solar thermal collector, shown in equation [6-6]) in the multiple-throughout-flowing array compared to the one-to-one-connection array.

$$EER = \frac{Q_{aq}}{W_c} \qquad [6\text{-}6]$$

The EERs for the one-to-one-connection and multiple-throughout-flowing modes are 205 and 368 respectively, indicating that the multiple-throughout-flowing mode has a 79.5% higher EER compared to the one-to-one type; this represents another advantage of the multiple-throughout-flowing mode.

6.4.2.3 Impact of the number of panels in an array

The impact of the panels' number on the performance of the system was investigated by fixing other parameters in 6 situations (shown in Table 6-2) and varying the number

of the panels from 5 to 25.

Table 6-3 Operational conditions

No.	Inlet Temperature (°C)	Ambient temperature (°C)	Solar Radiation (W/m^2)	(Tin – Ta)/I
1	23	5	600	0.03
2	47	5	600	0.07
3	65	5	600	0.1
4	25	5	666.6	0.03
5	25	5	285.7	0.07
6	25	5	200	0.1

As shown in Table 6, the solar radiation and ambient temperature are the same for situation No.1 to No.3, the solar radiation is the variant in these three situations. And the inlet temperature and ambient temperature are the same for situation No.4 to No.6, the solar radiation is the variant in these three situations. As a result, the analysing will take situation No.1 to No.3 as a group and No.4 to No.6 as a group respectively.

The overall solar thermal efficiency of the panels-array against the panel number under the situation No.1 to No.3 and No.4 to No.6 is shown in Figs. 6-34 and Figs. 6-35. It is found that the solar thermal efficiency of the panels-array decreases with the number of panels increasing from 5 to 25, indicating that the solar efficiency of panels-array is in inverse proportion to the number of panels. The reason for this phenomenon lies in the increased temperature of the panels at the rear part of the array which leads to the reduced overall solar thermal efficiency with the increased panels' number.

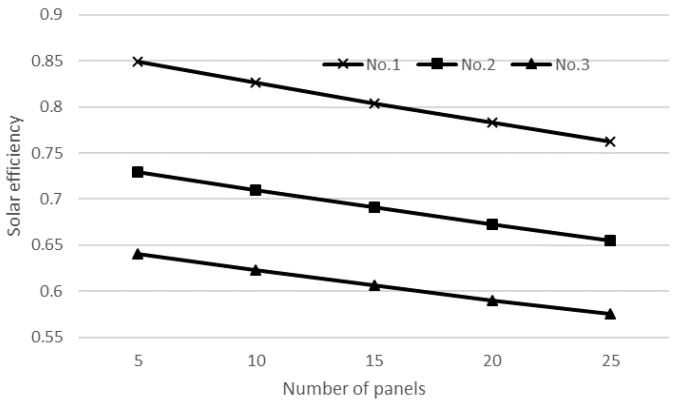

Fig. 6-34 The variation of the solar thermal efficiency under situation No.1 to No.3

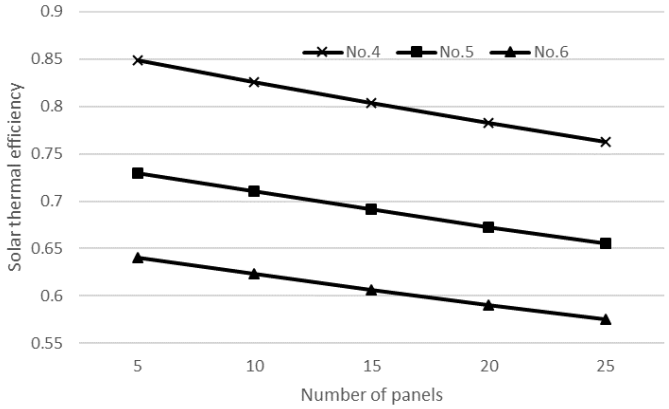

Fig. 6-35 The variation of the solar thermal efficiency under situation No.4 to No.6

Meanwhile, the EER against the panels' number under the situation No.1 to No.3 and No.4 to No.6 is shown in Figs. 6-36 and Figs. 6-37. It is found that the EER of panels-array initially increases with the increase of the panels' number and then decreases with the increase of the panels' number, and the maximum EER of the panels-array occurs at the panel number of 10. This can be explained as such: when an increasing number of the panels in an array, the heat output of the array is in a fast-growth trend and meanwhile, the power consumption of the pump also grows steadily. The ratio of the heat output to the pump power is quickly going up and when the panels' number is above 10, this ratio value falls owing to the fast-growing fluid flow resistance and

less fast increase in the array's heat output.

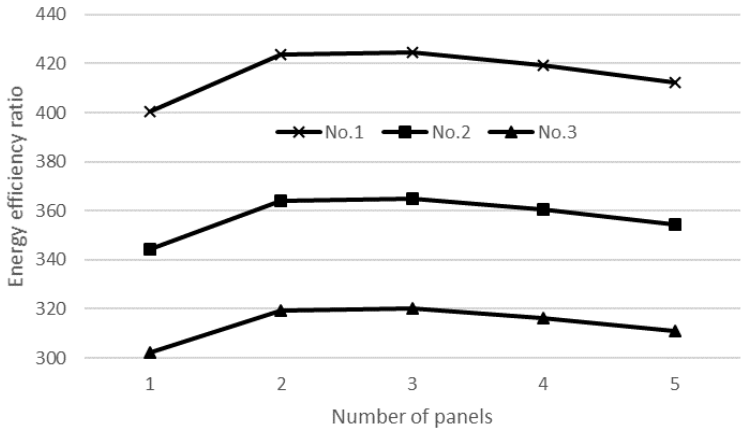

Fig. 6-36 The variation of the energy efficiency ratio under situation No.1 to No.3

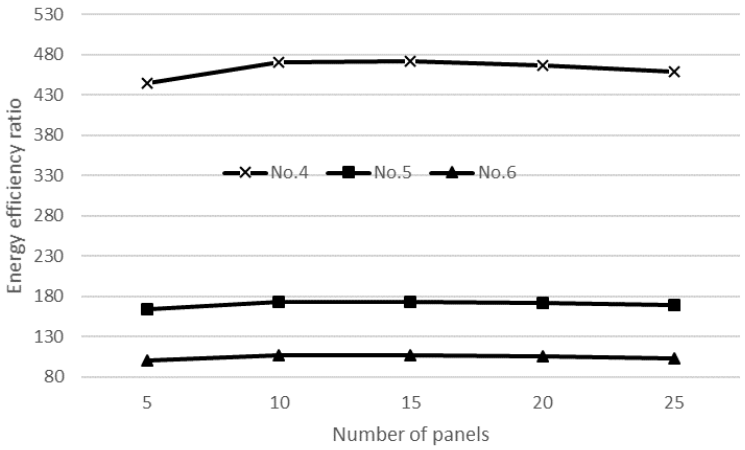

Fig. 6-37 The variation of the energy efficiency ratio under situation No.4 to No.6

6.4.2.4 Impact of the turning number of panels in an array

According to the results, under different circumstances, the variations of the solar thermal efficiency and the solar EER are similar. Hence, for analysing the other characteristics of the solar thermal collectors' array, No.1 situation is used for analysing, which is shown in Table 6-2.

The impact of the fluid flow turning number was investigated by fixing other parameters (shown in Table 6-2) and varying the turning number from 2 to 10. The overall efficiency of the collectors array against the fluid flow turning number is shown in Fig. 6-38. It is found that increasing the fluid flow turning number within an array leads to the continuous growth of the solar thermal efficiency of the array. However, the growth rate is higher when the turning number is less than 5 and this is getting lower when the turning number is more than 5.

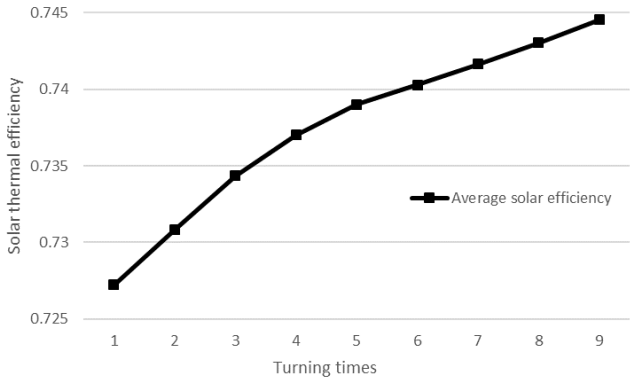

Fig. 6-38 Solar thermal efficiencies with different fluid flow turning number for the multiple-throughout-flowing type

Fig. 6-39 shows the variation of the EER of the array against the fluid flow turning number. It is found that increasing the fluid flow turning number within an array leads to the continuous fall of the solar thermal efficiency of the array. However, the reduction rate of the EER is initially higher when the turning number is less than 5 and this is getting lower when the turning number is more than 5.

Combination of the both Figs indicates that the adequate fluid flow turning number is 5; beyond which the performance of the panels' array tends to more stable with a less dramatic change in both the solar thermal efficiency and EER.

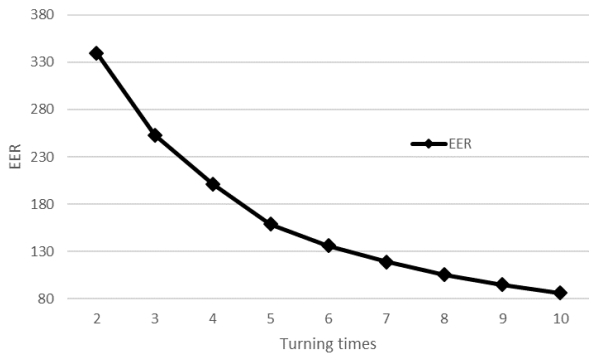

Fig. 6-39 EER with different fluid flow turning number for the multiple-throughout-flowing type

6.4.2.5 Impact of the fluid flow speed in an array

Impact of the fluid flow speed was investigated by fixing other parameters (shown in Table 6-2) and varying the volume flow rate from $0.1m^3/h$ to $1m^3/h$. The overall efficiency of the collectors array against the panel number is shown in Fig 6-40. It is found that increasing the fluid flow speed leads to a continuous increase in volume flow rate and fluid flow speed, indicating that a higher fluid speed benefits the performance of the panels-array. However, the solar thermal efficiency experiences a very fast growth when the volume flow rate increases from $0.1m^3/h$ to $0.3m^3/h$; the growth rate tends to be slow when the flow rate exceeds $0.3m^3/h$. Besides, there is a great increase of solar efficiency from 0.25 to 0.35 m/s. The reason is that the flow regime transforms from the laminar flow to the turbulent flow which leads a great increment of the heat transfer capacity of the working fluid, thus giving a high solar thermal efficiency increase.

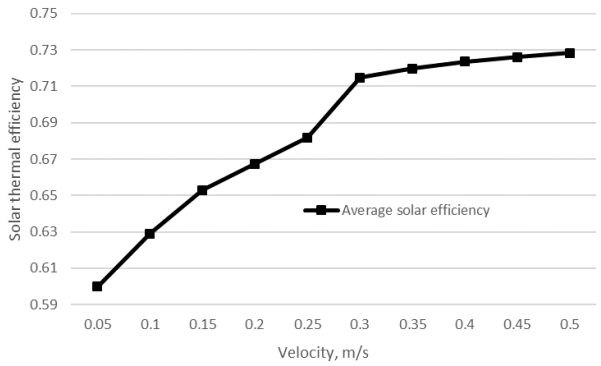

Fig. 6-40 Solar thermal efficiencies with different volume flow rate for the multiple-throughout-flowing type

Variation of the EER against the fluid flow rate (speed) is shown in Fig. 6-41. It is found that increasing the fluid flow speed leads to a continuous fall in energy efficiency rate (EER), indicating that a higher fluid speed has a negative effect on the energy performance of the collectors array. The fast fall of the EER occurs when the fluid flow velocity varies from 0.1m/s to 0.3m/s; this figure tends to be less varying when the flow rate exceeds 0.3m/s. This again proves that the most favourite flow speed is 0.3m/s from the solar collection effect.

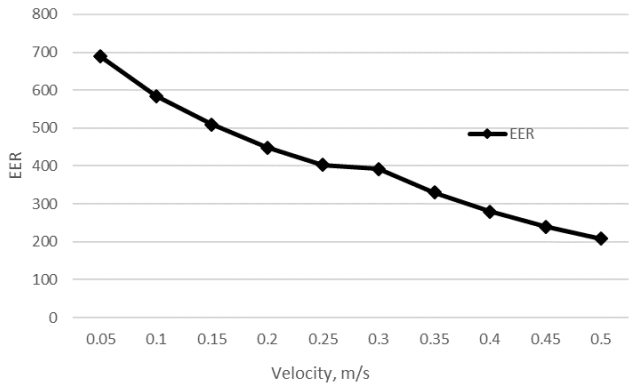

Fig. 6-41 EER with different volume flow rate for the multiple-throughout-flowing type

6.5 Chapter Summary

This chapter conducted the model validation and the simulation of the components of the novel SAHR-HP system. These simulation models were preliminarily validated by the published test results with a reasonable accuracy in predicting SAHR-HP system performance.

The numerical study of the VIHR-ASHP is conducted to explore the influences caused by the associated factors, i.e., the ambient temperature, the condensation temperature, the vapor injection temperature, and the mass flow ratio of ambient air to exhaust air. In addition, the performance of the VIHR-ASHP is compared with the conventional vapour injection heat pump (VIHP) and an air source heat pump (ASHP). The result shows that compared to existing heat pump technologies, this proposed system comprises unique features. It is the first time that vapour injection heat pump has been used to recover waste heat of exhaust air from the buildings. The new VIHR-ASHP system overcomes technical challenges and gives several advantages: (1) Minimizing the ventilation heat loss. Unlike a conventional EAHP that extracts energy from exhaust air to heat the fresh supply air, the VIHR-ASHP uses both exhaust and outdoor air as the heat sources. It has a higher heating capacity at a given mass flow rate of exhaust air and the waste heat recovery ratio is more than 100%. By recovering the ventilation heat loss, the VIHR-ASHP can save about 23% of electricity consumption as compared with a conventional ASHP at normal operation conditions of condensation temperature of 45°C and an ambient temperature of -10°C; (2) Defrosting of heat pump in cold climate areas. The VIHR-ASHP has flexible operation modes. In the defrosting mode for which the vents for the ambient air are shut down, the VIHR-ASHP provides a promising solution to frosting by using the exhaust waste heat without additional electricity consumption. The seasonal performance factor is expected to be significantly higher than that of a conventional ASHP regarding the near-zero electricity consumption for defrosting; (3) The performance of the VIHR-ASHP is affected by the ambient temperature, condensation temperature, vapor injection temperature and air flow ratio. A lower ambient temperature will increase its advantages over conventional air source heat pump and vapor injection heat pump. An

increment in the condensation temperature leads to a decrement in the COP but has no impact on the waste heat recovery. The optimum vapor injection temperature is about 5°C at an ambient temperature of - 10°C, which increases as the condensation temperature rises. The flow ratio of the ambient air to the exhaust air influences the COP and heating capacity. A higher flow ratio is accompanied with a lower proportion of ventilation heat loss; (4) The largest exergy destruction takes place in the compressor, which accounts for about a third of the total exergy losses in the VIHR-ASHP. This is followed by the exergy destruction in the condenser (about 20%) and LP evaporator (about 10%). Among the components, the MP evaporator has the least exergy destruction. In all the simulation scenarios, the proposed heat pump is most beneficial under the conditions of an ambient temperature of about -10°C and the condensation temperature of about 40-45°C.

The numerical study of the mini-channel solar collectors array with multiple-throughout-flowing connection method is conducted, and the performance is compared with the performance of that with the one-to-one connection method. The results show that, compared to the traditional one-to-one panels connection approach, the novel multiple-throughout-flowing mode can achieve around 10% overall solar thermal efficiency and 80% higher energy efficiency ratio (EER) while the cost of the whole panels-array remains the same between both modes.

Compared to the one-to-one-connection mode, the multiple-throughout-flowing mode creates a higher flow speed within the panel flow channels, thus leading to a higher solar thermal efficiency for the individual panels, with the potential increase rate in the range from 7.5% to 15.4%. Furthermore, the multiple-throughout-flowing mode, by circulating the working fluid throughout the panels-array several times, can reduce the temperature difference between the head and rear panels and thus increase the overall solar thermal efficiency of the array be around 10%. Last but not least, the multiple-throughout-flowing mode reduces the fluid flow turning number within the panels, thus leading to a significantly lower fluid flow resistance and thus a very higher

energy efficiency rate (EER), with the potential rate in the range of 62% to 68%.

The panels' number, fluid flow turning number and fluid flow speed have a great impact to the performance of the multiple-throughout-flowing panels-array. It is found that the most favourite panels' number in an array is 10, the associate fluid flow turning number is 5, and the fluid flow speed with the array channels is 0.3m/s.

As a result, the prototype system was proven to have reliable performance in real climatic conditions. Such a dedicated dynamic simulation model is thus regarded as being reliable in predicting the annual system performance in Chapter 7.

CHAPTER 7: ENERGY SAVING, ECONOMIC, ENVIRONMENTAL AND REGIONAL ACCEPTANCE ANALYSIS

7.1 Chapter Introduction

In this chapter, a feasibility study of the prototype system in 3 locations of China, i.e., Chongqing, Taiyuan, and Urumqi is carried out, involving an annual energy performance prediction, economic analysis and environmental sustainability assessment. The three cities are from middle to north of China where the climate conditions are from cold to extreme cold. Accordingly, the weather of the cities can represent most of the weather conditions, and the simulation results can be extended to most cold areas worldwide, i.e., The UK and the European countries.

The main works involved in this chapter include:

(1) The annual energy performance of the prototype system is predicted using the dedicated dynamic simulation model validated in the previous chapter.

(2) The environmental benefits of the system prototype are analysed in comparison with conventional coal-based heating systems

(3) This socio-economic analysis is undertaken based on life-cycle assessment methods, including the cost payback period, cost-saving, and CO_2 emission reduction across the system's life span in the above three regions.

This part of the research develops a socio-economic model that can predict the energy saving, economic and environmental benefits of the SAHR-HP system prototype in 3 regions of China.

7.2 Annual Operational Performance

7.2.1 Case study model set-up

In this section, 3 case study of the energy performance of a rural house equipped with the novel SAHR-HP system is simulated under 3 locations needs heating, cooling, and domestic hot water. From south to north, the 3 locations are Chongqing (29.43°N, 106.91°E), Taiyuan (37.87°N, 112.54°E), and Urumqi (43.83°N, 87.62° E). According to the guidance of China, Chongqing, Taiyuan, and Urumqi are located in the hot summer and cold winter area, cold area, and extreme cold area separately. In the hot summer and cold winter area, the average temperature of the coldest month is from 0 to 10°C, and the average temperature of the hottest month is from 25 to 30°C. In the cold area, the average temperature of the coldest month is from -10 to 0°C, the number of days in which the daily average temperature is lower than 5°C is between 90 to 145 days. In the extreme cold area, the average temperature of the coldest month is lower than -10°C, the number of days in which the daily average temperature is lower than 5°C is more than 145 days.

In these cities, Chongqing is suffering from no central heating under the cold climate, and the other two cities are suffering from severe air pollution because of the coal-based winter heating system. Accordingly, using a renewable energy heating system to relieve the environment contamination is urgent. The novel SAHR-HP system provides space heating, cooling, and domestic hot water flexibly by using renewable energy sources.

The served house has an area of $100m^2$, a length of 14m, a width of 7m and a height of 4m. The front façade of the house faces south. The schematic of the served house is shown in Fig. 7-1, and the heat transfer coefficients of the building envelopes are listed in Table 7-1. The thermal properties of the building components are the same as the actual parameters for a common house, thus providing an accurate reflection of the heat load for a residential house.

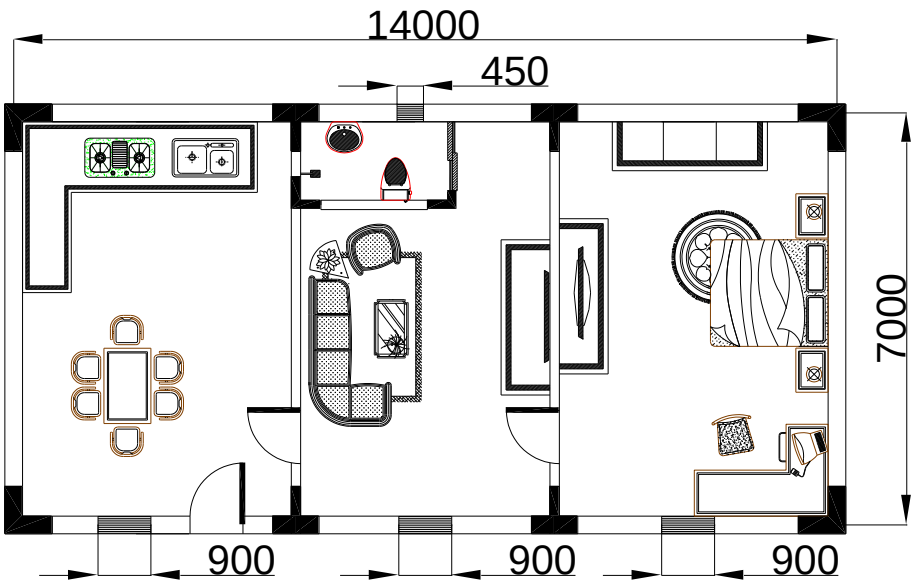

Fig. 7-1 The floor plan and corresponding dimensions of the served house

Table 7-1 The heat transfer coefficients of the building envelope

Part	**Structure**	**K [W/(m²·°C)]**
Wall	370mm brick wall Plastering + 50mm extruded polystyrene board	0.47
External doors	Pinewood door	2.9
Window	3mm common glass aluminium alloy window frame (two layers)	1.54
Roof	Cement mortar +Insulation layer + Waterproof layer + Tile.	0.37

The corresponding initial and boundary conditions, i.e. solar radiation, air temperature, wind speed and water temperature were extracted from the weather database by using Energy-Plus software (537720_CSWD) for Chongqing, Taiyuan, and Urumqi [216]. During the operation of the model, it is assumed that the system works 24 hours every day, and the heat pump operates at a

condensation temperature of 50°C for space heating in winter and an evaporation temperature of 10°C for cooling in summer. The installation angles of solar PV and thermal panels are the same as the local altitude in the city. The economic figures, such as capital cost, renewable feed-in tariffs, system life span and air contaminant emission factors also input into the program for calculation. The algorithm is presented in a flow diagram in Fig. 4-14 (Chapter 4).

The hourly dry-bulb ambient temperature within one year in Chongqing, Taiyuan and Urumqi city is shown in Fig. 7-2. The ambient dry-bulb temperature of Taiyuan varies from -15˚C to 35˚C. The ambient dry-bulb temperature of Chongqing varies from 0˚C to 40˚C. The ambient dry-bulb temperature of Chongqing varies from -25˚C to 30˚C. The highest ambient dry-bulb temperature appears in August, and the lowest ambient temperature appears in January.

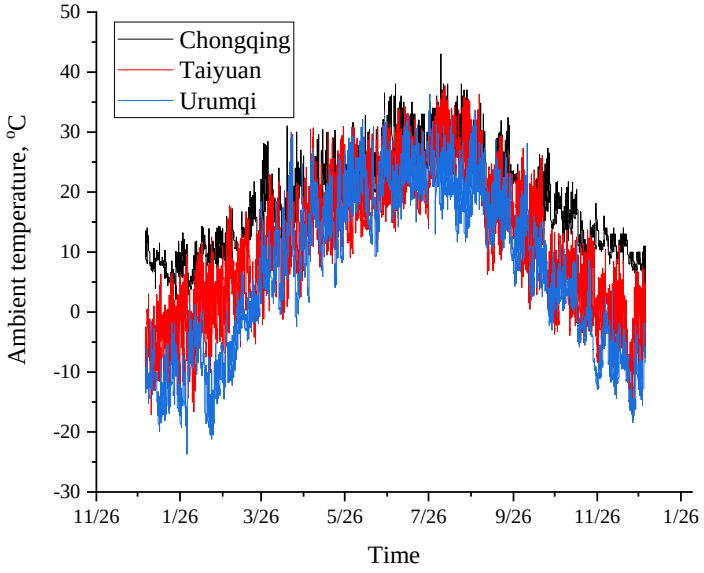

Fig. 7-2 The hourly ambient dry-bulb temperature variation of different cities along a year

The variation of the hourly solar radiation within one year in Chongqing, Taiyuan and Urumqi city is shown in Fig. 7-3, Fig. 7-4, and Fig. 7-5 separately. The solar radiation of three cities varies from 200W/m^2 to 1000W/m^2. Besides,

the variation tendency of solar radiation of three cities is similar, which is low in winter and high in summer. According to the degree of density of the lines, the weather condition of the city can be concluded. Chongqing and Urumqi have relatively sparse lines so that the overall weather of these two cities is always cloudy. The situation of Taiyuan city is the opposite.

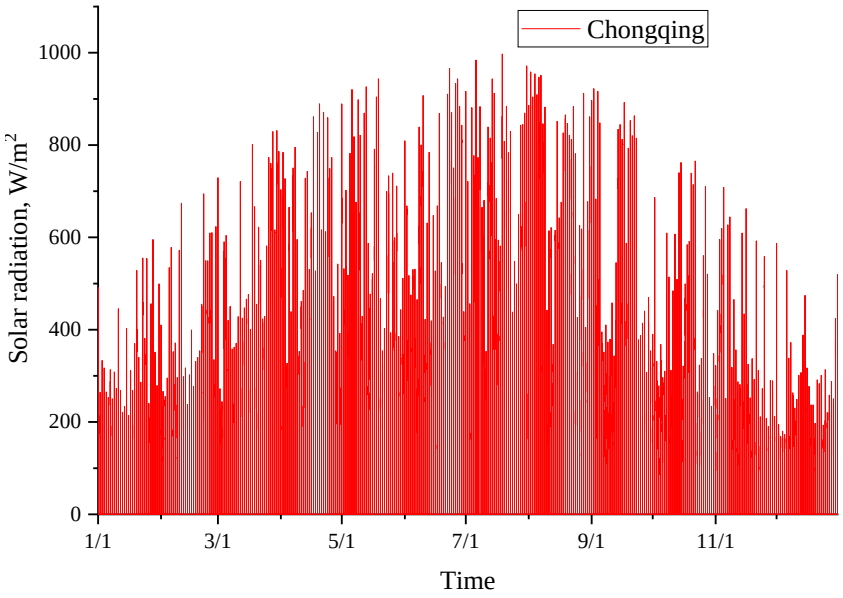

Fig. 7-3The hourly solar radiation variation along a year of Chongqing

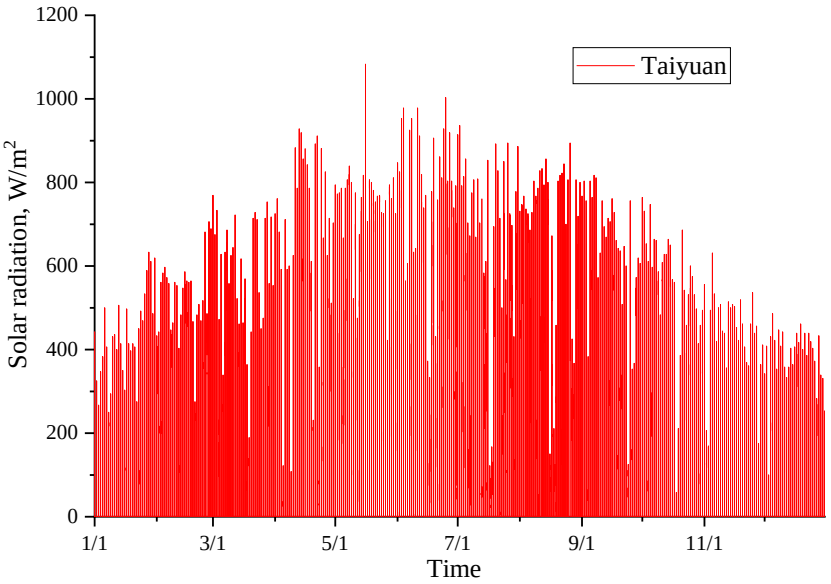

Fig. 7-4 The hourly solar radiation variation along a year of Taiyuan

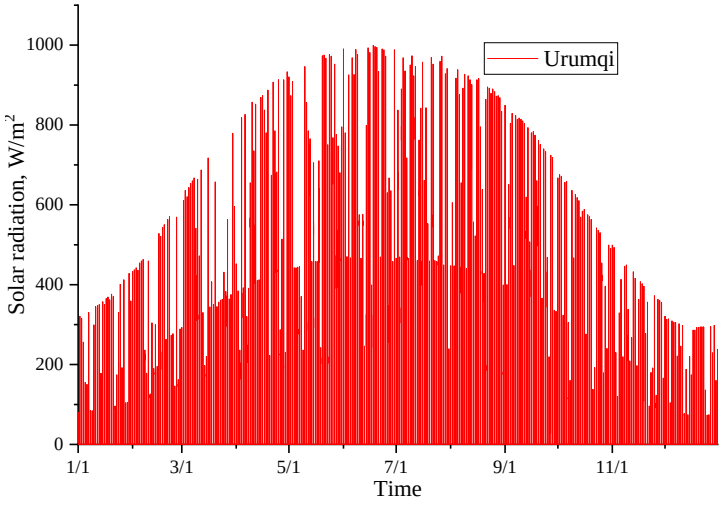

Fig. 7-5 The hourly solar radiation variation along a year of Urumqi

7.2.2 Energy performance of the system in different cities

According to the local weather conditions and the dynamic simulation, the real-time load of the house located in different cities is presented in Fig. 7-6, Fig. 7-7, and Fig. 7-8. The overall load of the house includes the load based on the temperature difference between the ambient temperature and the room temperature, the load caused by solar radiation and the direction of the house envelopes, and the load introduced by the fresh air. Apparently, the variation trend of the overall load is similar to the temperature difference load, which means the overall load is dominated by the temperature difference load. In the summer, except for the temperature difference load, the solar radiation load is another main factor that introduces the cooling load to the house. The overall load of the house has a 5kW daily load difference in Chongqing, 7kW in Taiyuan, and 5kW in Urumqi, thus giving the system a great challenge in maintaining the room temperature and adjusting the operation status timely and flexibly. The highest heating load reaches 12kW during the coldest months in Taiyuan and Urumqi, i.e., January and December, and the highest cooling load reaches 4.5kW in August. Accordingly, the house situated in Taiyuan and Urumqi city is dominated by the heating load. Chongqing has the same absolute value of the

heating and cooling load, which is 6kW.

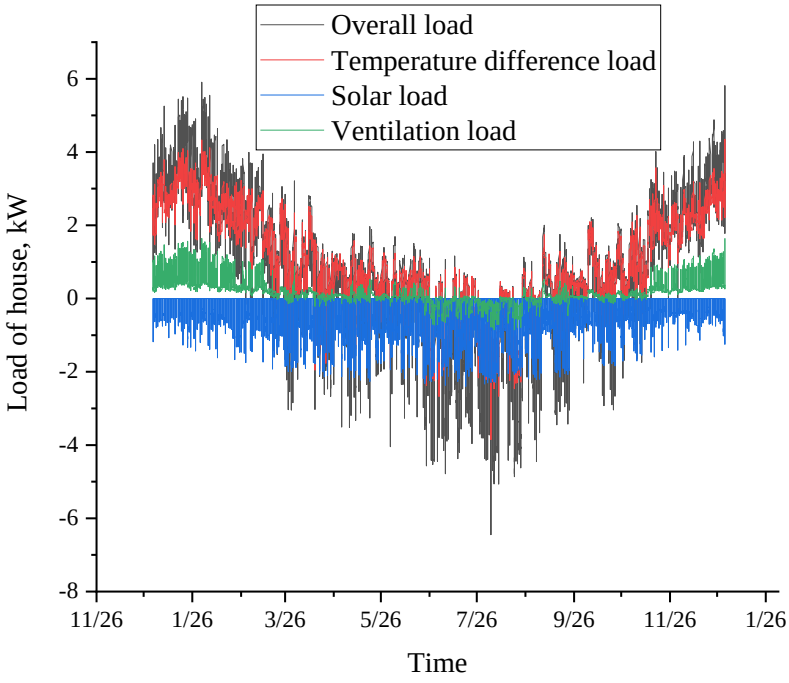

Fig. 7-6 Daily variations of the solar energy collection, heating and cooling load of Chongqing along a year

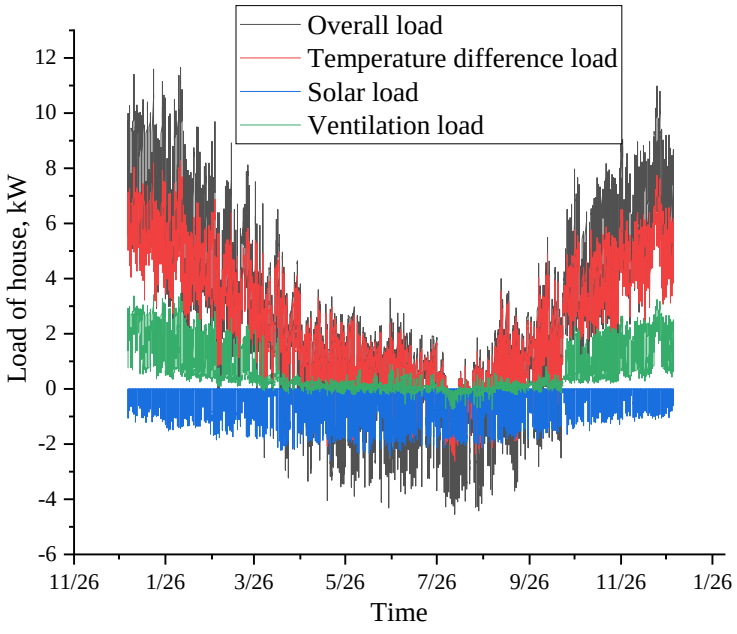

Fig. 7-7 Daily variations of the solar energy collection, heating and cooling load of Taiyuan along a year

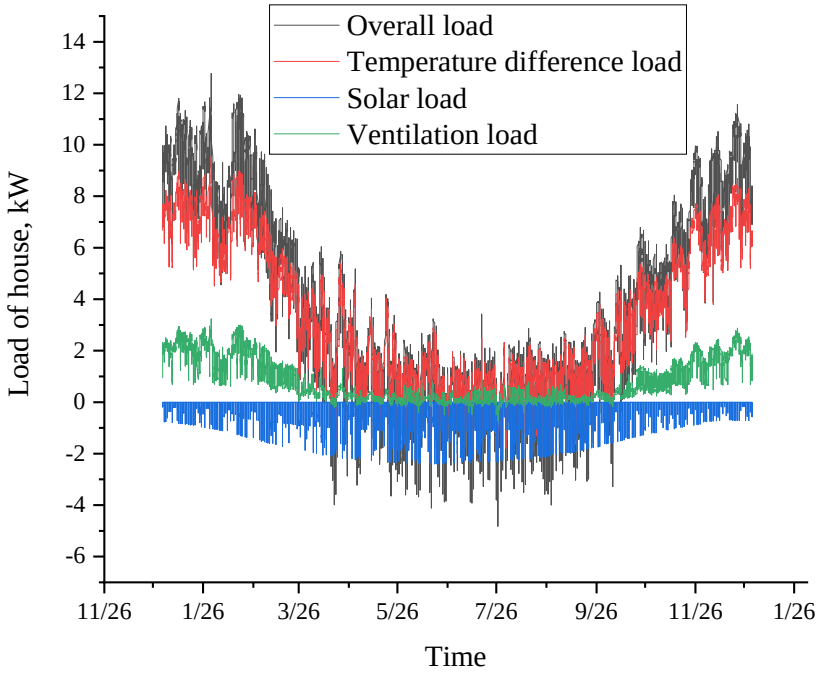

Fig. 7-8 Daily variations of the solar energy collection, heating and cooling load of Urumqi along a year

Fig. 7-9 shows the monthly heating load and cooling load of different cities. The heating load of the house in Urumqi is bigger than that of Taiyuan city, and Chongqing has the lowest heating load. The annual space heating load of the house from different cities is 10563.63kWh, 25997.66kWh, and 34317.52kWh separately. The cooling load of these cities is the opposite. The annual space cooling load is -4066.36kWh, -3242.42kWh, and -2584.19kWh separately.

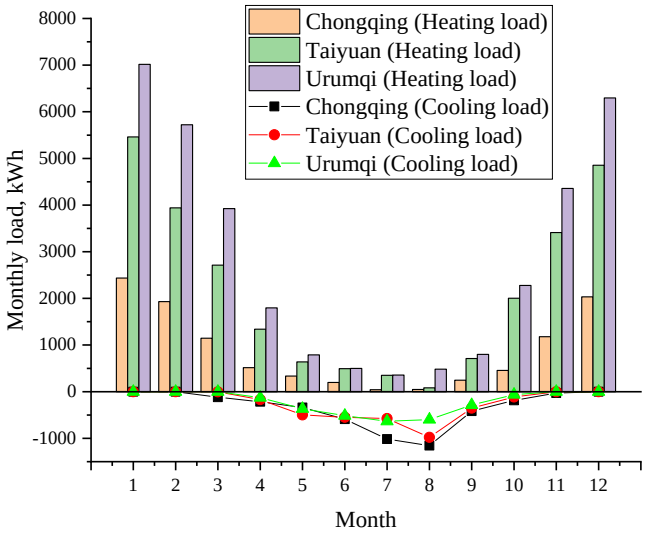

Fig. 7-9 Monthly heating and cooling load variation in three cities

The variation of the annual temperature difference and ventilation heating load in different cities are shown in Fig. 7-10. The annual temperature difference heating load of the house from different cities is 8196.07kWh, 20675.01kWh, and 28406.13kWh separately. The annual ventilation heating load from different cities is 1403.56kWh, 5487.97kWh, and 6654.93kWh separately.

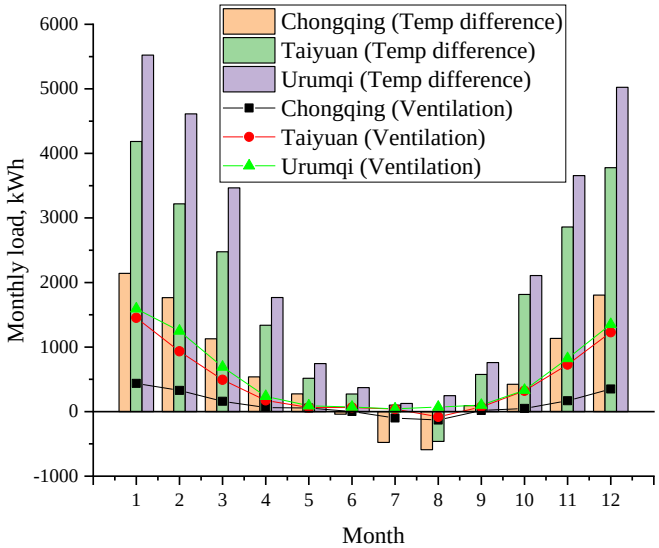

Fig. 7-10 Monthly temperature difference and ventilation load variation in three cities

The variation of the annual solar radiation cooling load in different cities is shown in Fig. 7-11. The total solar radiation cooling load of the house from different cities is -3102.36kWh, -3407.74kWh, and -3327.74kWh separately.

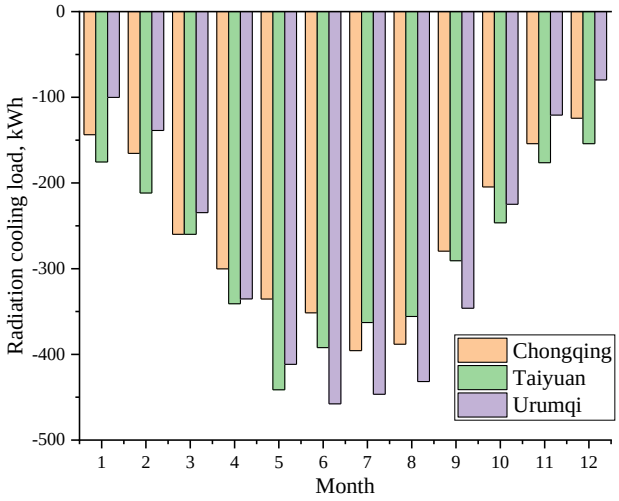

Fig. 7-11 Monthly solar radiation load variation in three cities

The variation of the daily room temperature under the operation of the system in different cities is shown in Fig. 7-12. Despite the huge fluctuation of the ambient temperature, the room temperature varies from 19°C to 22°C in winter heating season, and from 24°C to 27°C in summer cooling season. In January and December, the room temperature sometimes reaches the lowest, 18°C, because of the low ambient temperature, thus forming a high space heating load. During the hottest month, August, the room temperature can reach 27°C, which is also under a comfortable room temperature range. The stable room temperature is a direct illustration that the SAHR-HP system can perform well all year around.

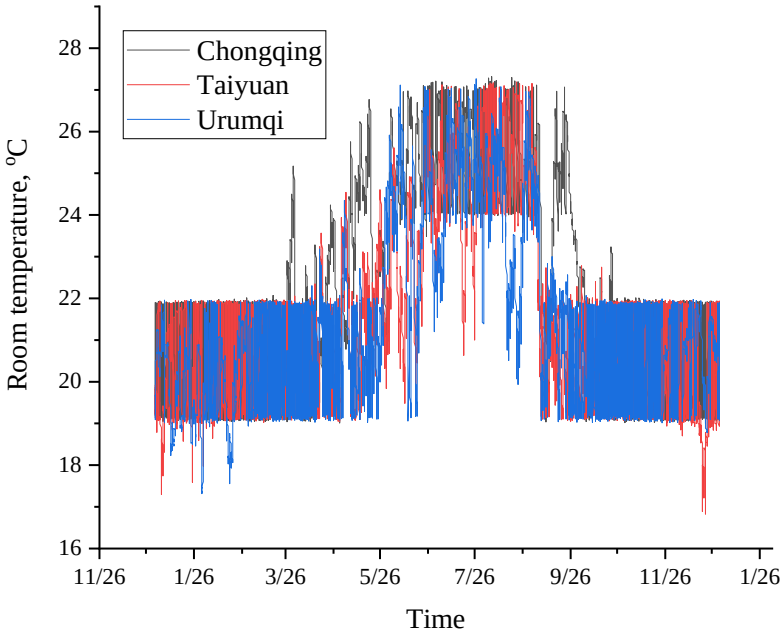

Fig. 7-12 Whole year room temperature variation in three cities

The heating and cooling supply capacity by different components of the system in different cities are shown in Fig. 7-13, Fig. 7-14, and Fig. 7-16 separately. Fig. 7-13 shows the heating and cooling supply capacity by VIHR-ASHP in different cities. Undoubtedly, during the operation of the system, the main heating and cooling capacity comes from VIHR-ASHP which can provide 6411.75kWh, 18276.33kWh, 27583kWh heating capacity in Chongqing, Taiyuan, and Urumqi separately which account for 60.7%, 70.3%, and 80.4% heating loads in different cities. In summer, the VIHR-ASHP provides 100% cooling capacity to the served house which is 5045.57kWh, 2242.87kWh, 1966.54kWh separately in Chongqing, Taiyuan, and Urumqi.

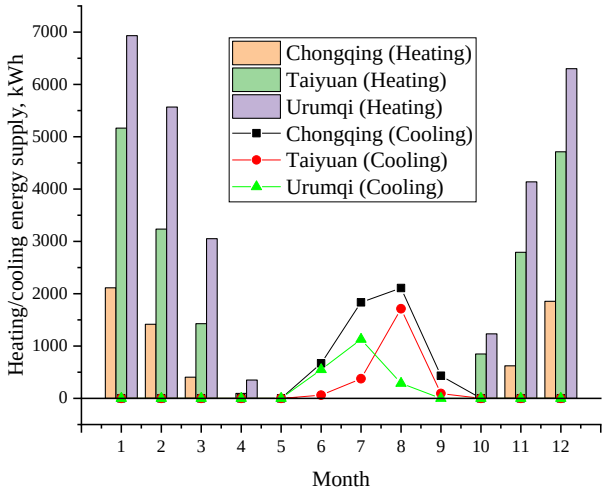

Fig. 7-13 Monthly heating and cooling capacity supplied by the VIHR-ASHP

Fig. 7-14 shows the heating capacity supplied by solar collectors in different cities. The heat collected from the solar collectors is mainly used to provide heating and domestic hot water. The collected heat of solar collectors is remained at a relatively low level in summer because of the low heating demand of the house and domestic hot water. In Chongqing, the collected heat peaks at 706.92kWh in March, and it peaks at 964.02kWh and 945.62kWh in April in Taiyuan and Urumqi separately.

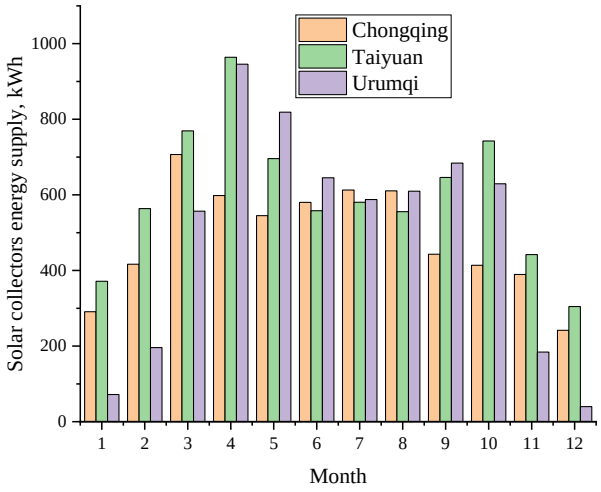

Fig. 7-14 Monthly collected heat by solar collectors

The percentage of the collected heat from the solar collectors accounting for the total heating demand in different cities is shown in Fig. 7-15. The percentage increases from January to July, and decreases from August to December. From March to October in Chongqing, April to September in Taiyuan, and May to September in Urumqi, the percentage accounts for the most heating load which means that the solar thermal collector can provide most of the heating capacity to meet the heating demand of the served house. More panels can be employed to increase the solar heat gain. However, the roof area and cost limit this option. Nonetheless, owing to the flexibility of the proposed system, it can perfectly fit the polytropic and complicated thermal environment, and maintain the room temperature at a relatively stable range, i.e. 19°C to 23°C.

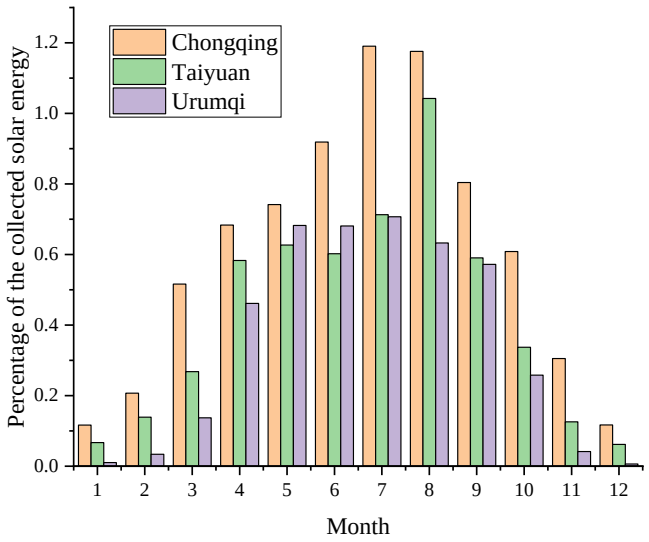

Fig. 7-15 Percentage of the collected heat by solar collectors over the heating demands

The heat recovery device (HRD) is also an important auxiliary heating and cooling device to reduce the heating and cooling load of the fresh air, and a counter-flow air-to-air plate-fin heat exchanger (PFHE) is chosen to recover the heat from exhaust air. Besides, when the temperature of the fresh air is lower than the room temperature in summer, the device can provide the fresh air

directly to the served house without a heat exchange process. As shown in Fig. 7-16, HRD can annually provide 2007.29kWh, 2852.33kWh, and 4730.77kWh heating capacity in Chongqing, Taiyuan, and Urumqi, and can provide 399.21kWh, 382.65kWh, and 344.21kWh cooling capacity in Chongqing, Taiyuan, and Urumqi. Among the cooling capacity, 98.19kWh in Chongqing, 112.28kWh in Taiyuan, and 183.46kWh in Urumqi, are provided by the direct cooling supply mode.

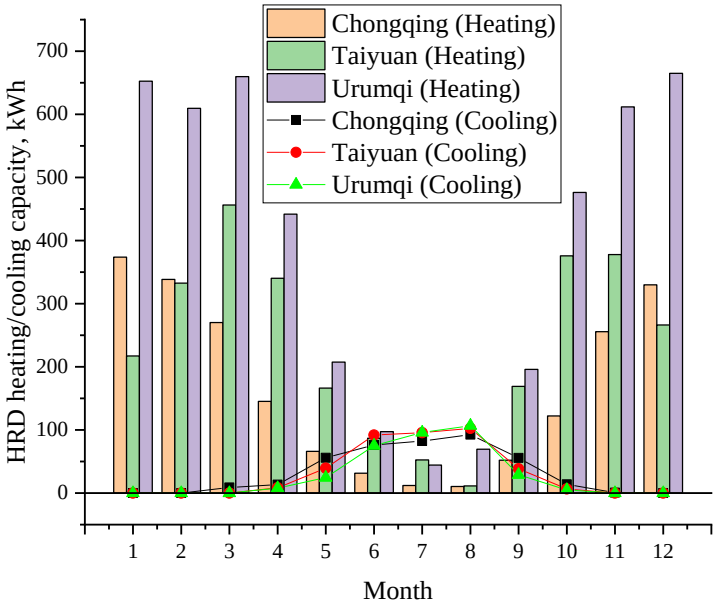

Fig. 7-16 Monthly heating and cooling capacity by HRD

The operation time of different components of the system, i.e., VIHR-ASHP and solar collectors array in different cities is shown in Fig. 7-17 and Fig. 7-18 separately. Under the heating mode, the operation time of VIHR-ASHP in March, April, and October is lower than the operation time from December to January because the heat load of the house is lower, and the solar energy provided by the solar collectors array is higher in March, April, and October. The total operation time of VIHR-ASHP for heating is 665.42h, 1988.92h, and 1531.42h in Chongqing, Taiyuan and Urumqi separately. When it comes to cooling, the operation time of VIHR-ASHP in Chongqing is higher than that of other cities.

The operation time of VIHR-ASHP under cooling mode is 543.58h, 232.25h, and 100.67h in Chongqing, Taiyuan and Urumqi separately.

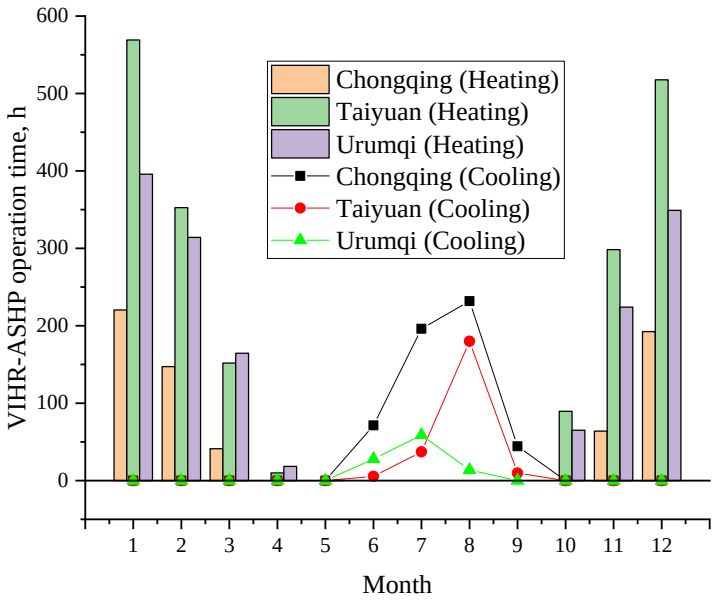

Fig. 7-17 Monthly heating and cooling time of VIHR-ASHP

As shown in Fig. 7-18, The solar collectors in Chongqing and Urumqi have the lowest operation time in December and January, and the operation time increases from January to July along with the increase of solar radiation. The operation time of the solar collectors in Taiyuan experiences a similar variation tendency, but the lowest operation time appears in March because of the rainy season. Eventually, the operation time of solar collectors in Chongqing, Taiyuan, and Urumqi is 893.99h, 945.92h, and 813.58h.

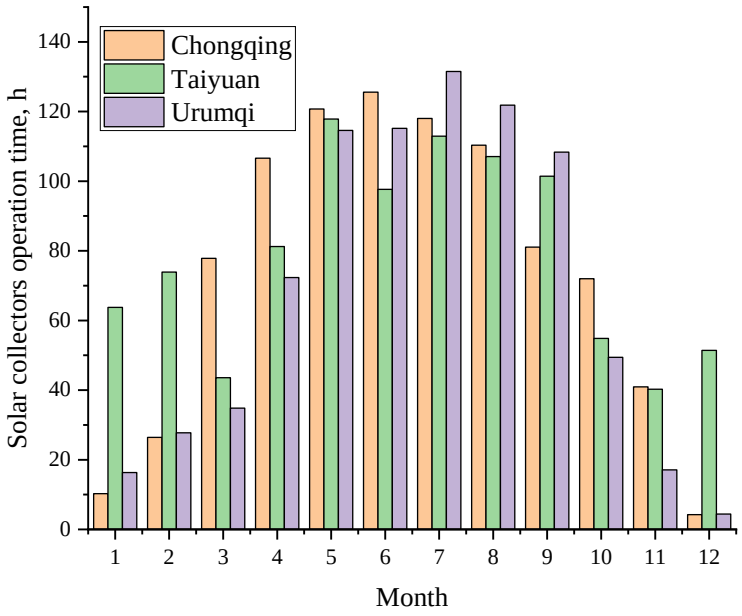

Fig. 7-18 Monthly operation time of the solar collectors

The PFHE operates all year to provide fresh air to the served house and recovery heating and cooling capacity from the exhausted air which can greatly help reduce the heat load of the house.

The variation of the daily average solar thermal efficiency of the solar collectors array in different cities is shown in Fig. 7-19, Fig. 7-20 and Fig. 7-21. There are two factors that can influence the variation of the solar thermal efficiency of the solar collectors, including solar radiation and the inlet temperature of the solar collectors array. Moreover, there are many factors that can influence the inlet temperature of the solar collectors array, i.e., the heat load of the house, HSEU operation status, and the outlet temperature of the underfloor coil. Consequently, the variation of the daily average solar thermal efficiency is complicated. However, most of the daily average solar thermal efficiency is situated from 40% to 60%, and the annual average solar thermal efficiency is 46.9%, 47.6%, and 42.9% in Chongqing, Taiyuan and Urumqi.

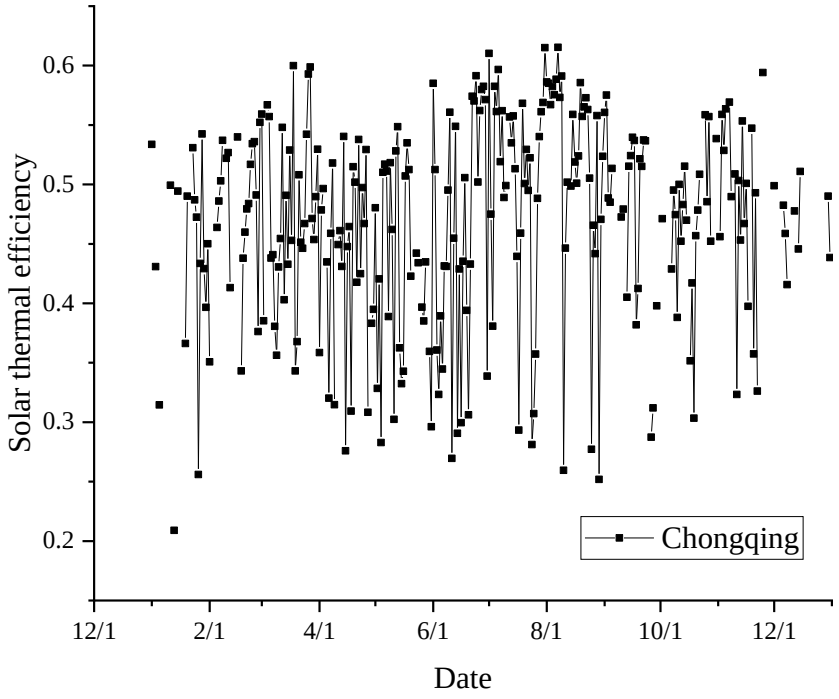

Fig. 7-19 Daily average solar thermal efficiency of the solar collectors array in Chongqing

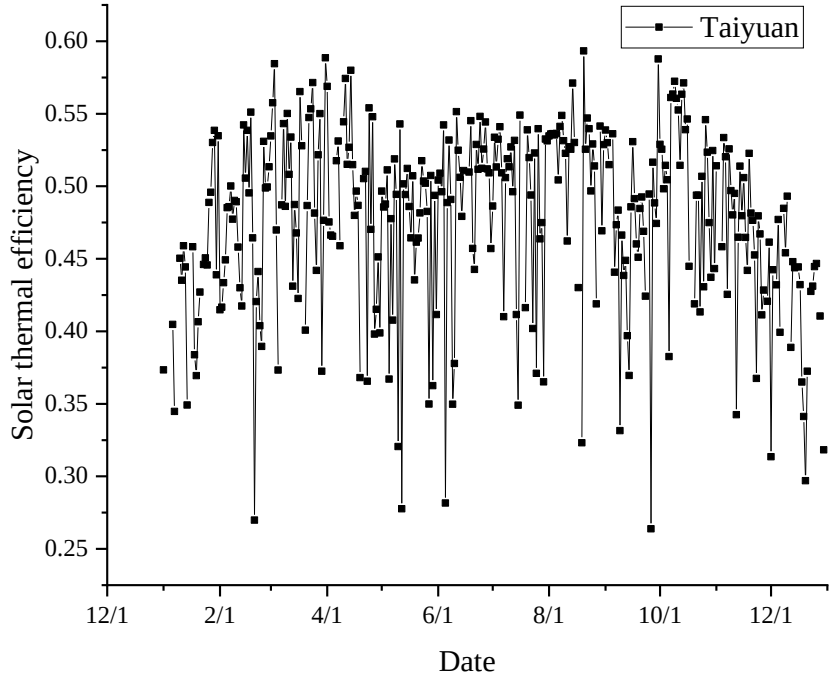

Fig. 7-20 Daily average solar thermal efficiency of the solar collectors array in Taiyuan

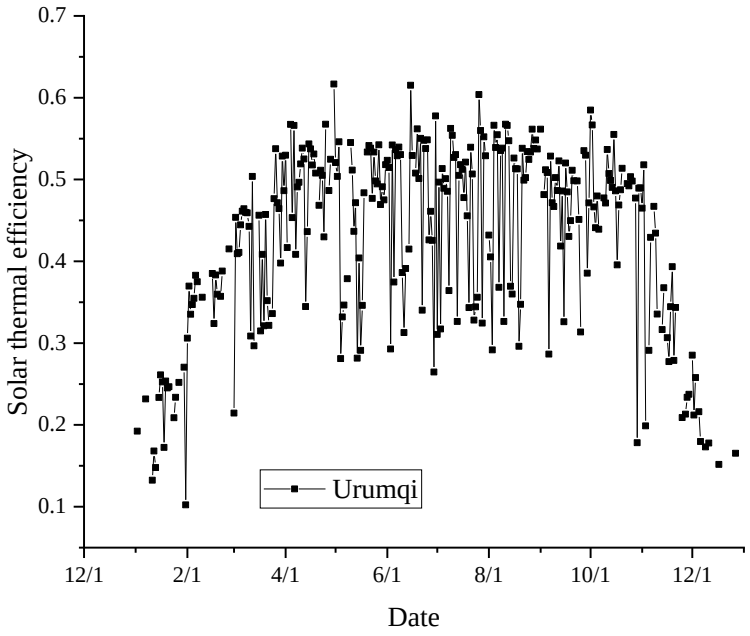

Fig. 7-21 Daily average solar thermal efficiency of the solar collectors array in Urumqi

The stored heat in HSEU and the heating supply time by the stored heat in different cities are shown in Fig. 7-22. The stored heat in HSEU and the HSEU heating supply time have similar variations. During the winter heating season from October to March, the stored heat and the heating supply time reach lowest in December and January because of the low collected heat from the solar collectors array, then reach high levels in February and November. From March to October, the stored heat in HSEU and the HSEU heating supply time have a similar variation with the variation of the heat load of the served house. The HSEU can annually provide 963.92kwh, 1926.23kwh, and 1669.23kwh heating capacity to the served house, and the heating supply time is 248.5h, 475.75h, and 397.08h in Chongqing, Taiyuan and Urumqi separately. Consequently, the HSEU can store 9.12%, 7.41%, and 4.86%, heating load of the house in Chongqing, Taiyuan and Urumqi respectively. The increasing heating supply time means the increased collected heat from the solar collectors array and the decreased heat load along with the increase of the ambient temperature.

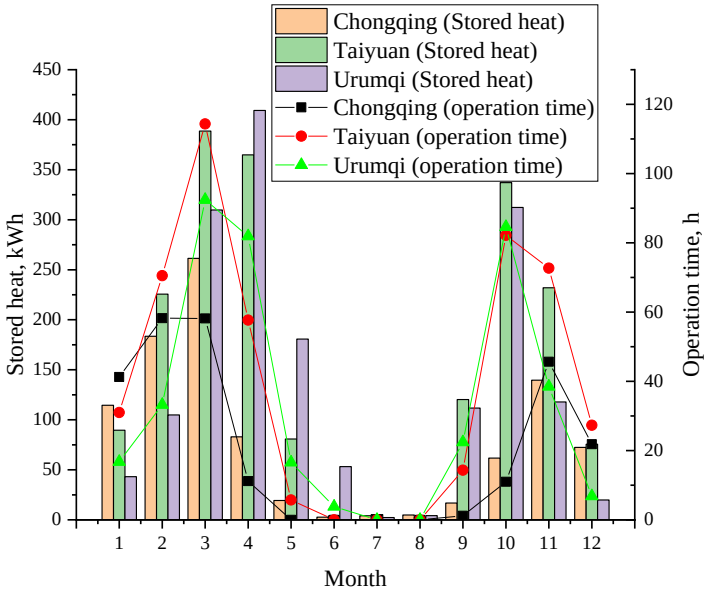

Fig. 7-22 Monthly HSEU stored heat and operation time of the HSEU

Given the specific system operation condition, the daily average COP of VIHR-ASHP in winter heating mode and summer cooling mode and the daily average COP of the solar collectors array in Chongqing, Taiyuan, and Urumqi are shown in Fig. 7-23, Fig. 7-24, and Fig. 7-25 separately. The results show that the COP of the solar collectors array fluctuates throughout the whole year because many factors can influence the performance of the solar collectors array. The annually average COP of the solar collectors array is 6.39, 7.68, and 6.91 in Chongqing, Taiyuan, and Urumqi respectively.

When it comes to VIHR-ASHP, the daily average COP increases slowly from January to April, and decreases slowly from October to December, the trend of which is in accordance with the variation of the ambient temperature. The annually average COP of VIHR-ASHP is 3.63, 3.40, and 3.01 in Chongqing, Taiyuan, and Urumqi respectively. In addition, the annually average COP under cooling mode is 2.70, 2.84, and 2.87 in Chongqing, Taiyuan, and Urumqi respectively.

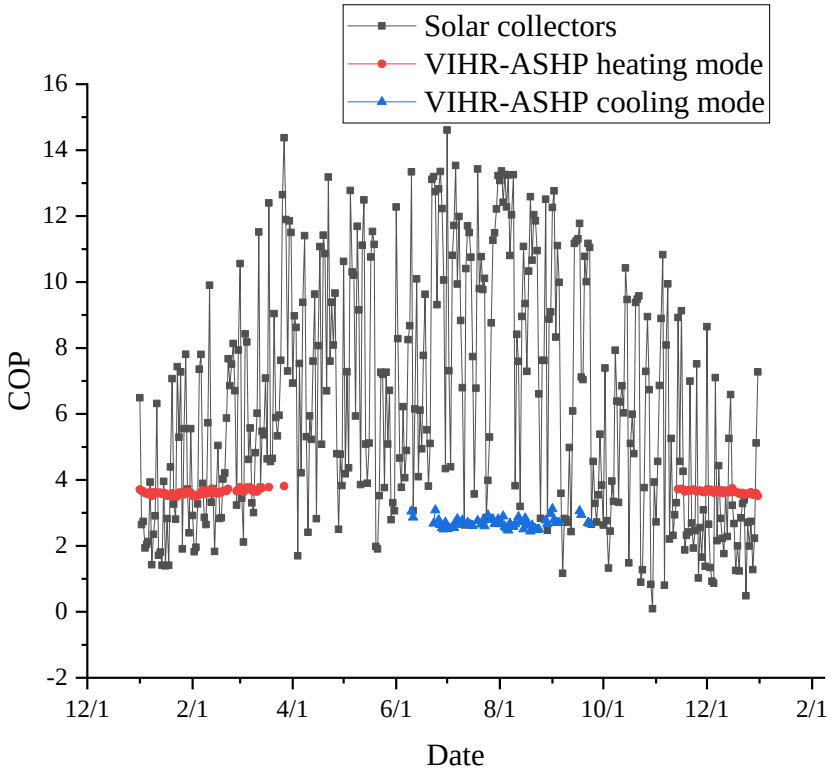

Fig. 7-23 Daily COP variation of the components of the system in Chongqing

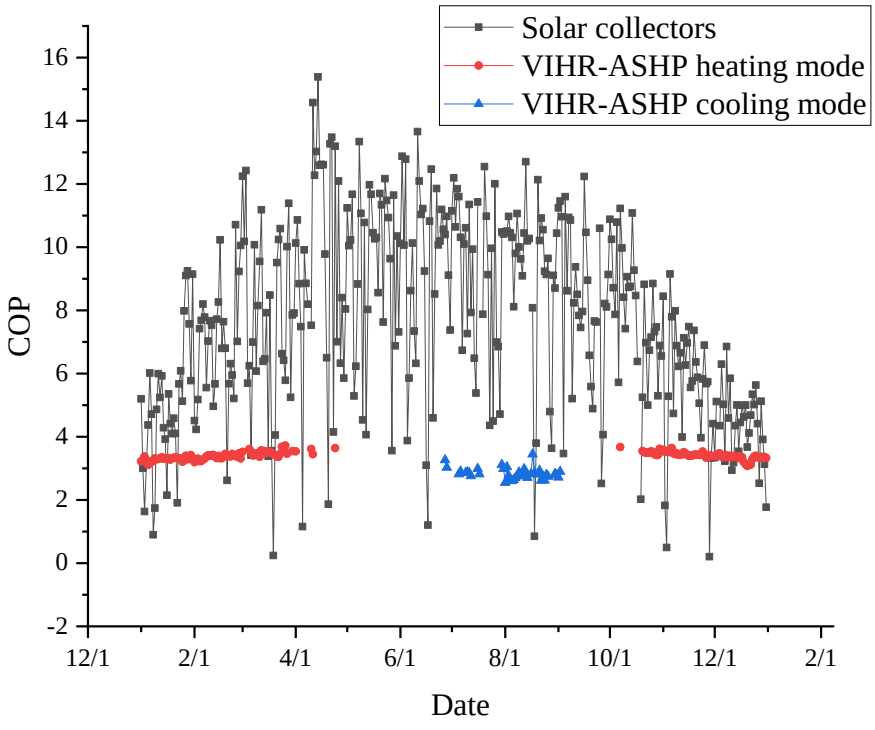

Fig. 7-24 Daily COP variation of the components of the system in Taiyuan

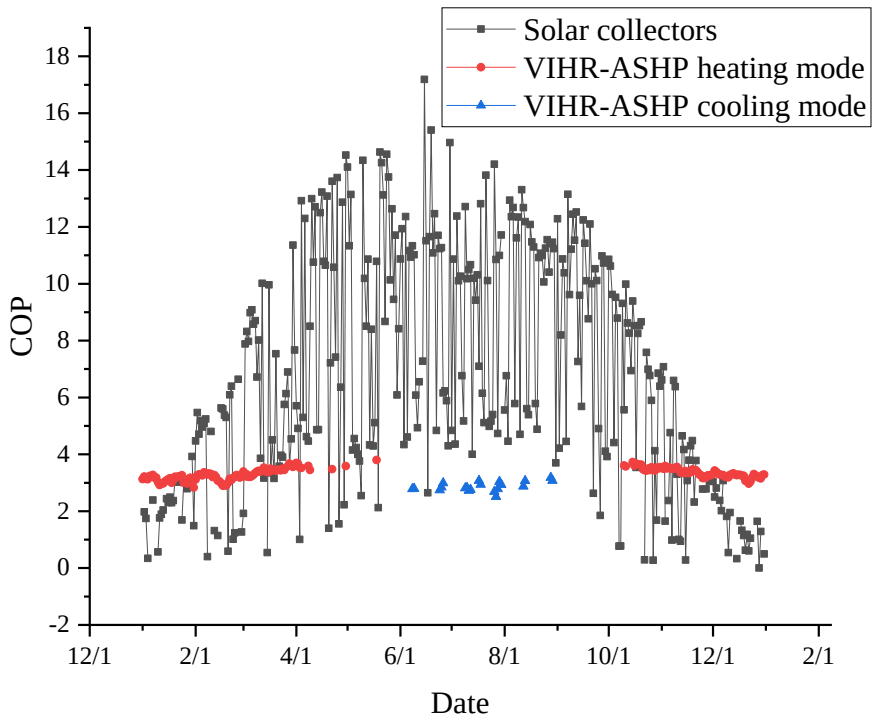

Fig. 7-25 Daily COP variation of the components of the system in Urumqi

The daily average COP of the PFHE under the heat recovery mode and fresh air supplying mode in Chongqing, Taiyuan, and Urumqi is shown in Fig. 7-26, Fig. 7-27, and Fig. 7-28 separately. The COP of the PFHE is high in winter heating season and low in summer cooling season because the temperature difference between the room temperature and the ambient temperature is high in winter and low in summer. The annually average COP of the PFHE under the heat recovery mode is 2.24, 4.10, and 5.71 in Chongqing, Taiyuan, and Urumqi. Besides, during the summer cooling season, the PFHE can provide cooling capacity directly under fresh air direct supplying mode when the ambient temperature lower than the room temperature. The COP of the PFHE under fresh air mode is higher than the heat recovery mode in summer, and the average COP of the fresh air mode is 2.14, 2.65, and 2.74 in Chongqing, Taiyuan, and Urumqi.

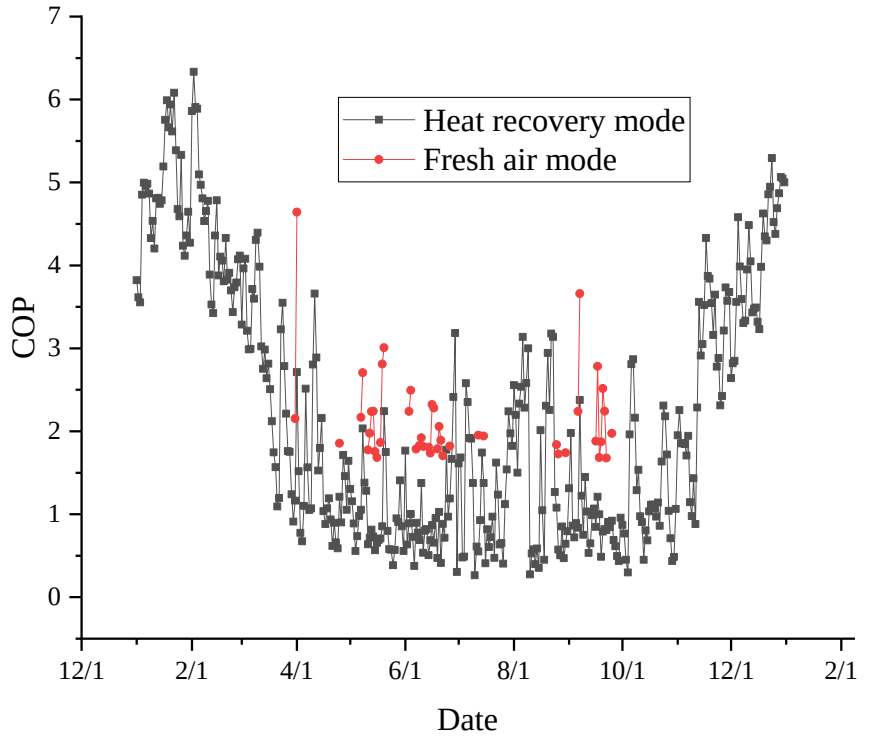

Fig. 7-26 Daily COP variation of the HRD of the system in Chongqing

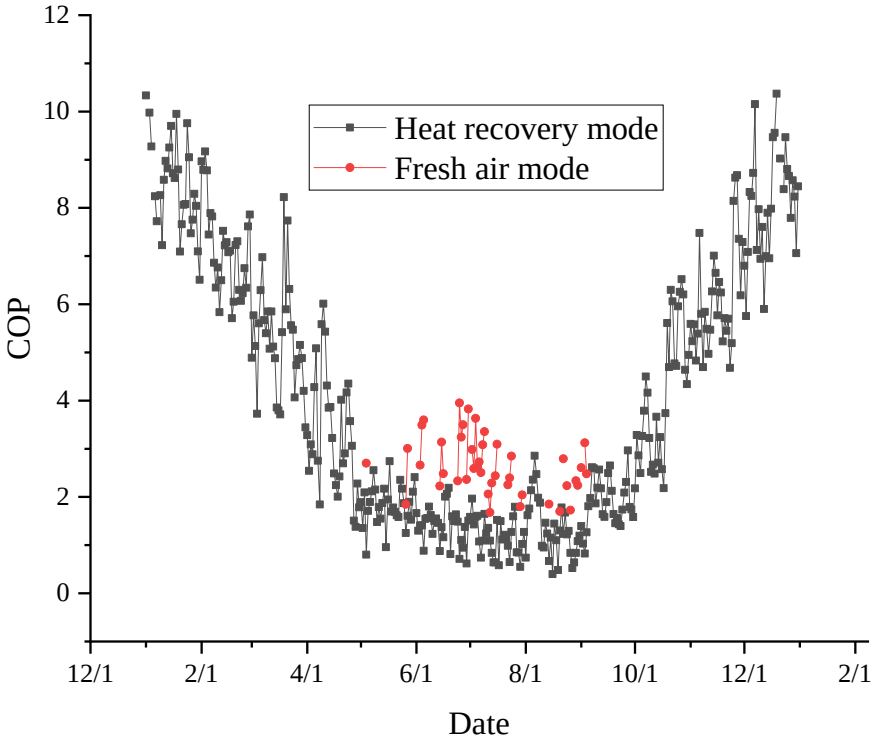

Fig. 7-27 Daily COP variation of the HRD of the system in Taiyuan

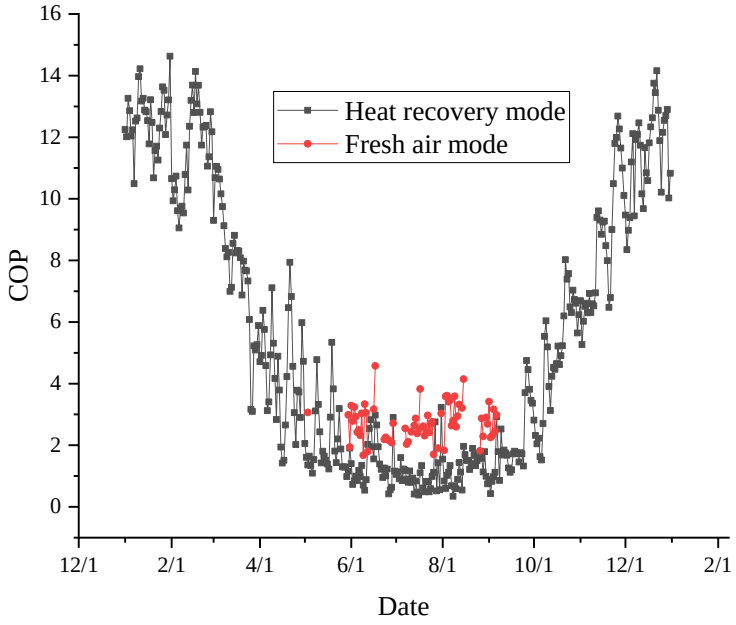

Fig. 7-28 Daily COP variation of the HRD of the system in Urumqi

According to the performance of the different components of the system, the monthly generated heat and COP of the SAHR-HP system in different cities can be concluded, and are shown in Fig. 7-29. The generated heating and cooling capacity are high in the winter heating season and summer cooling season. Under the transition seasons, from April to July, and September to November, the generated heating and cooling capacity are relatively low. Conversely, the COP of the system is high when the generated energy capacity is low, and is low when the generated energy capacity is high. The annually average COP of the system of a whole year is 3.86, 4.40, and 4.39 and the annually generated energy of the system is 19111.35kWh, 30406.84kWh, and 40272.09kWh in Chongqing, Taiyuan, and Urumqi separately.

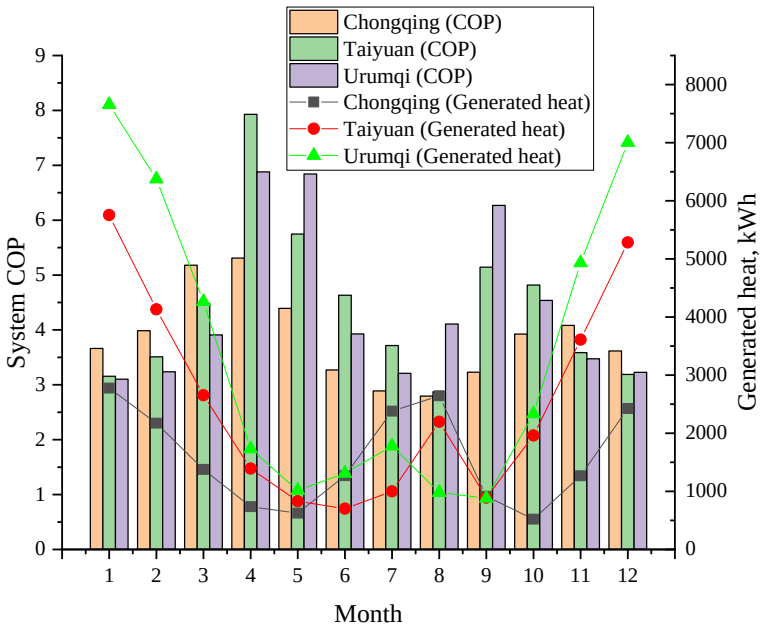

Fig. 7-29 Monthly system COP and energy generation

The collected heat of the domestic hot water tank from the collected solar energy is shown in Fig. 7-30. The collected heat is high in summer and low in winter because solar energy is mainly used for heating supply. The annually total collected heat of the domestic hot water tank is 3162.84kWh, 3245.81kWh, and 2975.30kWh in Chongqing, Taiyuan, and Urumqi, which can provide a total of 90.37tons, 92.74tons, and 85.01tons of domestic hot water separately.

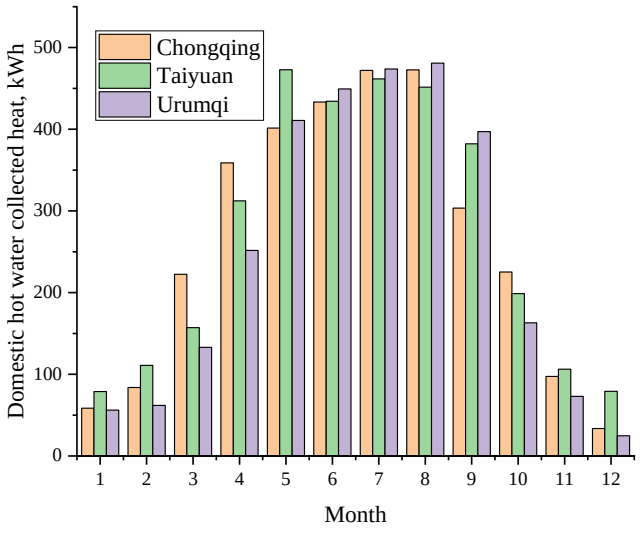

Fig. 7-30 Monthly generated heat of the domestic hot water tank

Heat recovery is the main characteristic of the novel system. The daily recovery heat of the VIHR-ASHP from the exhausted air of the building is shown in Fig. 7-31, Fig. 7-32 and Fig. 7-33 for the served house in Chongqing, Taiyuan, and Urumqi separately. The recovery heat of the VIHR-ASHP is high in winter and low in summer. There are no data during the transition season because the VIHR-ASHP stops. The annually total recovery energy of the VIHR-ASHP is 896.11kWh, 3900.71kWh, and 3724.41kWh in Chongqing, Taiyuan, and Urumqi separately.

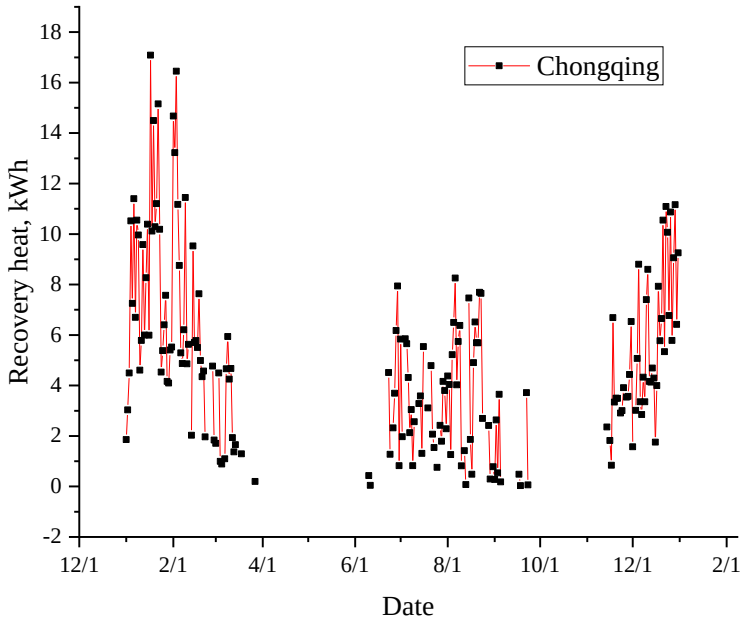

Fig. 7-31 Daily recovery heat of VIHR-ASHP in Chongqing

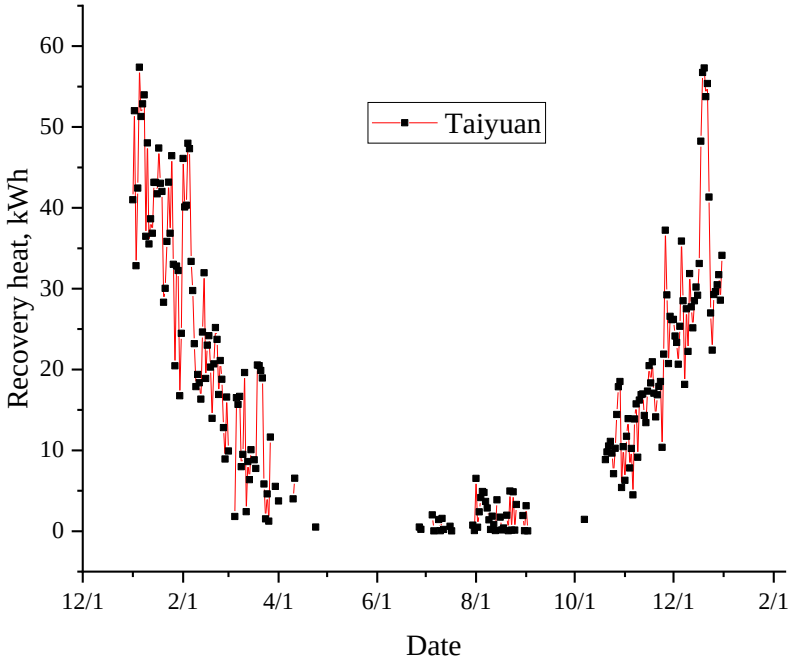

Fig. 7-32 Daily recovery heat of VIHR-ASHP in Taiyuan

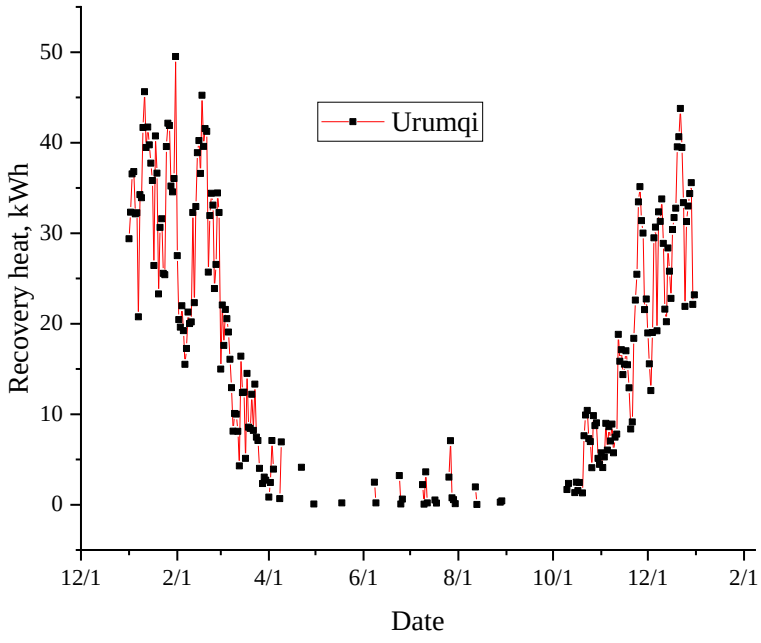

Fig. 7-33 Daily recovery heat of VIHR-ASHP in Urumqi

The HRD is an auxiliary device that can recover part of the heat from the exhausted air from the building while the VIHR-ASHP is stopped. The recovery heat of the HRD is the generated heating and cooling capacity under the heat

recovery mode which is shown in Fig. 7-16, and the annually total recovering heat of the HRD is 2308.31kWh, 3122.70kWh, and 4891.52kWh in Chongqing, Taiyuan, and Urumqi separately. Thus, the annually total recovering heat of the system is 3204.42kWh, 7023.41kWh, and 8615.93kWh in Chongqing, Taiyuan, and Urumqi separately, which accounts for 21.9%, 24.1%, and 23.3% load of house in the corresponding cities.

7.2.3 Electrical performance of the system in different cities

7.2.3.1 Electricity consumption of the system

The electricity consumption of the different components of the system, i.e., the water pumps, VIHR-ASHP, and the PFHE in different cities is shown in Fig. 7-34, Fig.7-35, and Table 7-2. The main electricity consuming component of the system is VIHR-ASHP. The electricity consumption of the VIHR-ASHP peaks in January. The total electricity consumption of the VIHR-ASHP under heating and cooling mode is 3669.02kWh, 6270.47kWh, and 9256.42kWh in Chongqing, Taiyuan, and Urumqi separately.

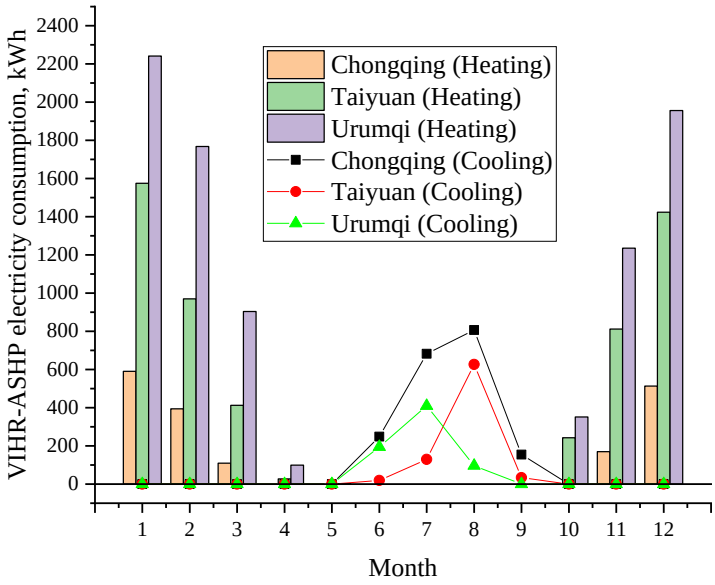

Fig. 7-34 Monthly electricity consumption of VIHR-ASHP

The annual electricity consumption of water pumps of the system is 421.94kWh, 758.05kWh, and 731.24kWh in Chongqing, Taiyuan, and Urumqi separately.

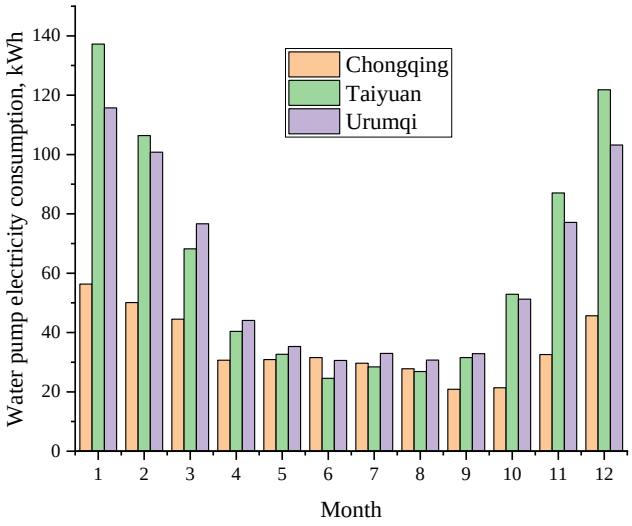

Fig. 7-35 Monthly electricity consumption of water pumps of the system

Table 7-2 HRD electricity consumption

Month	Jan	Feb	Mar	Apr	May	Jun
Consumption (kWh)	111.6	100.8	111.6	108	111.6	108
Month	Jul	Aug	Sep	Oct	Nov	Dec
Consumption (kWh)	111.6	111.6	108	111.6	108	111.6

7.2.3.2 Electricity generation of the system

The electricity generated by a PV panel can be expressed as [34]:

$$Q_{se} = NA_e I \eta_e \tau_{wy} \quad [7\text{- }1]$$

The photoelectric efficiency of the PV panel can be expressed as:

$$\eta_e = \eta_{rc}[7 - 1 - \beta_{PV}(T_c - T_{rc})] \quad [7\text{- }2]$$

The temperature of the PV cell can be expressed as:

$$T_c = T_a + \frac{(NOTC-20)}{0.8} I \quad [7\text{- }3]$$

To further reduce the electricity consumption of the system, four photovoltaic panels are applied, and each has an aperture area of $2m^2$. The electricity generation per square meter every month is shown in Fig. 7-36, which is $218.2kWh/m^2$, $244.43kWh/m^2$, and $239.66kWh/m^2$ annually in Chongqing, Taiyuan, and Urumqi. Hence, the total photovoltaic electricity production is 1745.58kWh, 1955.42kWh, and 1917.31kWh annually in Chongqing, Taiyuan, and Urumqi. The feed-in tariff is 0.75RMB/kWh, which means that the served house can earn a total of 1309.18RMB, 1466.57RMB, and 1437.98RMB per year separately by transferring the generated electricity into the power grid.

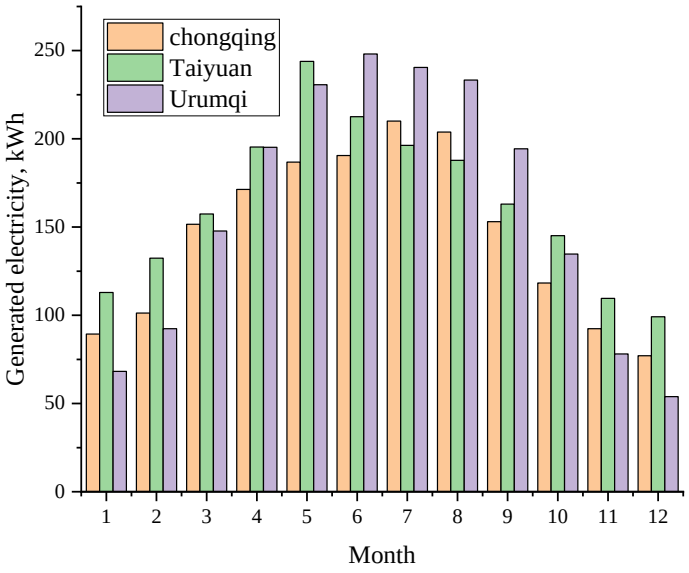

Fig. 7-36 Monthly electricity generation of PV panels in different cities

Table 7-3 The electricity utility price

Utility price	X≤ 170 kWh	171<X≤ 260 kWh	X>260 kWh
(RMB/kWh) [217]	0.477	0.527	0.777

According to the monthly electricity price as displayed in Table 7-3, the monthly electricity consumption and the corresponding cost of the whole system are shown in Fig. 7-37. The annual electricity consumption of the system is 5404.96kWh, 8342.52kWh, and 11301.66kWh in Chongqing, Taiyuan, and Urumqi separately.

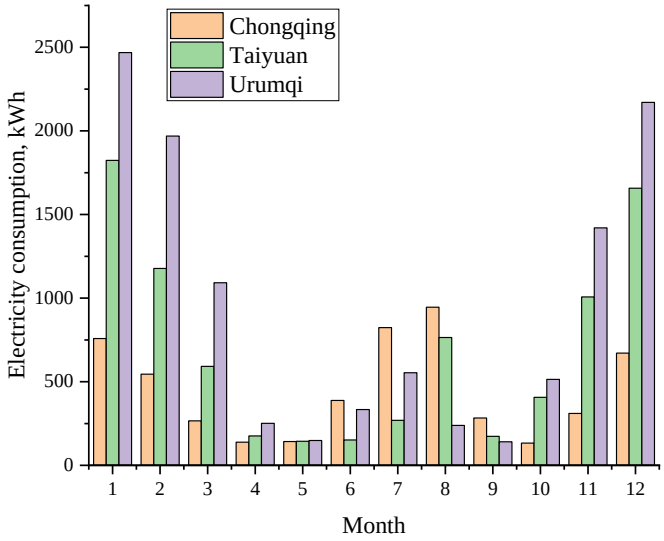

Fig. 7-37 Monthly electricity consumption of the system in different cities

The electricity cost of the system is shown in Fig. 3-38, and it is remarkably higher than that in other months in Taiyuan and Urumqi in January and December, since the low ambient temperature is accompanied by a high heat load for the building. In Chongqing, according to the high cooling load in summer, the electricity cost is higher. The total annual electricity cost for the system in Chongqing, Taiyuan, and Urumqi is 3413.9RMB, 5701.13RMB, and 7969.01RMB separately. Taking the earned money from the generated electricity of the PV panels into account, the annual operational cost of the system is

1086.46RMB, 3093.89RMB, and 5410.59RMB in Chongqing, Taiyuan, and Urumqi separately for space heating, cooling and hot water supply.

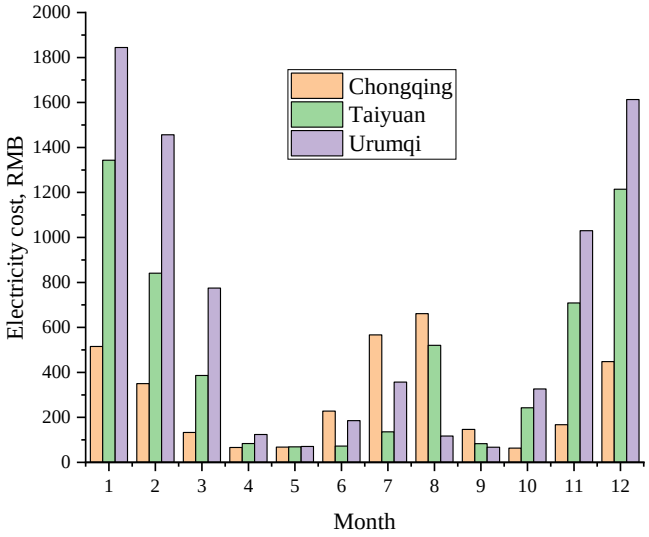

Fig. 7-38 Monthly electricity cost of the system in different cities

7.2.4 Energy proportions of the system

The energy proportions in terms of all generated energy of the different components of the system in different cities are shown in Fig. 7-39. VIHR-ASHP provides most of the energy to the system. HRD provides around 12% energy to the system in different cities.

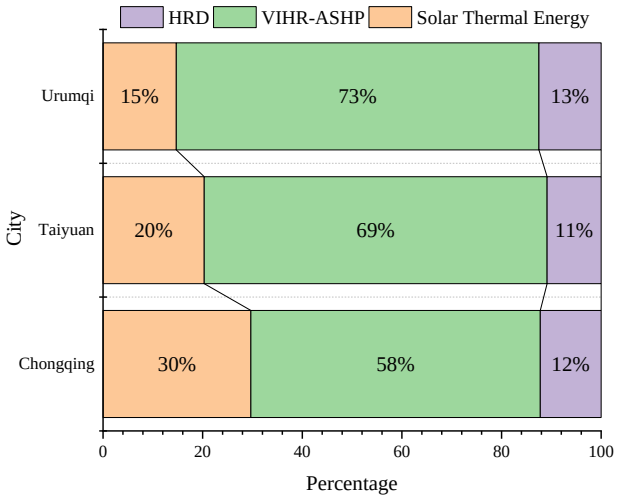

Fig. 7-39 Energy breakdown of the system

Overall, the photovoltaic profit provides 38%, 26%, and 18% of the total operation cost in Chongqing, Taiyuan, and Urumqi, as shown in Fig. 7-40, thereby making the system more economic and considerably decreasing fossil fuel consumption.

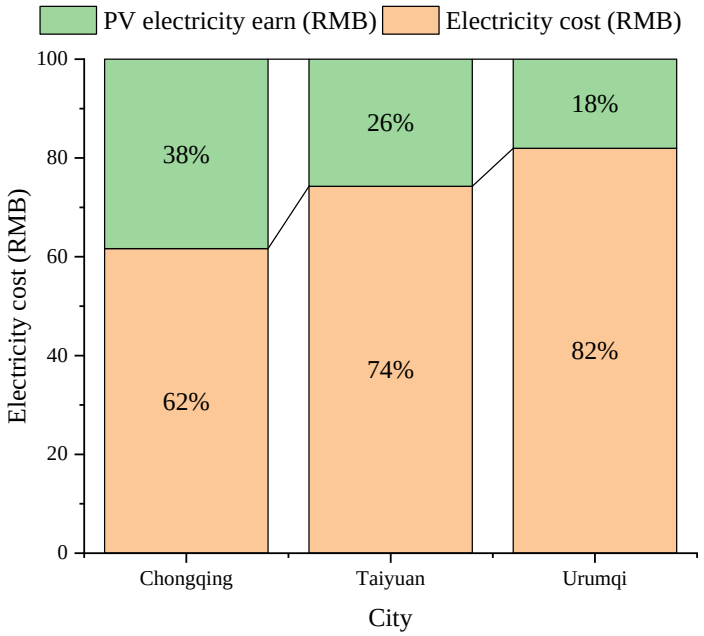

Fig. 7-40 Electricity breakdown of the system

7.3 Life-Cycle Economic Analysis

Energy consumption for space heating [218] and hot water [219] accounts for the majority of total building energy consumption in the north of China, and so far most of the rural houses have been using coal as the main energy source for cooking, space heating and hot water supplying. This has caused severe fossil fuel shortage and environmental pollution including a high level of harmful dust, PM2.5 concentration, greenhouse gas, CO_2 and harmful gases, i.e. SO_2 and NO_x [220]. The summer in most areas of northern China is hot and an ambient temperature above 30°C is common. The demand for cooling in rural houses is growing with improvements in people's living standards.

The initial capital cost of the novel SAHR-HP system includes the individual cost of all the system components, which we increase by 20% as a mark up to allow for commercial profits. The basic equipment cost is mainly divided into five parts: the solar thermal collectors array; PV panels; heat storage and exchange unit; VIHR-ASHP and all other miscellaneous costs, which include additional equipment such as pipes and pipe fittings, water pump, grid inverter and installation cost. Consequently, the initial capital cost can be expressed as:

$$C_{c,sp} = (\mathrm{C}_{PT} + \mathrm{C}_{PV} + \mathrm{C}_{HSEU} + \mathrm{C}_{HP} + \mathrm{C}_{ADD}) \cdot (1 + 20\%) \quad [7\text{- }4]$$

The other cost C_{ADD} is assumed to be 10% of the equipment cost, and is expressed as [221]:

$$\mathrm{C}_{ADD} = (\mathrm{C}_{PT} + \mathrm{C}_{PV} + \mathrm{C}_{HSEU} + \mathrm{C}_{HP}) \cdot 10\% \quad [7\text{- }5]$$

The cost payback period (PP) for operating this novel solar-powered space heating system to replace a conventional coal-powered space heating system can be expressed as[7-7]:

$$PP_{sp} = \frac{CapitalCost - Incentives}{Annual\ (Operational\ \&\ maintenance) CostSaving}$$

$$PP_{sp-c} = \frac{C_{c,sp} - C_{c,c} - C_{RE}}{\sum_1^{25}[(C_{o,c} + C_{m,c})_n - (C_{o,sp} + C_{m,sp})_n]} \quad [7\text{- }6]$$

Where $C_{o,sp}$ and $C_{m,sp}$ are operational cost and maintenance costs of the novel solar-powered heating system respectively.

To help fund the installation of a novel solar-powered heating system it may be possible to receive grants through the government's renewable policy. For example, the Renewable Heat Incentive (RHI) scheme is intended to encourage the uptake of renewable heating technologies within households, communities and businesses through the provision of financial incentives. Whilst there is

currently no financial incentive for solar thermal energy, the current feed-in tariff price for photovoltaic electricity is '¥0.75/kWh'[222]. As a result, the ultimate operational cost of such a system equals the basic operational cost including the operational cost by the VIHR-ASHP and water pumps minus the total earning of the generated electricity, which can be expressed by

$$C_{o,sp} = C_{o,hp} + C_{o,wp} - C_{te} \quad [7\text{-}7]$$

The maintenance cost of the systems in n year can be expressed as:

$$C_{m.n} = C_c[1 + z\frac{1+g_m}{g_m - 1}[(1+g_m)^n - 1]]$$

z represents the annual maintenance cost which is estimated at 2% of the initial system cost [223]. g_m is the inflation rate which is 3% in China [224]. As a solar-based system is usually considered to have a lifespan of 25 years [225], the life-cycle net cost saving, CS_{sp}, of this system in energy bills can be determined by

$$CS_{sp} = (Lifetime - paybacktime) \times Annual(Operational\ \&\ maintenance)CostSaving$$

$$CS_{sp-c} = \left(25 - PP_{sp-c}\right)\left[\left(C_{o,c} + C_{m,c}\right) - \left(C_{o,sp} + C_{m,sp}\right)\right] \quad [7\text{-}8]$$

Because the case study is set under the weather conditions in cities of China, the economic analysis in this study is based on the Chinese market. The initial capital cost of the proposed system is 30290RMB in Chongqing and Taiyuan, and a cost breakdown is shown in Table 7-4. Furthermore, the cost details of the components are presented in Fig. 7-41. Due to the higher heating load of the served house in Urumqi, the initial capital cost of the proposed system is 30290RMB in Urumqi, and a cost breakdown is shown in Table 7-5. Furthermore, the cost details of the components are presented in Fig. 7-42. Compared with the

SAHR-HP system, the coal-based heating system has a lower initial capital cost of 10400RMB, and a cost breakdown is shown in Table 7-6.

Table 7-4 Initial capital cost of the systems in Chongqing and Taiyuan

Solar assisted VI-ASHP system (Chongqing, Taiyuan)				
No.	Component	Quantity/Size	Unit Price (RMB)	Cost (RMB)
1	PV panels	4	1000	4000
2	Solar thermal collectors	8	787.5	6300
3	Heat storage and exchange unit	1	5000	5000
4	VI-ASHP	1	6000	6000
5	PFHE	1	2000	2000
Additional cost				10%
Additional profit				20%
Initial capital cost (RMB)				30290

Table 7- 5 Initial capital cost of the systems in Urumqi

Solar assisted VI-ASHP system (Urumqi)				
No.	Component	Quantity/Size	Unit Price (RMB)	Cost (RMB)
1	PV panels	4	1000	4000
2	Solar thermal collectors	8	787.5	6300
3	Heat storage and exchange unit	1	5000	5000
4	VI-ASHP	1	8000	8000
5	PFHE	1	2000	2000
Additional cost				10%
Additional profit				20%
Initial capital cost (RMB)				32890

Table 7-6 Initial capital cost of the systems

Coal-driven system				
No.	Component	Quantity/Size	Unit Price (RMB)	Cost (RMB)
1	Coal boiler	1	8000	8000
Additional cost				10%
Additional profit				20%
Initial capital cost (RMB)				10400

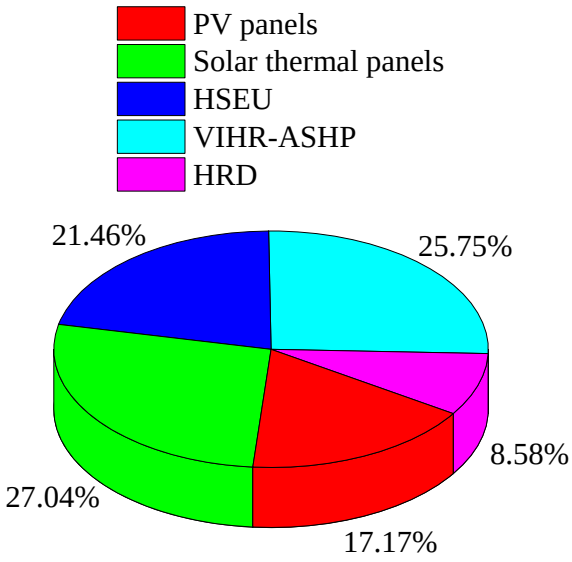

Fig. 7-41 Cost details of the different system components in Chongqing and Taiyuan

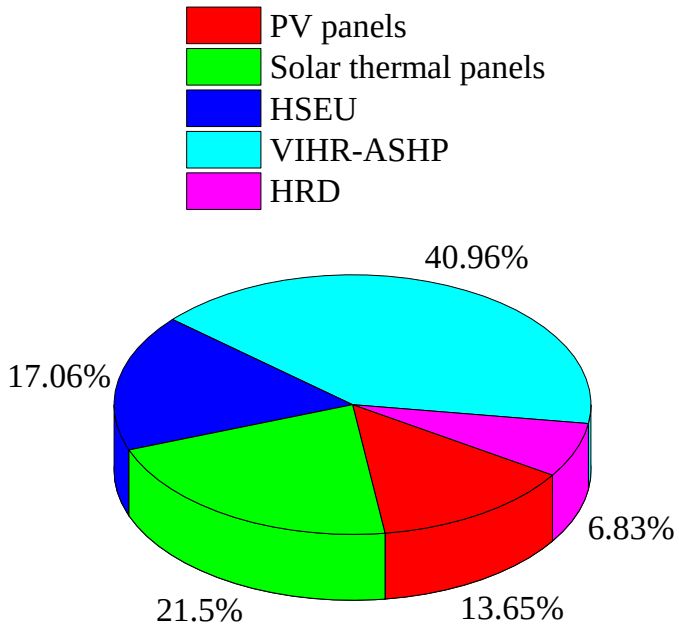

Fig. 7-42 Cost details of the different system components in Urumqi

According to the energy analysis of the system in different cities above, the annual operating costs, cost payback period and Life-cycle cost saving of the system in Chongqing, Taiyuan, and Urumqi are shown in Table 7-7, Table 7-8, and Table 7-9 separately. Coal is the most common energy source used for conventional heating systems in northern China, with a typical efficiency of 75% for a domestic heating system. The heat generated by burning 1kg of anthracite coal is 8kWh. Accordingly, in Chongqing, the required coal energy and quantity are 25481.8kWh and 3185.2kg separately. In addition, compared with the coal-driven system, the novel system has a cost payback period of 13.8 years and a life-cycle net cost saving of nearly 16145.84RMB in Chongqing city.

Table 7-7 Annual operating costs, cost payback period and Life-cycle cost saving of Chongqing

Required coal energy (kWh/yr)	25481.8
Required coal (kg/yr)	3185.22
Operational cost of coal-powered system (RMB/yr)	3873.23

Maintenance fee of coal-powered system (RMB/yr)	208
Operational cost of SAHR-HP system (RMB/yr)	2034
Maintenance fee of SAHR-HP system (RMB/yr)	605.8
Cost payback period	13.80
Life-cycle cost saving (RMB)	16145.84

In Taiyuan, the required coal energy and quantity are 40542.45kWh and 5067.81kg separately. In addition, compared with the coal-driven system, the novel system has a cost payback period of 12.37 years and a life-cycle net cost saving of nearly 20317.82RMB in Taiyuan city.

Table 7-8 Annual operating costs, cost payback period and Life-cycle cost saving of Taiyuan

Required coal energy (kWh/yr)	40542.45
Required coal (kg/yr)	5067.81
Operational cost of coal-powered system (RMB/yr)	6162.45
Maintenance fee of coal-powered system (RMB/yr)	208
Operational cost of SAHR-HP system (RMB/yr)	4156.34
Maintenance fee of SAHR-HP system (RMB/yr)	605.8
Cost payback period	12.37
Life-cycle cost saving (RMB)	20317.82

In Urumqi, the required coal energy and quantity are 40542.45kWh and 5067.81kg separately. In addition, compared with the coal-driven system, the novel system has a cost payback period of 12.37 years and a life-cycle net cost saving of nearly 20317.82RMB in Urumqi city.

Table 7-9 Annual operating costs, cost payback period and Life-cycle cost saving of Urumqi

Required coal energy (kWh/yr)	53696.12
Required coal (kg/yr)	6712.02
Operational cost of coal-powered system (RMB/yr)	8161.81
Maintenance fee of coal-powered system (RMB/yr)	208
Operational cost of SAHR-HP system (RMB/yr)	6452.33
Maintenance fee of SAHR-HP system (RMB/yr)	657.8
Cost payback period	17.85
Life-cycle cost saving (RMB)	9002

The results show the superior economic performance of the novel solar-powered system.

7.4 Life-Cycle Environmental Benefits

Four kinds of air contaminations, CO_2, harmful dust, SO_2, and NO_x, are measured in this study and the quantity can be expressed as:

$$m_{p.c} = m_{pu.c} m_{c.c} \quad [7\text{-}9]$$

Where $m_{p.c}$ is the mass of air contaminations generated by the coal-powered heating system, kg; and $m_{pu.c}$ is the mass of air contaminations generated by per unit anthracite coal separately, kg/kg.

As a result of the combustion of fossil fuel, harmful dust and other pollutants will be diffused into the air and cause severe pollution and global warming. The air contaminants generated from the combustion of 1kg of anthracite coal are shown in Table 7-10, and the annual contaminants for a standard Chinese rural house in different cities are shown in Table 7-11.

Table 7-10 The contaminants generated by per unit anthracite coal [226]

Per unit fossil fuel	Harmful dust	CO_2	SO_2	NO_x
Anthracite Coal /kg	0.0068kg	2.57kg	0.02kg	0.004kg

Table 7-11 The annual contaminants generated by coal-driven system

Contaminants	Chongqing	Taiyuan	Urumqi
Harmful dust	21.66	34.46	45.64
CO_2	8186.03	13024.26	17249.88
SO_2	63.70	101.36	134.24
NO_x	12.74	20.27	26.85

The reduction of contaminants by the SAHR-HP system is highlighted in Table 7-12, on the assumption that 100 sets of the systems (e.g., to meet the demand of a village) are used. The reductions in fossil fuel consumption and pollutants are significant. During the 25-year life span of the systems, the total carbon emission savings could reach 20465.1tons, 32560.7tons, and 43124.7tons in Chongqing, Taiyuan, and Urumqi compared with the coal-based system. Furthermore, the system diminishes the emission of a lot of other harmful substances, i.e., dust, SO_2 and NO_x, and therefore is a desirable approach to environmental sustainability.

Table 7-12 fossil fuel saving and air pollutant reduction

Contaminants	Chongqing	Taiyuan	Urumqi
Harmful dust (kg)	54148.82	86152.71	114104.3
CO_2 (kg)	20465070.63	32560658	43124696
SO_2 (kg)	159261.25	253390.3	335600.8
NO_x (kg)	31852.25	50678.07	67120.15

7.5 Uncertainty analysis

Uncertainty factors are common in the life cycle assessment (LCA), which could affect the reliability of results in quantifying the carbon emissions. The uncertainties in LCA-related studies could be summarised as parameter uncertainty and model uncertainty. Model uncertainty sourced from assumptions in modelling were usually evaluated by the sensitivity (or called scenario) analysis. However, parameter uncertainty due to either lack of knowledge or inaccuracy in input data needs to be analysed using statistical methods.

Parameter uncertainty of the life cycle emissions was made based on the data quality indicators (DQIs) statistical analysis, and Monte Carlo simulation (MCS) was implemented using MATLAB. It could be concluded that, the results of the stochastic simulation were in accordance with the results by deterministic analysis with respect to relative errors less than ±4.2%.

7.6 Chapter Summary

This chapter provided a feasibility study for the use of the prototype SAHR-HP system in three different cities which belong to three different climatic regions: Chongqing, Taiyuan, and Urumqi. Chongqing, Taiyuan, and Urumqi are located in the hot summer and cold winter area, cold area, and extreme cold area separately. The overall analysis included a prediction of the annual operational performance, economic rewards, and associated environmental benefits.

In these cities, Chongqing is suffering from no central heating method under the cold climate, and the other two cities are suffering from air pollution severely because of the coal-based winter heating system. Accordingly, using a renewable energy heating system to relieve environmental contamination is urgent. The simulation results involve the prediction of fossil fuel energy savings, cost payback period on investment and life cycle carbon emission reduction of the novel system, compared to

conventional coal-based heating systems.

The energy performances of the proposed SAHR-HP system for the served house in three cities are simulated and the results indicate that the annual heating load of the served house in Chongqing, Taiyuan, and Urumqi is 10563.63kWh, 25997.66kWh, and 34317.52kWh separately. The annual space cooling load of the served house are -4066.36kWh, -3242.42kWh, and -2584.19kWh separately. Under the operation of the SAHR-HP system, the room temperature of the served house can be maintained from 19°C to 22°C in winter heating season, and from 24°C to 27°C in summer cooling season. The stable room temperature is a direct illustration that the SAHR-HP system can perform well all year around.

Undoubtedly, during the operation of the system, the main heating and cooling capacity comes from VIHR-ASHP which can provide 6411.75kWh, 18276.33kWh, 27583kWh heating capacity in Chongqing, Taiyuan, and Urumqi separately which accounts for and accounts 60.7%, 70.3%, and 80.4% heating loads in different cities. In summer, the VIHR-ASHP provides 100% cooling capacity to the served house which is 5045.57kWh, 2242.87kWh, 1966.54kWh separately in Chongqing, Taiyuan, and Urumqi.

HRD can annually provide 2007.29kWh, 2852.33kWh, and 4730.77kWh heating capacity in Chongqing, Taiyuan, and Urumqi, and can provide 399.21kWh, 382.65kWh, and 344.21kWh cooling capacity in Chongqing, Taiyuan, and Urumqi. Among the cooling capacity, 98.19kWh in Chongqing, 112.28kWh in Taiyuan, and 183.46kWh in Urumqi, are provided by the direct cooling supply mode.

The total collected heat of the domestic hot water tank of the whole year is 3162.84kWh, 3245.81kWh, and 2975.30kWh in Chongqing, Taiyuan, and Urumqi, which can provide a total of 90.37tons, 92.74tons, and 85.01tons of domestic hot water separately.

Thus, the annually total recovering heat of the system is 3204.42kWh, 7023.41kWh, and 8615.93kWh in Chongqing, Taiyuan, and Urumqi separately, which accounts for 21.9%, 24.1%, and 23.3% load of the house in the corresponding cities.

The average COP of the system of a whole year is 3.86, 4.40, and 4.39 and the generated energy of the system of a whole year is 19111.35kWh, 30406.84kWh, and 40272.09kWh in Chongqing, Taiyuan, and Urumqi separately.

There are four photovoltaic panels, and each has an aperture area of $2m^2$. The total photovoltaic electricity production is 1745.58kWh, 1955.42kWh, and 1917.31kWh annually in Chongqing, Taiyuan, and Urumqi. The feed-in tariff in Shanxi is 0.75RMB/kWh, which means that the served house can earn a total of 1309.18RMB, 1466.57RMB, and 1437.98RMB per year separately by transferring the generated electricity into the power grid. Taking into account the earned money from the generated electricity of the PV panels, the annual operational cost of the system is 1086.46RMB, 3093.89RMB, and 5410.59RMB in Chongqing, Taiyuan, and Urumqi separately for space heating, cooling and hot water supply. Overall, the photovoltaic profit provides 38%, 26%, and 18% of the total operation cost in Chongqing, Taiyuan, and Urumqi.

In addition, compared with the coal-driven system, the novel system has a cost payback period of 13.8 years, 12.37 years, and 17.85 years in Chongqing, Taiyuan, and Urumqi and a life-cycle net cost saving of nearly 16145.84RMB, 20317.82RMB, and 9002RMB.

On the assumption that 100 sets of the systems (e.g., to meet the demand of a village) are used. The reductions in fossil fuel consumption and pollutants are significant. During the 25-year life span of the systems, the total carbon emission savings could reach 20465.1tons, 32560.7tons, and 43124.7tons in Chongqing, Taiyuan, and Urumqi compared with the coal-based system. Furthermore, the system diminishes the emission of a lot of other harmful substances, i.e. dust, SO_2 and NO_x, and therefore is

a desirable approach to the environment sustainability.

In summary, the novel SAHR-HP system can significantly improve energy efficiency and reduce the energy consumption for space heating, cooling, and hot water supply. It is a promising approach to near-zero carbon emission from buildings. Although the system is demonstrated in northern China, it is expected to be applicable in other cold regions of the world. The research results should assist in configuring feasible solutions for SAHP technologies and developing the basis of novel solar-driven heating systems for space heating/cooling, hot water supply and natural ventilation in the future. The core technologies could enable a significant reduction in fossil fuel energy and the associated carbon footprint in a built environment.

CHAPTER 8: CONCLUSION AND FURTHER WORK

8.1 Conclusions

This research has presented an in-depth study of a novel solar assisted heat recovery heat pump (SAHR-HP) system. To summarise, the study included the following elements; a critical literature review, optimal preliminary design, theoretical analysis, the development of simulation models, prototype construction, laboratory-controlled and field testing, validation of the simulation models, energy performance, economic performance and environmental influence analysis.

Key achievements of this study include: (1) A novel mini-channel solar thermal collector with a multiple-throughout-flowing connection; (2) A novel double-layer HSEU; (3) A novel vapour injection heat recovery air source heat pump (VIHR-ASHP); (4) An integral SAHR-HP system assembled using our novel components; (5) Individual simulation models for each major part of the system and an integrated model for the whole SAHR-HP system; and (6) An energy performance, socio-economic numerical model that can predict the system performance, energy savings and economic/environmental benefits of using the prototype technology in a certain climatic region. The major conclusions derived from this PhD research are given below.

8.1.1 Multiple-throughout-flowing connection of the solar collectors array

An innovative multiple-throughout-flowing mini-channel solar-panels-array was investigated theoretically and experimentally. Compared to traditional one-to-one connected panels, the novel multiple-throughout-flowing mode can achieve around a 10% higher overall solar thermal efficiency and an 80% higher energy efficiency ratio (EER), while the cost of the solar-panels-array is the same for both modes. Furthermore, the multiple-throughout-flowing mode creates a higher flow speed

within the panel flow channels, which leads to a higher solar thermal efficiency for the individual panels ranging from 7.5% to 15.4%. In addition, the multiple-throughout-flowing mode circulates the working fluid throughout the panels-array several times. This can reduce the temperature difference between the head and rear panels and thus increase the overall solar thermal efficiency of the array by around 10%. Last but not least, the multiple-throughout-flowing mode reduces the fluid flow turning points within the panels. This leads to a significantly lower fluid flow resistance and hence a much higher EER, ranging from 62% to 68% higher. The performance of the multiple-throughout-flowing panel-array is greatly impacted by the number of panels, the number of fluid flow turning points and the fluid flow speed. It was found that the optimum parameters were 10 panels in the array, 5 fluid flow turning points and a fluid flow speed of 0.3m/s. The established analytical model in this research shows good accuracy in predicting the performance of the multiple-throughout-flow collectors array, with a discrepancy of less than 10%.

8.1.2 Fast response heat storage and exchange unit

A novel double-layer stratified HSEU was developed to provide a solar heating system with high-efficiency and fast-response. The proposed HSEU is divided into two parts; the upper part with a large water volume to store heat and the bottom part with a low water volume to increase the heat transfer process. An insulative plate board with a one-way valve is set between two layers to prevent heat exchange between the upper and lower tanks. The bottom part of the HSEU is designed for fast heat transfer from the solar energy conversion loop to the heating loop, without the need to heat up the large volume of water within the whole HSEU tank. The large part of the HSEU is designed to charge and discharge heat into the small heat exchange tank, thus storing spare heat and then releasing stored heat for space heating as required. Several features of the HSEU have been investigated; the heat transfer between the solar loop and heating loop fluids, the heat and mass transfer between the small and larger part fluids and the associated operational strategy, both experimentally and theoretically. The

interactive double-layer structure enables the novel HSEU to respond to the heat demand of the served space in a faster and more energy efficient way. While a conventional HSEU is much slower to provide heating after sunrise, the system with the new HSEU can provide heating to the served space within approximately 20 minutes of sunrise. With a relatively low solar radiation level of 200 - 300 W/m^2, the system can deliver 40°C hot water to the heating loop system for the purpose of space heating. The analytical model developed by the authors achieved a good accuracy in predicting the performance of the HSEUs, giving a discrepancy of less than 10% compared to experimental results. The new HSEU design can significantly increase the heat transfer effect. According to theoretical calculation, the new HSEU has a considerably higher heat transfer coefficient (391W/m^2·K) compared to that of the conventional HSEU (60.5 W/m^2·K). In addition, the novel HSEU led to an increase in solar thermal efficiency for the panel-array, due to a reduced temperature at the inlet. This leads to enhanced heat transfer between the solar loop and heating loop fluids and between the small and large tank. Experimental Results showed an increase in the solar thermal efficiency for the panel-array of 7.5% under a solar radiation level of 500 W/m2. The capability of the novel HSEU to store the spare heat and maintain the room temperature was also investigated. During the day time the temperature of the HSEU increased from 35°C to 48°C, thus storing 25kWh of heat within the tank. At night when the room temperature fell to the lower limit, the HSEU released the stored heat to maintain the room temperature, which shows that the HSEU can extend the heating service time.

8.1.3 Vapour injection heat recovery air source heat pump (VIHR-ASHP)

This is the first time that a novel VIHR-ASHP with two evaporators has been proposed. In order to improve the performance, a vapour injection compressor has been embedded into a heat recovery heat pump system (HRHPS). The vapour injection compressor is characterised with two suction nozzles which are connected to the intermediate-pressure side (vapour injection line) and low-pressure side (evaporation

line) respectively. The novel VIHR-ASHP can make full use of the structural characteristics of the vapour injection compressor with the addition of an evaporator into the vapour injection line. The newly designed structure of the VIHR-ASHP can flexibly use either exhaust air or fresh air as the energy source, thus removing restrictions introduced by the heating capacity and the limited volume of exhaust air. In addition, the evaporator in the vapour injection line can significantly increase the heat transfer capacity and refrigerant mass flow rate on the intermediate pressure side. This results in a lower final compression ratio, leading to an increased performance for the heat pump. Another advantage of the novel VIHR-ASHP lies in the effective defrosting process, which uses exhaust air to defrost the heat pump and can significantly decrease the defrosting time and energy consumption.

An experimental platform of the VIHR-ASHP was built to carry out a system performance experiment in a specialised heat pump laboratory. In order to ensure the accuracy of the experimental data and the derived parameters, the uncertainties were calculated for; the generated heat, the coefficient of performance (COP), the total refrigerant mass flow rate, the final compression ratio and the intermediate compression ratio. The calculated uncertainties were in the range of 0.35%-0.61%, which is considered satisfactory for this study.

In order to get fresh air and exhaust air simultaneously the experimental platform utilised both a controlled laboratory environment and the surrounding ambient environment. This allowed us to simulate winter ambient air with a low temperature and the inside air of the building with a high temperature. Following is a summary of the key findings and conclusions of the study.

First, the experiment tested the influence of the refrigerant charging quantity on the heat pump performance. The results showed that the COP reached 2.5 when the refrigerant charging quantity reached 2.7kg, as the increased refrigerant mass flow rate directly results in an increased heat transfer capacity for the heat pump. When the

refrigerant charging quantity increased further, the COP remained constant, which means that the optimal refrigerant charging quantity is 2.7kg.

Second, we tested the performance of the VIHR-ASHP under different Electrical Expansion Valve (EEV) apertures. The heat pump cannot operate under 10% Evaporation Line Aperture (ELA), as a shortage of refrigerant in the compressor will trigger the self-protection programme, causing the heat pump to shut down automatically. When the ELA increased from 15% to 30%, the generated heat and COP of the heat pump increased with vapour injection line aperture (VILA) from 5% to 10% and then decreased with VILA from 10% to 30%. When ELA and VILA were under 20% and 10% respectively, the generated heat and the COP of the heat pump peaked at 8.3kW and 3.65kW respectively, and the final compression ratio reached its lowest level. When the heat pump was under the optimal working conditions, the evaporation temperature in the evaporation line also reached its highest value.

Different exhaust air volume flow rates were tested for the VIHR-ASHP. It was found that the heat capacity and the COP increased with an increase in air velocity, and remained constant when the air volume flow rate passed 1584m^3/h. At 1584m^3/h, the refrigerant mass flow rate increased and the two compression ratios decreased, with the increase of the exhaust airflow rate.

For the defrosting process, the novel VIHR-ASHP does not use the compressor to perform a reverse-compression cycle, unlike conventional air-source heat pumps. The exhaust air can directly perform the defrosting process. According to the experimental results, the defrosting process of the VIHR-ASHP took just 4mins without any power consumption, showing that it is very quick and energy efficient.

The numerical study of the VIHR-ASHP is conducted to explore the influences caused by the associated factors, i.e., the ambient temperature, the condensation temperature, the vapor injection temperature, and the mass flow ratio of ambient air to exhaust air. In addition, the performance of the VIHR-ASHP is compared with the conventional

vapour injection heat pump (VIHP) and an air source heat pump (ASHP). The result shows that compared to existing heat pump technologies, this proposed system comprises unique features. It is the first time that vapour injection heat pump has been used to recover waste heat of exhaust air from the buildings. The new VIHR-ASHP system overcomes technical challenges and gives several advantages: (1) Minimizing the ventilation heat loss. Unlike a conventional EAHP that extracts energy from exhaust air to heat the fresh supply air, the VIHR-ASHP uses both exhaust and outdoor air as the heat sources. It has a higher heating capacity at a given mass flow rate of exhaust air and the waste heat recovery ratio is more than 100%. By recovering the ventilation heat loss, the VIHR-ASHP can save about 23% of electricity consumption as compared with a conventional ASHP at normal operation conditions of condensation temperature of 45°C and an ambient temperature of -10°C; (2) Defrosting of heat pump in cold climate areas. The VIHR-ASHP has flexible operation modes. In the defrosting mode for which the vents for the ambient air are shut down, the VIHR-ASHP provides a promising solution to frosting by using the exhaust waste heat without additional electricity consumption. The seasonal performance factor is expected to be significantly higher than that of a conventional ASHP regarding the near-zero electricity consumption for defrosting; (3) The performance of the VIHR-ASHP is affected by the ambient temperature, condensation temperature, vapor injection temperature and air flow ratio. A lower ambient temperature will increase its advantages over conventional air source heat pump and vapor injection heat pump. An increment in the condensation temperature leads to a decrement in the COP but has no impact on the waste heat recovery. The optimum vapor injection temperature is about 5°C at an ambient temperature of - 10°C, which increases as the condensation temperature rises. The flow ratio of the ambient air to the exhaust air influences the COP and heating capacity. A higher flow ratio is accompanied with a lower proportion of ventilation heat loss; (4) The largest exergy destruction takes place in the compressor, which accounts for about a third of the total exergy losses in the VIHR-ASHP. This is followed by the exergy destruction in the condenser (about 20%) and

LP evaporator (about 10%). Among the components, the MP evaporator has the least exergy destruction. In all the simulation scenarios, the proposed heat pump is most beneficial under the conditions of an ambient temperature of about -10°C and the condensation temperature of about 40-45°C.

In summary, the novel VIHR-ASHP provides a new design for a heat recovery device (HRD) with enhanced performance, flexibility and practicability. It can be widely applied within building ventilation systems to reduce energy consumption.

8.1.4 The integral SAHR-HP system test and its simulation/optimisation models

According to the test results from the integral system test, the solar array has an efficiency of approximately 80%, which is higher than that of a conventional flat plate solar collector operating at the same temperature, and the COP of the heat pump ranges from 3 to 4.5, depending on the operating temperature of the storage tank.

A dedicated economic and environmental performance study of the novel SAHR-HP system for space heating, cooling and domestic hot water in cold regions is proposed. The simulation is conducted based on the weather conditions of three cities; Chongqing (29.43°N, 106.91°E), Taiyuan (37.87°N, 112.54°E) and Urumqi (43.83°N, 87.62° E). Chongqing experiences hot summers and cold winters, Taiyuan has a cold climate and Urumqi has an extremely cold climate. Chongqing suffers from no central heating systems within a cold climate, whilst the other two cities suffer from severe air pollution caused by coal-based winter heating systems. Accordingly, using a renewable energy heating system to reduce pollution to the environment is urgent. The simulation results involve the prediction of fossil fuel energy savings, cost payback period on investment and life cycle carbon emission reduction for the novel system, compared to conventional coal-based heating systems.

The energy performances of the proposed SAHR-HP systems for the served houses in three cities are simulated. The results show that the annual heating load of the served houses in Chongqing, Taiyuan, and Urumqi is 10563.63kWh, 25997.66kWh, and 34317.52kWh respectively. The annual space cooling load of the served houses are -4066.36kWh, -3242.42kWh, and -2584.19kWh respectively. The SAHR-HP system can maintain the room temperature of the served houses from 19°C to 22°C during winter and from 24°C to 27°C in the summer. This stable room temperature is a clear indication that the SAHR-HP system can be expected to perform well all year round.

During the operation of the system, the main heating and cooling capacity comes from the VIHR-ASHP, which can provide 6411.75kWh, 18276.33kWh, 27583kWh heating capacity in Chongqing, Taiyuan, and Urumqi respectively. This is equivalent to 60.7%, 70.3%, and 80.4% of the heating load demands in the three cities. During summer, the VIHR-ASHP provides 100% cooling capacity to the served houses, which are 5045.57kWh, 2242.87kWh, 1966.54kWh respectively in Chongqing, Taiyuan, and Urumqi. HRD can annually provide 2007.29kWh, 2852.33kWh, and 4730.77kWh heating, and 399.21kWh, 382.65kWh and 344.21kWh cooling capacity in Chongqing, Taiyuan, and Urumqi. Part of the cooling capacities, 98.19kWh in Chongqing, 112.28kWh in Taiyuan, and 183.46kWh in Urumqi, are provided by the direct cooling supply mode. The total collected heat of the domestic hot water tank for the whole year is 3162.84kWh, 3245.81kWh, and 2975.30kWh in Chongqing, Taiyuan, and Urumqi, which can provide a total of 90.37tons, 92.74tons, and 85.01tons of domestic hot water respectively. Thus, the annual total recovered heat of the system is 3204.42kWh, 7023.41kWh, and 8615.93kWh in Chongqing, Taiyuan, and Urumqi respectively, which accounts for 21.9%, 24.1%, and 23.3% of the annual heat load of each house. The average COPs for the systems over a whole year are 3.86, 4.40, and 4.39 and the generated energy of the system is 19111.35kWh, 30406.84kWh, and 40272.09kWh in Chongqing, Taiyuan, and

Urumqi respectively.

There are four photovoltaic panels, each with an aperture area of $2m^2$. The total photovoltaic electricity production is 1745.58kWh, 1955.42kWh, and 1917.31kWh annually in Chongqing, Taiyuan, and Urumqi respectively. The feed-in tariff in Shanxi is 0.75RMB/kWh, which means that the served house can earn a total of 1309.18RMB, 1466.57RMB, and 1437.98RMB per year in each city respectively, by transferring the generated electricity into the power grid. Taking into account the earned money from the generated electricity of the PV panels, the annual operational cost of the system is 1086.46RMB, 3093.89RMB, and 5410.59RMB in Chongqing, Taiyuan, and Urumqi respectively for space heating, cooling and hot water supply. Overall, the photovoltaic profit provides 38%, 26%, and 18% of the total operation cost in each city.

In addition, compared with the coal-driven system, the novel system has a cost payback period of 13.8 years, 12.37 years, and 17.85 years in Chongqing, Taiyuan, and Urumqi and a life-cycle net cost saving of nearly 16145.84RMB, 20317.82RMB, and 9002RMB.

Based on the assumption that 100 sets of the systems are used (e.g., to meet the demand of a village), the reduction of fossil fuel consumption and pollutants are significant. Over the 25-year life span of the systems, the total carbon emission savings could reach 20465.1tons, 32560.7tons, and 43124.7tons in Chongqing, Taiyuan, and Urumqi compared with coal-based systems. Furthermore, the system reduces the emission of many other harmful substances, i.e., dust, SO_2 and NO_x, and is therefore a desirable approach for environment sustainability and clean air.

In summary, the novel SAHR-HP system can significantly improve energy efficiency and reduce energy consumption for space heating, cooling, and hot water supply. It is a promising approach to achieve near-zero carbon emissions from buildings. Although

the system has been demonstrated in northern China, it is also expected to be applicable in other cold regions of the world. Furthermore, the research results can guide the development a novel SAHP system for space heating/cooling, hot water supply and ventilation, and help to configure feasible solutions to optimise the SAHP technologies. The wide promotion of these core technologies worldwide could significantly reduce consumption of fossil fuel and the associated carbon footprint in a built-up environment, thus providing a more ecological environment.

8.2 Further Opportunities and Challenges

8.2.1 Pilot demonstration and future project

Based on substantial investigations and relevant results, the optimised SAHR-HP system was constructed and demonstrated on a pilot scale in Shanxi China. The system for demonstration was designed to provide space heating, cooling and domestic hot water for an independent rural house in northern China, where heating and hot water are the main energy demand of the building. The mini-channel solar thermal collectors array of 36m^2 and VIHR-ASHP of 40kW were successfully demonstrated. Photographs of the system are shown in Fig. 8-1 and Fig. 8-2.

Fig. 8-1 Demonstration of installed solar thermal collector

Fig. 8-2 Demonstration of installed VIHR-ASHP

There were two solar collectors arrays in parallel. The solar collectors arrays contained 10 and 8 mini-channel solar thermal collectors respectively, and they were connected using the multiple-throughout-flowing method. The collectors were fixed to a 60° tilted frame, and fitted with a single-glazing cover on top.

In the future, more novel SAHR-HP systems will be installed. In 2020, a 20kW system will be installed on the roof of the Hull City Library to supply heating and hot water. In addition, more demonstrative SAHR-HP systems will be installed within council houses in Hull during 2021.

8.2.2 Using artificial intelligent programming to optimise solar assisted heat pump system and its modules

According to the current investigations, there are many energy sources that can be used in the SAHPSs, i.e., solar energy, air source, geothermal energy, exhausted air energy, water source, and electricity. Correspondingly, there are many devices applied to transfer energy from different energy sources to achieve different functions, such as cooling, heating, and DWH. The devices include solar collectors, HSEU, heat pump, heat recovery device, and so on. Apparently, with different energy sources, devices, and system configurations, the SAHP system performs differently under a certain building, environmental condition, and control strategy. Coupled with the economic and social factors, designing an optimal SAHP system is difficult and complicated. Implementation of Computational Fluid Dynamics (CFD) into SAHP system

investigations has been a reassuring approach for years. However, it might be time-consuming and costly to simulate a myriad of systems to find their optimum performance parameters.

Accordingly, using the novel computational techniques, such as Artificial Neural Networks (ANNs), Genetic Algorithm (GA), Model Tree (MT) and GEP, to improve the simulation speed is significant and have attracted lots of attention in this area. When it comes to the optimisation of a single module of the SAHP system, much relevant research has been reported in recent few years. In summary, whether a single module or a SAHPS, the artificial intelligent programming can optimise it effectively, thus efficiently integrating modularized devices into an integral SAHPS and fully reaching the potential of the SAHPS.

8.2.3 SAHR-HP system stakeholders

In order to promote the widely practical application of such an SAHR-HP system, the detailed advantages and barriers for stakeholders have been analysed and summarised in Table 8-1. According to the identified barriers existing for the SAHR-HP technologies, more investigation and collaboration between the stakeholders needs to be conducted during the coming decades. Thus, an interdisciplinary working group in SAHR-HP technologies is expected to be established, which could enable the beneficial exchange of information, results and experiences. The information includes R&D specifications, system design, component design, test strategies, practical installation challenges, market expectation analysis, policy formulation and improvement. Consequently, this efficient interdisciplinary unity can provide a comprehensive understanding of the potential development challenges in SAHR-HP technologies.

Table 8-1 Opportunities and challenges for SAHR-HP system stakeholders

Stakeholders	Advantages	Barriers

R&D institutes	Find new solutions by using scientific and technological tools	● Practical performance ● Reliability of the proposed technologies
Architects	Seek new methods for building integration	● Integrate the system into the initial design of a building
Engineering Consultants	Initiative technology with high-profile design	● Commercial development strategy ● Novel concepts for R&D
Manufacturers	Mature markets	● Cost-effective production tools and strategies ● Easy installation and operation of systems
Building Industry	Sound industrial chain from production to installation	● Install the SAHR-HP system within the building construction ● Prefabrication system
Installers	Familiarity to installation tools and methods	● Plug-and-play application to reduce effort needed ● Comprehensive knowledge about all relevant specialties
Policy makers	effectively promote the development of renewable energy	● Comprehensive information coming from all other stakeholders

8.2.4 Technical development

Although the SAHR-HP technology has been comprehensively investigated and dynamically evaluated, further technical optimisation and improvement still needs to be investigated in respect of the following targets: (1) Achieve more efficient thermal

interaction control strategies between the heat pump and solar collectors array, by employing a variable-frequency vapour injection compressor; (2) Evaluate the energy performance and economic/environmental benefits under different operational control strategies. For example, by fully employing the low price electricity tariff available at night using an overnight heat storage mode; (3) Involve more renewable energy sources within the system to improve the system efficiency and further reduce electricity consumption; (4) Extend the SAHR-HP system applications in other energy demand areas, such as drying, desalination, and agricultural greenhouse heating; (5) Enhance the physical properties of the solar thermal collector by employing new materials; (6) Integrate the system as a structural building module facade; and (7) Create feasible options in terms of aesthetics and textures.

8.2.5 Evaluation standards

Currently, there are no legal standards in the SAHR-HP field due to the innovative characteristics of the system. Accordingly, common standards for such a practical system need to be introduced rapidly. So far, the performance evaluation of SAHR-HP systems has been conducted in terms of the researchers' general investigation methods or standards for SAHP systems, heat recovery heat pumps and solar thermal collectors. These methods are undesirable for comparing the novel SAHR-HP systems with other energy systems equally, because the conclusions will be different under various types of SAHP systems, experimental environment, etc. Consequently, new normative evaluation procedures and standards should be established to for relevant suitability on the basis of the current standards of independent heat pumps and solar thermal collectors.

8.2.6 Long-term reliability measurement and SWOT analysis

A short-term performance evaluation of the SAHR-HP system under real climate conditions has been conducted. However, a seasonal or annual operation test is still important to discover the uncertainties of the SAHR-HP system in practice. This long-

term test contains several challenges, including seasonal variation of weather conditions and system stability and robustness.

Strengths, Weaknesses, Opportunities, and Threats (SWOT) analysis of the SAHR-HP system should be conducted to detect its advantages and disadvantages and understand its opportunity and challenge. The SWOT analysis can also adjust the development method and resources at the level of strategy and tactics to ensure the analysed object to achieve the expected goal. In addition, comparing the novel SAHR-HP system with existing SAHP systems is also a good way to investigate the pros and cons of the novel SAHR-HP system.

8.2.7 Market analysis

An in-depth study of the market potential is important for the promotion and development of SAHR-HP technologies and products. It is generally acknowledged that solar-based systems are projected to supply around 49% of the energy for systems within low-and-medium temperature climates within the EU, and provide 4.8% of electricity consumed globally by 2030. A market analysis of SAHP systems is required, exploring the following aspects : (1) a comprehensive survey of case studies of current SAHR-HP system products to characterise their practical applicability for buildings within different climatic regions, and market positions and recommendations for different end users; (2) a feasibility research investigating the SAHP-HP application in various building types; (3) a dedicated market survey of preferences for different customers; and (4) the establishment of a generic extrapolating methodology for market analysis of the SAHP systems.

8.2.8 Manufacturing cost

Current SAHR-HP system construction is accomplished using independent production lines of heat pumps, HSEU and solar thermal collectors. In future, the system production for large-scale applications should integrate those three separate

production processes and build up sound and effective upstream/downstream supply chains. Accordingly, the capital cost of the SAHR-HP system can be cut down, and the economic efficiency will be further increased. The design of the relevant products can also be tailored for the energy specifications of buildings, production process, and installation and mounting requirements. The manufacturing cost is a key factor in promoting SAHR-HP systems across the worldwide market. Furthermore, under collaboration between the market players and local authorities, the SAHR-HP systems manufacturing cost could be further reduced.

8.2.9 Dissemination activities

For the purpose of promoting SAHR-HP technologies, further dissemination activities should be conducted to demonstrate this technology to the public. This can be achieved by applying several business approaches, including the presentation of case studies, roadmaps of the products, holding workshops, on-site tours, conferences and open days.

8.2.10 Policy support

Innovations for the reduction in building energy consumption and environmental pollution will be obtained and analysed by the public energy agencies, which have connections with many industries in this area. In addition, government and policymakers play an important role in eliminating market challenges by proposing relevant public funding and financing strategies to improve the competitiveness of SAHR-HP systems compared to conventional ones. Moreover, combination with local building standards would further promote the development of the SAHR-HP technologies. Accordingly, the payback time of SAHR-HP system would be substantially decreased. However, there are no relevant policies issued for this technology currently.

Consequently, specialised policies which can support the deployment of this new

technology should be proposed, and local authorities could subsidise the corresponding financial benefits for end users.

APPENDIX: REFERENCES

[1] Zhang H, Zhao H, Li Z. Waste heat recovery and water-saving modification for a water-cooled gas-steam combined cycle cogeneration system with absorption heat pump. Energy Convers Manag 2019;180:1129–38. https://doi.org/10.1016/j.enconman.2018.11.051.

[2] Kelishadi R. Environmental pollution: Health effects and operational implications for pollutants removal. J Environ Public Health 2012. https://doi.org/10.1155/2012/341637.

[3] Coogan PF, White LF, Jerrett M, Brook RD, Su JG, Seto E, et al. Air pollution and incidence of hypertension and diabetes mellitus in black women living in Los Angeles. Circulation 2012;125:767–72. https://doi.org/10.1161/CIRCULATIONAHA.111.052753.

[4] Climate Change 2014 Synthesis Report Summary for Policymakers. 2014.

[5] Global Climate Change Indicators n.d. https://www.ncdc.noaa.gov/monitoring-references/faq/indicators.php.

[6] Fossil Fuels n.d. https://ourworldindata.org/fossil-fuels.

[7] Shah SK, Aye L, Rismanchi B. Multi-objective optimisation of a seasonal solar thermal energy storage system for space heating in cold climate. Appl Energy 2020;268:115047. https://doi.org/10.1016/j.apenergy.2020.115047.

[8] ENERGY EFFICIENCY FOR BUILDINGS. n.d.

[9] Ma Q, Wang P. Underground solar energy storage via energy piles. Appl Energy 2020;261:114361. https://doi.org/10.1016/j.apenergy.2019.114361.

[10] Chenari B, Carrilho JD, Gameiro M. Towards sustainable , energy-ef fi cient and healthy ventilation strategies in buildings : A review. Renew Sustain Energy Rev 2016;59:1426–47. https://doi.org/10.1016/j.rser.2016.01.074.

[11] Lin HW, Hong T. On variations of space-heating energy use in office buildings. Appl Energy 2013;111:515–28. https://doi.org/10.1016/j.apenergy.2013.05.040.

[12] Afroz Z, Shafiullah GM, Urmee T, Higgins G. Modeling techniques used in building HVAC control systems: A review. Renew Sustain Energy Rev 2018;83:64–84. https://doi.org/10.1016/j.rser.2017.10.044.

[13] Dos Santos Coelho L, Askarzadeh A. An enhanced bat algorithm approach for reducing electrical power consumption of air conditioning systems based on differential operator. Appl Therm Eng 2016;99:834–40. https://doi.org/10.1016/j.applthermaleng.2016.01.155.

[14] Wei X, Kusiak A, Li M, Tang F, Zeng Y. Multi-objective optimization of the HVAC (heating, ventilation, and air conditioning) system performance. Energy 2015;83:294–306. https://doi.org/10.1016/j.energy.2015.02.024.

[15] Zeng Y, Zhang Z, Kusiak A. Predictive modeling and optimization of a multi-zone HVAC system with data mining and firefly algorithms. Energy 2015;86:393–402. https://doi.org/10.1016/j.energy.2015.04.045.

[16] Chen S, Zhang G, Xia X, Setunge S, Shi L. A review of internal and external

influencing factors on energy efficiency design of buildings. Energy Build 2020;216. https://doi.org/10.1016/j.enbuild.2020.109944.

[17] Tenpierik MJ, Hasselaar E. Reflective multi-foil insulations for buildings: A review. Energy Build 2013;56:233–43. https://doi.org/10.1016/j.enbuild.2012.10.003.

[18] Yu J, Yang C, Tian L, Liao D. A study on optimum insulation thicknesses of external walls in hot summer and cold winter zone of China. Appl Energy 2009;86:2520–9. https://doi.org/10.1016/j.apenergy.2009.03.010.

[19] Marinelli S, Lolli F, Gamberini R, Rimini B. Life Cycle Thinking (LCT) applied to residential heat pump systems: A critical review. Energy Build 2019;185:210–23. https://doi.org/10.1016/j.enbuild.2018.12.035.

[20] Cui C, Zhang X, Cai W. An energy-saving oriented air balancing method for demand controlled ventilation systems with branch and black-box model. Appl Energy 2020;264:114734. https://doi.org/10.1016/j.apenergy.2020.114734.

[21] BP Statistical Review – 2019（China's energy market in 2018）. 2019.

[22] Statistical Review – 2019 (UK energy market in 2018). 2019.

[23] BP Statistical Review – 2019 (European Union's energy market in 2018). 2019.

[24] Ruschenburg J, Herkel S, Henning HM. A statistical analysis on market-available solar thermal heat pump systems. Sol Energy 2013;95:79–89. https://doi.org/10.1016/j.solener.2013.06.005.

[25] SAHP company n.d. https://www.sahp.info/.

[26] Eco Greenenergy Solutions n.d. https://egesolutionsltd.co.uk/solar-assisted-heat-pump/.

[27] Energy How UK n.d. https://energyhowuk.com/energy-how-uk/.

[28] Arkaya n.d. http://www.arkaya.co.uk/.

[29] SunHorizon n.d.

[30] HEAT4COOL n.d.

[31] Harrison S. The Potential and Challenges of Solar Boosted Heat Pumps for Domestic Hot Water Heating. 12th IEA Heat Pump Conf., 2017.

[32] Li J, Huang J. The expansion of China' s solar energy : Challenges and policy options. Renew Sustain Energy Rev 2020;132:110002. https://doi.org/10.1016/j.rser.2020.110002.

[33] Stokes LC, Breetz HL. Politics in the U.S. energy transition: Case studies of solar, wind, biofuels and electric vehicles policy. Energy Policy 2018;113:76–86. https://doi.org/10.1016/j.enpol.2017.10.057.

[34] Zhou J, Zhao X, Ma X, Du Z, Fan Y, Cheng Y, et al. Clear-days operational performance of a hybrid experimental space heating system employing the novel mini-channel solar thermal & PV/T panels and a heat pump. Sol Energy 2017;155:464–77. https://doi.org/10.1016/j.solener.2017.06.056.

[35] Kim T, Choi B Il, Han YS, Do KH. A comparative investigation of solar-assisted heat pumps with solar thermal collectors for a hot water supply system. Energy Convers Manag 2018;172:472–84. https://doi.org/10.1016/j.enconman.2018.07.035.

[36] Wang L, Ma G, Ma A, Zhou F, Li F. Experimental study on the characteristics of

triplex loop heat pump for exhaust air heat recovery in winter. Energy Convers Manag 2018;176:384–92. https://doi.org/10.1016/j.enconman.2018.09.052.

[37] Buker MS, Riffat SB. Solar assisted heat pump systems for low temperature water heating applications: A systematic review. Renew Sustain Energy Rev 2016;55:399–413. https://doi.org/10.1016/j.rser.2015.10.157.

[38] Ruschenburg J, Herkel S. A Review of Market-Available Solar Thermal Heat Pump Systems. 2013.

[39] Freeman TL, Mitchell JW, Audit TE. Performance of combined solar-heat pump systems. Sol Energy 1979;22:125–35. https://doi.org/https://doi.org/10.1016/0038-092X(79)90096-3.

[40] Vega J, Cuevas C. Parallel vs series con figurations in combined solar and heat pump systems : A control system analysis. Appl Therm Eng 2020;166:1146--1150. https://doi.org/10.1016/j.applthermaleng.2019.114650.

[41] Kjellson E. Solar collectors combined with ground-source heat pumps in dwellings. Lund University, Sweden., 2009.

[42] Nowak T, Murphy P. outlook 2011 European Heat Pump Statistics. Brussels, Belgium: 2011.

[43] Lazzarin R. Heat pumps and solar energy: A review with some insights in the future. Int J Refrig 2020;116:146–60. https://doi.org/10.1016/j.ijrefrig.2020.03.031.

[44] Kaygusuz K, Ayhan T. Experimental and theoretical investigation of combined solar heat pump system for residential heating. Energy Convers Manag 1999;40:1377–96.

[45] Bertram E, Pärisch P, Tepe R. Impact of solar heat pump system concepts on seasonal performance - Simulation studies. EuroSun 2012 Conf., 2012.

[46] Haller MY, Frank E. On the potential of using heat from solar thermal collectors for heat pump evaporators. ISES Sol. Word Congr., 2011.

[47] Chandrashekar M, Le NT, Sullivan HF, Hollands KGT. A comparative study of solar assisted heat pump systems for canadian locations. Sol Energy 1982;28:217–26. https://doi.org/https://doi.org/10.1016/0038-092X(82)90160-8.

[48] Vega J, Cuevas C. Parallel vs series configurations in combined solar and heat pump systems : A control system analysis. Appl Therm Eng 2020;166:1146–50. https://doi.org/10.1016/j.applthermaleng.2019.114650.

[49] Poppi S, Sommerfeldt N, Bales C, Madani H, Lundqvist P. Techno-economic review of solar heat pump systems for residential heating applications. Renew Sustain Energy Rev 2018;81:22–32. https://doi.org/10.1016/j.rser.2017.07.041.

[50] Poppi S, Bales C. Influence of hydraulics and control of thermal storage in solar assisted heat pump combisystems. SHC 2013, Int. Conf. Sol. Heat. Cool. Build. Ind., vol. 48, Elsevier B.V.; 2014, p. 946–55. https://doi.org/10.1016/j.egypro.2014.02.108.

[51] Poppi S, Bales C, Heinz A, Hengel F, Chèze D, Mojic I, et al. Analysis of system improvements in solar thermal and air source heat pump combisystems. Appl Energy 2016;173:606–23. https://doi.org/10.1016/j.apenergy.2016.04.048.

[52] Haller MY, Haberl R, Mojic I, Frank E. Hydraulic integration and control of heat

pump and combi-storage : Same components , big differences. SHC 2013, Int. Conf. Sol. Heat. Cool. Build. Ind., vol. 48, Elsevier B.V.; 2014, p. 571–80. https://doi.org/10.1016/j.egypro.2014.02.067.

[53] Phillips W., Dave R. Effects of stratification on the performance of liquid-based solar heating systems. Sol Energy 1982;29:111–20.

[54] Fischer D, Rautenberg F, Wirtz T, Wille-haussmann B. Smart Meter Enabled Control for Variable Speed Heat Pumps to Increase PV Self-Consumption. 24th IIR Int Congr Refrig 2015ID580., 2015. https://doi.org/10.13140/RG.2.1.2566.3762.

[55] Salpakari J, Lund P. Optimal and rule-based control strategies for energy flexibility in buildings with PV. Appl Energy 2016;161:425–36. https://doi.org/10.1016/j.apenergy.2015.10.036.

[56] Evangelisti L, De Lieto Vollaro R, Asdrubali F. Latest advances on solar thermal collectors: A comprehensive review. Renew Sustain Energy Rev 2019;114:109318. https://doi.org/10.1016/j.rser.2019.109318.

[57] Pranesh V, Velraj R, Christopher S, Kumaresan V. A 50 year review of basic and applied research in compound parabolic concentrating solar thermal collector for domestic and industrial applications. Sol Energy 2019;187:293–340. https://doi.org/10.1016/j.solener.2019.04.056.

[58] Sultan SM, Ervina Efzan MN. Review on recent Photovoltaic/Thermal (PV/T) technology advances and applications. Sol Energy 2018;173:939–54. https://doi.org/10.1016/j.solener.2018.08.032.

[59] Xu G, Zhang X, Deng S. Experimental study on the operating characteristics of a novel low-concentrating solar photovoltaic/thermal integrated heat pump water heating system. Appl Therm Eng 2011;31:3689–95. https://doi.org/10.1016/j.applthermaleng.2011.01.030.

[60] Majumdar R, Saha SK, Patki A. Novel dimension scaling for optimal mass flow rate estimation in low temperature flat plate solar collector based on thermal performance parameters. Therm Sci Eng Prog 2020;19:100569. https://doi.org/10.1016/j.tsep.2020.100569.

[61] Fudholi A, Sopian K. A review of solar air flat plate collector for drying application. Renew Sustain Energy Rev 2019;102:333–45. https://doi.org/10.1016/j.rser.2018.12.032.

[62] Kalogirou SA. Solar thermal collectors and applications. vol. 30. 2004. https://doi.org/10.1016/j.pecs.2004.02.001.

[63] Yogi Goswami D. Principles of Solar Engineering. third edit. CRC Press; 2015.

[64] Shyam, Tiwari GN, Fischer O, Mishra RK, Al-Helal IM. Performance evaluation of N-photovoltaic thermal (PVT) water collectors partially covered by photovoltaic module connected in series: An experimental study. Sol Energy 2016;134:302–13. https://doi.org/10.1016/j.solener.2016.05.013.

[65] Joshi SS, Dhoble AS. Photovoltaic -Thermal systems (PVT): Technology review and future trends. Renew Sustain Energy Rev 2018;92:848–82. https://doi.org/10.1016/j.rser.2018.04.067.

[66] Walter D, Everett V, Blakers A, Vivar M, Harvey J, Muric-Nesic J. A 20-sun

hybrid PV–Thermal linear micro-concentrator system for urban rooftop applications. Proc. IEEE 35th Photovolt. Spec. Conf., 2010, p. 831–6.

[67] Esen M. Thermal performance of a solar cooker integrated vacuum-tube collector with heat pipes containing different refrigerants. Sol Energy 2004;76:751–7. https://doi.org/10.1016/j.solener.2003.12.009.

[68] Kim YS, Balkoski K, Jiang L, Winston R. Efficient stationary solar thermal collector systems operating at a medium-temperature range. Appl Energy 2013;111:1071–9. https://doi.org/10.1016/j.apenergy.2013.06.051.

[69] Moss R, Shire S, Henshall P, Arya F, Eames P, Hyde T. Performance of evacuated flat plate solar thermal collectors. Therm Sci Eng Prog 2018;8:296–306. https://doi.org/10.1016/j.tsep.2018.09.003.

[70] Panagopoulos AA, Chalkiadakis G, Jennings NR. Towards optimal solar tracking: A dynamic programming approach. Proc Natl Conf Artif Intell 2015;1:695–701.

[71] Solar Thermal Collectors Market Size, Share & Trends Analysis Report By Product (Concentrating, Non-Concentrating (Flat Plate, Evacuated Tube, Unglazed Water Collector, Air Collector)), By Application, By Region, And Segment Forecasts, 2018 - 2025. 2018.

[72] Solar Thermal Market Size, Share & Industry Analysis, By Collector Type (Evacuated Tube Collector, Flat Plate Collector, Uglazed Water Collector, Air Collector), By Type of System (Thermosiphon Solar Heating Systems, Pumped Solar Heating System) By Applic. 2020.

[73] Elguezabal P, Lopez A, Blanco JM, Chica JA. CFD model-based analysis and experimental assessment of key design parameters for an integrated unglazed metallic thermal collector façade. Renew Energy 2020;146:1766–80. https://doi.org/10.1016/j.renene.2019.07.151.

[74] Thomas R. Existing PVT systems and solutions - IEA SHC Task 60. 2020. https://doi.org/10.18777/ieashc-task60-2020-0001.

[75] Weiss W, Spörk-Dür M. Solar Heat Worldwide. Global Market Development and Trends in 2018. Sol Heat Worldw Rep 2019;1:86.

[76] Aldabbagh LBY, Egelioglu F, Ilkan M. Single and double pass solar air heaters with wire mesh as packing bed. Energy 2010;35:3783–7. https://doi.org/10.1016/j.energy.2010.05.028.

[77] Kolb A, Winter ERF, Viskanta R. Experimental studies on a solar air collector with metal matrix absorber. Sol Energy 1999;65:91–8. https://doi.org/10.1016/S0038-092X(98)00117-0.

[78] Matrawy KK. Theoretical analysis for an air heater with a box-type absorber. Sol Energy 1998;63:191–8. https://doi.org/10.1016/S0038-092X(98)00044-9.

[79] Abdullah AH, Abou-Ziyan HZ, Ghoneim AA. Thermal performance of flat plate solar collector using various arrangements of compound honeycomb. Energy Convers Manag 2003;44:3093–112. https://doi.org/10.1016/S0196-8904(03)00013-X.

[80] Naphon P. Heat transfer characteristics and pressure drop in channel with V corrugated upper and lower plates. Energy Convers Manag 2007;48:1516–24.

https://doi.org/10.1016/j.enconman.2006.11.020.

[81] Kabeel AE, Khalil A, Shalaby SM, Zayed ME. Improvement of thermal performance of the finned plate solar air heater by using latent heat thermal storage. Appl Therm Eng 2017;123:546–53. https://doi.org/10.1016/j.applthermaleng.2017.05.126.

[82] Kabeel AE, Hamed MH, Omara ZM, Kandeal AW. Influence of fin height on the performance of a glazed and bladed entrance single-pass solar air heater. Sol Energy 2018;162:410–9. https://doi.org/10.1016/j.solener.2018.01.037.

[83] Ammari HD. A mathematical model of thermal performance of a solar air heater with slats. Renew Energy 2003;28:1597–615. https://doi.org/10.1016/S0960-1481(02)00253-7.

[84] Kabeel AE, Hamed MH, Omara ZM, Kandel AW. On the performance of a baffled glazed-bladed entrance solar air heater. Appl Therm Eng 2018;139:367–75. https://doi.org/10.1016/j.applthermaleng.2018.04.141.

[85] Abene A, Dubois V, Le Ray M, Ouagued A. Study of a solar air flat plate collector: Use of obstacles and application for the drying of grape. J Food Eng 2004;65:15–22. https://doi.org/10.1016/j.jfoodeng.2003.11.002.

[86] Abdullah AS, Abou Al-sood MM, Omara ZM, Bek MA, Kabeel AE. Performance evaluation of a new counter flow double pass solar air heater with turbulators. Sol Energy 2018;173:398–406. https://doi.org/10.1016/j.solener.2018.07.073.

[87] Sakhaei SA, Valipour MS. Performance enhancement analysis of The flat plate collectors: A comprehensive review. Renew Sustain Energy Rev 2019;102:186–204. https://doi.org/10.1016/j.rser.2018.11.014.

[88] Del Col D, Padovan A, Bortolato M, Dai Prè M, Zambolin E. Thermal performance of flat plate solar collectors with sheet-and-tube and roll-bond absorbers. Energy 2013;58:258–69. https://doi.org/10.1016/j.energy.2013.05.058.

[89] Amin ZM, Hawlader MNA. A review on solar assisted heat pump systems in Singapore. Renew Sustain Energy Rev 2013;26:286–93. https://doi.org/10.1016/j.rser.2013.05.032.

[90] Kauffman J, Lee KM. Handbook of Sustainable Engineering. 2013. https://doi.org/10.1007/978-1-4020-8939-8.

[91] Evangelisti L, De Lieto Vollaro R, Asdrubali F. Latest advances on solar thermal collectors: A comprehensive review. Renew Sustain Energy Rev 2019;114:109318. https://doi.org/10.1016/j.rser.2019.109318.

[92] Ma L, Lu Z, Zhang J, Liang R. Thermal performance analysis of the glass evacuated tube solar collector with U-tube. Build Environ 2010;45:1959–67. https://doi.org/10.1016/j.buildenv.2010.01.015.

[93] Evacuated tube collector n.d. http://www.alternative-energy-tutorials.com/solar-hot- water/evacuated-tube-collector.html (accessed June 8, 2020).

[94] Good C, Chen J, Dai Y, Grete A. Hybrid photovoltaic/thermal systems in buildings – a review. Energy Procedia 2015;70:683–90. https://doi.org/10.1016/j.egypro.2015.02.176.

[95] Zondag HAÃ. Flat-plate PV-Thermal collectors and systems : A review. Renew Sustain Energy Rev 2008;12:891–959. https://doi.org/10.1016/j.rser.2005.12.012.

[96] Vaishak S, Bhale P V. Photovoltaic/thermal-solar assisted heat pump system: Current status and future prospects. Sol Energy 2019;189:268–84. https://doi.org/10.1016/j.solener.2019.07.051.

[97] Poppi S, Bales C, Heinz A, Hengel F, Chèze D, Mojic I, et al. Analysis of system improvements in solar thermal and air source heat pump combisystems. Appl Energy 2016;173:606–23. https://doi.org/10.1016/j.apenergy.2016.04.048.

[98] Mader G, Madani H. Capacity control in air – water heat pumps : Total cost of ownership analysis. Energy Build 2014;81:296–304. https://doi.org/10.1016/j.enbuild.2014.06.029.

[99] Madani H, Claesson J, Lundqvist P. Capacity control in ground source heat pump systems part II : Comparative analysis between on / off controlled and variable capacity systems. Int J Refrig 2011;34:1934–42. https://doi.org/10.1016/j.ijrefrig.2011.05.012.

[100] Mohanraj M, Belyayev Y, Jayaraj S, Kaltayev A. Research and developments on solar assisted compression heat pump systems – A comprehensive review (Part A: Modeling and modifications). Renew Sustain Energy Rev 2018;83:90–123. https://doi.org/10.1016/j.rser.2017.08.022.

[101] Chaturvedi SK, Abdel-salam TM, Sreedharan SS, Gorozabel FB. Two-stage direct expansion solar-assisted heat pump for high temperature applications. Appl Therm Eng 2009;29:2093–9. https://doi.org/10.1016/j.applthermaleng.2008.10.010.

[102] Wang W, Ma Z, Jiang Y, Yang Y, Xu S, Yang Z. Field test investigation of a double-stage coupled heat pumps heating system for cold regions. Int J Refrig 2005;28:672–9. https://doi.org/10.1016/j.ijrefrig.2005.01.001.

[103] Li F, Chang Z, Li X, Tian Q. Energy and exergy analyses of a solar-driven ejector-cascade heat pump cycle. Energy 2018;165:419–31. https://doi.org/10.1016/j.energy.2018.09.173.

[104] Zhao L, Zheng N, Deng S. A thermodynamic analysis of an auto-cascade heat pump cycle for heating application in cold regions. Energy Build 2014;82:621–31. https://doi.org/10.1016/j.enbuild.2014.07.083.

[105] Deng S, Dai YJ, Wang RZ. Performance optimization and analysis of solar combi-system with carbon dioxide heat pump. Sol Energy 2013;98:212–25. https://doi.org/10.1016/j.solener.2013.10.001.

[106] Schimpf S, Span R. Techno-economic evaluation of a solar assisted combined heat pump – Organic Rankine Cycle system. Energy Convers Manag 2015;94:430–7. https://doi.org/10.1016/j.enconman.2015.02.011.

[107] Schimpf S, Span R. Simulation of a solar assisted combined heat pump – Organic rankine cycle system. Energy Convers Manag 2015;102:151–60. https://doi.org/10.1016/j.enconman.2015.01.083.

[108] Chaichana C, Aye L, Charters WWS. Natural working fluids for solar-boosted heat pumps. Int J Refrig 2003;26:637–43. https://doi.org/10.1016/S0140-

7007(03)00046-X.

[109] Olfa A, Hatem M, Bournot P. CFD analysis of thermal stratification in domestic hot water storage tank during dynamic mode. Build Simul 2015;8:421–9.

[110] Robin W. Advanced District Heating and Cooling (DHC) Systems. Woodhead Publishing; 2016.

[111] Guelpa E, Verda V. Thermal energy storage in district heating and cooling systems: A review. Appl Energy 2019;252:1134–74. https://doi.org/10.1016/j.apenergy.2019.113474.

[112] Dahash A, Ochs F, Janetti MB, Streicher W. Advances in seasonal thermal energy storage for solar district heating applications: A critical review on large-scale hot-water tank and pit thermal energy storage systems. Appl Energy 2019;239:296–315. https://doi.org/10.1016/j.apenergy.2019.01.189.

[113] Li Y, Huang G, Xu T, Liu X, Wu H. Optimal design of PCM thermal storage tank and its application for winter available open-air swimming pool. Appl Energy 2018;209:224–35. https://doi.org/10.1016/j.apenergy.2017.10.095.

[114] Knudsen S, Furbo S. Thermal stratification in vertical mantle heat-exchangers with application to solar domestic hot-water systems. Appl Energy 2004;78:257–72. https://doi.org/10.1016/j.apenergy.2003.09.002.

[115] Anuj Kumar G. Emerging Trends in Engineering Research and Technology Vol. 1. Book Publisher International; 2020. https://doi.org/10.9734/bpi/etert/v1.

[116] Zalman L, James T. Experimental study of thermally stratified hot water storage tanks. Sol Energy 1977;19:519–24.

[117] Hussain MI. Numerical thermal analysis of helical-shaped heat exchanger to improve thermal stratification inside solar storage tank. Conf. AgEng 2014At Zurich, Switz., 2014.

[118] Haller MY, Haberl R, Mojic I, Frank E. Hydraulic integration and control of heat pump and combi-storage: Same components, big differences. Energy Procedia 2014;48:571–80. https://doi.org/10.1016/j.egypro.2014.02.067.

[119] Glembin J, Rockendorf G. Simulation and evaluation of stratified discharging and charging devices in combined solar thermal systems. Sol Energy 2012;86:407–20. https://doi.org/10.1016/j.solener.2011.10.013.

[120] Werner W. Solar Heating Systems for Houses: A Design Handbook for Solar Combisystems. James & James Ltd; 2003.

[121] Shah LJ, Andersen E, Furbo S. Theoretical and experimental investigations of inlet stratifiers for solar storage tanks. Appl Therm Eng 2005;25:2086–99. https://doi.org/10.1016/j.applthermaleng.2005.01.011.

[122] Dragsted J, Furbo S, Dannemand M, Bava F. Thermal stratification built up in hot water tank with different inlet stratifiers. Sol Energy 2017;147:414–25. https://doi.org/10.1016/j.solener.2017.03.008.

[123] Davidson JH, Adams DA, Miller JA. A coefficient to characterize mixing in solar water storage tanks. J Sol Energy Eng 1994;116:94–9.

[124] Andersen E, Furbo S, Fan J. Multilayer fabric stratification pipes for solar tanks. Sol Energy 2007;81:1219–26. https://doi.org/10.1016/j.solener.2007.01.008.

[125] Furbo S, Andersen E, Thür A, Shah LJ, Andersen KD. Performance

improvement by discharge from different levels in solar storage tanks. Sol Energy 2005;79:431–9. https://doi.org/10.1016/j.solener.2005.01.005.

[126] Bales C, Persson T. External DHW units for solar combisystems. Sol Energy 2003;74:193–204. https://doi.org/10.1016/S0038-092X(03)00158-0.

[127] Swiatek M, Fraisse G, Pailha M. Stratification enhancement for an integrated collector storage solar water heater (ICSSWH). Energy Build 2015;106:35–43. https://doi.org/10.1016/j.enbuild.2015.07.005.

[128] González-Altozano P, Sanchis L., Gasque M, García-Marí E, Ibáñez F, Gutiérrez-Colomer R. Improvement of thermal stratification in a hot water solar storage tank by using a sintered bronze conical equalizer. World Renew. Energy Forum, Incl. World Renew. Energy Congr. XII Color. Renew. Energy Soc. Annu. Conf. May 13– May 17, Am. Sol. Energy Soc., 2012.

[129] Li S, Zhang Y, Li Y, Zhang X. Experimental study of inlet structure on the discharging performance of a solar water storage tank. Energy Build 2014;70:490–6. https://doi.org/10.1016/j.enbuild.2013.11.086.

[130] Rhee J, Campbell A, Mariadass A, Morhous B. Temperature stratification from thermal diodes in solar hot water storage tank. Sol Energy 2010;84:507–11. https://doi.org/10.1016/j.solener.2009.12.007.

[131] Altuntop N, Mevlut A, Veysel O, Kanoglu M. Effect of obstacles on thermal stratification in hot water storage tanks. Appl Therm Eng 2005;25:2285–98. https://doi.org/10.1016/j.applthermaleng.2004.12.013.

[132] Chung JD, Hwan S, Seob C, Yoo H. The effect of diffuser configuration on thermal stratification in a rectangular storage tank. Renew Energy 2008;33:2236–45. https://doi.org/10.1016/j.renene.2007.12.013.

[133] Yang Z, Chen H, Wang L, Sheng Y, Wang Y. Comparative study of the influences of different water tank shapes on thermal energy storage capacity and thermal stratification. Renew Energy 2016;85:31–44. https://doi.org/10.1016/j.renene.2015.06.016.

[134] Wang Z, Zhang H, Dou B, Huang H, Zhang G. The thermal stratification characteristics affected by a novel equalizer in a dynamic hot water storage tank. Appl Therm Eng 2017;126:1006–16. https://doi.org/10.1016/j.applthermaleng.2017.06.045.

[135] Wang Z, Zhang H, Dou B, Zhang G, Wu W, Zhou L. An experimental study for the enhancement of stratification in heat-storage tank by equalizer and PCM module. J Energy Storage 2020;27:101010. https://doi.org/10.1016/j.est.2019.101010.

[136] Karim A, Burnett A, Fawzia S. Investigation of stratified thermal storage tank performance for heating and cooling applications. Energies 2018;11. https://doi.org/10.3390/en11051049.

[137] Reza M, Basirat H, Savadkohy M. Numerical and experimental study of inlet-outlet locations e ff ect in horizontal storage tank of solar water heater. Sustain Energy Technol Assessments 2018;25:181–90. https://doi.org/10.1016/j.seta.2017.12.009.

[138] Gómez MA, Collazo J, Porteiro J, Míguez JL. Numerical study of an external

device for the improvement of the thermal stratification in hot water storage tanks. Appl Therm Eng 2018;144:996–1009. https://doi.org/10.1016/j.applthermaleng.2018.09.023.

[139] Daghigh R, Ruslan MH, Sulaiman MY, Sopian K. Review of solar assisted heat pump drying systems for agricultural and marine products. Renew Sustain Energy Rev 2010;14:2564–79. https://doi.org/10.1016/j.rser.2010.04.004.

[140] Mohanraj M, Belyayev Y, Jayaraj S, Kaltayev A. Research and developments on solar assisted compression heat pump systems – A comprehensive review (Part-B: Applications). Renew Sustain Energy Rev 2018;83:124–55. https://doi.org/10.1016/j.rser.2017.08.086.

[141] Ozgener O, Hepbasli A. Performance analysis of a solar-assisted ground-source heat pump system for greenhouse heating: An experimental study. Build Environ 2005;40:1040–50. https://doi.org/10.1016/j.buildenv.2004.08.030.

[142] Kalogirou SA. Seawater desalination using renewable energy sources. Prog Energy Combust Sci 2005;31:242–81. https://doi.org/10.1016/j.pecs.2005.03.001.

[143] Colak N, Hepbasli A. A review of heat pump drying: Part 1 - Systems, models and studies. Energy Convers Manag 2009;50:2180–6. https://doi.org/10.1016/j.enconman.2009.04.031.

[144] Solar-assisted fluidized bed dryer integrated with a heat pump for mint leaves. Appl Therm Eng J 2016;106:899–905. https://doi.org/10.1016/j.applthermaleng.2016.06.077.

[145] Dezfouli M, Mat, Ruslan M. Evaluation of drying chili by two Methods: Solar assisted heat pump dryer and open sun drying. Proceeding 1st Int. Conf. Environ. Informatics (ENINF'13), Kuala Lumpur, Malaysia, 2013, p. 112–6.

[146] Koçak S, Dog H. Mushroom drying with solar assisted heat pump system. Energy Convers Manag 2013;72:171–8. https://doi.org/10.1016/j.enconman.2012.09.035.

[147] Mohanraj M. Performance of a solar-ambient hybrid source heat pump drier for copra drying under hot-humid weather conditions. Energy Sustain Dev 2014;23:165–9. https://doi.org/10.1016/j.esd.2014.09.001.

[148] Jia T, Dou P, Chu P, Dai Y. Proposal and performance analysis of a novel solar-assisted resorption-subcooled compression hybrid heat pump system for space heating in cold climate condition. Renew Energy 2020;150:1136–50. https://doi.org/10.1016/j.renene.2019.10.062.

[149] Zhang L, Jiang Y, Dong J, Yao Y. Advances in vapor compression air source heat pump system in cold regions : A review. Renew Sustain Energy Rev 2018;81:353–65. https://doi.org/10.1016/j.rser.2017.08.009.

[150] Erbay Z, Hepbasli A. Application of conventional and advanced exergy analyses to evaluate the performance of a ground-source heat pump (GSHP) dryer used in food drying. Energy Convers Manag 2014;78:499–507. https://doi.org/10.1016/j.enconman.2013.11.009.

[151] Awani S, Chargui R, Kooli S, Farhat A, Guizani A. Performance of the coupling of the flat plate collector and a heat pump system associated with a vertical heat

exchanger for heating of the two types of greenhouses system. Energy Convers Manag 2015;103:266–75. https://doi.org/10.1016/j.enconman.2015.06.032.

[152] Chaturvedi SK, Gagrani VD, Abdel-Salam TM. Solar-assisted heat pump - A sustainable system for low-temperature water heating applications. Energy Convers Manag 2014;77:550–7. https://doi.org/10.1016/j.enconman.2013.09.050.

[153] Xu H, Zhao Y, Jia T, Dai YJ. Experimental investigation on a solar assisted heat pump desalination system with humidification-dehumidification. Desalination 2018;437:89–99. https://doi.org/10.1016/j.desal.2018.03.001.

[154] Yiing S, Munusamy Y, Seng K. Review of solar water heaters incorporating solid-liquid organic phase change materials as thermal storage. Appl Therm Eng 2018;131:455–71. https://doi.org/10.1016/j.applthermaleng.2017.12.032.

[155] Zhang J, Park JM, Kim DH, Kim HS. Effect of strain rate on compressive behavior of Ti45Zr16Ni9Cu10Be20 bulk metallic glass. Mater Sci Eng A 2007;448–451:290–4. https://doi.org/10.1016/j.msea.2006.02.405.

[156] Zhang Y, Ma Q, Li B, Fan X, Fu Z. Application of an air source heat pump (ASHP) for heating in Harbin, the coldest provincial capital of China. Energy Build 2017;138:96–103. https://doi.org/10.1016/j.enbuild.2016.12.044.

[157] Choi HJ, Kim BS, Kang D, Kim KC. Defrosting method adopting dual hot gas bypass for an air-to-air heat pump. Appl Energy 2011;88:4544–55. https://doi.org/10.1016/j.apenergy.2011.05.039.

[158] Qin F, Xue Q, Velez GMA, Zhang G, Zou H, Tian C. Experimental investigation on heating performance of heat pump for electric vehicles at -20°C ambient temperature. Energy Convers Manag 2015;102:39–49. https://doi.org/10.1016/j.enconman.2015.01.024.

[159] Martin C, Oppenheim P, Bush J, Stillman H, Martin C;, Oppenheim P;, et al. Alternative Defrost Strategies for Residential Heat Pumps Alternative Defrost Strategies for Residential Heat Pumps. Int. Refrig. AIR Cond. Conf., 2018.

[160] Wang W, Xiao J, Feng Y, Guo Q, Wang L. Characteristics of an air source heat pump with novel photoelectric sensors during periodic frost-defrost cycles. Appl Therm Eng 2013;50:177–86. https://doi.org/10.1016/j.applthermaleng.2012.06.019.

[161] Zhang Y. Asset price volatility and banks. J Math Econ 2017;71:96–103. https://doi.org/10.1016/j.jmateco.2017.05.001.

[162] Ma J, Fung AS, Brands M, Juan N, Mohammad O, Moyeed A. Performance analysis of indirect-expansion solar assisted heat pump using CO2 as refrigerant for space heating in cold climate. Sol Energy 2020;208:195–205. https://doi.org/10.1016/j.solener.2020.07.001.

[163] Liu H, Jiang Y, Yao Y. The field test and optimization of a solar assisted heat pump system for space heating in extremely cold area. Sustain Cities Soc 2014;13:97–104. https://doi.org/10.1016/j.scs.2014.05.002.

[164] Ji W, Cai J, Ji J, Huang W. Experimental study of a direct expansion solar-assisted heat pump (DX-SAHP) with finned-tube evaporator and comparison with conventional DX-SAHP. Energy Build J 2020;207:109632.

https://doi.org/10.1016/j.enbuild.2019.109632.

[165] Kong X, Yang Y, Zhang M, Li Y, Li J. Experimental investigation on a direct-expansion solar-assisted heat pump water heater using R290 with micro-channel heat transfer technology during the winter period. Int J Refrig 2020;113:38–48. https://doi.org/10.1016/j.ijrefrig.2020.01.019.

[166] Ge Y, Tassou SA, Youssef W, Energy A. Indirect expansion solar assisted heat pump system for hot water production with latent heat storage and applicable control strategy. Energy Procedia 2017;123:180–7. https://doi.org/10.1016/j.egypro.2017.07.258.

[167] Lu S, Liang R, Zhang J, Zhou C. Performance improvement of solar photovoltaic/thermal heat pump system in winter by employing vapor injection cycle. Appl Therm Eng 2019;155:135–46. https://doi.org/10.1016/j.applthermaleng.2019.03.038.

[168] Wang X, Hwang Y, Radermacher R. Two-stage heat pump system with vapor-injected scroll compressor using R410A as a refrigerant. Int J Refrig 2009;32:1442–51. https://doi.org/10.1016/j.ijrefrig.2009.03.004.

[169] Xi C, Lin L, Hongxing Y. Long term operation of a solar assisted ground coupled heat pump system for space heating and domestic hot water. Energy Build 2011;43:1835–44. https://doi.org/10.1016/j.enbuild.2011.03.033.

[170] Aziz W, Chaturvedi SK, Kheireddine A. Thermodynamic analysis of two-component, two-phase flow in solar collectors with application to a direct-expansion solar-assisted heat pump. Energy 1999;24:247–59. https://doi.org/10.1016/S0360-5442(98)00089-9.

[171] Cai J, Ji J, Wang Y, Huang W. Numerical simulation and experimental validation of indirect expansion solar-assisted multi-functional heat pump. Renew Energy 2016;93:280–90. https://doi.org/10.1016/j.renene.2016.02.082.

[172] Mohanraj M, Belyayev Y, Jayaraj S, Kaltayev A. Research and developments on solar assisted compression heat pump systems-A comprehensive review (Part A: Modeling and modifications). Renew Sustain Energy Rev 2018;83:90–123. https://doi.org/10.1016/j.rser.2017.08.022.

[173] Youssef W, Ge YT, Tassou SA. CFD modelling development and experimental validation of a phase change material (PCM) heat exchanger with spiral-wired tubes. Energy Convers Manag 2018;157:498–510. https://doi.org/10.1016/j.enconman.2017.12.036.

[174] Diao YH, Wang S, Zhao YH, Zhu TT, Li CZ, Li FF. Experimental study of the heat transfer characteristics of a new-type flat micro-heat pipe thermal storage unit. Appl Therm Eng J 2015;89:871–82. https://doi.org/10.1016/j.applthermaleng.2015.06.070.

[175] Lee S, Mudawar I. Investigation of flow boiling in large micro-channel heat exchangers in a refrigeration loop for space applications. Int J Heat Mass Transf 2016;97:110–29. https://doi.org/10.1016/j.ijheatmasstransfer.2016.01.072.

[176] DENG Y, QUAN Z. Experimental investigations on the heat transfer characteristics of micro heat pipe array applied to flat plate solar collector. Sci CHINA Technol Sci 2013;56:1177–85.

[177] Ling D, Mo G, Jiao Q, Wei J, Wang X. Research on Solar Heating System with Phase Change Thermal Energy Storage. Energy Procedia 2016;91:415–20. https://doi.org/10.1016/j.egypro.2016.06.277.

[178] Bava F, Furbo S, Perers B. Simulation of a Solar collectors array Consisting of two Types of Solar Collectors, with and Without Convection Barrier. Energy Procedia 2015;70:4–12. https://doi.org/10.1016/j.egypro.2015.02.091.

[179] Pe L. A review on buildings energy consumption information. Energy Build 2008;40:394–8. https://doi.org/10.1016/j.enbuild.2007.03.007.

[180] Dodoo A, Gustavsson L, Sathre R. Primary energy implications of ventilation heat recovery in residential buildings. Energy Build 2011;43:1566–72. https://doi.org/10.1016/j.enbuild.2011.02.019.

[181] Wallin J, Madani H, Claesson J. Run-around coil ventilation heat recovery system: A comparative study between different system configurations. Appl Energy 2012;90:258–65. https://doi.org/10.1016/j.apenergy.2011.05.012.

[182] Li B, Wild P, Rowe A. Performance of a heat recovery ventilator coupled with an air-to-air heat pump for residential suites in Canadian cities. J Build Eng 2019;21:343–54. https://doi.org/10.1016/j.jobe.2018.10.025.

[183] Mardiana-Idayu A, Riffat SB. Review on heat recovery technologies for building applications. Renew Sustain Energy Rev 2012;16:1241–55. https://doi.org/10.1016/j.rser.2011.09.026.

[184] Shurcliff WA. Air-to-air heat-exchangers for houses. Annu Rev 1988;13:1–22.

[185] O'connor D, Calautit JKS, Hughes BR. A review of heat recovery technology for passive ventilation applications. Renew Sustain Energy Rev 2016;54:1481–93. https://doi.org/10.1016/j.rser.2015.10.039.

[186] Liu XP, Niu JL. An optimal design analysis method for heat recovery devices in building applications. Appl Energy 2014;129:364–72. https://doi.org/10.1016/j.apenergy.2014.05.024.

[187] Wang L, Ma G, Ma A, Liu Y, Zhou F. Experimental investigations on a heat pump system for ventilation heat recovery of a novel dual-cylinder rotary compressor. Int J Refrig 2019;108:26–36. https://doi.org/10.1016/j.ijrefrig.2019.08.021.

[188] Juodis E. Extracted ventilation air heat recovery efficiency as a function of a building's thermal properties. Energy Build 2006;38:568–73. https://doi.org/10.1016/j.enbuild.2005.07.002.

[189] Wu W, Skye HM, Domanski PA. Selecting HVAC systems to achieve comfortable and cost-effective residential net-zero energy buildings. Appl Energy 2018;212:577–91. https://doi.org/10.1016/j.apenergy.2017.12.046.

[190] Hughes BR, Chaudhry HN, Calautit JK. Passive energy recovery from natural ventilation air streams. Appl Energy 2014;113:127–40. https://doi.org/10.1016/j.apenergy.2013.07.019.

[191] Plytaria MT, Tzivanidis C, Bellos E, Antonopoulos KA. Energetic investigation of solar assisted heat pump underfloor heating systems with and without phase change materials. Energy Convers Manag 2018;173:626–39. https://doi.org/10.1016/j.enconman.2018.08.010.

[192] Weeratunge H, Narsilio G, de Hoog J, Dunstall S, Halgamuge S. Model predictive control for a solar assisted ground source heat pump system. Energy 2018;152:974–84. https://doi.org/10.1016/j.energy.2018.03.079.

[193] Badescu V. Model of a solar-assisted heat-pump system for space heating integrating a thermal energy storage unit. Energy Build 2002;34:715–26. https://doi.org/10.1016/S0378-7788(01)00139-6.

[194] Zhao CY, Wu ZG. Thermal property characterization of a low melting-temperature ternary nitrate salt mixture for thermal energy storage systems. Sol Energy Mater Sol Cells 2011;95:3341–6. https://doi.org/10.1016/j.solmat.2011.07.029.

[195] Lerch W, Heinz A, Heimrath R. Direct use of solar energy as heat source for a heat pump in comparison to a conventional parallel solar air heat pump system. Energy Build 2015;100:34–42. https://doi.org/10.1016/j.enbuild.2015.03.006.

[196] Johra H, Filonenko K, Heiselberg P, Veje C, Dall'Olio S, Engelbrecht K, et al. Integration of a magnetocaloric heat pump in an energy flexible residential building. Renew Energy 2019;136:115–26. https://doi.org/10.1016/j.renene.2018.12.102.

[197] Gavaldà L, Garcia-Nuñez M, Quero S, Gutierrez-Milla C, Sabrià M. Role of hot water temperature and water system use on Legionella control in a tertiary hospital: An 8-year longitudinal study. Water Res 2019;149:460–6. https://doi.org/10.1016/j.watres.2018.11.032.

[198] Farabi-Asl H, Fujii H, Kosukegawa H. Cooling tests, numerical modeling and economic analysis of semi-open loop ground source heat pump system. Geothermics 2018;71:34–45. https://doi.org/10.1016/j.geothermics.2017.08.005.

[199] Nouri G, Noorollahi Y, Youse H. Geothermics Designing and optimization of solar assisted ground source heat pump system to supply heating, cooling and hot water demands 2019;82:212–31. https://doi.org/10.1016/j.geothermics.2019.06.011.

[200] Nouri G, Noorollahi Y, Yousefi H. Solar assisted ground source heat pump systems – A review. Appl Therm Eng 2019;163:1143–51. https://doi.org/10.1016/j.applthermaleng.2019.114351.

[201] Nouri G, Noorollahi Y, Youse H. Designing and optimization of solar assisted ground source heat pump system to supply heating , cooling and hot water demands. Geothermics 2019;82:212–31. https://doi.org/10.1016/j.geothermics.2019.06.011.

[202] Technical standards for the application of solar water heating systems in civil buildings （GB 50364-2018）. Ministry of Housing and Urban-Rural Development of the People's Republic of China; 2018.

[203] Lunde PJ. New heat transfer factors for flat plate solar collectors. Sol Energy 1981;27:109–13. https://doi.org/10.1016/0038-092X(81)90031-1.

[204] Peng X, Wang D, Wang G, Yang Y, Xiang S. Numerical investigation on the heating performance of a transcritical CO2 vapor-injection heat pump system. Appl Therm Eng 2020;166:114656. https://doi.org/10.1016/j.applthermaleng.2019.114656.

[205] Davis GL, Scott TC. Component , Modeling Requirements for Refrigeration System Simulation 1976.

[206] Heo J, Yun R, Kim Y. Simulations on the performance of a vapor-injection heat pump for different cylinder volume ratios of a twin rotary compressor. Int J Refrig 2013;36:730–44. https://doi.org/10.1016/j.ijrefrig.2012.10.015.

[207] Dobson MK, Chato JC. Condensation in Smooth Horizontal Tubes. J Heat Transfer 1998;120:193–213.

[208] McAdams WH. Heat Transmission. 3rd ed. New York: McGraw-Hill; 1954.

[209] Sparrow EM. Advances in Heat Transfer. Academic Press; 2018.

[210] Kleinbach EM. Performance Study of One-Dimensional Models for Stratified Thermal Storage Tank. Sol Energy 1990;50:155–66.

[211] Han YM, Wang RZ, Dai YJ. Thermal stratification within the water tank. Renew Sustain Energy Rev 2009;13:1014–26. https://doi.org/10.1016/j.rser.2008.03.001.

[212] De Ridder F, Coomans M. Grey-box model and identification procedure for domestic thermal storage vessels. Appl Therm Eng 2014;67:147–58. https://doi.org/10.1016/j.applthermaleng.2014.03.003.

[213] J Heat Transfer. Heat Exchanger Efficiency. J Heat Transfer 2007;129:1268–76.

[214] Xudong Z, Xiaoli M. Advanced Energy Efficiency Technologies for Solar Heating, Cooling and Power Generation. Springer; 2019.

[215] B E Noltingk. Mechanical Measurements. 4th Editio. Butterworth-Heinemann; 1985.

[216] CHN_Shanxi.Taiyuan. 537720_CSWD. Weather Data n.d. https://energyplus.net/.

[217] Taiyuan electricity price 2018. http://www.sdfcxw.com/dianfei/lvliang.html.

[218] Evans M, Yu S, Song B, Deng Q, Liu J, Delgado A. Building energy efficiency in rural China. Energy Policy 2014;64:243–51. https://doi.org/10.1016/j.enpol.2013.06.040.

[219] Zhu Saihong, Su Shan L shuang. The strategy of rural residential thermal environment adjustment in cold areas (in Chinese). Art Technol 2016;29:306–7.

[220] Shan M, Wang P, Li J, Yue G, Yang X. Energy and environment in Chinese rural buildings: Situations, challenges, and intervention strategies. Build Environ 2015;91:271–82. https://doi.org/10.1016/j.buildenv.2015.03.016.

[221] Zhang X, Shen J, Xu P, Zhao X, Xu Y. Socio-economic performance of a novel solar photovoltaic/loop-heat-pipe heat pump water heating system in three different climatic regions. Appl Energy 2014;135:20–34. https://doi.org/10.1016/j.apenergy.2014.08.074.

[222] The feed-in tariff price for PV panel 2018. http://www.ndrc.gov.cn/xwzx/xwfb/201712/t20171222_871333.html.

[223] Nottingham T, User NE. Wang , Zhangyuan (2012) Investigation of a novel façade-based solar loop heat pipe water heating system . PhD thesis , University of Nottingham . Investigation of a Novel Façade-Based Solar Loop Heat Pipe Water Heating System. 2012.

[224] Lin WM, Chang KC, Chung KM. Payback period for residential solar water

heaters in Taiwan. Renew Sustain Energy Rev 2015;41:901–6. https://doi.org/10.1016/j.rser.2014.09.005.

[225] Kannan R, Leong KC, Osman R, Ho HK, Tso CP. Life cycle assessment study of solar PV systems: An example of a 2.7 kWp distributed solar PV system in Singapore. Sol Energy 2006;80:555–63. https://doi.org/10.1016/j.solener.2005.04.008.

[226] The contaminants generated by per unit anthracite coal n.d. https://www3.epa.gov/ttn/chief/ap42/ch01/final/c01s02.pdf.